The Dissertation Committee for Stephany García Certifies that this is the approved version of the following dissertation:

Synthesis and Development of Novel Cost-effective Nanocatalysts for Hydrogenation Purposes

Committee:

Simon M. Humphrey, Supervisor

Bradley J. Holliday

Keith J. Stevenson

Richard M. Crooks

Brian A. Korgel

Synthesis and Development of Novel Cost-effective Nanocatalysts for Hydrogenation Purposes

by

Stephany García, B. S.

Dissertation

Presented to the Faculty of the Graduate School of

The University of Texas at Austin

in Partial Fulfillment

of the Requirements

for the Degree of

Doctor of Philosophy

The University of Texas at Austin

December, 2014

Dedication

Esta tesis está dedicada a mi eterna inspiración: Papá, te extraño, te amo y espero esto te haga muy orgulloso. Esta dedicación también es para la mujer que me enseñó el valor del esfuerzo, la disciplina y el compromiso. Gracias mami, por todo tu amor y apoyo, te amo!

Acknowledgements

I would like to start by thanking my research advisor Dr. Simon M. Humphrey for all his guidance, wisdom and infinite patience during my time in graduate school. I would also like to acknowledge my research group for all the support and motivation: to Dr. Ana Nuñez, thank you for the many laughs, great memories, and for keeping my Spanish alive; to Alisha Bohnsack, thank you for your friendship, for the infinite head scratches and braids, and for all the great book discussions; to Dr. Ilich Ibarra, thank you for being one of my biggest supporters; to Nolan Waggoner, thank you for all the taco runs and the great talks about everything in the world that does not involve chemistry (especially about Colombia!).

I would like to express gratitude to all my collaborators for all their great scientific input. Many thanks to all the fantastic researchers at the Texas Materials Institute, including Dr. Hugo Celio, Dr. Andrei Dolocan and Dr. Karalee Jarvis. I would like to express great gratitude to Dr. Vince Lynch for lightening such a daunting topic such as crystallography and for reminding me, every so often, of why I'm passionate about science. I would also like to show appreciation to Dr. Liang Zhang, Dr. Graeme Henkelman, Rachel Anderson, and Dr. Richard Crooks for their scientific knowledge and reliability.

I am grateful for the amazing friendships I have built during my time at UT, so I would like to acknowledge Dr. Kate Biberdorf and Owen Williams for all their support, motivation and for all the welcomed distractions as the three musketeers. I would also like to thank Nellymar Membreño, Rachel Anderson, Marlene Gutierrez, Leigh Krueger,

Karen Scida and Katharine Diehl for all the adventures, stories, and best times I've had in Austin (from day one of graduate school).

I cannot express enough gratitude to my family who has been by my side every step of the way. Thank you for being my biggest supporters, for all the sacrifices you have made to help me achieve my dreams and most importantly, for believing in me. To Dr. Paulo Garcia, thank you for understanding who I am as a person, for all your advice and support, and for never letting me give up. To Steven Shaw, infinite thanks for holding my hand through tough times, for cheering me on, and for always letting me know how proud I make you. I cannot imagine going through all of these endeavors without my family's love and care.

Synthesis and Development of Novel Cost-effective Nanocatalysts for Hydrogenation Purposes

Stephany García, Ph. D.

The University of Texas at Austin, 2014

Supervisor: Simon. M. Humphrey

This research has focused on the controlled synthesis of mono- and bimetallic noble metal nanoparticles (MNPs) for catalytic applications.

MNPs such as Au, Rh, Pd, Pt and Ag have been synthesized with the aid of microwave heating (μwH) which provides a greener heating method. Furthermore, it provides kinetic control over the size, shape and composition of these NPs. Several bimetallic core-shell NPs have also been synthesized using this method, making it possible to overcome thermodynamic energy barriers that arise with this type of assembly when the metals used, greatly differ in surface energy and lattice constant. It has also been possible to tune the shell thickness of the NPs in order to have an impact in the kinetics of hydrogenation catalytic processes performed. 'Non-equilibrium' alloyed structures have been generated in the nanoscale as well, with the aid of μwH. These types of nanostructures are of particular interest because due to synergistic effects, the mixture of heteroatoms resulted in enhancement of catalytic activity and in chemical/physical stability in comparison to their monometallic components. These Rh_xM_{100-x} (M = Ag or Au) NPs displayed remarkable catalytic activities, as compared to pure Rh NPs. Furthermore, the composition was systematically varied in order to optimize the catalytic properties. These experimental observations were supported by theoretical modeling and

calculations (DFT). Thus, very cost effective nanocatalysts have been prepared by diluting relatively inexpensive and catalytically inactive metals, such as Au and Ag, with active precious metals such as Rh.

This research has also focused on the design and synthesis of novel capping agents for small metal NPs. The ultimate goal is to generate self-activating particles that when placed in a hydrogenation catalysis environment (reducing conditions), these will chemically rid themselves of the stabilizing agents in a clean and controlled fashion under mild conditions. Thus, naked NPs that are extremely active and still have defined facets that can potentially provide selectivity in certain catalytic processes will be left behind. These NPs are more cost-effective and have a lower impact on the environment due to the milder reaction conditions applied, yielding great candidates for hydrogenation catalysts in industrial processes.

Table of Contents

List of Tables

List of Figures

List of Schemes

1. Introduction

1.1 Noble Metal Nanoparticles

Metal nanoparticles (MNPs) are metallic structures, in which at least one of the dimensions falls in the range of 1 nm to 100 nm.[1] Recently, the study of noble MNPs has gained interest due to their tunable magnetic,[2–4] optical,[5–7] and catalytic[8–10] properties. Currently, a major goal in nanoscience is the development of synthetic routes and techniques that allow for the precise control of the size, shape and assembly of these types of materials.[11] Synthetic control is vital because the aforementioned properties are directly dependent on these parameters;[12] thus, magnetic, catalytic and optical properties can, in principle, be tailored by synthetic design. In the nanoscale, unlike for bulk materials, size and shape are physical features that directly affect solid-state phenomena.[13] Hartog and Van Hardeveld have reported that the ratio of (111) and (100) planes exposed on the MNPs (which induce selectivity in catalytic cycles) can vary with size.[14] In fact, the biggest changes in facets, edges and corners in NPs occur in the size range of 1 nm to 5 nm.[15]

NPs are usually considered as a hybrid between homogeneous and heterogeneous catalysts.[16] Analogous to molecular catalysts, they are soluble metallic structures with high surface areas. Furthermore, they possess multiple edges, corners and kinks that

---

The work in this chapter has been previously published as a book chapter ("Microwave-assisted synthesis of metallic nanoparticles." Garcia, S.; Piburn, G. W.; Humphrey, S. M., *Microwave Engineering of Materials and Nanomaterials*, Pan Stanford Ed., 2014.). Humphrey, S. M. conceived the scientific idea and Garcia, S. and Piburn, G. W. collected previously reported data and wrote the book chapter.

provide enhanced reactivity, while still conserving selectivity. They are equally similar to heterogeneous catalysts in that they are recyclable, and the chemistry is surface-based.

It is of critical importance to develop synthetic methods that provide control over size and shape, as these can lead to the establishment of correlations between nanoparticle structure and performance. Thus, target properties like catalysis, can be optimized. Classical, 'top-down' approaches to prepare MNPs such as mechanical grinding of bulk metal are ideal for large-scale preparations, but they are severely limited by the failure to obtain very small particles, and by the size and morphological non-uniformity of the resulting MNPs.[17–19] Conversely, 'bottom-up' approaches—which rely on the controlled reduction of molecular metal precursors to construct larger clusters and particles—usually suffer from scalability issues, but importantly offer vastly improved control over MNP size, shape and functionalization.[1,19–21] Indeed, it has been shown that extremely small (>1.5 nm) MNPs can be obtained, in which small clusters of atoms (*e.g.*, Ag_4, Rh_{55}, Pt_{147}) display atomic packing arrangements that differ from the bulk metal.[22–25] Arguably, the most common type of bottom-up synthetic approach involves the solvent-based *in situ* chemical reduction of readily-available metal precursors (*e.g.*, metal halides, nitrates, acetates, simple organometallic species, *etc*.) in the presence of suitable reducing agents,[19] or alternatively by using the solvent itself as a sacrificial reductant (*e.g.*, the polyol method).[26,27] It is also common for surface passivation ligands, or 'capping agents', to be employed. These are commonly organic molecules, polymers, or bulky ions that bind weakly to the surfaces of the growing MNPs, thus inhibiting particle-on-particle aggregation.[28,29] In some cases, capping agents have been shown to preferentially bind to certain faces of growing MNPs, which pacifies growth along certain atomic directions and can result in enhanced morphological control of the resulting structures.[30–32] An extensively-used capping polymer and flexible

membrane for both metallic nanocrystals and metallic colloids is *poly*(vinylpyrrolidone) (PVP) since it easily affords control of size and even morphology, in some cases.[15,33] However, it has also been reported that surfactants like PVP can diminish the catalytic activity of the nanoclusters produced,[34–36] as the capping functional groups can strongly interact with the catalytic metal, thus resulting in significant surface interactions.[33,37] Manipulation of the interaction between the stabilizer and the nanoparticle surface can lead to the design of more efficient stabilizing ligands that can also help find a balance between catalytic activity and stability. Thus, it is also imperative to control the properties of the capping agents used for stabilization,[38] in order to maximize the catalytic potential of the MNPs.

Physical parameters such as reaction time and temperature have also been shown to play vital roles in the synthesis of defined MNPs. Some less obvious reaction parameters such as precursor addition rate or reaction stirring rate are also important in ensuring reproducibility between individual reactions.[39,40] Furthermore, the kinetics that govern the initial phases of MNP nucleation are quite different to the kinetics that control subsequent growth at existing nucleates to yield larger MNPs.[21,41] For this reason, seeded growth methods have been recently developed as a synthetic route for NPs. It is a two-step approach in which the thermodynamically disfavored nucleation process is separated from growth steps that usually occur spontaneously by the addition of monomers to the existing NPs (Scheme 1.1).[34] The seeds are generated by fast reduction of a given metal in solution at high temperatures in the presence of stabilizing agents, and are then isolated, purified and functionalized as needed. Growth can occur with the addition of further metal to the seeds under conditions that prevent nucleation of this new metallic particles.[42]

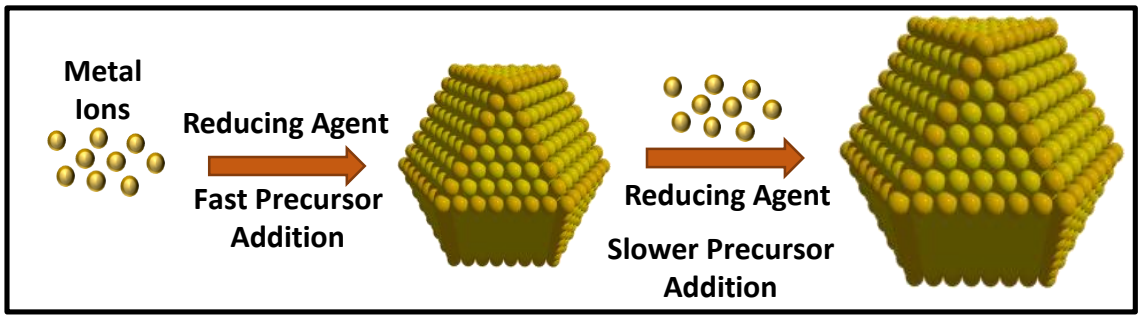

Scheme 1.1. Schematic representation of a seeded growth synthetic method in which the nucleation process is separated from subsequent growth steps.

These physical effects have been thoroughly examined in a number of seminal reports, the details of which are too numerous to cover in detail in this dissertation. However, it is important to acknowledge that the coupling of these factors with the vast library of solvents, metal precursors and additives available, provide a wealth of synthetic possibilities. A multitude of methods for the preparation of a vast array of MNPs have been reported in a relatively short period of time. Unfortunately, many existing methods are not generally applicable to the synthesis of a broad range of MNPs, and many are fraught with difficulties concerning reproducibility.

1.2 Microwave Synthesis of Noble MNPs

MNPs display properties and chemical behaviors that vastly differ from those of bulk metal due to quantum size confinement effects[43] caused by their inherent high surface area to volume ratios.[44] However, these spectroscopic, electronic and chemical properties are greatly dependent on shape (surface structure) and size; thus, it is relevant to have control over these parameters during the synthesis of uniform NPs. Microwave

heating (μwH) provides many advantages to the controlled synthesis of metallic nanostructures. For instance, μwH affords bulk heating of the reaction medium without gradients, and having randomly dispersed hot spots. Furthermore, it efficiently transfers heat to reactants in the reaction vessel, reducing crystallization times.[45,46] Thermal induction periods can also be shortened using μwH. This heating regime is also known to generate localized high temperature regions where ion reduction takes place at a faster rate compared to convective heating.[45] Since the early studies of nanocrystal formation, it has been known that a clear distinction between the nucleation and growth stages in a reaction mechanism is required in order to access uniform nanostructures with narrow size distributions.[47] This means that in order to prepare highly uniform NPs, it is necessary to have a controlled nucleation event and to prevent further nucleation from occurring during subsequent growth processes.[48] Due to the rapid heating rates, reduction of thermal gradients and higher effective temperatures that μwH provides, it offers ideal conditions for homogeneous nucleation and controlled growth of nanocrystals.

Depending on the microwave absorption capabilities of the solvents used during synthetic processes, superheating of the solvent above the normal boiling point can also be achieved as a consequence of microwave dissipation throughout the reaction volume.[45] Since NP formation in solution is a heterogeneous process that follows nucleation and growth in succession, the sorption properties of the solid (solid-liquid interface) play a dominant role.[49] It is believed that the accessibility of higher temperatures can lower both thermodynamic and kinetic barriers at this interface, facilitating growth and formation of different morphologies.[50] Selective heating and energy variation of intermediates also lead to surface structure control, because these parameters can induce preferential growth of some crystalline facets over others, thus potentially yielding a wide range of shapes. Therefore, the increased reaction rates and enhanced crystallinity observed in inorganic

nanostructures synthesized using μwH are partly attributed to the high effective temperatures that metal ions and the reaction medium can reach. This high temperatures also aid in the selective decrease in energy of intermediate species.

1.2.1 Equipment

Microwaves are generated using a magnetron. A magnetron is a thermoionic diode consisting of a cathode that is directly heated and an anode that contains an even number of cavities. Electrons are released as the cathode is heated and these are attracted to the anode. The cavities in the anode behave as tuned circuits while the gap across the edge of each cavity acts as capacitance. The anode is comprised of a series of circuits that are tuned to oscillate at a target frequency, or its overtones.[51] A magnetic field is applied to the anode in a perpendicular fashion to bend the electrons' path as they travel from the cathode to the anode. These deflected electrons then pass through the cavity gaps, which induces a small charge into the circuits, thus generating oscillation of the cavity itself. This oscillation process continues until it has achieved a high enough amplitude, and the electromagnetic energy is then transferred away from the anode using an antenna.[51]

Microwaves can vary in frequency between 0.3 and 300 GHz and the corresponding wavelength can fluctuate between 1 mm and 1 m. However, microwave ovens usually operate using photons with a frequency of 2.45 GHz (12.2 cm wavelength). This frequency roughly translates to an energy value of 1 $J \cdot mol^{-1}$. This energy is too low to cleave bonds; hence, it only affects molecular rotations within the reacting species.

Although domestic ovens and dedicated microwave reactors both function utilizing photons of similar frequency and wavelength, the use of domestic microwave ovens for research purposes is discouraged. The microwave density in a household

microwave oven is not homogeneous throughout the cavity. For this reason, certain experimental parameters such as reaction temperature, pressure and irradiation power cannot be precisely monitored using domestic ovens, which restricts reproducibility and can represent safety concerns when performing experiments. Moreover, in specific research cases where the species being heated are poor absorbers of microwave energy or are only available in small quantities, multi-mode or continuous mode ovens do not heat the materials effectively. In such cases, a different experimental set-up should be used in which a single mode resonant cavity is tuned to the characteristics of the material being heated. This is especially helpful if the materials need to be heated to high temperatures in a controlled fashion.[51] Single mode ovens with options for batch or continuous processing have only been designed for research purposes given that this experimental set-up is more expensive.[52]

Modern and commercially-available dedicated research instruments are equipped with built-in magnetic stirrers, and pressure and temperature sensors that allow for the accurate control of these parameters. In addition, they are also usually coupled with software that automatically adjusts the power output of the reactor in order to regulate the temperature and pressure of the reaction throughout the synthetic process[46] as can be observed in Figure 1.1. A thorough review of instrumentation currently available for microwave ovens can be found in the book recently published by Kappe, Dallinger and Murphree.[53]

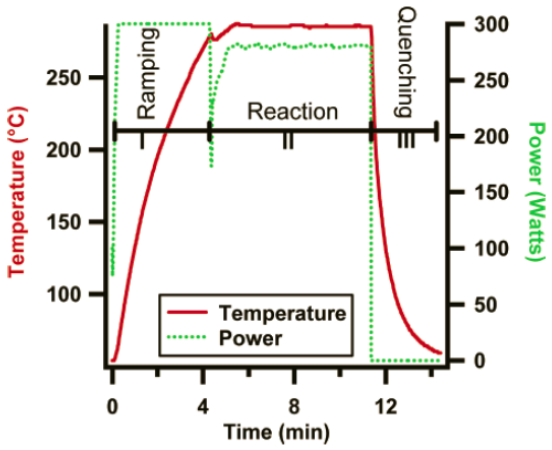

Figure 1.1. Temperature (°C) and power (W) profiles of a typical nanoparticle synthesis reaction (InGaP synthesis). During the reaction period (II), power output is regulated by the microwave reactor in order maintain a constant temperature throughout the process. Reprinted (adapted) with permission from Ref. 50. Copyright 2014 American Chemical Society.

1.2.2 Heating Mechanism of Microwave Heating

To prevent interference with wireless communications, the microwave units used in industry, science, and medicine are restricted to five different frequencies; 2.45 GHz is by far the most common.[54] The energy of the photons produced by such devices is $1x10^{-5}$ eV, which is on the same order as molecular rotations.[55] Distinct rotational modes are observable for polar gas molecules *via* microwave spectroscopy. Due to molecular collisions in liquids and restricted motion in solids, discrete signals are quenched and unobservable in other phases.[56]

μwH is an example of dielectric heating, since it converts energy from an alternating electric field (often in the form of electromagnetic radiation) into heat by a dielectric material. When exposed to an external electric field, polar molecules will try to

align themselves with that field; if the direction of the field oscillates, the molecules will rotate to stay aligned with the field. In liquids, field oscillations of up to 10^6 Hz are easily accommodated by the already rapidly rotating molecules. The alternating flow of charge generated as the dipoles rotate is known as the Maxwell displacement current, and at these lower frequencies it stays 90° out of phase with the fluctuations of the electric field. Above 10^{12} Hz, the molecules cannot move significantly before the direction of the field reverses, so no displacement current is produced. No heating occurs in either case.

The microwave region lies between these two extremes: the frequency of the electric field oscillation is slow enough that polar molecules rotate sympathetically with the field, but it is fast enough that they cannot keep pace perfectly. The increase in the lag phase between the displacement current and the electric field results in a component of the current that directly opposes the field. This resistance is related to collisions between the rotationally excited molecules and is responsible for producing heat. It also helps to explain the decrease in the penetration depth of μwH as the frequency of the radiation increases. The resistive current weakens the electric field as the field travels into the medium, until such time that the energy is entirely dissipated as heat. As the lag between the displacement current and the electric field grows larger, so does the resistive component of the current, decreasing the distance the radiation can travel into the medium.[57]

In addition to its rotational effects on polar molecules, microwaves can also transfer energy to ions by dragging them back and forth as the electric field oscillates. Maxwell displacement current arguments similar to those discussed for rotating dipoles can also be constructed for ionic conduction. Ions have full positive or negative charges rather than partial ones like dipolar molecules, so the interaction between ions and the electric field is much stronger and is responsible for more heat per particle than dipole

polarization.[53,57] This variant of the μwH mechanism dominates in solids, where rotation is severely restricted.

1.2.3 Dielectric Properties: Requirements and Parameters

It is undeniable that microwave chemistry generates enhanced results compared to convective heating. However, the exact reasons why this success is observed when using μwH is still a topic of controversy. The dispute usually revolves around the issue of how to rationalize the observed outcomes and this leads to thermal and non-thermal effects. Thermal effects are those generated by different temperature regimes such as rapid heating and high bulk reaction temperatures. Non-thermal effects are those related to the microwaves themselves and not caused by differing temperature regimes; they are believed to arouse from a direct interaction of the electromagnetic field with the reacting molecules, intermediates or even transition states.[58] However, non-thermal effects are still not well understood. For this reason, this section will be focused on the thermal effects caused by μwH mechanisms.

As mentioned above, the mechanism of μwH involves two main processes: dipolar polarization and ionic conduction.[59] Electromagnetic radiation produces an oscillating field that causes the dipoles and ions to continually attempt to realign in the electric field. Depending on the frequency of the irradiation and the time it takes for the dipoles and ions to align and misalign with the field, the molecules might have the ability to release heat *via* molecular friction or dielectric loss,[60,61] minimizing thermal gradient effects[62,63] that lead to poor nucleation processes and broadened size distributions in nanomaterials.[50] In order to produce resistive heating in the reaction medium, the dipoles should lag behind the electric field oscillation but the frequency of the field should not be

that much greater than the response time of the dipoles.[46] In other words, the dipoles should still have time to realign themselves with the field. This type of heating is commonly referred to as dielectric loss and it refers to the input of microwave energy that is lost to the sample by being dissipated as heat.[64] Electronic and atomic polarizations are much faster (10^{-9} Hz) than the frequency of the microwaves, which means that they do not contribute to μwH effects.[51] Thus, this effect is mostly observed for polar molecules.

Ionic conduction is based on the oscillation of dissolved charged particles under the influence of μwH, generating collisions among neighboring particles that ultimately create heat.[46] The irradiated sample can act as an electrical conductor enabling charged particles such as ions and electrons to move through the material under the influence of the electric field, causing polarization within the sample and inducing currents that generate heat as a result of electrical resistance.[60] Figure 1.2 depicts this homogeneous heating effect. It is relevant to mention that the ionic conduction mechanism has a greater impact than dipolar polarization in μwH, yielding enhanced results for the synthesis of NPs in ionic liquids.

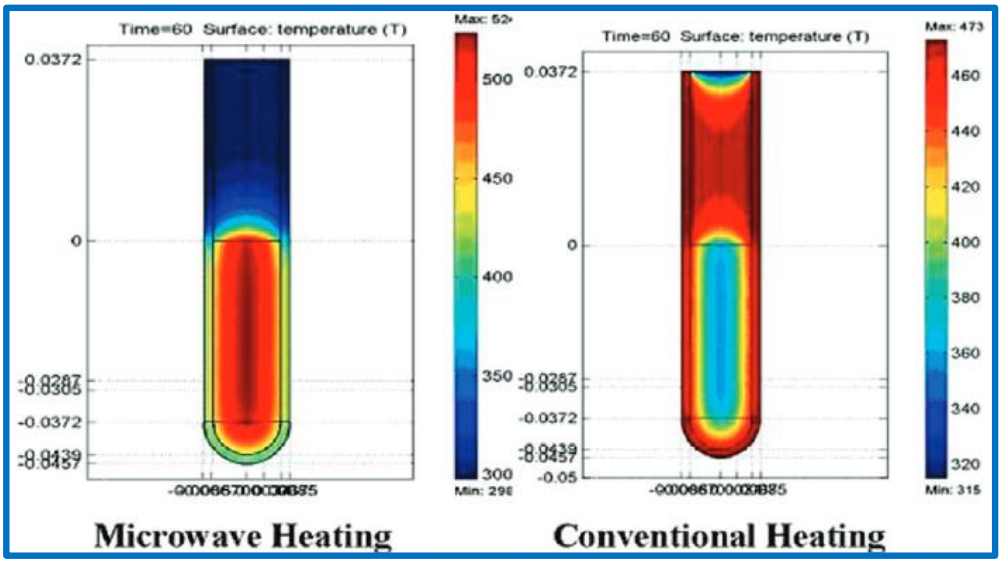

Figure 1.2. Temperature profile of reaction vessel after 60 sec of μwH exposure (left) and convective heating using an oil bath (right). μwH simultaneously increases the temperature of the entire reaction medium; whilst using conventional heating, the reaction medium that is in contact with the vessel wall achieves higher temperatures first compared to the rest of the reaction (temperature gradient). Reproduced with permission from Springer Science+Business Media B.V., [ref. 65].

The dielectric properties of a substance can be defined by two parameters: the dielectric constant and the dielectric loss. The dielectric constant (ε′) is the ability of a molecule to be polarized by an electric field. The dielectric loss (ε″) is the efficiency with which the energy of electromagnetic radiation can be converted to heat.[51,61] The ability of the material to convert electromagnetic energy into heat at a certain temperature and frequency is then expressed by the ratio of these two parameters, and it is defined as the dielectric loss tangent (tan δ= ε″/ε′). Thus, a material with a high loss factor will efficiently convert electromagnetic radiation into heat and will in turn rapidly heat. This means that the loss tangents of solvents depend on the relaxation times of the molecules,

which are clearly related to the nature of the specific functional groups, and the volume of the molecules. Having these criteria in mind, it is possible to categorize solvents based on their microwave absorbing properties. Solvents with a loss tangent greater than 0.5 are consider to be high absorbers while solvents with loss tangents between 0.1 and 0.5 are categorized as medium absorbers. Solvents with a loss tangent of less than 0.1 are weak absorbers, and may sometimes be referred to as microwave transparent (non-absorbing).

Since the energy output is not great enough to induce chemical reactions, microwave-enhanced chemistry relies on the efficient heating of materials. For this reason, it is helpful to have components in a chemical reaction that strongly couple with microwave energy in order to potentially achieve higher heating rates than those attained using convective heating. Organic and inorganic solvents with low molecular weight and high dipole moments effectively couple with microwaves with a frequency of 2.45 GHz.[51] Furthermore, it is beneficial to carry out reactions in solvents with dielectric constants that vary from that of the reactants in order to induce selective μwH. Selective heating enhances energy transfer directly to the reactants, which triggers an instantaneous internal temperature increase.[57,64] This rapid temperature change lowers the activation energy of the reaction, as compared with conventional heating methods, and enhances the reaction rate accordingly.[66] On the other hand, if metal precursors with large microwave absorption cross sections (relative to the solvent) are used, high effective reaction temperatures can be achieved, leading to the rapid decomposition of the precursors used and to the creation of highly supersaturated solutions. These conditions promote nucleation and growth of NPs in solution, which favors the formation of small nanocrystals depending on the supersaturation degree of the solution.[67,68] The synthesis of bimetallic NPs is dependent upon the decomposition profiles of the metals involved. In the case of core-shell NPs, the shell atoms heterogeneously nucleate on pre-existing core

nuclei so the decomposition profiles of the metals can vary without having a great impact on the synthetic method. However, in the case of binary alloys, the experimental conditions should ensure that the decomposition profiles of the metal precursors are similar, or close to identical, in order for a binary nucleation event to take place and for the initial nuclei composition to reflect the molar ratio of the metals added.[62] In either case, microwave-assisted synthetic methods can yield nanomaterials with narrow size distributions by reducing the formation of agglomerates when the starting materials are rapidly consumed, and when the chemical reaction is kinetically driven.[60]

It is relevant to note that strongly absorbing solvents have been classically used in the fabrication of inorganic NPs using convective heating, especially in bottom-up approaches and the so-called polyol method, which involves the chemical reaction of metal salts with glycols.[69–71] Polyalcohols like ethylene glycol, propanediols and butanediols have permanent dipoles that result in high loss tangents, which makes them ideal candidates for microwave synthesis.[46] Moreover, polyol solvents act as both dissolving medium and reducing agents at high temperatures. In a typical polyol process, the polyol decomposes homogeneously at raised temperatures yielding reducing species for the reduction of the metal ions.[72] This mechanism provides certain level of control over the size distribution and shape of the NPs being synthesized.

Exposing metal powders to microwave fields result in very high temperatures that have been used to form ‘hot spots’ that dramatically affect the reaction heating rates of the metals with gases and other organic and inorganic substrates.[52,61,73] ‘Hot spots’ occur due to discrepancies in the electric field and energy distribution within the microwave cavity. Although in some cases, mostly organic syntheses, ‘hot spots’ may be considered an undesirable effect,[74,75] they are very advantageous in inorganic syntheses; especially in MNPs syntheses as they are believed to serve as nucleation sites.

1.3 Direct Microwave-Assisted Synthesis of Unsupported MNPs

The direct synthesis of unsupported MNPs—whose surfaces are pacified with capping agents—is a popular strategy because such MNPs can be easily isolated by precipitation and subsequently re-dispersed in a number of alternative solvent systems. The chemical identity of the particular surface passivating agent employed in a given synthesis commonly determines which solvents can be used to form stable MNP dispersions. Hence, this synthetic strategy offers attractive flexibility for a range of subsequent applications, such as controlled deposition onto secondary support materials in the construction of heterogeneous catalyst composites.[76,77] Alternatively, MNPs synthesized in strongly reducing solvents can be isolated and transferred into biologically-compatible solutions for use in biomedical applications such as DNA tagging.[78–80]

The controlled synthesis of unsupported MNPs has attracted a great deal of attention in the past two decades due to their tunable chemical properties that greatly differ from bulk metal surfaces, and also for their high surface-area-to-volume ratios that provide enhanced catalytic activity.[10,81] The vast majority of previously reported methods utilize conventional heating to facilitate reduction of metal precursors, using one-pot protocols that involve the chemical reduction of metal salts in aqueous solution, or by using reducing organic solvents (*e.g.*, alcohols, *N,N*-dimethylformamide; DMF). Similar methods have recently been studied using μwH as the mode of heating, with the intention of determining how microwaves affect MNP formation in solution.

1.3.1 Monometallic NPs

Perhaps the best starting point for this discussion is the synthesis of AuNPs, which represents one of the most well-studied systems to date. The microwave-assisted preparation of AuNPs of various sizes and shapes was reported by Kundu *et al.*, who used 2,7-dihydroxynaphthalene (2,7-DHN) to reduce Au^{3+} ions in aqueous solution.[82] It was shown that variation of the ratio of metal precursor to capping agent (cetryltrimethylammonium bromide; CTAB) as well as the concentration of 2,7-DHN selectively afforded a range of particle shapes such as trigonal prisms, rods or nanospheres (cuboctahedra). Under μwH, it was possible to obtain large (20+ nm) but well-defined AuNPs in only 90 s. El-Shall and co-workers proposed that the size and morphology of AuNPs obtained under μwH can be tailored by adjustment of the concentration of Au^{3+} ions in solution, the microwave exposure time, and the ratio of capping agents in a mixture of oleic acid and oleylamine (OAc/OAm), as depicted in Figure 1.3.[68] It was suggested that the presence of polar carboxylate functional groups in OAc increased the growth rate and also enhanced the formation of more anisotropic shapes through the formation of stronger OAc-AuNP capping interactions at particular faces of the growing crystals. In the absence of OAc, only spherical AuNPs were obtained. A previously reported (and somewhat counter-intuitive) observation was also confirmed in this work, whereby increasing the heating duration, ramping rate and reaction temperature smaller AuNPs with narrower size distributions were afforded.[83] In comparison to conventional synthesis methods, the physical effects of μwH have been found to strongly influence the size and morphology of AuNPs in a number of ways.

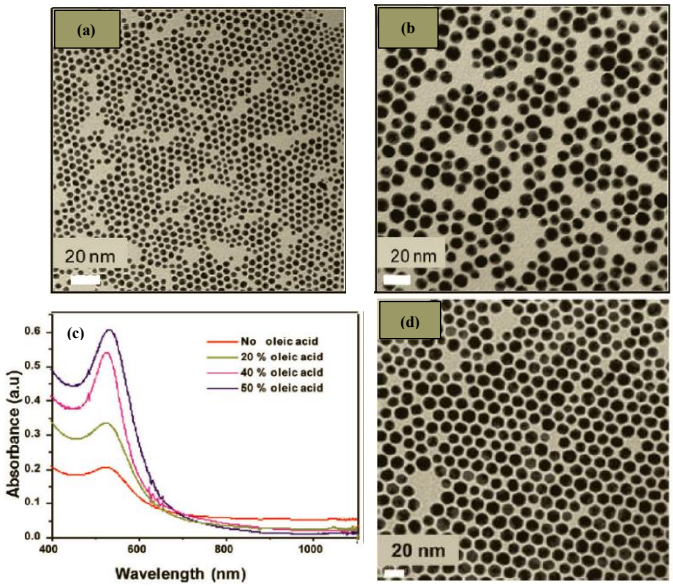

Figure 1.3. TEM images of AuNPs prepared by μwH methods after 60 s exposure using a fixed concentration of HAuCl4 precursor and (a) pure oleylamine and (b) 1:1 ratio of oleic acid:oleylamine as capping agents; (c) the UV-vis spectrum displays a clear change in plasmon resonance of AuNPs as a function of varying ratios of OAc to OAm. Shifts in the plasmon resonance of these nanostructures are strongly related to changes in average AuNP size and distribution; (d) a TEM image of AuNPs prepared using 9mM of Au3+ ions in the presence of 3:1 OAc/OAm. Reproduced with kind permission from the American Chemical Society, [ref. 68].

The synthesis of AgNPs has also been widely studied, due in large part to their potential antibacterial properties. Microwave-based procedures to obtain AgNPs have focused on 'green' reactions. For example, uniform AgNPs have been prepared using basic amino acids as reducing agents, soluble starch as a surface stabilizer, and by irradiation for only 10 s.[84] Near-monodisperse AgNPs have also been prepared using carboxymethyl cellulose sodium (CMS) as both reducing and capping agent in a green microwave-assisted synthesis.[85] A detailed review of these types of methodologies has

been reported by Sharma and coworkers.[86] NPs of Ag and Au have also been prepared with the use of organic solvents such as DMF and organic polymer stabilizing agents, such as the ubiquitous *poly*(*N*-vinylpyrrolidone) (PVP). It has been shown that small (*ca.* 3.5 nm) and near-monodisperse Ag and AuNPs are preferentially formed in the presence of PVP and DMF under μwH, compared to conventional heating which yields much larger structures. It was suggested by Pastoriza-Santos and Liz-Marzán that complexation of metal ions by PVP and their subsequent reduction occur under favorable conditions due to μwH because both PVP and DMF contain polar functional groups that couple strongly with microwaves.[87]

It has similarly been shown that small (3.6 nm) and near-monodisperse PtNPs can be formed rapidly using μwH because the metal precursors employed are also strongly coupled with microwaves.[88,89] Such is the case for the reduction of H_2PtCl_6. This convenient and widely available Pt precursor induces such a high degree of heating homogeneity under μwH that even stirring of the reaction is not always necessary to obtain defined products (see Figure 1.4).[88] Size-controlled synthesis of PtNPs has also been achieved by μwH of aqueous solutions of the same Pt^{4+} precursor in the presence of 3-thiophenemalonic acid.[90]

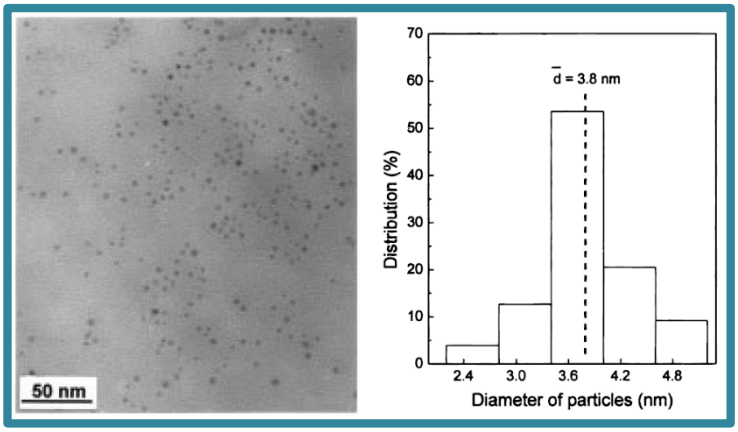

Figure 1.4. TEM image and histogram of PVP-stabilized Pt colloids synthesized by μwH without any magnetic stirring. Reproduced with the permission from the American Chemical Society, [ref. 88].

μwH has also been exploited in the rapid formation of monometallic Ru, Rh, Pd, Cu and Ni NPs by exposure of cationic molecular precursors to repeated cycles of μwH that aid in metal ion reduction by DMF.[62] In most cases, the particles are stabilized with monomeric capping agents such as OAc/OAm mixtures. In the same study, adjustment of μwH time allowed the resulting mean MNP size to be adjusted.

Ionic liquids (ILs) are excellent absorbers of microwaves since they are highly polarizable and exhibit large ionic conductivities. For this reason, they have been used in microwave-assisted preparation of MNPs. A one-step procedure has been reported by Ren *et. al.*, in which AuNPs are afforded *via* μwH in a variety of ILs (*e.g.*, imidazolium- and pyridium-based ILs with different anions such as PF_6^-, $[Tos]^-$ (*p*-toluene sulfonate) or Br^-) and notably in the absence of any other solvents or reducing agents.[91] It was shown that the anionic components of the ILs employed were most influential in the resulting topologies of the MNPs; it is expected that negatively charged fragments

interact most closely with the MNP surfaces in the formation of charge bilayers.[92] It was also established that reaction temperature and the heating regime were key parameters in the control of morphology and size of these Au nanoclusters.

Organic solvents such as polyols that have the ability to serve as both the reducing agent and reaction medium are broadly used in microwave-assisted chemical synthesis of MNPs due to their high microwave absorption capabilities. 3*d*-MNPs comprising Cu, Ni and Co have been fabricated using a microwave-assisted hydrothermal process developed by Komarneni and co-workers.[93] They observed that the kinetics associated with the formation of these MNPs increased by at least an order of magnitude compared to convective heating techniques. Microwave-assisted reactions also promoted reduction of the 3*d*-metal precursors at lower temperatures than were required to reduce the same metals under conventional heating. Suryawanshi *et al.* employed a similar methodology for the preparation of RuNPs (Figure 1.5a).[94] Parameters such as reaction temperature, time and irradiating power were systematically varied in order to determine their individual effects on the products. Lower reaction temperatures led to the formation of larger RuNPs. High irradiation power (400 & 500 W) led to rapid heating rates and favored the formation of very small Ru nuclei. The interaction between stabilizer and RuNP surface was in turn weakened as the effective concentration of capping agent was reduced with the increase in number of Ru seeds; this ultimately led to agglomeration. Conversely, low irradiation power (100 & 200 W) increased the induction period required for the onset of RuNP nucleation, which in turn shortened the actual reaction time and resulted in the formation of fewer, larger RuNPs. Control over the size of NiNPs can also be achieved through the passivation of NP surfaces using a combination of capping ligands: dodecylamine and PVP capping agents have been jointly utilized for the

stabilization of uniform NiNPs with an average diameter of 63 nm, generated using a polyol approach in a microwave reactor (Figure 1.5b).[95]

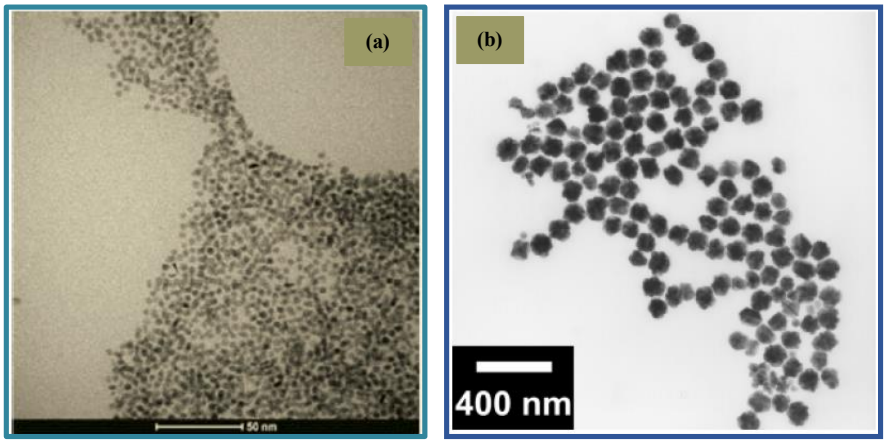

Figure 1.5. TEM images of PVP-capped microwave-synthesised (a) RuNPs and (b) NiNPs with narrow size distributions. Reproduced with the permission from John Wiley and Sons, [refs. 94 and 95, respectively].

1.3.2 Bimetallic NPs

Bimetallic NPs have attracted significant attention in the past few years due to the enhanced optical and catalytic properties that are obtained due to *d*-band intermixing and quantum size confinement effects.[45] Bimetallic MNPs can be broadly divided into two categories: core-shell MNPs in which the two metals are segregated at a common interface, and alloyed MNPs in which two metals are mixed throughout. Both types of MNPs usually display surface plasmon band energies that differ relative to their monometallic counterparts. Bimetallic MNPs can also exhibit enhanced surface catalytic

properties because the original reactivity of metal 'A' can be tuned by interaction with metal 'B' to achieve optimal resulting reactivity for a given reaction. This effect can even be observed for combinations of metals in which one of the metals is not catalytically active in isolation. Thus, bimetallic MNPs can provide advantages for the preparation of cost-effective nanomaterials, in which expensive and rare metals can be diluted with more earth-abundant metals.

A number of important physical parameters facilitate or restrict the generation of heterobimetallic nanospecies. Crystal packing parameters are intrinsically important for the preparation of both core-shell and alloy MNPs. Metals with common crystal packing arrangements are more likely to form ordered interfaces, or to form mixed alloy phases. Even so, combinations of metals that share the same crystal structure but have significantly different lattice parameters (corresponding to their respective atomic radii) might not form stable alloys or core-shell structures. Some combinations of metals will lead to metastable arrangements, while other combinations of metals may be entirely thermodynamically unstable (otherwise termed immiscible metals). So-called strain effects may be induced when a few monolayers of metal A are deposited over metal B, in which there is a lattice mismatch between A and B. Such considerations are identical to those encountered in bulk alloy chemistry,[96] but it should be noted that combinations of metals that are thermodynamically unstable in the bulk can often be rendered stable (or metastable) on the nanoscale.[97,98] This section provides a summary of known examples of microwave-assisted methodologies that have been employed to prepare heterobimetallic MNPs for specific applications.

1.3.2.1 Core-shell NPs

Microwave-assisted synthesis of core-shell NPs has been performed in a two-step process that involves formation of monometallic core MNPs followed by over-growth of a shell layer using a secondary metal precursor onto the pre-existing core MNPs (Scheme 1.2).[62] Since no two metals have exactly the same lattice parameter, strain properties are usually imposed in core-shell MNPs for which the shell thickness is less than 5 or 6 monolayers. MNPs with thicker shells show greatly reduced strain effects because atoms on the surface are sufficiently distant from lattice mis-matching effects at the bimetallic interface. In instances where the shell is comprised of only 1-2 monolayers, electronic interactions can also be observed even though the metals are not actually alloyed.[99,100]

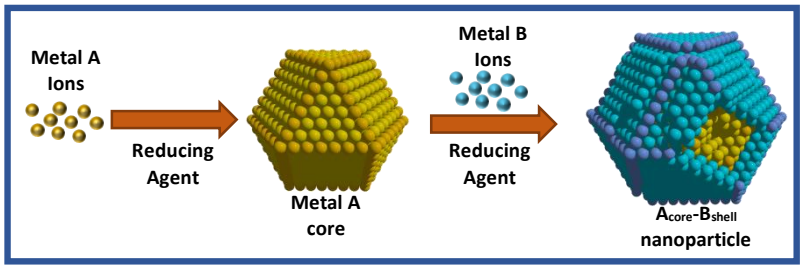

Scheme 1.2. Schematic representation of the proposed two-pot growth mechanism of core-shell MNPs in which the metal core is first synthesized and isolated. Metal ions of the target shell metal are then reduced and deposited on the existing nuclei.

The benefits of μwH have been established in the synthesis of Cu-Ag core-shell MNPs.[101] These heterostructures have been shown to display excellent temporal and thermal stability against oxidation because the Ag shell provides an effective physical barrier to oxygen, while there is a beneficial electronic interaction between Cu and Ag at

the interface. Another example is the microwave-assisted preparation of PVP-capped Ag-Au core-shell structures by reaction in ethylene glycol or glycerol.[102] Although Ag and Au are miscible metals across all composition ranges in the bulk, μwH allows for the reduction rate of these metal ions to be managed, which has been shown to facilitate better structural control in the formation of MNPs with segregated structures. Under the reported experimental conditions, a proportion of the metal ions were not reduced prior to nuclei formation. This was thought to lower the probability of atoms colliding in solution to form alloyed AgAu nuclei, thus favoring the generation of true core-shell structures.

It is possible to generate core-shell structures in a direct one-pot reaction that involve co-addition of both metal precursors, if the reduction potentials of the metal ions are significantly different. Large differences in the corresponding rates of metal ion reduction result in control over the nucleation and growth events, which result in the spontaneous assembly of ordered core-shell MNPs. Such is the case of Au-Pd core-shell MNPs as synthesized by Harpeness and Gedanken.[103] The reduction potential of Au^{3+} is 0.015 V more positive than Pd^{2+} (relative to SHE). Au ions undergo reduction first to form cores that are then encapsulated with Pd metal, without the competing formation of any monometallic PdNPs (Figure 1.6).

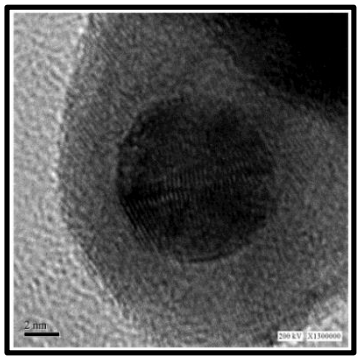

Figure 1.6. HRTEM image of a single Au-Pd core-shell MNPs synthesized using μwH. Reproduced with the permission from the American Chemical Society, [ref. 103].

1.3.2.2 Alloyed NPs

Converse to the previous example, MNPs with randomly alloyed structures are usually favored from mixtures of metal ions in solution that undergo reduction at similar rates, leading to binary nucleation.[62] Alloy MNPs can also be achieved through successive reduction of two metal ions in the presence of a surface passivating agent. Generally, the atoms of the less noble metal transfer electrons to the more noble metal atoms, which in turn aids in the complete reduction of the latter into metallic clusters.[104] Subsequent inter-diffusion of the metals in solution then leads to alloy formation. A unique property of bimetallic alloy MNPs relates to the fact that different metals display different binding strengths toward particular capping agents. Hence, the size and shape of alloyed MNPs can be controlled due to selective adsorption of the surface stabilizing agents in ways that differ from the preparation of monometallic MNPs.[62]

Bimetallic alloy MNPs display enhanced optical and catalytic properties that are directly related to the synergistic effects that arise due to electronic interactions of

neighboring heteroatoms in the alloy. Electronic mixing leads to charge-transfer between metals as their *d*-band centers are shifted, which ultimately alters substrate adsorption kinetics and surface binding energies.[105] It is believed that microwave-assisted synthesis facilitates the formation of bimetallic MNPs with enhanced properties by lowering the alloying temperature[106] and by providing good mixing of the two components.[107] Furthermore, as observed in other methodologies for both monometallic and core-shell structures, reactions rates are dramatically increased with μwH.

Bimetallic Pt_xRu_{100-x} NPs (x = 25−75) have been synthesized using a simple polyol method coupled with μwH. These MNPs were shown to exhibit superior catalytic properties in the methanol oxidation reaction and when utilized in direct methanol fuel cells, compared to their monometallic counterparts.[104,106] The microwave-assisted methodologies employed displayed excellent control and tunability of the alloy's physicochemical properties such as the number of *d*-band vacancies, which in turn resulted in MNPs with highly tunable catalytic properties. Pt and Ru form metastable alloys in the bulk and they do not share the same crystal structures (face-centered cubic and hexagonal close-packed, respectively). It is believed that the mechanism for the formation of the alloy Pt_xRu_{100-x} NPs is based on the formation of initial Pt-rich nuclei that undergo atom substitution through Ru diffusion, which results in alloyed seed particles that subsequently engage in microwave-assisted growth (Figure 1.7).

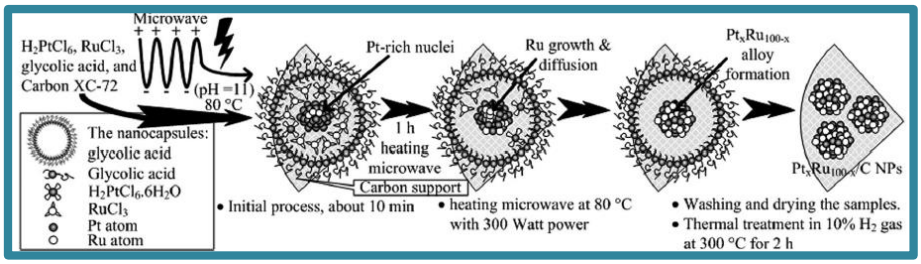

Figure 1.7. Schematic representation of the formation of alloy PtRuNPs via a diffusion process, aided by μwH. Reproduced with the permission from John Wiley and Sons, [ref. 107].

PdAu alloys are popular in catalysis for a number of reactions involving CO oxidation.[62] The microwave-assisted preparation of alloy PdAuNPs has been used to prepare catalysts for the oxidation of methanol and other alcohols and carboxylic acids (*e.g.*, ethanol and formic acid) for potential use in fuel cell technologies. Mehta and co-workers have synthesized isotropic PdAuNPs with average diameters of 5 nm, in reaction times as short as 20 seconds.[108] Microwave-synthesized PdAuNPs have also been supported on ceria and used as catalysts for similar oxidation reactions; other bimetallic alloy MNPs such as PtAu, PtRh, RhCu and PdCu have also all been prepared using the same microwave-assisted protocol (Figure 1.8).[62] This example underlines how microwave-assisted methodologies are both simple and versatile, enabling the synthesis of a wide range of supported and unsupported bimetallic nanoalloys for a variety of applications.

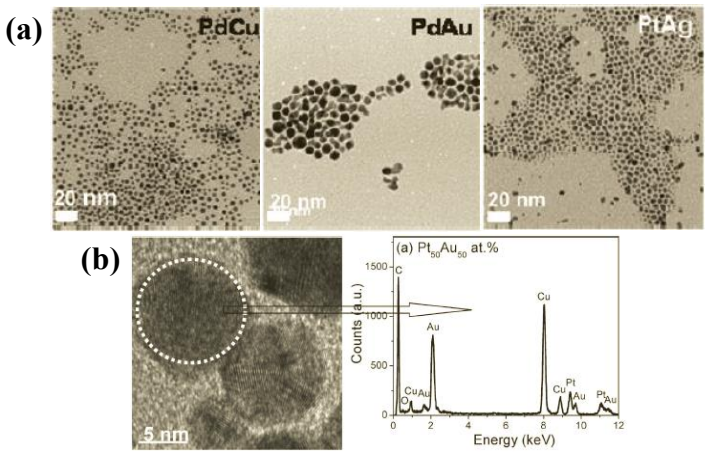

Figure 1.8. TEM images of (a) PdCu, PdAu and PtAgNPs prepared utilizing a μwH method. (b) HRTEM image and EDX spectrum that shows atomic composition of a single PtAuNP, confirming that an alloyed structure is indeed formed using this methodology. Reproduced with the permission from the American Chemical Society, [ref. 62].

Microwave-assisted polyol methods have been applied to prepare FeRuNPs of different sizes and compositions (Figure 1.9), which have shown extremely high catalytic activities in the water-gas shift reaction due synergistic effects between the metals.[69] The relative metallic compositions were observed to be an influential factor in the catalytic performance of these systems.

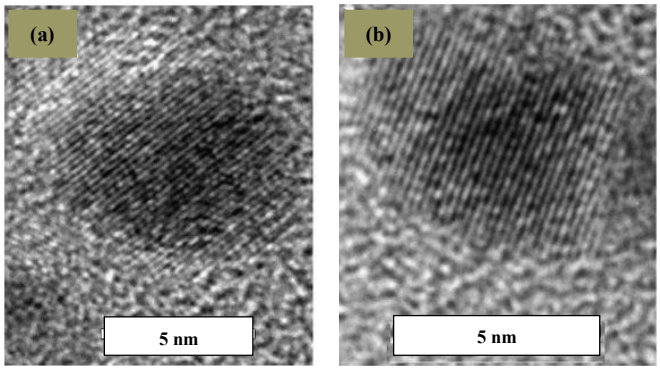

Figure 1.9. HRTEM images of FeRuNPs of varying atomic compositions, synthesized by a microwave-assisted polyol reduction method utilizing PVP as a stabilizing agent; (a) $Fe_{33}Ru_{67}$NPs, and (b) $Fe_{50}Ru_{50}$NPs. No core-shell structure or metal segregation is observed in the images, further confirming that the alloy structures of these FeRuNPs are stable. Reproduced with permission from Elsevier, [ref. 109].

Although metals that are close in proximity in the periodic table have similar properties, the observed synergistic effects are usually greatest for bimetallic NPs of this type. Such is the case for RhPdNPs that have been synthesized through a modified polyacrylamide sol-gel method under μwH.[110] Impurity-free RhPdNPs were generated with ethylenediaminetetraacetic acid (EDTA) as the initial stabilizing agent, which was removed *post*-synthetically *via* thermal treatment. A sol-gel method was employed in this case because it provided additional control over the particle size through control over the reaction pH, coupled with heat treatment. μwH has also been coupled with similar polyacrylamide methods for the synthesis of cuboctahedral alloyed AgAuNPs with different Ag:Au compositions.[111]

Pd- and Pt-containing composites have also attracted significant attention due their enhanced catalytic activity and selectivity in the hydrogen evolution reaction using

visible light, and in hydrogenation reactions. Patel *et. al.* have synthesized both PVP-stabilized PtAgNPs and PdAgNPs through a microwave-assisted polyol method.[102,103] They conducted several experiments in an attempt to understand the mechanism of formation of these alloyed NPs. When the viscous solvent glycerol was employed as the reaction medium, it was possible to monitor the diffusion process of the metal atoms spectrophotometrically by decreasing the rate of diffusion of the metals. Very small PdPtNPs with an average size of 1.05 nm have also been synthesized for hydrogenation purposes, which have been successfully employed in the hydrogenation of palm olein at ambient temperature and atmospheric pressure.[112] Compared to syntheses performed under conventional heating or sonication, the microwave-prepared PdPtNPs were formed three times faster, and were also catalytically highly more active.

1.4 *EX-SITU* SYNTHETIC METHODS OF SUPPORTED NPS

Enhancement in the catalytic activity of MNPs has been observed in several instances as a direct consequence of microwave synthesis. A number of microwave-synthesized monometallic, core-shell and alloy MNPs have been deposited onto various support media in an *ex-situ* manner to generate stable and easily recyclable composite catalyst materials, which have been studied in a range of catalytic applications, in both liquid- and vapor-phase settings. For example, microwave-synthesized Rh, Pd and PtNPs[39] and Au-Rh core-shell NPs[113] have been supported on amorphous silica by simple incipient wetness impregnation methods, which do not induce any measurable morphological changes to the MNPs. The resulting composite catalysts were shown to act as superior hydrogenation catalysts in the room temperature, vapor-phase hydrogenation of cyclohexene using H_2 gas. The supported catalysts were highly resistant to sintering or

agglomeration under these catalytic conditions after several repeated cycles of hydrogenation (Figure 1.10). Similarly, microwave-synthesized Cu and AgNPs have been supported on silica-coated hollow polystyrene beads,[114] silica beads,[115] and activated carbon granules[116] and tested for a number of catalytic applications. One specific example is the immobilization of AuCuNPs on TiO_2 to serve as catalysts for selective oxidation of 5-hydroxymethyl-2-furfural.[117] These alloy NPs were *pre*-synthesized by microwave-assisted reduction of Au^{3+} and Cu^{2+} precursors in the presence of β-D-glucose in an aqueous medium. Catalysts for the water-gas shift reaction have also been generated by supporting *pre*-formed FeRuNPs on $MgAl_2O_4$ at room temperature using potassium acetate as a promoter.[109] These are only a few examples of a larger number of methodologies that have been employed in the *ex-situ* deposition of *pre*-formed, microwave-synthesized MNPs onto support media to create recyclable catalyst materials.

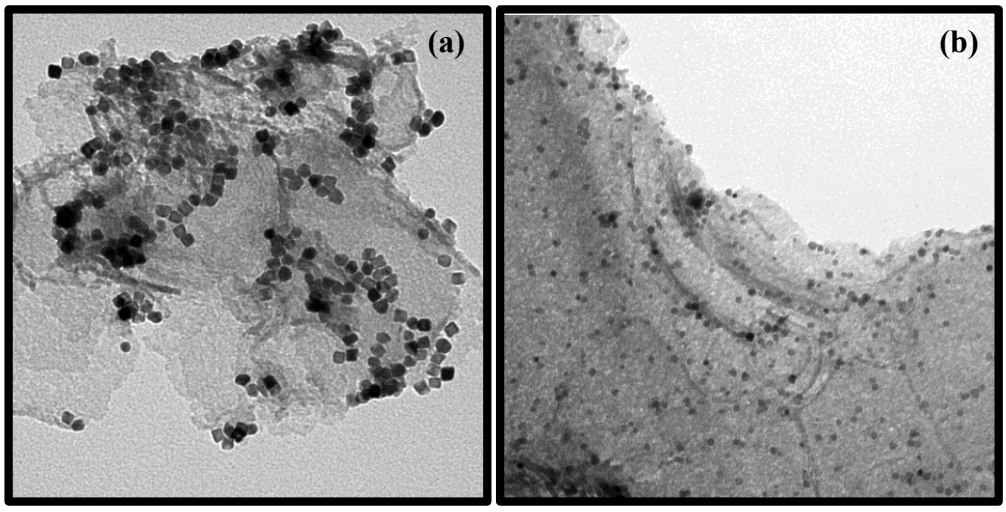

Figure 1.10. TEM images of (a) cubic RhNPs and (b) Au-Rh core-shell NPs synthesized using μwH and supported on amorphous silica using a simple *ex-situ* method. Reproduced with the permission from the American Chemical Society, [refs. 39 & 113].

In alternative works, others have demonstrated how conventionally-synthesized MNPs can be supported on a variety of substrates utilizing μwH to aid in the deposition process. For example, a hybrid catalyst consisting of multi-walled carbon nanotubes (MW-CNTs) decorated with conventionally-prepared RhNPs was prepared by direct mixing of MW-CNTs with tridecylamine-capped RhNPs followed by microwave exposure for 1 min at 350 W (Figure 1.11).[118] Similar methodologies performed using convective heating involve tedious synthetic procedures and require harsher experimental conditions. Another pertinent example involves the incorporation of *pre*-formed AgNPs into a mesoporous ZnO material with the aid of μwH under an Ar atmosphere, again with retention of the original structures of the AgNPs.[119]

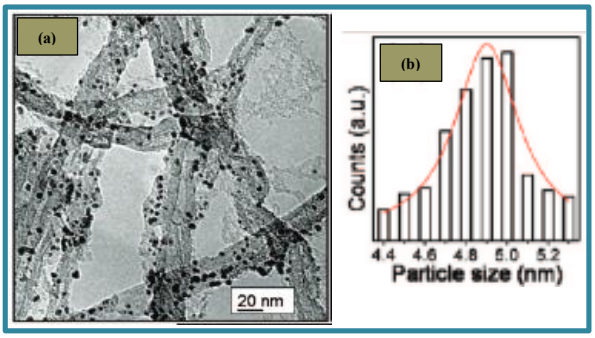

Figure 1.11. (a) TEM image and (b) histogram of RhNPs with narrow size distribution supported on multi-walled nanotubes synthesized using μwH. Reproduced with permission from the American Chemical Society, [ref. 118].

1.5 *IN-SITU* SYNTHETIC METHODS OF SUPPORTED NPS

The key advantages provided by microwave-assisted chemistry in the synthesis of MNPs that have been explored above (*e.g.*, short reaction times, and control over MNP

size and morphology) have recently been extended to the direct, *in-situ* preparation of mono- and bimetallic MNPs at, or inside, support media. This one-pot strategy negates the need to isolate unsupported MNPs and to deposit them onto support materials in separate steps, which, in some instances, can cause problems such as agglomeration or uneven spatial deposition. The majority of examples of *in-situ* microwave-assisted synthesis of supported MNPs involve the use of chemically inert supports, which prevent agglomeration and improve recyclability/recoverability of the MNPs. In some cases, chemically-reactive supports have been used to enhance the overall catalytic properties of the MNP-support composites *via* synergistic effects (*e.g.*, oxidation resistance, spill-over).[120–122] Microwave-assisted syntheses of such composite materials are applicable to many different polar solvents and metal precursors, and as such, there exists a large number of examples of syntheses of supported MNPs using microwave-assisted methods, some of which have been previously reviewed by Campelo *et al.*[123] In this section, some of the most recently identified *in-situ*, one-pot synthetic methods for the generation of even dispersions of defined MNPs on support materials will be explored.

The majority of such examples in the literature utilize the polyol process to assist in the *in-situ* reduction of molecular metal precursors that are *pre*-dispersed alongside the support matrices. The most commonly used solvent is ethylene glycol due to its high dielectric constant (41.4 at 298 K)[46] and effective reduction ability, which allows for fast and uniform heating using μwH. Readily-available metal precursors (akin to those used in *ex-situ* MNP syntheses) are commonly dissolved in polar solvents that encourage dissociation of metal cations from their co-anions, which ensures rapid heating by ionic conduction in the presence of microwaves. These beneficial effects have also been shown to allow access to configurations that can be challenging to achieve using conventional heating methods. For example, the decoration of single-walled (SW) and

MW-CNTs with noble metal ions, clusters and NPs at room temperature has been thoroughly studied in recent times. Nadagouda *et. al.*, recently reported the facile synthesis of Ag and PdNPs on CNTs wrapped with carboxymethyl cellulose (CMC) using a microwave method, which could not be achieved under conventional heating.[124]

*S*upported MNPs are ordinarily synthesized by the initial reduction of metal salts, followed by nucleation and growth of the initial nucleates upon the support itself. In most cases, the support material is simply suspended in the reaction medium and does not undergo any chemical transformations, other than providing preferential nucleation and growth sites for the formation of discrete MNPs. PtNPs have been directly synthesized at SW-CNTs and Vulcan carbon[125] to yield ideal composites (Figure 1.12), whereas analogous materials prepared using convective heating yielded unacceptably wide PtNP size distributions. These PtNP-containing composites have been applied in methanol electrooxidation,[126] selective hydrogenation and fuel cell applications.[127] Au, Ag and PdNPs have also been prepared inside the cylindrical mesopores of ordered mesoporous silica SBA-12 particles in very short reaction times (<2 min) using microwave-based methods; their catalytic properties have been assessed in reactions involving the liquid phase oxidation of styrene and benzyl alcohol with hydrogen peroxide.[128] The *in-situ* preparation of FeNPs on MCM-41, starch, cellulose and carbonaceous supports have also been demonstrated in ethanol solvent, which yielded catalysts that were active in the liquid-phase oxidation of alcohols.[129] Fe^{2+} is typically difficult to reduce toward the generation of FeNPs because it has a significantly lower reduction potential (−0.41 V) compared to other cations that are commonly used to prepare MNPs (*e.g.*, Ag^{+} = 0.79 V; Pd^{2+} = 0.98 V; Ru^{2+} = 0.45 V).[129] However, the formation of supported FeNPs mediated by ethanol as the sacrificial reductant has been successfully achieved under μwH.[129] El-Shall and co-workers have also extensively investigated the preparation of a range of

supported monometallic NPs, including Au and PdNPs on oxides such as CeO_2, MgO and SiO_2.[130,131] μwH has also afforded a number of heterometallic supported MNPs: binary PtRuNPs and ternary PtRuIrNPs have been prepared as nanocomposites supported on carbon (Figure 1.13) and utilized in proton-exchange membrane fuel cells,[132] and in direct methanol fuel cells.[133]

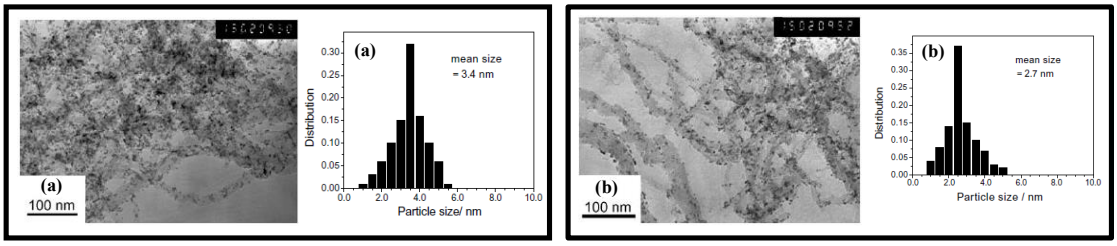

Figure 1.12. TEM images and histograms of PtNPs supported on CNTs synthesized in-situ using μwH and ethylene glycol for the reduction of the Pt4+ precursor at (a) pH = 7.4 and (b) pH = 9.2. Reproduced with permission from Elsevier, [ref. 126].

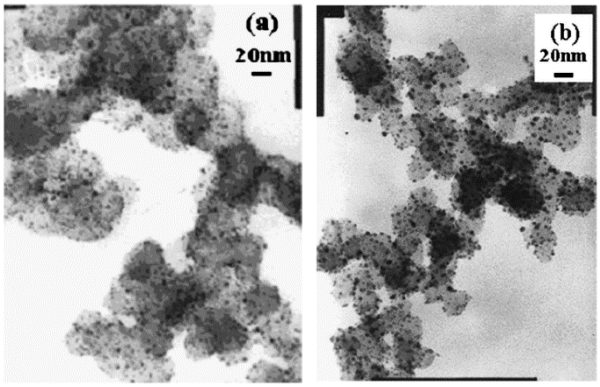

Figure 1.13. Bright field TEM images of (a) PtRuIrNPs and (b) PtRuNPs supported on carbon, synthesized in-situ using μwH. Reproduced with permission by Elsevier, [ref. 132].

It is even possible to generate supported MNPs composites in a simultaneous fashion. This is commonly achieved *via* multiple concomitant chemical reactions that involve metal ion reduction and monomer polymerization to form the support, or *via* chemical modifications to a pre-formed support material.[62,134] An example of the latter is provided by the preparation of graphene-supported PdNPs, which can be accessed by the simultaneous microwave-assisted reduction of Pd^{2+} and deoxygenation of graphite oxide using hydrazine hydrate.[134] In this particular setting, μwH has been shown to provide the required control over the extent of graphite oxide reduction, since the irradiating power and reaction time can be easily adjusted to optimize the parallel reduction processes (Figure 1.14). Another good example is the one-pot synthesis of mono- and bimetallic MNPs of Cu, Pd, CuPd, RuCu, AuPd, AuRu, PtRh, PdRh and AuPt supported on CeO_2, which is generated *in-situ*.[62] It is also possible to achieve well-dispersed MNPs within polymer matrices and thin films *via* concomitant metal ion reduction and monomer polymerization. Examples of this type of process include the formation of

homogeneously-dispersed Pt, Ag and Cu nanocomposites within polyacrylamide resins. These were obtained after the polymerization of an acrylamide monomer and simultaneous reduction of the corresponding metal salt in ethylene glycol under μwH.[135] Wada and co-workers have reported the formation of well-dispersed AgNPs in a polymer matrix *via* direct synthesis in the presence of reactive methacrylate monomers under μwH, followed by microwave-induced polymerization of the methacrylate monomers.[136]

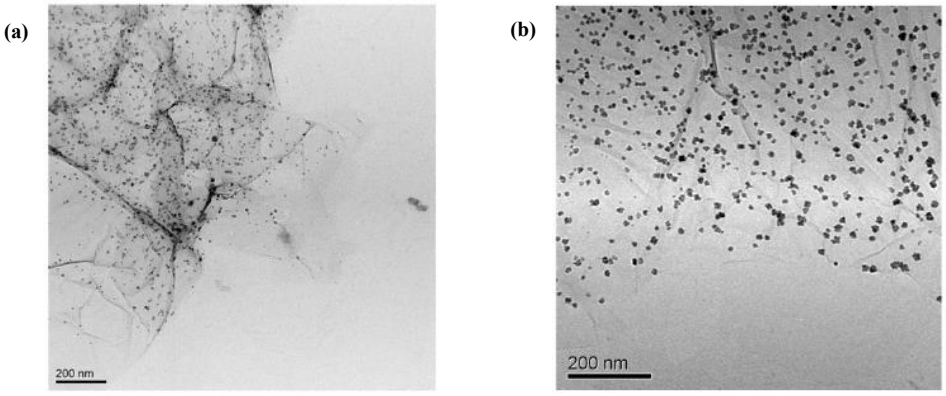

Figure 1.14. TEM images of supported PdNPs synthesized in-situ using μwH on (a) graphene and (b) graphite oxide. Reproduced with the permission from Elsevier, [ref. 134].

Some important correlations between the chemical nature of the support material used (or more specifically, its surface functionality) and the ability to effectively reduce metal cations have also been elucidated *via* microwave-assisted chemistry. In the case of MNPs of Au, Ag and Pd supported on SBA-12, it was reported that not only the ethanolic solvent, but also the hydroxyl-rich silica surface facilitated the reduction of the MNPs on

the support.[123,137] Well-dispersed Fe and PtNPs anchored on carbonaceous supports have been successfully prepared by utilizing chemically-modified supports that display a high density of carboxyl and/or carbonyl moieties. These functional groups were found to play an important role in the reduction process through coordinative binding of individual metal ions from solution, and by ion-exchange reactions, which consequently facilitated favorable nucleation events.[129,138,139]

The *in-situ* synthesis of supported MNPs sometimes imposes challenges related to the control of particle size and the extent of homogeneous distribution throughout the support. For this reason, the addition of stabilizers and capping agents have been found to enhance the outcome of several of the previously described synthetic schemes. For instance, the use of PVP and polyalcohols with established microwave-assisted polyol methods has resulted in the formation of composites with more uniform MNPs that have narrower size distributions.[140] Similarly, standard synthetic methods used to prepare supported Au and PdNPs mentioned above have been modified to include surface passivation agents such as polyethylene glycol and PVP to further stabilize the NPs and to prevent agglomeration.[130,131] It is believed that the rapid and uniform heating achieved using μwH allows for even faster reduction of the metal on the support. Near-monodisperse PtNPs supported on carbon have been obtained using acetate ions that promote favorable electrostatic interactions (Figure 1.15).[125]

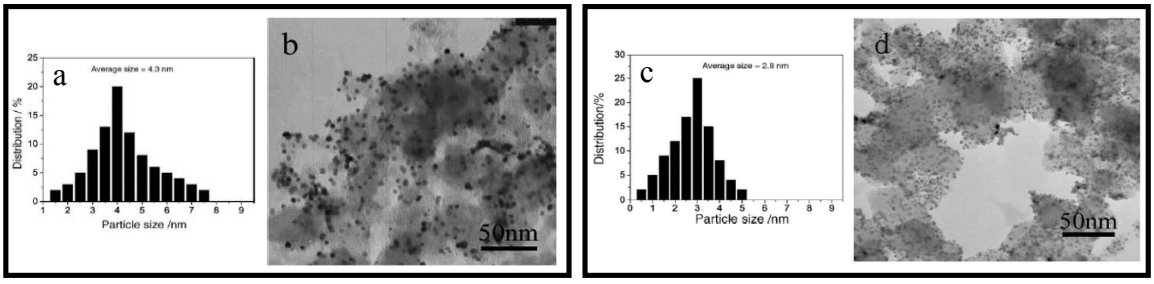

Figure 1.15. Histograms and TEM images of PtNPs supported on Vulcan carbon prepared by a microwave polyol method with addition of (a & b) 0.1 mL and (c & d) 0.5 mL 1.0 M sodium acetate solution. Reproduced with kind permission from Elsevier, [ref. 125].

1.6 HYDROGENATION CATALYSIS

Hydrogenation catalysis is the chemical reaction in which one or more hydrogen atoms are incorporated into the product or products with the aid of a catalyst (most commonly used for H_2 dissociation) that, conventionally, is in the same phase as the reactants.[141] Below 100 °C, H_2 is considered to be relatively chemically unreactive.[142] In fact, the process of $H_2(g)$ dissociation is endothermic with a thermodynamic barrier of approximately 104 kcal mol^{-1}, which partly accounts for its low reactivity.[142] There are two possible modes of H_2 activation: homolytic and heterolytic pathways. In the homolytic mechanism, H_2 dissociates into two hydrogen atoms while in the heterolytic pathway, both a proton and a hydride are generated.

$$H_2\,(aq) \rightarrow 2H\,(aq) \qquad \text{HOMOLYTIC}$$

$$H_2\,(aq) \rightarrow H^+\,(aq) + H^-\,(aq) \qquad \text{HETEROLYTIC}$$

Schemes 1.3 and 1.4 present the idealized picture of the two general possibilities for the hydrogenation of alkenes, which can only occur after the activation of hydrogen

has been achieved by either a homolytic or heterolytic pathway. Scheme 1.3 represents the process for alkene hydrogenation utilizing metal complexes that do not contain M–H bonds (including metal surfaces). There are two common possibilities for the generation of the saturated product through this route: (a) the substrate can initially coordinate followed by the activation of molecular hydrogen, or (b) an initial reaction with molecular hydrogen occurs followed by coordination of the substrate. Scheme 1.4 represents the hydrogenation mechanism adopted by complexes that contain an M–H bond.[141–144] The homolytic mechanism involves a thermodynamic barrier of 100 kcal mol^{-1} whilst the heterolytic one only requires an energy input of 37 kcal mol^{-1};[142] thus, a reasonably favorable energetic pathway is available through hydride formation in the heterolytic mechanism.

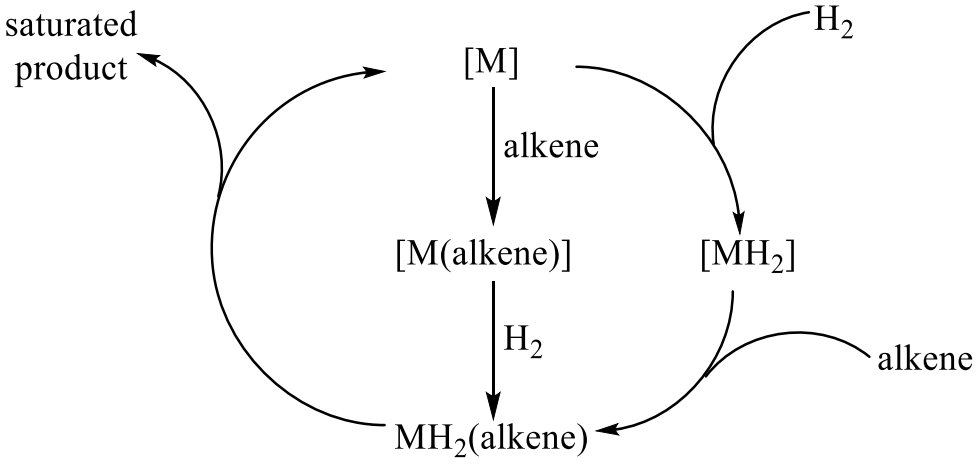

Scheme 1.3. Schematic representation of the cycle for the hydrogenation of alkenes involving metal complexes that initially do not contain M–H bonds.

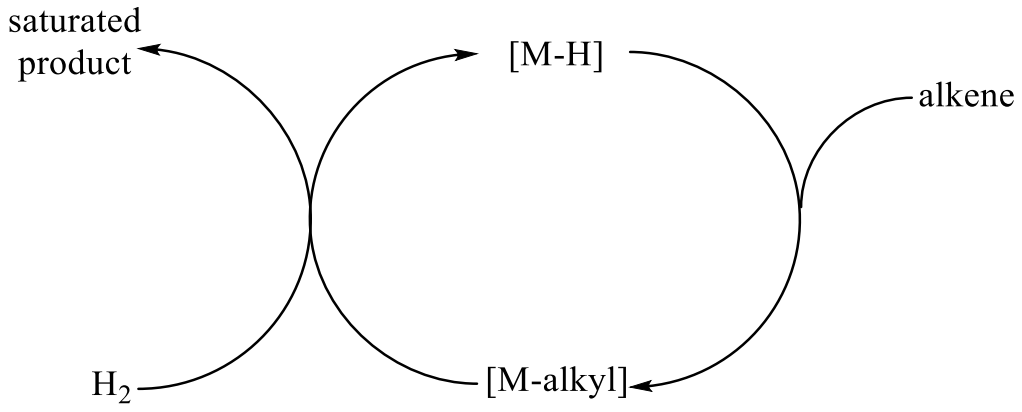

Scheme 1.4. Schematic representation of the hydrogenation mechanism adopted by metal complexes that contain an M–H bond.

For this reason, many transition metals are suitable for hydrogenation catalysis because they usually form hydrides. Furthermore, they have the ability to form strong bonds, towards compounds containing π–electron systems; this capability allows them to participate in redox cycles.[141] Transition metals also have the ability to coordinate to different ligands due to the variability in coordination numbers and variable oxidation states. Finally, it is also possible to modify and tune the electronic and/or steric environment at the active site with both innocent and non-innocent ligands.[141]

Platinum was the first transition metal used as a hydrogenation catalyst in 1863, when Debus found that methylamine could be produced by passing hydrogen cyanide vapor mixed with molecular hydrogen over platinum black.[145] In fact, among all the platinum group metals, Pt and Pd have been used the most since the earlier stages of catalytic hydrogenation history. Both of these metals are highly active under mild conditions and they have been conveniently used in liquid phase hydrogenation at room temperature and atmospheric (or slightly elevated) pressures of hydrogen.[146] Rh has also

attracted a lot of attention since the mid-1950s due to its high activity and selectivity in the hydrogenation of various compounds. Rh has been proven to be the most active transition metal for ethylene hydrogenation[147] as well as in the catalytic hydrogenation of aromatic molecules.[148,149]

Homogeneous catalysts have been commonly used for small reactions as they provide great selectivity and control over the hydrogenation products. Molecular catalysts are known to be very sensitive to experimental conditions and poisoning. Furthermore, they usually are unable to activate substrates with high-enthalpy bonds such as O_2 and it is very challenging to recycle the catalysts after use. Heterogeneous catalysts can also be easily recycled and restored to their initial activity many times over and they provide very fast turnovers for bulk catalytic reactions. For industrial purposes, heterogeneous (or at least supported) catalysts are widely used because: a) the active component has a larger exposed surface area; b) they are more stable at elevated temperatures and pressures; c) they facilitate metal catalyst recovery; and, d) they display greater resistance to poisoning.[146] Nonetheless, heterogeneous catalysts lack control over many regio- and enantioselective hydrogenation reactions.

In the past decade or more, homogeneous catalysts have been shown to be truly "nanoheterogeneous".[150–152] The nature of these active and selective catalysts has allowed NPs and colloids to become a very appealing alternative to bridge the gap between conventional homogeneous and heterogeneous catalysis.[153] Recycling of the nanocatalysts is of major interest as well as they are considered to be "*pseudo*-homogeneous" with clear catalytic advantages over the robust heterogeneous counterparts.[153]

2. Microwave Synthesis of monometallic Rh, Pd and Pt NPs

2.1 INTRODUCTION

New methods to prepare noble metal nanoparticles (MNPs) with well-defined surface structure have attracted significant interest over the past few years[42,154–170] due to the importance of metals such as Rh, Pd and Pt as heterogeneous catalysts in a range of critical industrial processes (*e.g.* regioselective hydrogenation, benzene reduction, NO_x reduction). More recently, many synthetic methods have been developed for the controlled preparation of Pd and PtNPs using metal salts in the presence of polymeric stabilizing agents, along with high boiling refluxing alcohols such as ethanol and polyols.[171–175]

Specifically for Rh, Pd and Pt, previous studies have identified suitable conditions for the preparation of a range of NP morphologies *via in situ* reduction of M(II, IV) (M = Pd or Pt) or Rh(III) precursors in hot, reducing solvents, commonly high boiling-point polyols.[42,154,155,176,177] Most recently, these basic synthetic strategies have been refined to significantly improve morphological control by paying particular attention to the kinetics of NP nucleation and growth. Notable examples include the correlation between polyol oxidizing strength and resulting RhNP[155] and Pd or PtNPs structure,[178] and the direct manipulation of growth kinetics as a function of molecular metal precursor addition rate.[169] As a result of this work, it is now possible to prepare MNPs with particular

---

Part of the work in this chapter has been previously published as a journal article ("Beneficial Effects of Microwave-Assisted Heating *versus* Conventional Heating in Noble Metal Nanoparticle Synthesis." Dahal, N.; Garcia, S.; Zhou, J.; Humphrey, S. M., *ACS Nano*, **2012**, *6*, 9433.). Humphrey, S. M. conceived the scientific idea, Dahal, N. and Garcia, S. performed the experiments and data analysis, and Zhou, J. aided with TEM image collection and data analysis.

surface structures to a high degree of specificity. All of the previous studies have relied on conventional (convective) heating of solvents, which involves slow heating and cooling of the solvent medium and the potential for non-uniform temperatures. Microwave-assisted heating has attracted significant interest in a range of synthetic fields, including organic synthesis[58,179] and inorganic materials preparation,[46,60] owing to the fast reaction times, high throughput capabilities, and beneficial crystallization effects induced by unusual, localized 'hotspot' heating.[46] It has also been used to prepare MNPs directly inside support media.[46] However to the best of our knowledge, a systematic and comparative study of the effects of microwave heating (μwH) upon Rh, Pd and PtNP nucleation and growth has not been previously reported. Nor has any such method been shown to be universally applicable for the synthesis of other important MNPs.

The results from this study reveal the comparative effects of μwH versus conventional heating (CvH) in nanoparticle synthesis. The popular polyol reduction method has been coupled to syringe-pump control of precursor addition rate to achieve a convenient and highly reproducible procedure, which has shown to be broadly applicable to the synthesis of Rh, Pd and PtNPs, with comparable control over size and structure. In-depth quantitative studies indicate a number of beneficial effects of the μwH method: (a) under identical reaction conditions, NP morphological control and crystallinity are significantly improved due to μwH; (b) the microwave-induced nucleation process is faster and more reproducible compared to conventional methods; and, (c) microwave synthesis results in incorporation of less polymer capping agent, which ultimately results in more highly active catalysts.

2.2 SYNTHESIS AND CHARACTERIZATION

2.2.1 Materials

Rhodium trichloride hydrate ($RhCl_3 \cdot xH_2O$, 98%; Johnson Matthey), hydrogen tetrachloroaurate ($HAuCl_4 \cdot 3H_2O$, 98%; Sigma Aldrich), potassium tetrachloropalladate ($K_2[PdCl_4]$, 99%; Strem Chemicals), potassium tetrachloroplatinate ($K_2[PtCl_4]$, 99.9%, Alfa Aesar), poly(vinylpyrrolidone) (PVP, $<M_w>$ = 55,000; Sigma Aldrich), ethylene glycol ($\{CH_2OH\}_2$, 99.8%; Fisher Scientific) and 1-cyclohexene (C_6H_{10}, 99%; Alfa Aesar) were used as received. All other reagents and solvents (analytical grade) were employed without further purification unless stated otherwise.

2.2.2 Synthesis Methods

A MARS 5 (CEM Corp.) microwave system with a maximum power of 1600 W (2.45 GHz) was used to perform all microwave-based reactions. The reaction temperature inside the microwave cavity was finely controlled by power modulation *via* a RTP-300+ fiber-optic temperature sensor located in a beaker of solvent identical to that utilized in the reaction. A 50 mL round-bottomed flask fitted with a water-cooled reflux condenser was placed in the center of the microwave cavity. The solvent and reactants were magnetically stirred (1,100 rpm) and the metal precursor was then added directly into the stirred solvent through a disposable, fine-bore PTFE tubing that was maintained at a position above the solvent level to ensure constant addition. The rate of the metal precursor addition was controlled using an Aladdin Programmable Syringe Pump (WPI, Inc.) that was directly attached to the Teflon tubing. The reactions were carried out at ambient pressure in air, with venting at the top of the reflux condenser. Scheme 2.1 is a

schematic representation of the glassware and experimental set-up used in the synthesis of Rh, Pd and PtNPs using μwH. For reactions carried out using conventional heating, the same apparatus was employed. A simple mineral oil thermal bath and hot plate/stirrer apparatus fitted with a thermocouple temperature-feedback control was used instead of the microwave.

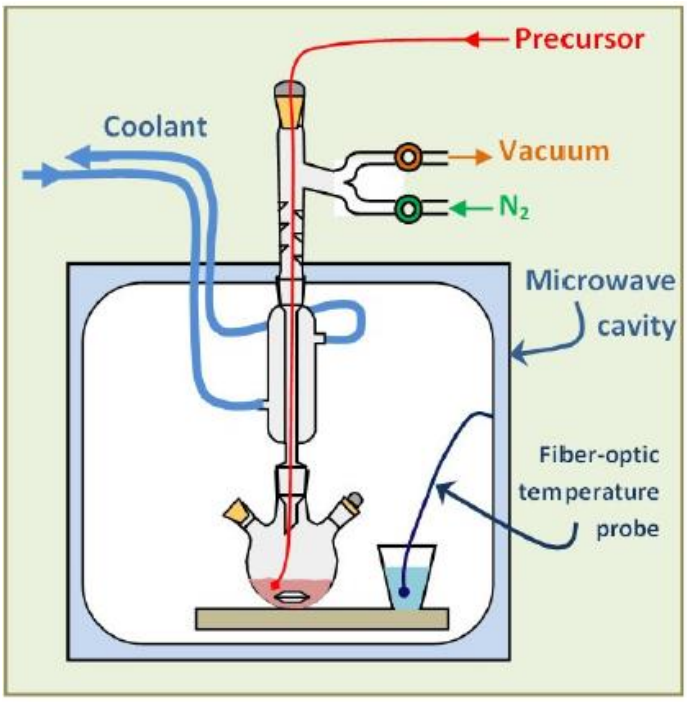

Scheme 2.1. Apparatus arrangement used for the microwave-assisted synthesis of Pd, Pt and Rh NPs.

2.2.3 Characterization Methods

Powder X-ray diffraction (PXRD) patterns were collected in the 30–90° 2θ range using a Rigaku R-Axis Spider diffractometer functioning at 40 mA and 40 kV and utilizing Cu $K\alpha$ radiation (λ = 1.5406 Å). The step size and collection time were 0.05° and 6 s per step, respectively. Transmission electron microscopy (TEM) images were acquired using an FEI Tecnai Spirit BioTwin operating at 80 kV. Samples for TEM studies were prepared by drop-casting a stable suspension of the metallic NPs in ethanol on a 400 mesh Cu grid coated with a carbon film (Ted Pella, Inc.). Average particle diameters and standard deviations were derived by measuring a minimum of 200 individual particles per experiment and by averaging over multiple images. Individual particles were measured using Image-J (http://rsbweb.nih.gov/ij), which finds the area of each nanoparticle by pixel counting. FT-IR spectra of the PVP-capped microwave-assisted and conventionally prepared, and of the oleic acid/oleylamine functionalized Pd and PtNPs were collected Thermo Nicolet iS50 spectrometer with attenuated total reflection (ATR). UV-vis data were collected using a Carry 6000i UV-vis NIR spectrometer equipped with a double beam and a wavelength range of 175−3300 nm.

2.2.4 Synthesis of Pd NPs

The capping agent, *poly*(vinylpyrrolidone) (135 mg, 1.23 mmol), was dissolved in ethylene glycol (15 mL) in the reaction flask and this solution was then heated to 150 °C using either μwH or CvH. A solution of the metal precursor was prepared by dissolving $K_2[PdCl_4]$ (20 mg, 0.061 mmol) in ethylene glycol (5 mL), and it was then loaded into a 10 mL disposable syringe. During the seeding phase, 2.5 mL of the Pd^{2+} solution was delivered to the hot polymer solution in the reaction vessel at a rate of 3.66 mmol h^{-1} *via*

PTFE tubing, yielding a dark brown solution. After this solution stirred for an additional 30 min at 150 °C, the remaining 2.5 mL of metal precursor were added to the reaction vessel at a slower rate of 0.24 mmol h^{-1}, in order to enhance layered growth on the seeds previously formed. Once the addition was completed, the mixture stirred for 30 min at the same temperature. The reaction was then allowed to slowly cool down to room temperature with no stirring. The PdNPs were precipitated with acetone (*ca.* 50 mL), and the precipitate was isolated via ultracentrifugation (5 krpm, 5 min). The solid NPs then underwent three cycles of redispersion in 10 mL ethanol, precipitation with 70 mL hexanes and isolation by ultracentrifugation, in order to remove any impurities or by-products.

2.2.5 Synthesis of Pt NPs

The synthesis of PtNPs followed a similar procedure to that stated above. The metal precursor solution was prepared by dissolving the analogous Pt salt, $K_2[PtCl_4]$ (78 mg, 0.19 mmol) in the same volume of ethylene glycol. The capping agent solution was prepared using a 20 molar excess of poly(vinylpyrrolidone) (422 mg, 3.8 mmol) dissolved in ethylene glycol as well (15 mL). During the seeding stage, 2.5 mL of the metal precursor solution was added at a rate of 11.4 mmol h^{-1}, while the remaining Pt^{2+} solution was added at a rate of 0.76 mmol h^{-1} in the latter growth phase. All the other reaction conditions (temperature and reaction time) and purification methods remained the same.

2.2.6 Pd and PtNPs Characterization

TEM images of Pd and PtNPs prepared using μwH and CvH (Figures 2.1 & 2.2, 2.5 & 2.6) clearly show that μwH constantly provided fine synthetic control over the morphology and size of the NPs, as compared to CvH. The microwave synthetic method yielded both μwH-Pd and μwH-PtNPs with narrow size distributions and uniform morphology. On the other hand, CvH generated NPs of a variety of shapes, and with extremely broad size distributions. This lack of control over the size and morphological parameters was also confirmed using other techniques such as UV-vis spectroscopy (UV-vis) and Powder X-ray diffraction (PXRD). Pd and PtNPs synthesized utilizing an oil bath did not display any surface plasmon resonances (SPR) in the visible light region. However, the absorption spectra for the Pd and Pt microwave synthesized counterparts do show some features at 225 nm and 252 nm, respectively (Figures 2.3 & 2.7). It appears then that convective heating increases the particles' electron scattering, thus increasing the damping tendencies of these precious metals in the nanoscale. Based on the PXRD patterns, it is not entirely clear if either mode of heating enhances crystallinity during the synthetic process (based on the intensity of the reflections observed). Nonetheless, the intensity of the reflections is a function of the crystal orientation as well, so crystallinity enhancement cannot be based solely on this parameter. It is however evident that the synthesis of Pd and PtNPs using conventional heating methods generates XRD patterns with broadened reflections, as compared to microwave-assisted metal NPs, which is consistent with anisotropic small nanostructures (Figures 2.4 & 2.8).

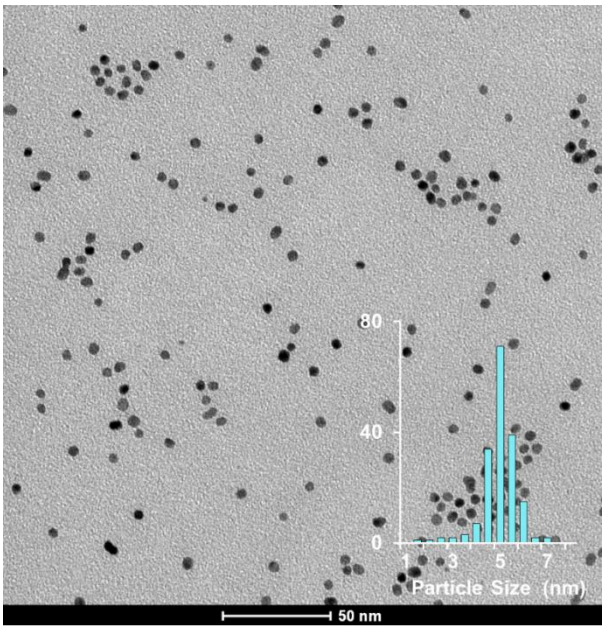

Figure 2.1. TEM image of PdNPs with an average diameter of 4.22 ± 0.75 nm synthesized using μwH.

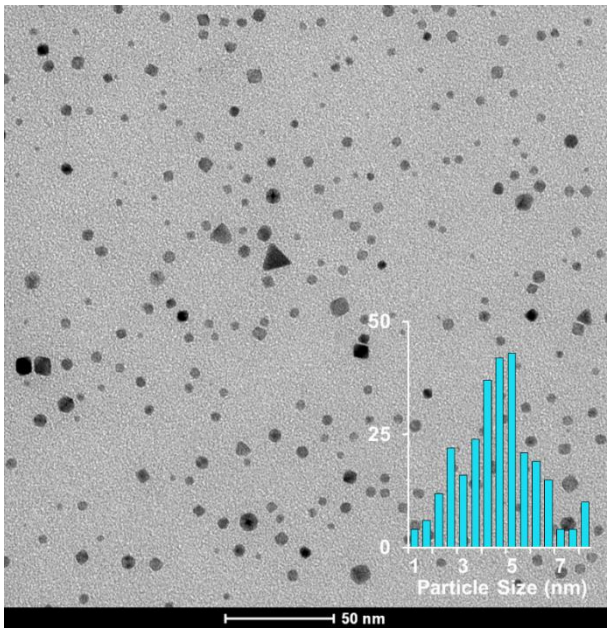

Figure 2.2. TEM image of 3.74 ± 1.62 nm PdNPs prepared utilizing CvH.

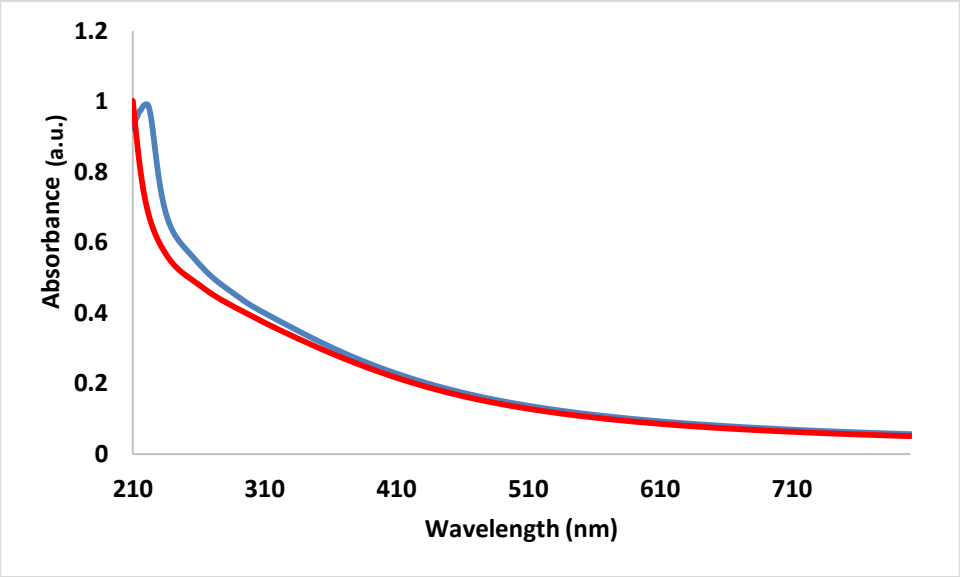

Figure 2.3. UV-vis spectra of µwH- (blue) and CvH-PdNPs (red).

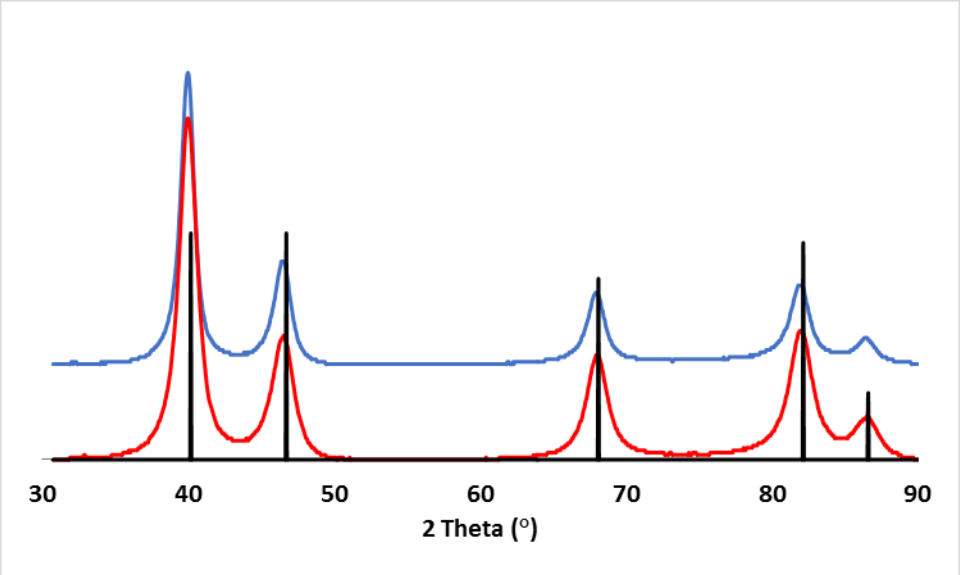

Figure 2.4. XRD pattern of µwH PdNPs (blue), CvH PdNPs (red) and reference diffraction lines for FCC Pd with lattice constant of 3.89 Å (black).

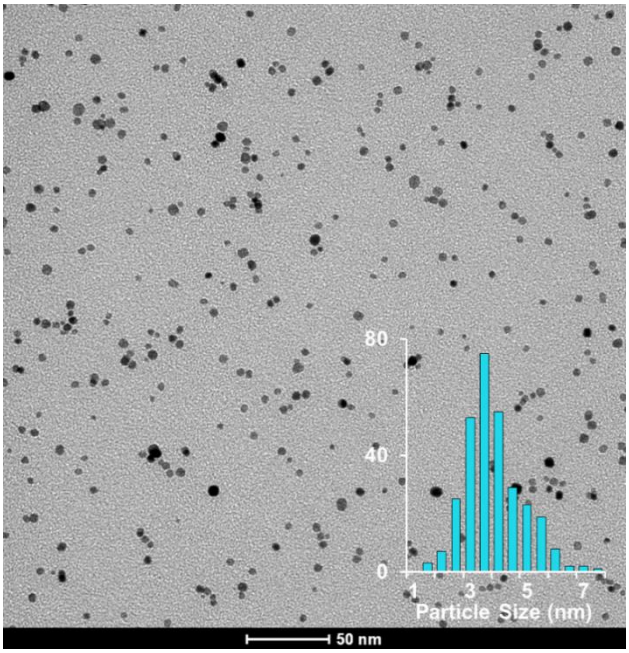

Figure 2.5. TEM image of microwave-assisted PtNPs with an average size of 3.09 ± 1.01 nm.

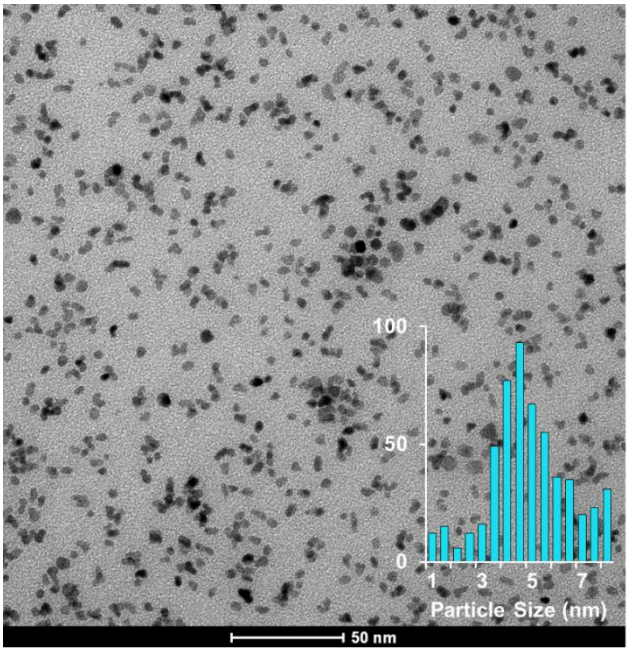

Figure 2.6. TEM image of 4.14 ± 1.64 nm PtNPs synthesized using CvH.

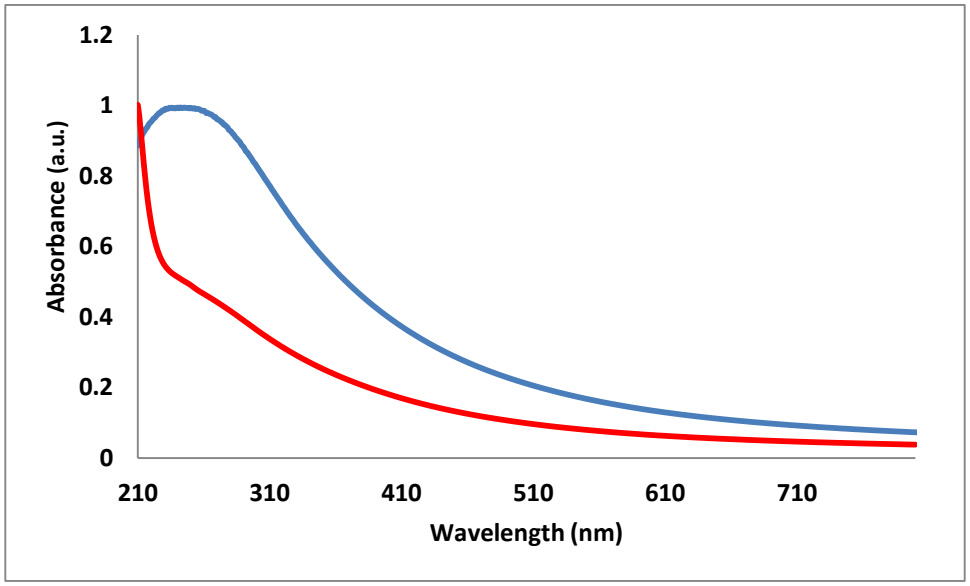

Figure 2.7. UV-vis spectra of µwH- (blue) and CvH-PtNPs (red).

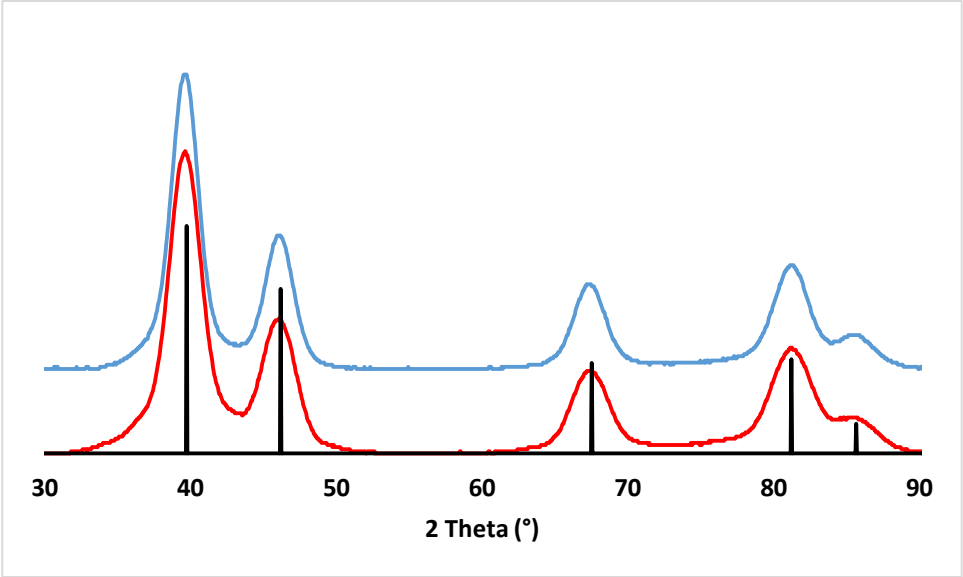

Figure 2.8. XRD pattern of µwH PtNPs (blue), CvH PtNPs (red) and reference diffraction lines for FCC Pt with lattice constant of 3.92 Å (black).

2.3 HYDROGENATION CATALYSIS USING RH NPS

The catalysts were prepared by addition of pre-calcined SiO_2 (100 mg) to suspensions of 25 mg of μwH- or CvH-RhNPs in ethanol/H_2O (20.0 mL; 1:1). The slurries were sonicated for 20 h, isolated by filtration, washed with copious amounts of ethanol/H_2O and dried at 80 °C in a static oven. For each catalytic study, a small amount of the composite catalyst (*ca.* 15–20 mg) was loaded into a custom made quartz U-tube, suspended above a D3-porosity frit. The sample was diluted with acid-washed and calcined sand and the temperature was maintained at 25 °C while the quartz reactor line was heated to 90 °C (see Scheme 2.2 for a detailed description of the experimental setup). The sample was then purged with the reactant gas mixture (1:1 H_2:He) for 30 min. The catalysis reaction commenced with the introduction of cyclohexene vapor into the gas stream *via* an in-line saturator held at 0 °C and fitted with a fritted bubbler. Conversion data was obtained in real-time by automated pneumatically-gated sampling of the exhaust stream, which was vented directly into an HP Agilent 6890 gas chromatograph fitted with Restex Stabiliwax 15 m column and tandem FID and TCD detectors. Peak areas were integrated and correction factors obtained from control studies were applied to obtain raw conversion values. Normalized turnover frequency (TOF) values were obtained based on estimation of the number of Rh surface sites (by measuring average supported particle sizes from TEM images) and from ICP-MS data for percent Rh loading on the SiO_2 supports.

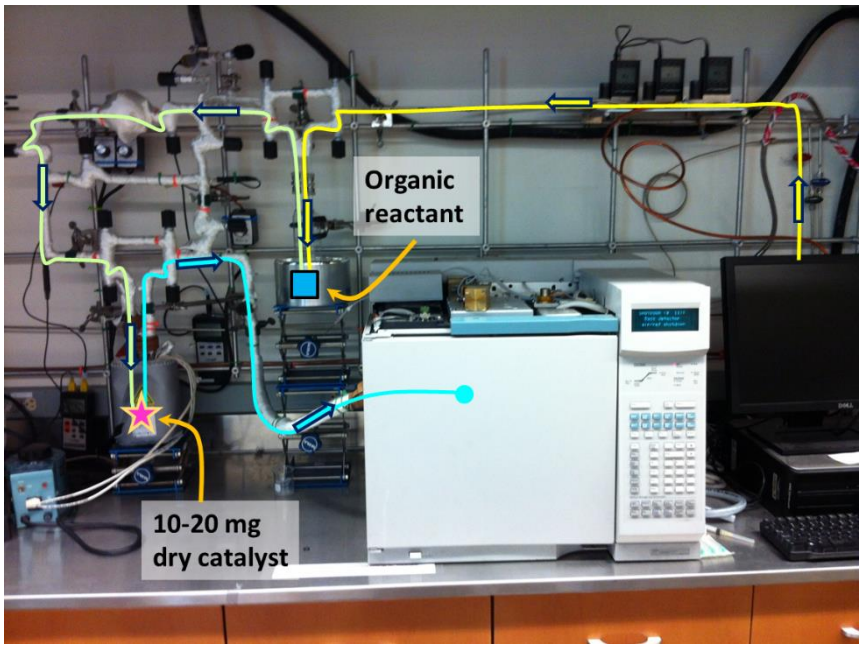

Scheme 2.2. Diagram of the experimental set-up for the vapor-phase hydrogenation of cyclohexene catalysis.

The microwave synthetic method was shown to be broadly applicable in the synthesis of a wide range of MNPs. The catalytic performance of these MNPs is of ultimate interest from an application standpoint. Thus, RhNPs were used as a model system for hydrogenation catalytic studies. To assess the relative catalytic properties as a function of preparation method, cyclohexene hydrogenation was studied using similarly-sized RhNPs obtained using both CvH and μwH methods. Specifically, fresh batches of 12.4 ± 2.1 nm μwH-Rh cubes and 10.9 ± 1.8 nm CvH-RhNPs were each directly supported on amorphous silica by sonication of suspensions of the as-synthesized PVP-capped RhNPs with acid-washed and pre-calcined silica (0.5–1 μm). The resulting composites were isolated by filtration. Characterization by TEM confirmed bulk uniformity and attachment of the NPs without agglomeration (Figure 2.9) and

inductively-coupled plasma mass spectrometry (ICP-MS) was employed to determine percent metal loading (μwH = 1.82; CvH = 2.02%). Milligram quantities of the RhNP-SiO_2 catalyst materials were then studied in the vapor-phase hydrogenation of cyclohexene with H_2 gas, using a single-pass flow reactor with on-line analysis performed by gas chromatography (GC) at 3.4 minute injection intervals. Importantly, all reactions were studied at 26 °C without the need for any pre-treatment (such as high-temperature calcination) to remove the PVP capping agent. Upon exposure to the reactant stream, both catalysts underwent a short initial induction period (*ca.* 4 min) which was followed by a sharp increase in TOF (turn-over frequency; units are for Rh surface site per second) for the hydrogenation of cyclohexene to cyclohexane (Figure 2.10). Both CvH and μwH catalysts reached steady-state after 20 min. The most striking result from this study was the two-fold higher steady-state TOF observed for the μwH catalyst (3.40 s^{-1} *versus* 1.77 s^{-1} for the CvH catalyst; Figure 2.11). The associated activation energies were 5.6 and 8.3 kJ mol^{-1} respectively. The superior hydrogenation ability of the μwH-RhNP catalyst is most likely because there are more accessible Rh surface sites due to the incorporation of less PVP polymer (as supported by microanalytical studies; Table 1). To demonstrate the effectiveness of the RhNP-SiO_2 catalysts, further runs were also performed using the same recycled catalysts, which showed no significant loss of the steady-state TOF (Figure 2.12); TEM analysis of the post-reaction catalysts did not reveal any significant morphological changes (Figure 2.13).

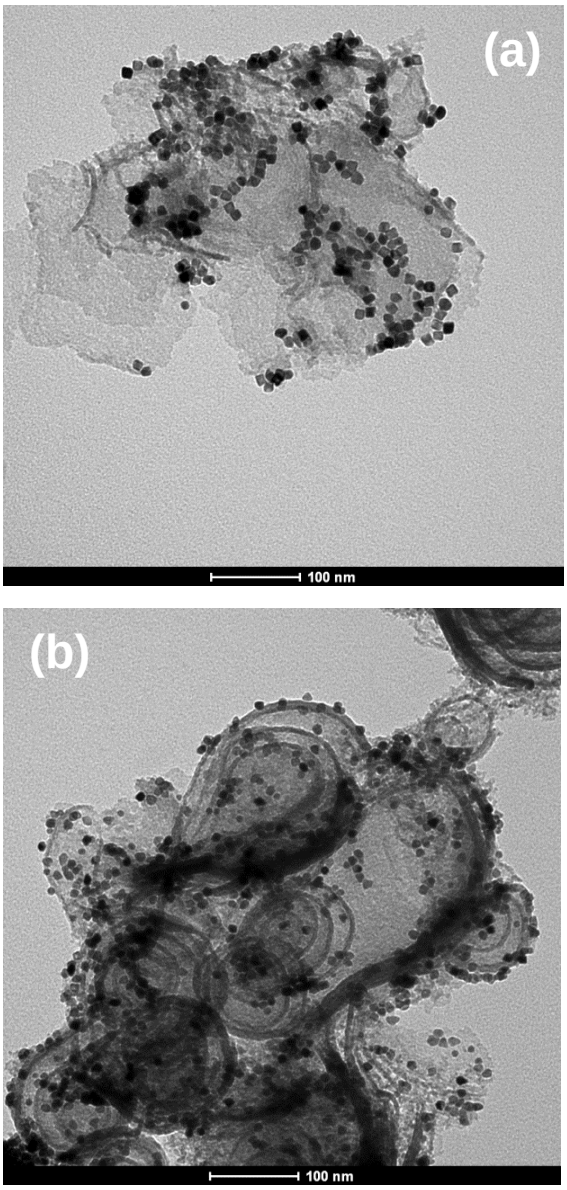

Figure 2.9. TEM images of composite materials generated after the support of (a) μwH-RhNPs and (b) CvH-RhNPs on amorphous silica.

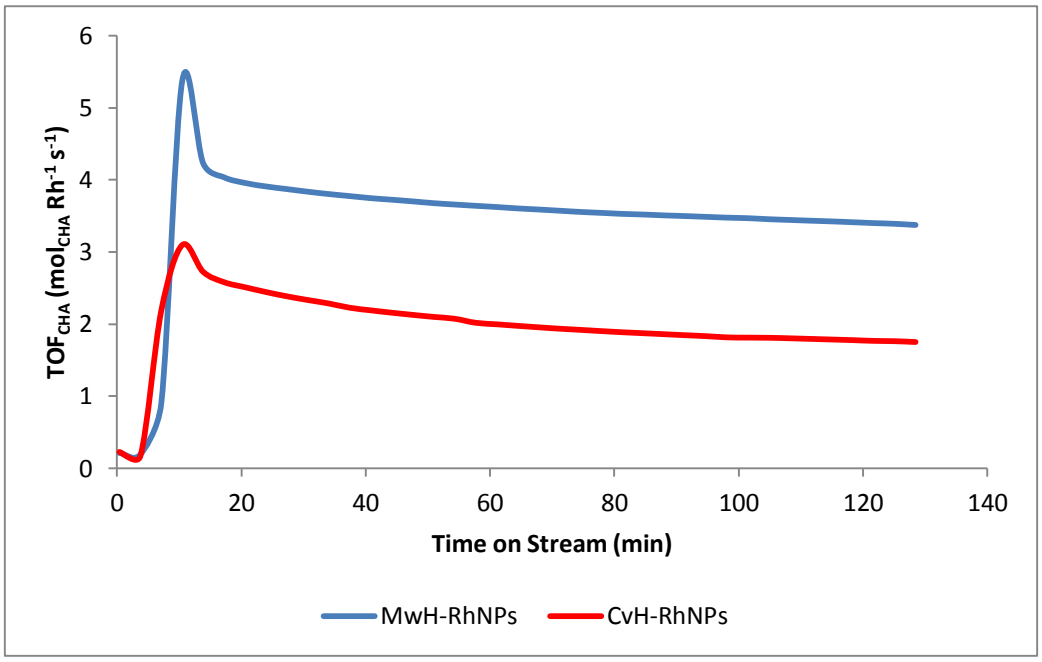

Figure 2.10. Turnover frequency of cyclohexane as a function of time in the hydrogenation catalysis of cyclohexene using RhNPs.

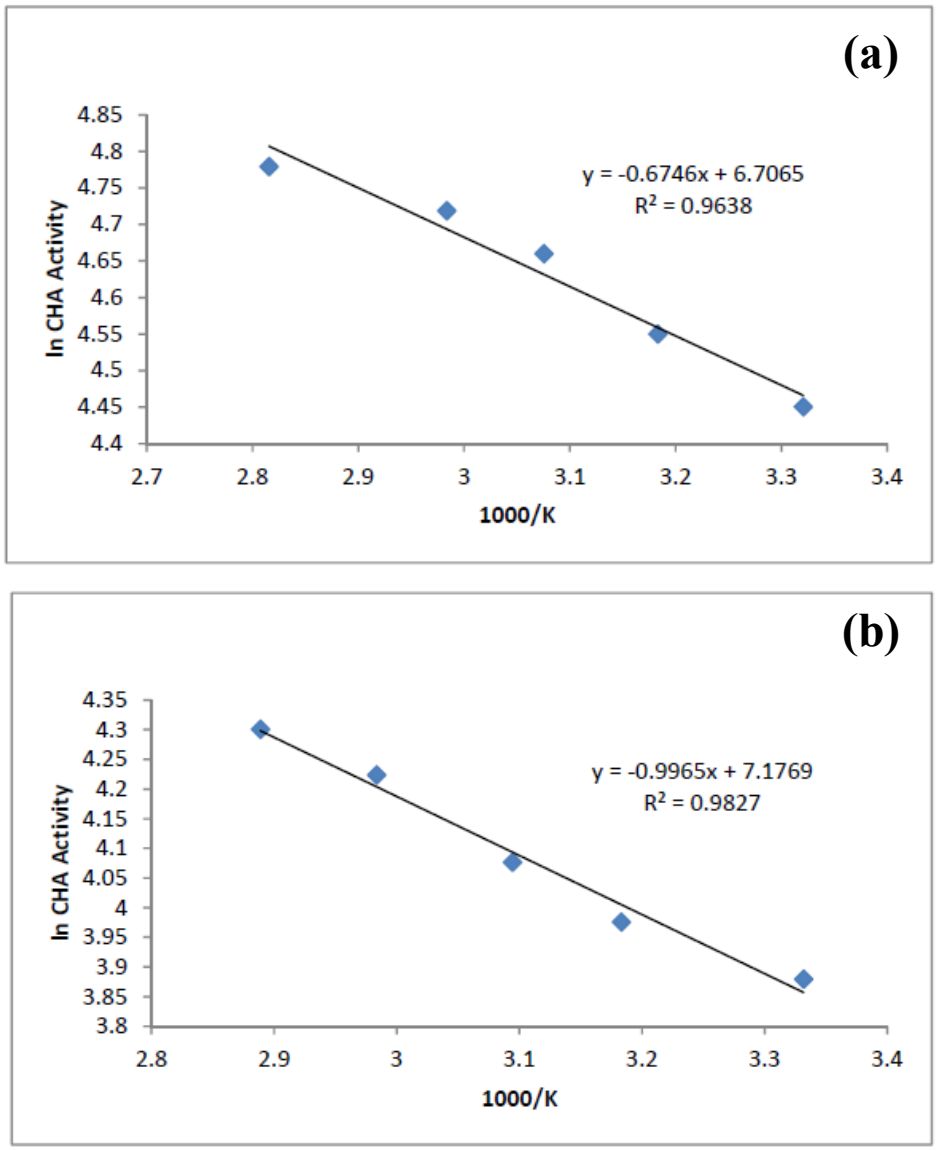

Figure 2.11. Arrhenius plots for the activation energies of the hydrogenation of cyclohexene using (a) μwH-RhNPs and (b) CvH-RhNPs.

Table 2.1. % C, N, H and Rh ICP-MS values for μwH- and CvH-RhNPs and Rh:N ratios as an estimate for the number of PVP monomers *per* Rh atom.

	% C	% N	% H	% Rh	% Rh:N
μwH-RhNPs	16.6	2.7	1.9	9.0	3.3
CvH-RhNPs	10.5	1.6	1.3	8.6	5.4

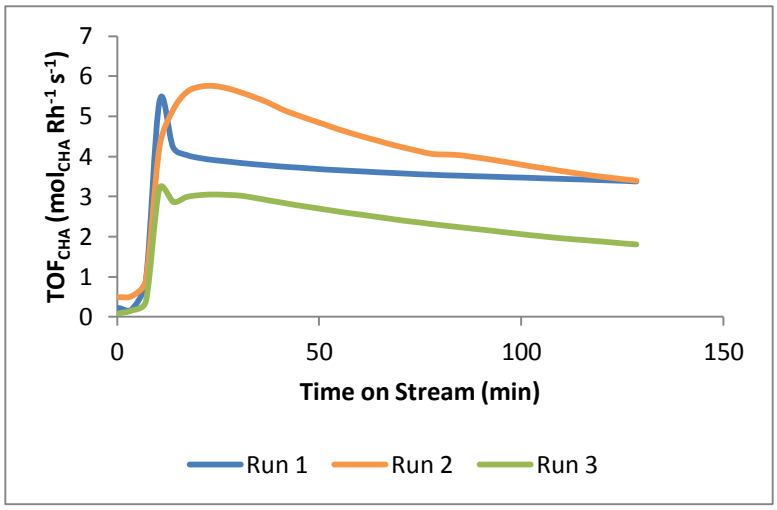

Figure 2.12. Recycled μwH-RhNPs catalytic runs in the vapor-phase hydrogenation of cyclohexene.

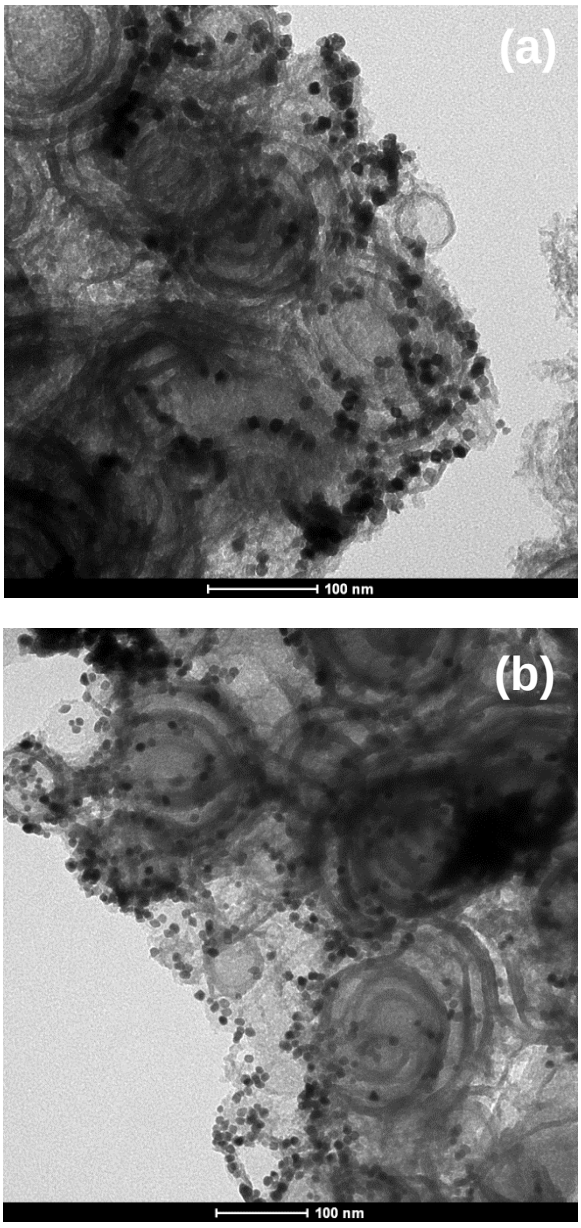

Figure 2.13. TEM images of (a) μwH-RhNPs and (b) CvH-RhNPs *post*- hydrogenation catalysis.

2.4 LIGAND EXCHANGE FOR PD AND PT NPS USING μWH

For ultimate catalytic applications of the synthesized NPs, it is highly desirable to employ labile stabilizing agents that can be removed under mild conditions.[33,37,180] In comparison to polymers, molecular stabilizing agents are particularly preferable because they can be removed without the need for high temperature treatment, which otherwise may cause NPs restructuring and/or carbonization. For this reason, a series of ligand exchange reactions were carried out in which the as-synthesized μwH- and CvH- Pd and PtNPs were reacted with 1:1 mixtures of oleic acid and oleylamine. These form ammonium carboxylate anion/cation pairs that are known to act as effective capping agents by forming moderately strong ionic interactions at the NP surface.[33,37,180]

The dried solid Pd NPs were redispersed in 15.0 mL ethylene glycol in a reaction flask. After a homogeneous mixture was achieved, 2.0 mL oleic acid and 2.0 mL oleylamine were added to the reaction vessel generating a biphasic mixture. This reaction was then heated to 150 °C for 1 hr, under stirring, using the same heating method employed during the synthesis (microwave or convective heating). After this period, the phases were separated and the organic phase (top layer; oleic acid/oleylamine) was gently treated with excess ethanol (*ca.* 30 mL), causing precipitation of the oleic acid/oleylamine functionalized NPs. The NPs were isolated by centrifugation (8.5 krpm, 10 min) and further washed with ethanol. The ligand exchange experiments for PtNPs were carried out in a similar fashion as described above but the reaction time had to be extended to 2 hr in order to achieve an acceptable degree of exchange.

The capping agent exchange for Pd seeds generated using μwH proved to be more efficient than the one carried out utilizing convective heating. After the reaction was carried out as explained above, using μwH, the ethylene glycol layer became colorless while the organic layer on top had turned brown. When the heating source was an oil

bath, only a slight color change was observed for the polyol phase indicating that only a fraction of the NPs had only partially been functionalized with the monomeric ligands and a large portion had not even undergone a phase transfer. These observations can be explained by the fact that μwH-PdNPs incorporate less PVP monomers per NP compared to CvH-PdNPs, as determined using inductively coupled plasma mass spectrometry (ICP-MS) and is displayed in Table 2.2. TEM images (Figures 2.14 & 2.15) show that the initially synthesized particles are very robust and stable as they do not undergo any noticeable transformation in size or shape during the ligand exchange reactions.

FT-IR spectroscopy confirmed that both heating methods lead to a certain degree of capping agent exchange as seen in Figure 2.16. In both cases, the C=O stretching vibration and weak C–H modes of PVP, at 1644 and1287 cm^{-1} respectively, decrease in intensity while new bands appear at 1557 and 1401 cm^{-1} corresponding to antisymmetric and symmetric C–O vibrations of the carboxylate groups generated by oleic acid and oleylamine. Although the intensity of the bands that evolve are comparable for both μwH and CvH exchange reactions, it seems that μwH leads to a more efficient exchange as the stretching frequencies that correspond to PVP are less intense in this case compared to experiments carried out using convective heating.

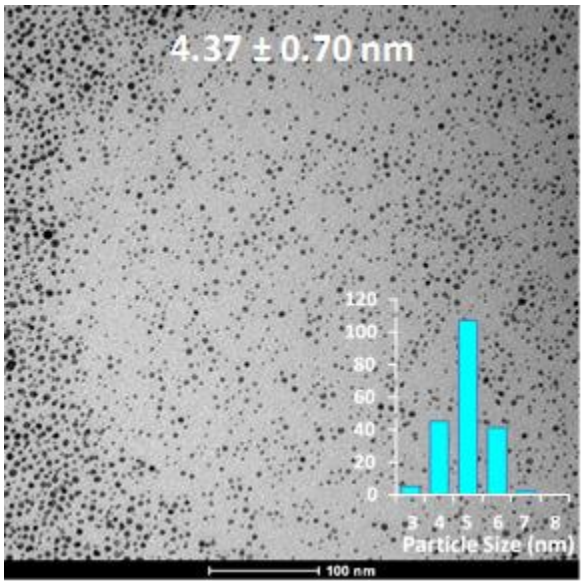

Figure 2.14. TEM image of μwH-PdNPs after a ligand exchange reaction utilizing a 1:1 mixture of oleic acid and oleylamine was conducted using μwH.

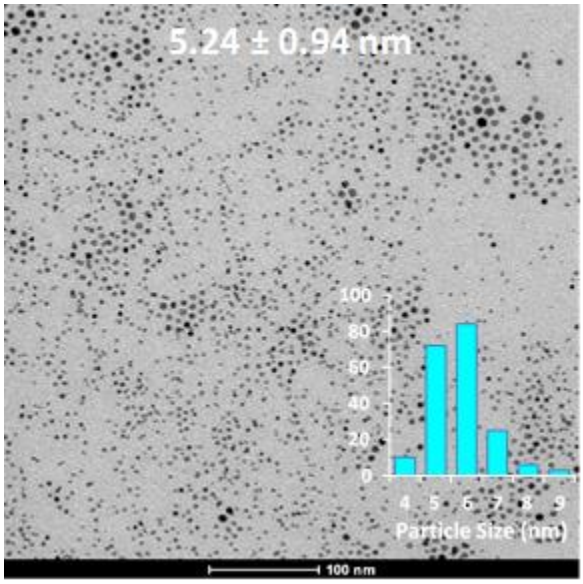

Figure 2.15. TEM image of CvH-PdNPs functionalized with 1:1 oleic acid : oleylamine using convective heating.

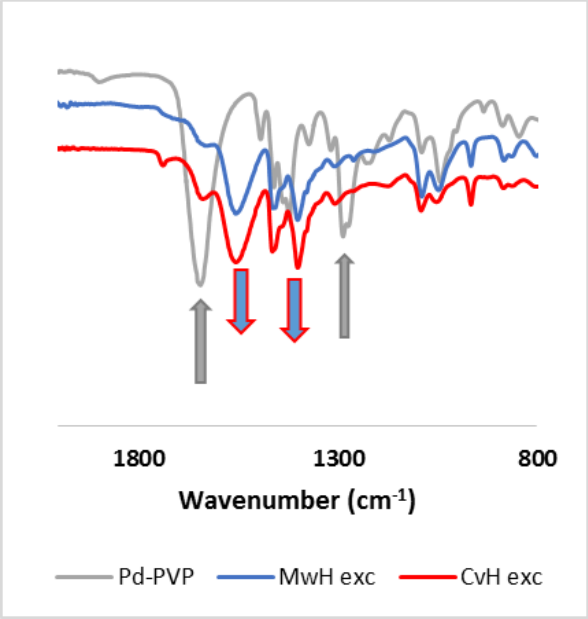

Figure 2.16. Comparative FT-IR spectra of ligand exchange studies conducted with PdNPs using dielectric and convective heating.

In the case of PtNPs, the ligand exchange reactions did not seem to be as efficient as that observed for the Pd counterparts. Even when the exposure time of the heat source was increased, complete phase transfer was not observed. This is most likely due to the fact that Pt has a greater affinity for the functional groups of the polymeric capping agent (the surface Pt atoms have more diffuse 5d orbitals that allow for a better overlap with the functional groups of PVP). Furthermore, elemental micro-analysis (ICP-MS) confirmed that PtNPs incorporate more PVP monomers per NP than Pd (Table 2.2). Despite only being able to achieve a partial ligand exchange for PtNPs, the reaction did not result in any noticeable change to the average particle size or morphology as can be observed in Figures 2.17 & 2.18. FT-IR spectroscopy of the reactants and products after ligand

exchange experiments confirmed that µwH provides a more efficient method to displace PVP and incorporate oleic acid and oleylamine as capping agents (Figure 2.19). In the case of microwave assisted ligand exchange reactions, the C=O stretching band of PVP at *ca*. 1640 cm^{-1} and less intense C–H modes (*ca*. 1287 cm^{-1}) disappeared and were replaced by strong antisymmetric C–O vibrations modes of the carboxylate groups *ca*. 1455 cm^{-1}, in addition to a new N–H bending mode at 1376 cm^{-1}. It is evident that convective heating does not aid in the complete displacement of the polymeric stabilizing agent as there are still remnants of stretching bands that correspond to PVP and the bands that can be assigned to the molecular stabilizing agents are weak (especially when compared to the microwave-assisted ligand exchange study).

Table 2.2. % C, N, H and M (M = Pd, Pt) ICP-MS values for µwH- and CvH-MNPs and M:N ratios as an estimate for the number of PVP monomers per M atom.

	% C	**% N**	**% H**	**% M**	**% M:N**
µwH-PdNPs	16.6	2.5	2.1	7.4	3.0
CvH-PdNPs	33.7	5.6	4.6	29.2	5.2
µwH-PtNPs	44.6	8.1	7.9	12.7	4.2
CvH-PtNPs	23.9	4.3	3.6	27.9	6.5

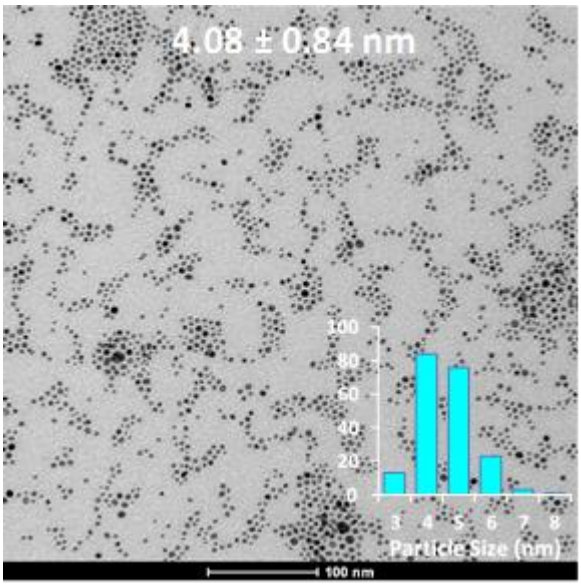

Figure 2.17. TEM image of μwH-PtNPs functionalized with 1:1 oleic acid : oleylamine using μwH.

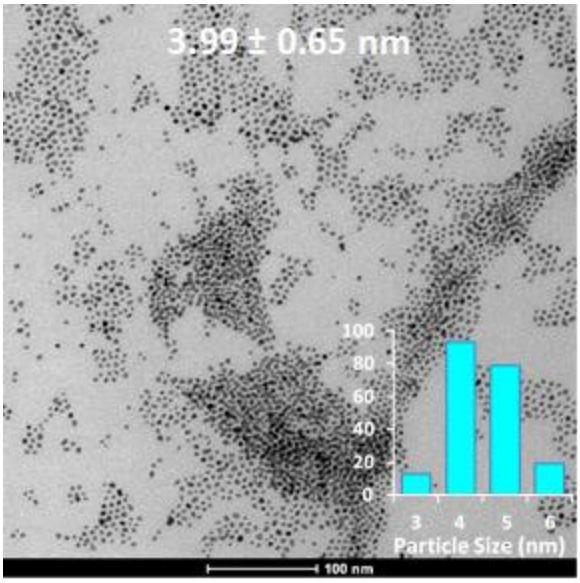

Figure 2.18. TEM image of CvH-PtNPs functionalized with 1:1 oleic acid : oleylamine using conventional heating.

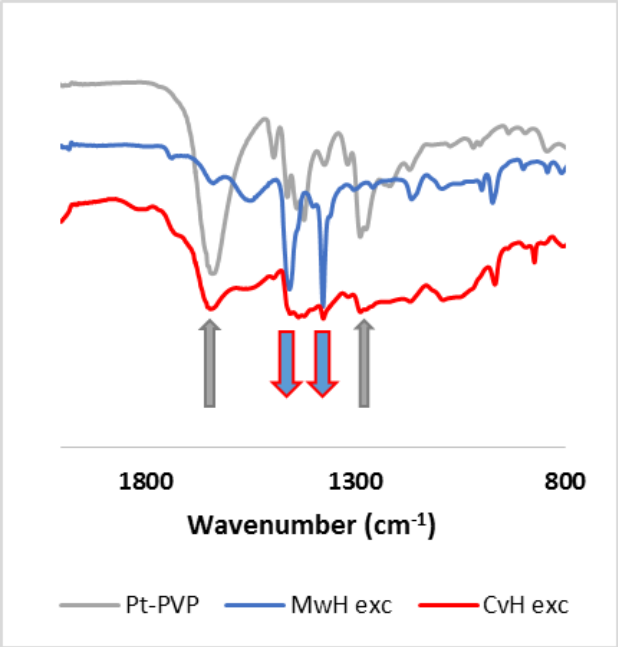

Figure 2.19. Comparative FT-IR spectra of ligand exchange studies conducted with PtNPs using µwH and conventional heating.

2.5 CONCLUSION

Several beneficial effects of µwH as an alternative to convective heating were demonstrated in the one-pot nucleation and growth of polymer-capped noble MNPs. µwH was found to have a marked effect on both nucleation and growth mechanisms, using the popular and convenient polyol method in which metal halide precursors were reduced by hot ethylene glycol in the presence of a polymeric capping agent, such as PVP. Nucleation is fast when performed under µwH and also leads to highly uniform particles, unlike identical reactions that were heated conventionally using an oil bath. Another attractive capability of microwave-assisted heating was observed in the exchange of PVP with oleic acid and oleylamine. The exchange reaction was efficient and proceeded cleanly under µwH at 150 °C, without any detectable change to the size or

morphology of the Pd or PtNPs. It was, however, difficult to achieve similar degrees of exchange under convective heating.

The superior catalytic activity of microwave-prepared cubic RhNPs *versus* conventionally-prepared RhNPs with assorted morphologies was also demonstrated in the vapor-phase hydrogenation of cyclohexene.

3. X core-Rh shell NPs (X = Au, Ag)

3.1 INTRODUCTION

Catalyst materials that contain highly dispersed, structurally-defined noble metal nanoparticles (MNPs) are of timely interest in a wide range of heterogeneously-catalyzed transformations.[181–184] The majority of critical industrial-scale reactions (oxidation, hydrogenation, cross-coupling, *etc.*) rely on expensive and often rare noble metals as the active catalytic species. MNPs are very attractive alternatives to bulk metal catalysts, because their intrinsically high surface area to volume ratios results in a far greater proportion of surface atoms that can affect catalytic transformations.[185] They also offer significant potential for superior, structure-related selectivity, based on intrinsic correlations between metal surface structure and catalytic reactivity.[184,185]

Mixed-noble metal core-shell NPs with defined surface structures are of particular current interest in this regard, because their catalytic properties are broadly tunable based on the identities and relative compositions of the two components.[186–189] Catalytic activity and selectivity of core-shell MNPs can be significantly enhanced *versus* individual, pure metal NPs due to mixing of the electronic properties of each element at the core-shell interface, or due to atomic ensemble effects.[190–194] Moreover, the construction of core-shell MNPs that display very thin shells (1-4 monolayers) of the

---

Part of the work in this chapter has been previously published as a journal article ("Microwave Synthesis of Au–Rh core–shell nanoparticles and implications of the shell thickness in hydrogenation catalysis." Garcia, S.; Anderson, R. M.; Celio, H.; Dahal, N.; Dolocan, A.; Zhou, J.; Humphrey, S. M., *Chem. Commun.*, **2013**, *49*, 4241.). Humphrey, S. M. conceived the scientific idea; Garcia, S. and Dahal, N. performed the experiments and data analysis; Anderson, R. M. performed EXAFS experiments; Celio, H., Dolocan, A. and Zhou, J. aided with data collection and analysis.

most expensive and rarest noble metals supported around cores consisting of less expensive, more abundant elements is emerging as an important synthetic strategy; a number of novel synthetic studies using molecular precursors and organic capping agents, have shown great promise.[195–198]

3.2 Synthesis and Characterization

3.2.1 Materials

Rhodium trichloride hydrate ($RhCl_3 \cdot xH_2O$, 98%; Johnson Matthey), hydrogen tetrachloroaurate ($HAuCl_4 \cdot 3H_2O$, 98%; Sigma Aldrich), silver nitrate ($AgNO_3$, 99%; Mallinckrodt Chemicals), sodium borohydride ($NaBH_4$, 98% ; Sigma Aldrich), poly(vinylpyrrolidone) (PVP, $<M_w>$ = 55,000; Sigma Aldrich), ethylene glycol ($\{CH_2OH\}_2$, 99.8%; Fisher Scientific) and 1-cyclohexene (C_6H_{10}, 99%; Alfa Aesar) were used as received. All other reagents and solvents (analytical grade) were employed without further purification unless stated otherwise.

3.2.2 Synthesis Methods

A MARS 5 (CEM Corp.) microwave system with a maximum power of 1600 W (2.45 GHz) was used to perform all the NP synthesis reactions. The reaction temperature inside the microwave cavity was finely controlled by power modulation *via* a RTP-300+ fiber optic temperature, located in a beaker of solvent identical to that employed in the reaction. *Note: Insertion of the temperature probe directly into the reaction vessel should be avoided; build-up of solid NPs on the probe sheath during the course of the reaction*

may lead to sparking and ignition. A 50 mL round-bottom flask fitted with a water-cooled reflux condenser was placed in the center of the microwave chamber. Both solvent and reactants were magnetically stirred (medium speed setting) and the Rh precursor was then added into the solvent using a disposable, fine-bore Teflon tube right above the solution, ensuring that the addition rate was constant. The addition rate of the precursors was controlled using an Aladdin Programmable Syringe Pump (WPI, Inc.) that was directly attached to the Teflon tubing. The reactions were carried-out at ambient pressure in air, with venting at the top of the reflux condenser *via* a three-way stopcock. Prior to each new reaction, glassware was thoroughly cleaned in a two-stage acid-base wash (12.0 M HCl aq., 1−2 d; 5 M NaOH in *i*-PrOH/H2O, 1−2 d), followed by oven drying at 110 °C.

3.2.3 Characterization Methods

Transmission Electron Microscopy (TEM) images were obtained from a FEI Tecnai microscope operating at 80 kV. The samples were prepared by drop-casting a single aliquot of NPs dispersed in ethanol onto 200 mesh carbon coated copper formvar grids (Ted Pella Inc.) and allowing for subsequent evaporation in air. MNPs sizes and standard deviations were derived by measuring a minimum of 200 individual particles per experiment, and by averaging multiple images from samples obtained from at least two separate syntheses. Individual particles were measured using Image-J (http://rsbweb.nih.gov/ij), which finds the area of each nanoparticle by pixel counting. High-resolution TEM (HRTEM) and energy dispersive X-ray analysis (EDX) were performed using a JEOL 2010F transmission electron microscope. This instrument was operated at 200 keV using a field-emission gun with 0.19 nm point-to-point resolution.

Powder X-ray diffraction patterns were recorded with a Rigaku R-Axis Spider diffractometer with an image plate detector using a graphite monochromator and CuKα radiation (λ = 1.5418Å) operated at 40 kV and 40 mA; spectra were collected using a scan speed of 3° min^{-1} with a step width of 0.020 (2θ). The instrument was controlled using Rapid/XRD diffractometer control software. The integration of the two dimensional data into a one dimensional pattern was accomplished using 2DP. UV-vis data were collected using a Carry 6000i UV-vis NIR spectrometer equipped with a double beam and a wavelength range of 175−3300 nm. Time-of-Flight Secondary Ion Mass Spectrometry (TOF–SIMS) analysis were done using a TOF–SIMS 5 instrument (ION-TOF GmbH, Germany 2010), which used a primary ion beam (Bi_1^+, 30 keV, 2.8 pA measured sample current) to raster-scan an area of 200 x 200 μm^2. The actual sputtering was done using a Cs^+ ion beam (500 eV energy, 63 nA measured sample current) on a 500 X 500 μm^2 area centered on the probing area. Due to strong charging of the surface, a constant, low energy electron beam (21 eV) was directed on the samples at all times during data acquisition for charge compensation. All detected secondary ions had negative polarity. X-ray photoelectron spectroscopy (XPS) was performed using a Kratos Axis Ultra Photoelectron Spectrometer. The XPS spectra were recorded utilizing a monochromated Al-K_α x-ray source (hγ=1486.5 eV), hybrid optics (employing a magnetic and electrostatic lens simultaneously) and a multi-channel plate coupled to a hemispherical photoelectron kinetic analyzer. All spectra were recorded using four sweeps for signal averaging, a dwell time of 1800 msec, an aperture slot of 300 x 700 μm, a pass energy of 20 eV and 0.1 eV per step. To minimize sample charging and band shape distortion due to charging, the XPS spectra were recorded using the Kratos charge neutralizer (20 eV electrons) while the sample stage was left floating (*i.e.* not connected to ground (earth)). The effectiveness of the neutralizer under these conditions notably

improved the resolution of the spectra since, for example, the Au 4*f* bands of the reference PVP-capped μwH-AuNPs were significantly sharper with a small tail in the high binding energy side of this transition. This tail may also be a contribution from oxidized Au atoms. Casa XPS analysis software was used for peak deconvolution and the stoichiometry of samples was determined from corrected peak areas and employing Kratos sensitivity factors for each element of interest. Samples for TOF–SIMS and XPS analysis were prepared by drop-casting ethanol solutions of the particles on ITO coated glass wafers allowing evaporation of the solvent in air. X-ray absorption spectroscopy (XAS) data were collected at beamline X18B at the National Synchrotron Light Source at Brookhaven National Laboratory. Approximately 115-130 mg of the SiO_2 supported NPs were pressed at a pressure of 3 tons for 30 s to form a pellet for analysis. Reference foils were collected in transmission mode between I_o and I_t gas ionization chambers and the data fit to yield the amplitude reduction factors for each edge. For the Au L_3 edge spectra, I_0 was purged with N_2 and I_t purged with 50% Ar and 50% N_2. For the Rh K–edge spectra, I_0 was purged with Ar and I_t with 80% Ar and 20% Kr. For the pellet analysis I_0 was the same as for the respective foils, but the spectra were collected in fluorescence mode using a passivated implanted planar silicon (PIPS) detector. The data were analyzed using the IFFEFIT software package.[199] Simultaneous first shell fitting of both edges was done using a k-weight of 2 and by constraining the bond length and Debye-Waller factors for the Au-Rh and Rh-Au scattering paths to be equivalent.

3.2.4 Synthesis of Au seeds

A solution of *poly*(vinylpyrrolidone) (200 mg, 1.8 mmol) and sodium borohydride (20 mg , 0.52 mmol) in ethylene glycol (15.0 mL) was prepared directly in

the reaction vessel and brought to 150 °C with stirring using microwave heating (μwH). A second solution of $HAuCl_4 \cdot 3H_2O$ (20 mg, 0.05 mmol) was prepared in the same solvent (5.0 mL) and loaded into a fresh 10 mL disposable syringe. For the preparation of Au seeds, 5.0 mL of the precursor solution was injected into the hot stirred PVP solution at a rate of 3 mmol h^{-1} (300 mL h^{-1}). The color of the solution rapidly became red/pink. The mixture was stirred for an additional 30 minutes at 150 °C after completion of the precursor addition. The reaction was then cooled quickly by transferring the reaction vessel to an ice-water bath. The Au NPs seeds were precipitated by adding acetone (*ca.* 60.0 mL) to give a red brown suspension, which was briefly sonicated (1 min). The precipitate was then isolated by ultracentrifugation (5 krpm, 5 min) and the colorless supernatant was decanted away to leave a red brown solid. This was further purified to remove excess PVP and ethylene glycol by 3 cycles of dissolution in ethanol (15.0 mL) followed by precipitation with hexane (75.0 mL) and isolation by centrifugation.

3.2.5 Synthesis of Ag seeds

A solution of *poly*(vinylpyrrolidone) (160 mg, 1.44 mmol) in ethylene glycol (20.0 mL) was prepared directly in the reaction vessel and the temperature was increased to 150 °C using μwH along with stirring. A second solution of $AgNO_3$ (95 mg, 0.56 mmol) was prepared in the same solvent (10.0 mL) and loaded into a fresh 10 mL disposable syringe. For the preparation of Ag seeds, the precursor solution was injected into the PVP mixture at a rate of 5.6 mmol h^{-1} (100 mL h^{-1}). The colorless solution turned light yellow as the metal precursor was added. The mixture continued stirring at 150 °C for 5 min after the Ag^+ precursor was added, at which time the yellow color intensified. The reaction was then cooled rapidly by transferring the reaction vessel to an

ice-water bath. The Ag seeds were precipitated by adding acetone (105.0 mL) to give a light yellow suspension, which was briefly sonicated (1 min). The precipitate was then isolated by ultracentrifugation (5.5 krpm, 5 min) and the colorless supernatant was decanted away to leave a yellow orange solid. This was further purified to remove excess PVP and ethylene glycol by two cycles of dissolution in ethanol (10.0 mL) followed by precipitation with hexane (60.0 mL) and isolation by centrifugation (2.5 krpm, 3 min).

3.2.6 Controlled growth of Rh over Au cores

A suspension of Au seeds was prepared directly in the reaction vessel by dissolving 3 mg of dried Au NPs and PVP (200 mg, 1.8 mmol) in ethylene glycol (15.0 mL), and it was then brought to 150 °C with stirring using μwH. A second solution of $RhCl_3 \cdot xH_2O$ (10 – 40 mg, 0.048 – 0.19 mmol) was prepared in the same solvent (5.0 mL) and loaded into a fresh 10 mL disposable syringe. The Rh solution was added into the hot stirred PVP/Au suspension at a rate of 20 mL h^{-1}. The Rh shell thickness was controlled by the concentration of the Rh solution, which affected the addition rate in terms of mmol of metal added per unit of time (0.19 mmol h^{-1} – 0.76 mmol h^{-1}). The red color of the initial Au suspension, rapidly became brown after the injection of the Rh precursor. The mixture was then stirred for an additional 30 min at 150 °C after the Rh precursor was added. After this period, the reaction was cooled down using an ice-water bath and the resulting particles were extracted and purified as stated above for the Au seeds.

3.2.7 Controlled growth of Rh over Ag cores

The as-synthesized Ag seeds were redispersed in ethylene glycol (20.0 mL) along with PVP (100 mg, 0.9 mmol). This mixture was heated to 130 °C utilizing μwH. Once

the target temperature was achieved, a solution of $RhCl_3 \cdot xH_2O$ in ethylene glycol (4 – 40 mg, 0.019 – 0.19 mmol, 5.0 mL) was added to the hot PVP/Ag mixture at a rate of 20 mL hr^{-1} (0.076 – 0.76 mmol hr^{-1}). The shell thickness of the Rh overlayers was controlled by the amount of Rh precursor added. During this addition period, the yellow mixture turned dark brown. The mixture continued stirring at the same temperature while still being exposed to μwH for an additional 30 min. After this stage was completed, the NP suspension was immediately quenched using an ice–water bath. The NP mixture was then treated with acetone (110.0 mL) and the particles were extracted by centrifugation (5 min, 5.5 krpm). The NPs were further purified by redispersion in ethanol (10.0 mL) and treatment with hexanes (60.0 mL) followed by another cycle of ultracentrifugation (3 min, 2.5 krpm).

3.3 Results and Discussion

Au-RhNPs and Ag-RhNPs were targeted for the following reasons: (i) Both Au and Ag are stable towards oxidation, so well-defined Au and AgNPs tend to be easily synthesized, and are highly stable once formed; (ii) All three metals, Au, Ag and Rh, exhibit face-centred-cubic (FCC) lattices with a slight (7%) lattice mismatch (4.08 & 4.09 *versus* 3.80 Å); (iii) Rh is highly active for hydrogenation, but Au and Ag are unable to dissociate H_2; and, (iv) there is an obvious economic motivation in limiting the quantity of Rh required per NP by using Au or Ag. According to the USGS, less than 30 t of Rh were mined annually during the period 2006−2010;[200] during the same period, the cost of Rh peaked at \$350 g^{-1}, approximately 7 times that of Au and an astonishing 360 times that of Ag.

3.3.1 Au-Rh core-shell NPs

AuNPs were prepared by reducing $HAuCl_4 \cdot H_2O$ with $NaBH_4$ in the presence of PVP in ethylene glycol at 150 °C for 30 min under μwH; borohydride was required because ethylene glycol alone cannot reduce Au(III) at 150 °C. The resulting isolated AuNPs were mostly spherical and near monodisperse, measuring 5.6 ±1.5 nm, determined by transmission electron microscopy (TEM; Figure 3.1a). The AuNPs were employed in the overgrowth step without further modification. Based on the desired thickness of the shell, a specific quantity of $RhCl_3 \cdot xH_2O$ in ethylene glycol was added at a precise rate of 20.0 mL h^{-1} to the suspended AuNPs under μwH (controlled by syringe-pump). *In situ* reduction of Rh(III) by ethylene glycol facilitated the isotropic overgrowth of Rh(0) onto the AuNP seeds under μwH at 150 °C (Scheme 3.1). It should be noted that Rh has a significantly higher surface energy than Au (2.8 *versus* 1.6 J m^{-2}), so a hybrid structure in which Rh is deposited outside of an Au core is not the most thermodynamically-favoured arrangement.[201] It should also be noted that although Au(0) and Rh(0) are immiscible in the bulk, alloying and/or core-shell inversion may still be possible on the nanoscale.[202]

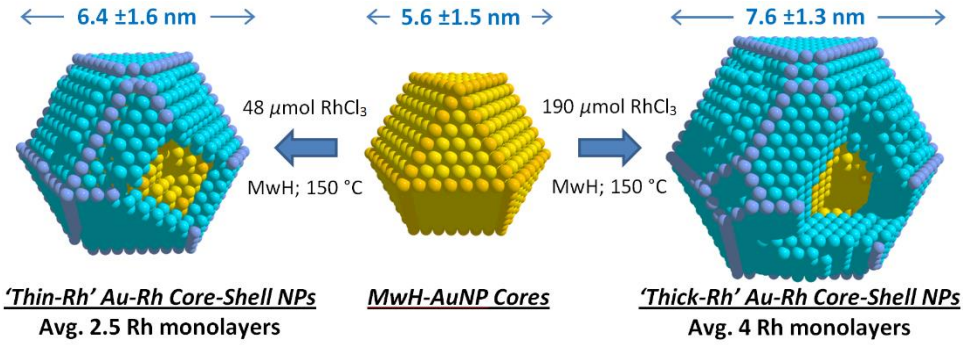

Scheme 3.1. Diagrammatical representation of the Au-Rh core-shell NPs structures, prepared using microwave–assisted synthesis: yellow/orange = Au; blue/violet = Rh.

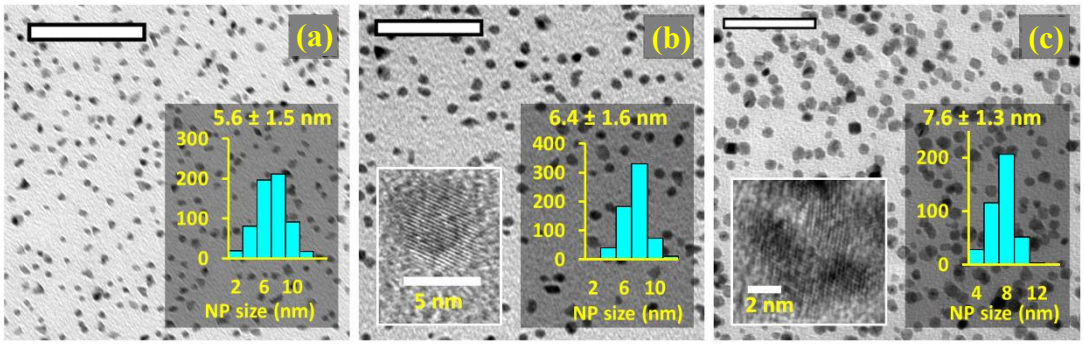

Figure 3.1. TEM images, histograms and HRTEM images (inset) for: (a) AuNP cores; (b) Thin-Rh core-shell NPs; (c) Thick-Rh core-shell NPs. Scale bars = 50 nm.

The synthetic method employed allows for simple modification of the Rh shell thickness over a broad range. In this chapter, the structural and catalytic properties of very thin and potentially strained Rh overlayers have been probed in detail, based on the assumption that increasingly thicker Rh shells should mimic the behavior of bulk Rh. Specifically, 48 and 190 μmol of $RhCl_3$ was added to separate 3.0 mg batches of as-synthesized AuNPs. Initial analysis of the products by low and high-resolution TEM showed in both instances a majority of crystalline, spherical particles with a minority of more highly anisotropic structures. The Au-RhNPs had size distributions of 6.4 ±1.6 nm and 7.3 ±1.3 nm (denoted 'thin-Rh' and 'thick-Rh,' respectively; Figures 3.1b & 3.1c; Figures 3.2 & 3.3), which correspond to average particle size increases of 0.8 and 2.0 nm. These size increases approximate to 2.5 Rh monolayers (thin-Rh) and 4.0 Rh monolayers (thick-Rh), based on a metallic Rh-Rh layer-separation distance of 0.269 nm and assuming isotropic thickness of the Rh shells (Scheme 3.1).

In order to confirm that only Rh was present on the Rh-AuNP surfaces, samples from multiple preparations of the thin-Rh and thick-Rh samples were initially probed using XPS, in which the C1s signal at 285.1 eV (arising from the incorporated PVP polymer) was used as a reference. Additional control studies were run on the μwH-AuNP cores and 12.4 ±2.1 nm μwH-RhNPs that were prepared using the same method (Figures 3.4 & 3.5 & Table 3.1).[39] The former displayed an intense peak for Au(0) (84.0 eV; $4f_{7/2}$) and the latter pure PVP-capped RhNPs gave a peak which was assigned to Rh(I) (308.5 eV; $3d_{5/2}$). Interestingly, the thin-Rh core-shell NPs showed a marked decrease in intensity of the Rh signal at 308.5 eV, accompanied by the appearance of a second, new signal corresponding to Rh(0) (307.2 eV; $3d_{5/2}$), where Rh(0)/Rh(I) = 0.59 (Figure 3.6 & Table 3.2). Thus, it appeared that the interaction of the Au core with the first 2-3 surface adlayers of Rh diminished the proportion of native oxidized Rh sites. As the amount of

Rh adlayers increased for thick-Rh, the XPS spectra more closely resembled the appearance of the pure RhNPs, with a single signal at 308.3 eV for Rh(I) (Figure 3.7). Meanwhile, the Au signal was extremely weak in thin-Rh samples (Rh/Au = 46) and was not observed for thick-RhNPs (Figures 3.6b & 3.7b), which indicated that Au was solely located in the core of the particles. The weak Au signal in the XPS spectrum of the Au-Rh core shell NPs does not indicate that the Rh layer is thicker than 10 nm. The particles have an overlayer of impurities and capping polymer that amount to several nanometers and may limit the escape pathway of the photoelectrons generated from the species in the core. A distinct Au(0) signal was only observed in both Rh-shell samples upon *in situ* Ar sputtering.

Comparison of the UV-vis absorption spectra for thin- and thick-Rh *versus* pure AuNPs and RhNPs prepared using the same μwH method also provided evidence for the deposition of Rh onto the Au cores (Figure 3.8a). The plasmon peak at 540 nm for the AuNPs was quickly dampened as Rh was deposited on the seeds. The original peak *ca.* 250 nm corresponding to the surface plasmon of the RhNPs was red shifted and became significantly more intense with increasing amount of added Rh, to resemble that of pure Rh. Powder X-ray diffraction analysis (PXRD) of the core-shell structures showed reflections in the range 35–90° 2θ corresponding to both pure Rh and Au (Figure 3.8a, inset). The relative intensities of Au reflections were largely unchanged as a result of Rh overgrowth. Rh reflections were very broad for the thin-Rh samples, as should be expected, and became slightly more defined as the Rh layer thickness was increased.

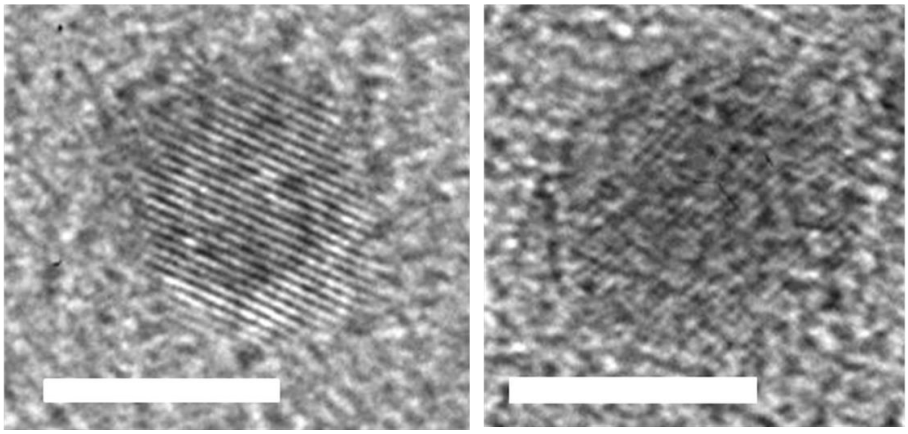

Figure 3.2. HRTEM images of thin Rh on Au NPs. The scale bars represent 5 nm.

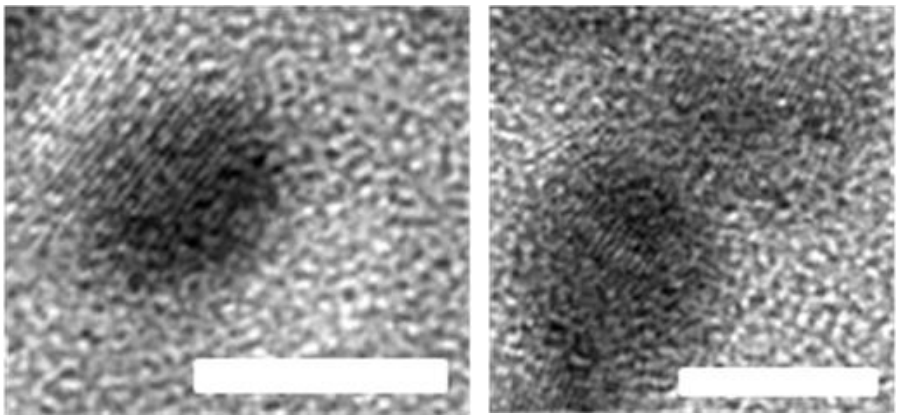

Figure 3.3. HRTEM images of Au-Rh core-shell NPs with a thick Rh layer. The scale bars represent 5 nm.

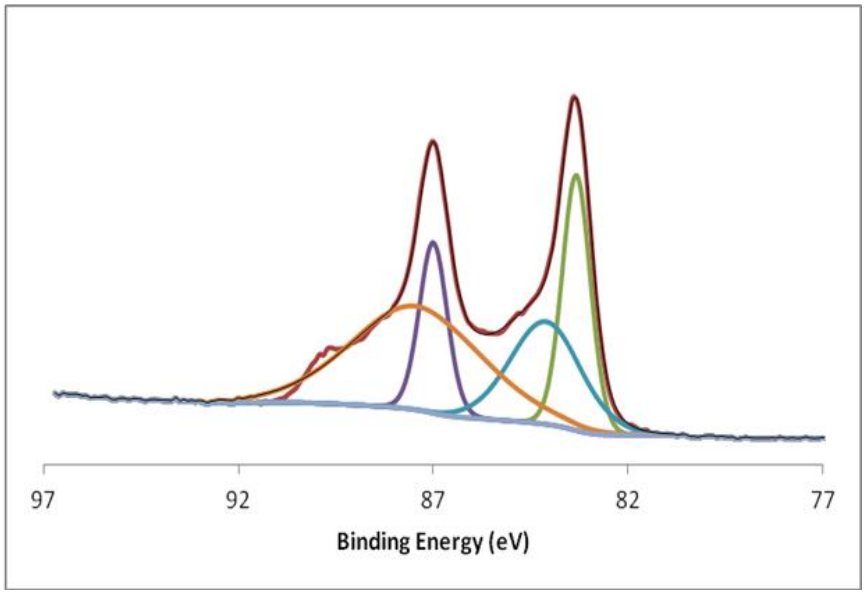

Figure 3.4. Fitted XPS data for PVP-capped μwH-AuNPs.

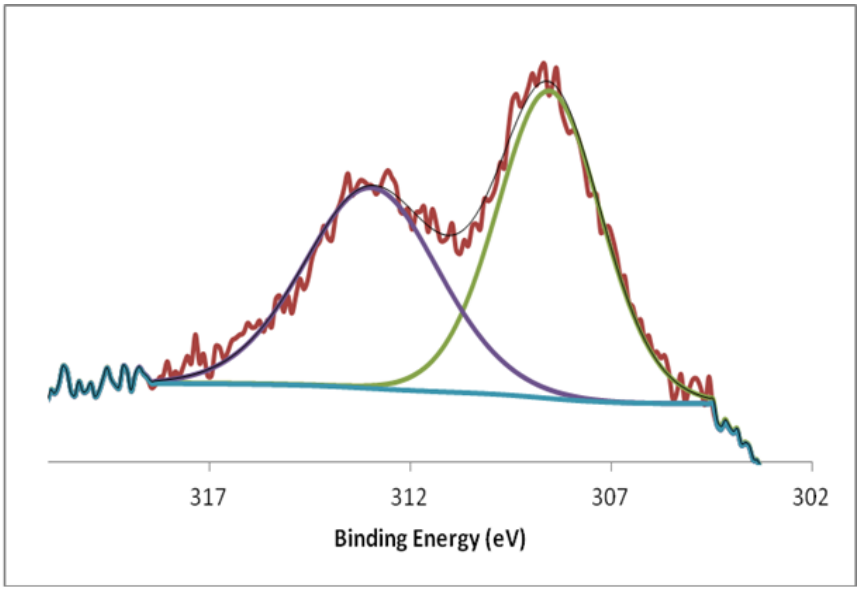

Figure 3.5. Fitted XPS data for pure PVP-capped RhNPs.

Table 3.1. Rh and Au binding energy values (eV) for μwH-Au seeds, μwH-RhNPs, thin- and thick-Rh acquired from XPS data.

	Rh $3d_{5/2}$ (0)	**Rh $3d_{3/2}$ (0)**	**Rh $3d_{5/2}$ (I)**	**Rh $3d_{3/2}$ (I)**	**Au $4f_{7/2}$ (0)**	**Au $4f_{5/2}$ (0)**	**Au $4f_{7/2}$ (I)**	**Au $4f_{5/2}$ (I)**
PVP-capped RhNPs	--	--	308.5	313.0	--	--	--	--
PVP-capped AuNPs	--	--	--	--	84.0	87.6	85.0	88.6
Thin Rh on Au	307.2	311.9	308.2	312.6	83.9	87.6	85.3	89.1
Thick Rh on Au	--	--	308.3	313.1	--	--	--	--

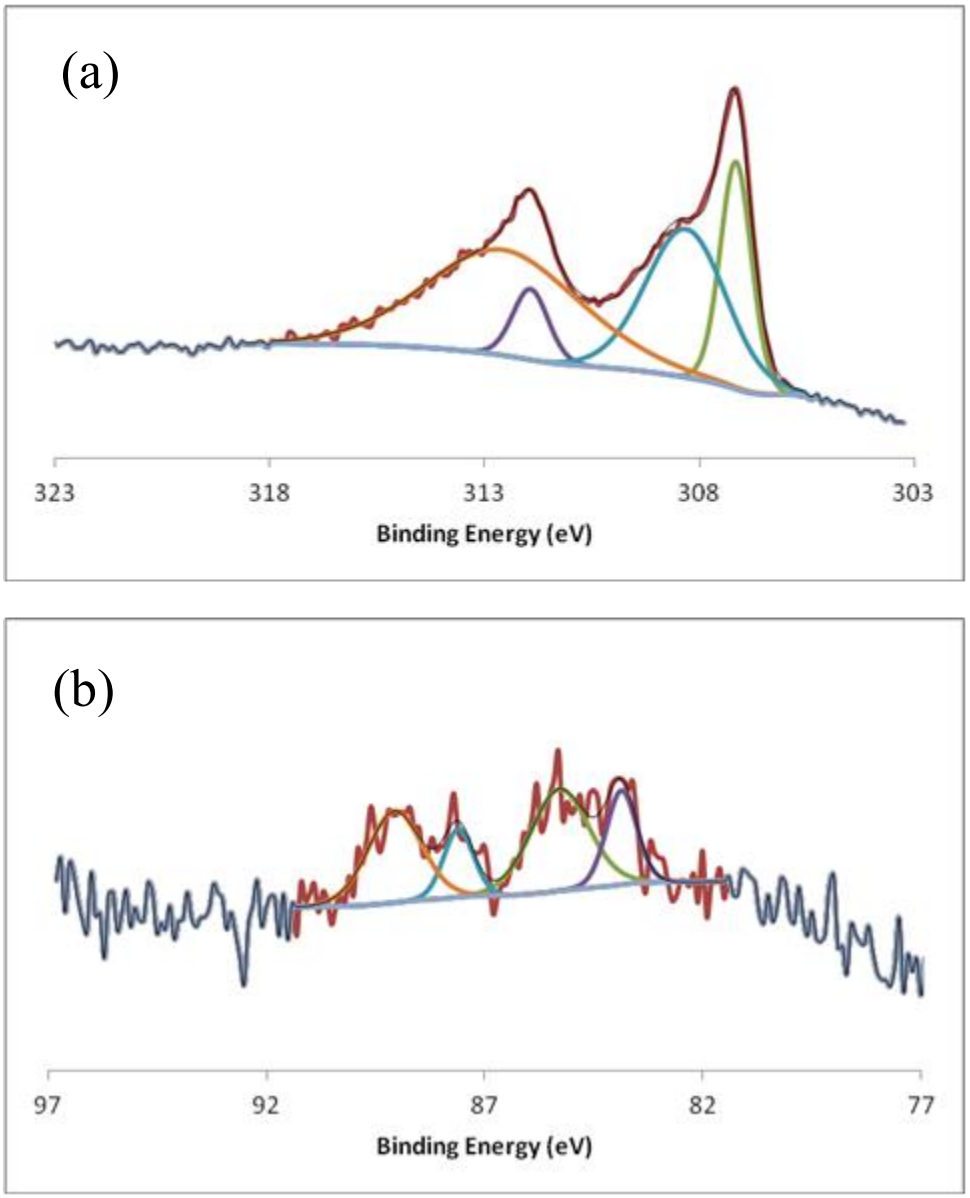

Figure 3.6. Fitted XPS data for Au-Rh core-shell NPs with a thin Rh layer; (a) Rh 3d signals corresponding to metallic Rh (307.2 eV) and Rh(I) (308.5 eV); (b) Au 4f signals indicating the presence of both Au(0) (83.9 eV) and Au(I) (85.3 eV).

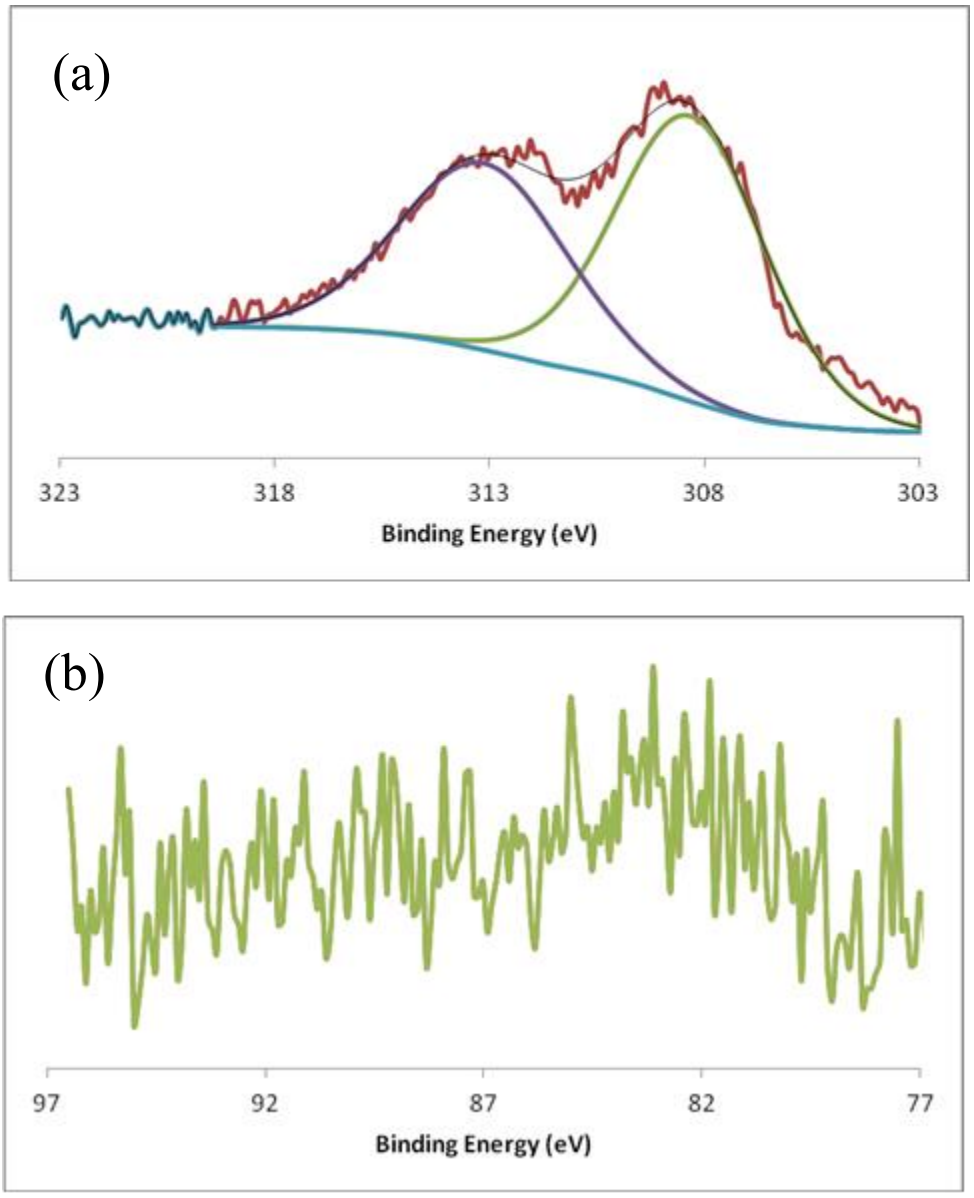

Figure 3.7. Fitted XPS data for Au-Rh ore-shell NPs with a thick Rh layer; (a) Rh 3d signals assigned to Rh(I) (308.3 eV); (b) Absence of Au 4f signal.

Table 3.2. Rh(I):Rh(0) and Au:Rh ratios, based on XPS values, for both thin-Rh and thick-Rh core-shell NPs prior to catalytic studies.

	Rh(I) : Rh(0)	**Au : Rh**
Thin-Rh NPs	1.7 : 1	1 : 46
Thick-Rh NPs	1 : 0	0 : 1

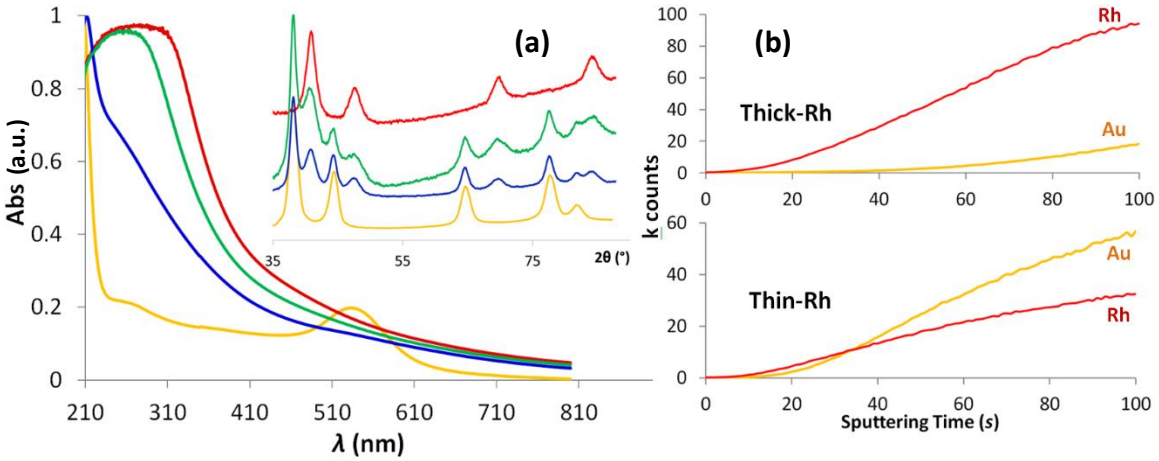

Figure 3.8. (a) Comparisons of UV-vis spectra and PXRD (inset): yellow = 5.1 nm AuNP cores; blue = thin-Rh core-shell NPs; green = thick-Rh core-shell NPs; red = 12 nm RhNPs. (b) TOF-SIMS bulk Rh and Au k-counts during the first 100 s of sputtering with Bi_1^+.

The Au-Rh core-shell structures were also analysed using TOF–SIMS to estimate the degree of surface separation between the two metals. Depth profiles for both Rh and Au were obtained from the secondary (ejected) ion counts as a function of sputtering time (Bi_1^+, 30 keV, 2.8 pA measured sample current; Fig. 3.9). For thin-Rh samples, the Rh/Au ratio was >1 for the first 30 seconds of sputtering and reached a maximum of ~8.5 after a few seconds. In comparison, the Rh/Au ratio for thick-Rh samples remained greater than parity for the first 350 seconds and reached a peak after 38 s, which suggested a thicker Rh shell (Figures 3.8b & 3.9).

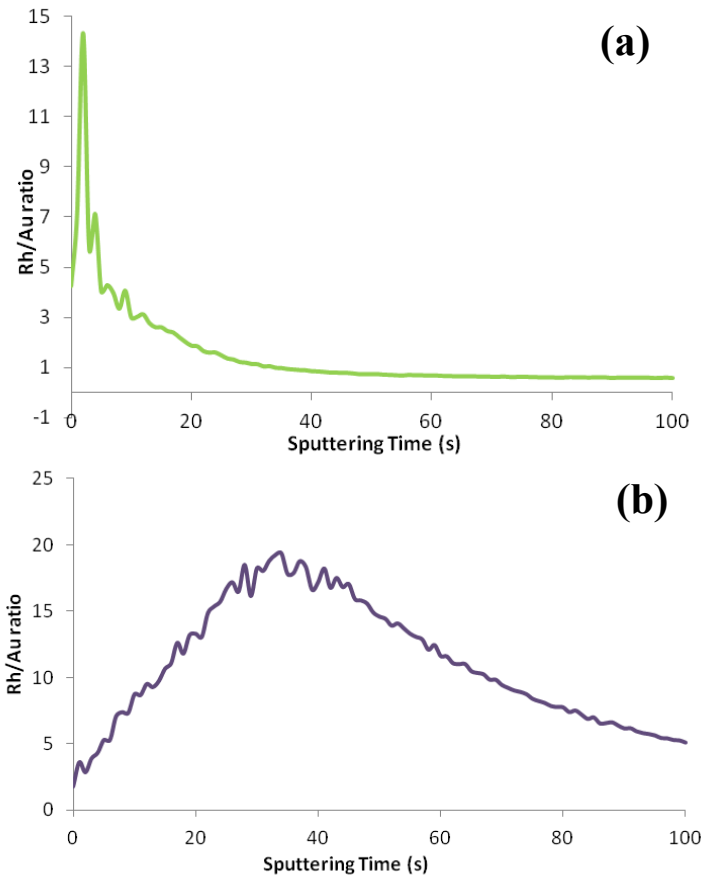

Figure 3.9. TOF SIMS: depth profiles for Rh and Au displayed as ratios as a function of sputtering time; (a) thin-Rh NPs; (b) thick-Rh NPs.

Line scan measurements and EDS analysis performed on thin Rh NPs (Figure 3.10) showed both Rh and Au on single particles. The distribution of these elements is consistent with an Au core-Rh shell structure. In the case of thick Rh on Au, no Au was observed (Figure 3.11). Area scans of several particle pockets did not display Au signals either. This observation rules out the existence of isolated monometallic Au NPs or Rh core-Au shell particles.

In further support of the successful assembly of stable Rh-Au core-shell NPs, we were able to study the core-shell NPs by extended X-ray absorption fine structure (EXAFS) spectroscopy analysis (Figure 3.12). Studies showed there was not a large contribution of Au-Rh or Rh-Au interactions in either the thin- or thick-Rh samples. This ruled out random alloying of the two metals and was also consistent with phase segregation. The Rh-Rh coordination number was found to be larger in the thick-Rh sample (7.9 ± 0.9) than in the thin-Rh sample (6.7 ± 0.8) (Table 3.3). The combined EDS and EXAFS data therefore clearly confirmed that both metals were present in the same particles, and having the desired core-shell structure.

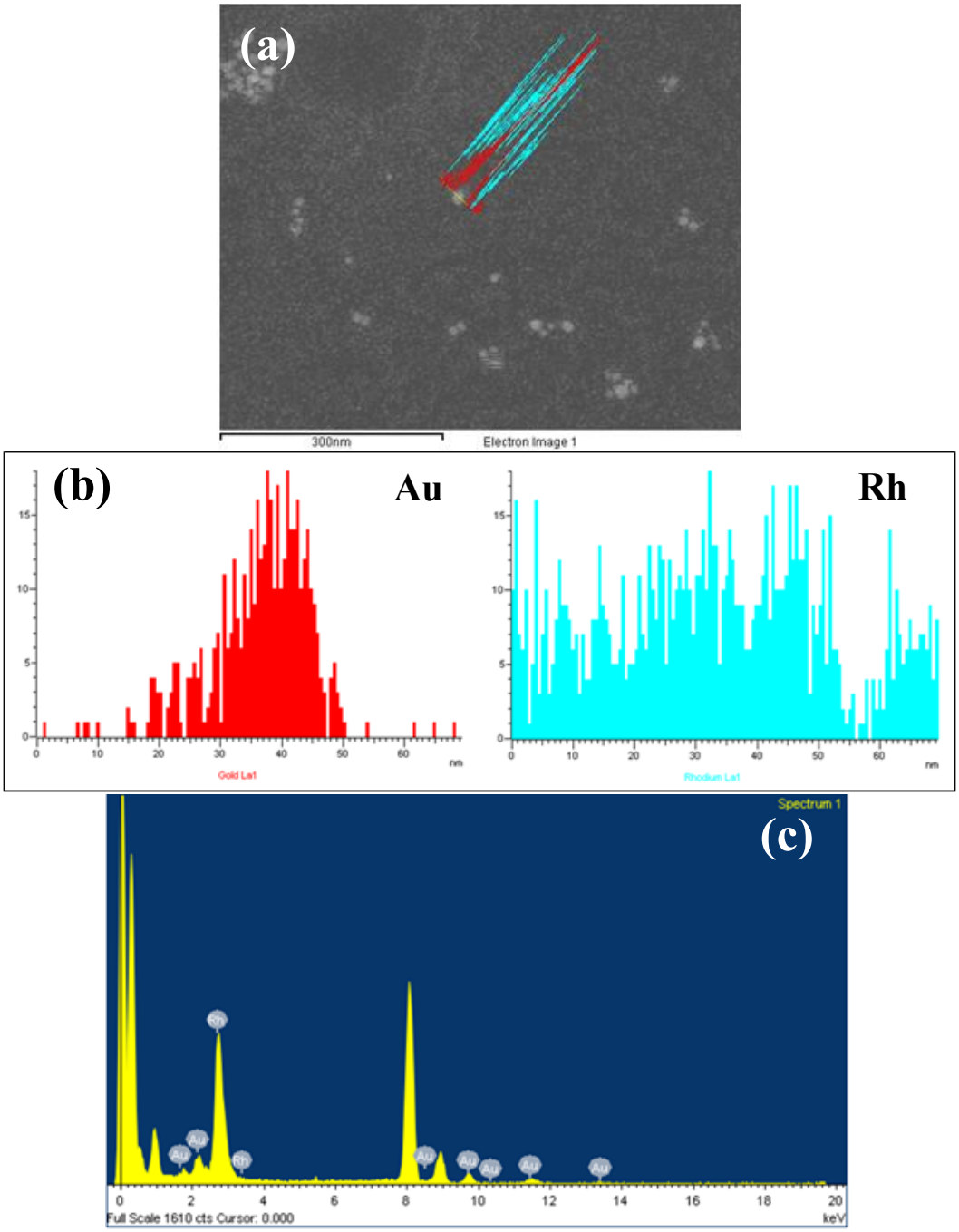

Figure 3.10. (a) TEM image and elemental profile of thin-Rh; (b) Au and Rh elemental distribution and (c) spectrum of a single thin-Rh on Au particle as given by EDS analysis. Any unlabeled peaks in the spectrum correspond to the C coated Cu grids used during TEM analysis.

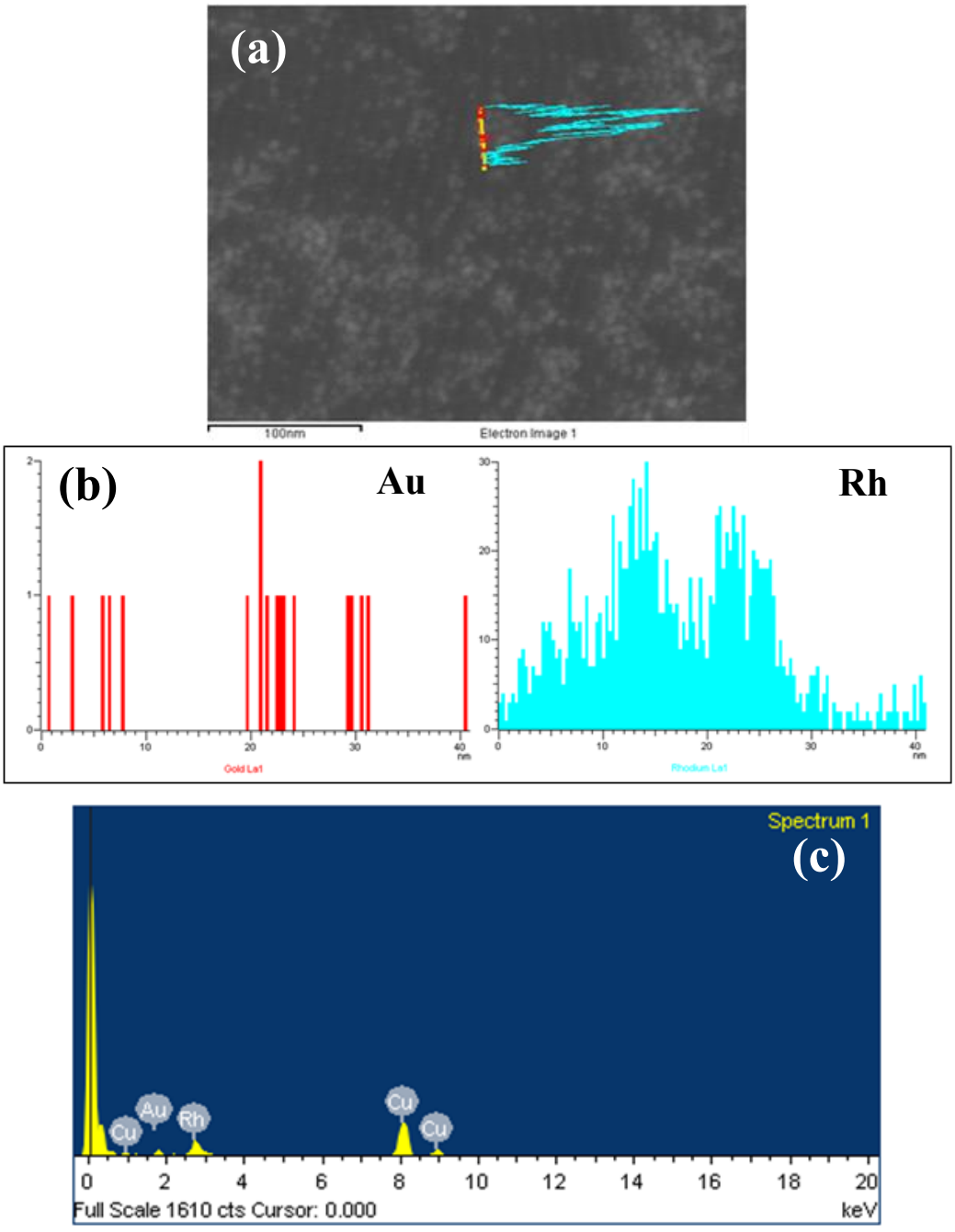

Figure 3.11. (a) TEM image and element profile of thick-Rh; (b) Au and Rh elemental distribution and (c) spectrum of two thick-Rh particles in a row given by EDS analysis. The Cu signals and other unlabeled peaks in the spectrum correspond to the C coated Cu grids used in TEM analysis.

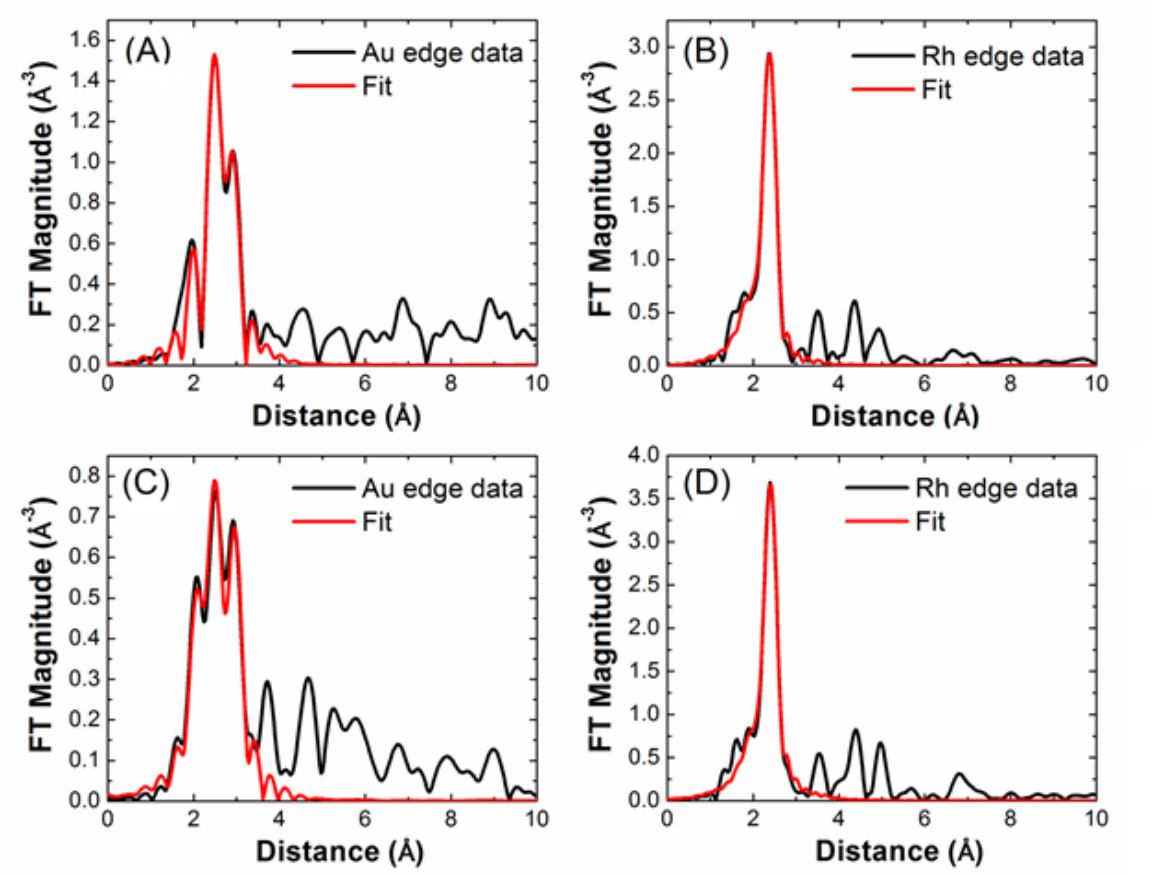

Figure 3.12. EXAFS analysis of (A and B) thin-Rh NPs and (C and D) thick-Rh NPs plotted in R-space. The black lines are the experimental data and the red lines are the calculated fits.

Table 3.3. Coordination numbers resulting from the EXAFS fitting analysis.

	CN_{Au-Au}	CN_{Au-Rh}	CN_{Rh-Rh}	CN_{Rh-Au}
Thin-Rh NPs	9.4 ± 5.0	1.0 ± 0.8	6.7 ± 0.8	0.7 ± 0.6
Thick-Rh NPs	11.0 ± 2.9	0.4 ± 0.4	7.9 ± 0.9	0.6 ± 0.8

3.3.2 Ag-Rh core-shell NPs

AgNPs were prepared employing a polyol method and μwH to reduce $AgNO_3$ in ethylene glycol at 150 °C in the presence of PVP for only 5 min. The resulting AgNPs were mostly spherical (cubeoctahedral) with an average diameter of 4.0 ± 0.9 nm as determined by TEM (Figure 3.13a). The seeds were then utilized in subsequent Rh shell growth without any further modifications. The amount of Rh precursor used in the growth steps was based on the desired thickness of the shell; the addition of Rh to the Ag seeds followed the same protocol described for Au-Rh core-shell NPs described previously. The same thermodynamic barriers (large differences in surface energies of the metals) and structural challenges (immiscibility of the metals in the bulk) that can be observed for the Au-Rh NPs can also be observed for the Ag-Rh system.

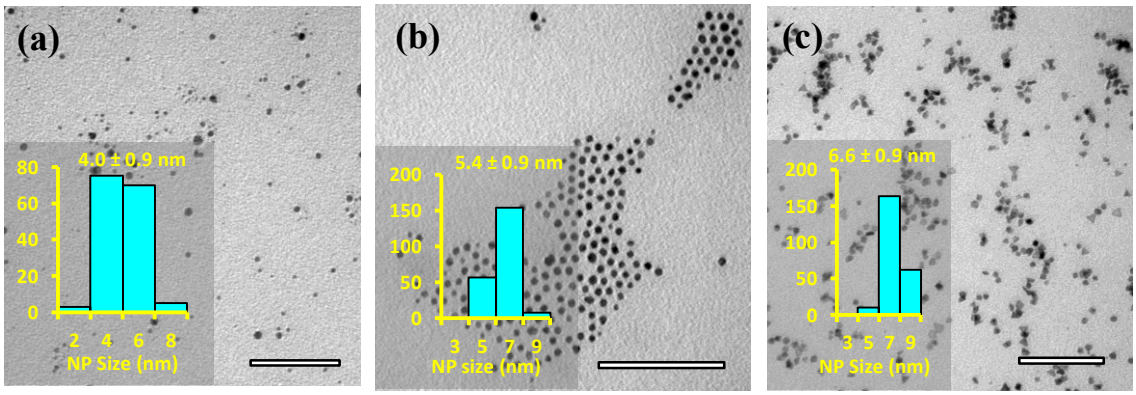

Figure 3.13. TEM images & histograms (insets) for: (a) AgNP cores; (b) Thin-Rh on Ag cores NPs; (c) Thick-Rh on Ag seeds NPs. Scale bars = 100 nm.

The Ag-RhNPs reported in this chapter were generated by the addition of 48 and 190 μmol of $RhCl_3$ to separate batches of Ag NPs. Analysis of the particles using both high and low resolution TEM showed that a vast majority of the particles formed after the Rh deposition were well-defined and crystalline (Figure 3.13 – 3.15). The Ag-RhNPs had an average size of 5.4 and 6.6 nm (Figure 13B & 13C; 14 & 15) displaying an enlargement of the initial Ag seeds by 1.4 and 2.6 nm. This increase in size corresponds to an approximate deposition of 2.6 and 4.8 Rh monolayers, respectively, based on a Rh-Rh inter–layer distance of 0.269 nm. Thus, it is appropriate to label these particles as 'thin-Rh' and 'thick-Rh' on Ag, similar to the shorthand terms used for the Au-Rh core-shell nanostructures.

Line scan EDS experiments were performed on both thin-Rh and thick-Rh in order to probe individual particles. Both Rh and Ag were detected on single particles and the distribution of the elements supports a core-shell structure (Figure 3.16 – 3.17). As expected, in the case of thick-Rh, the Ag signal was weaker. Both thin-Rh and thick-Rh NPs are very small in size, which caused significant drifting under the electron beam when performing EDS analyses and ultimately prevented high elemental counts to be acquired.

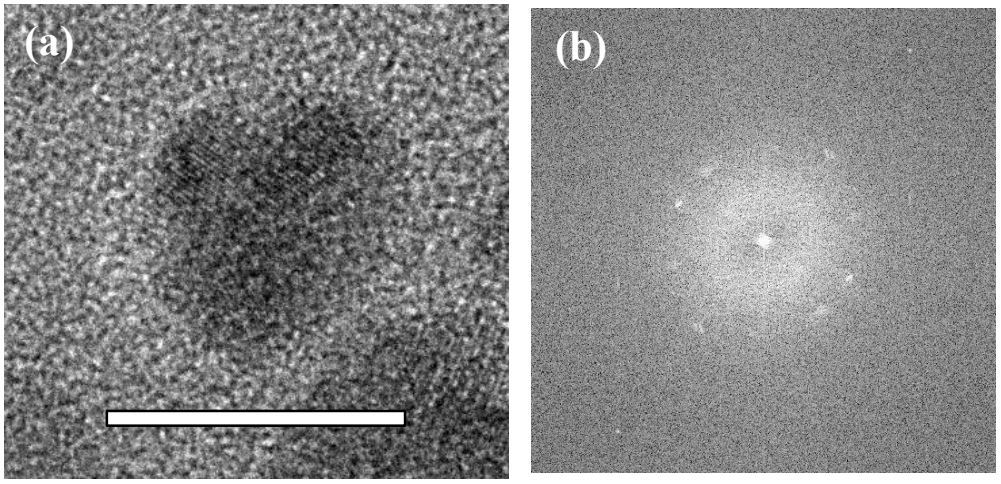

Figure 3.14. (a) HRTEM image (scale bar = 5 nm) and (b) FFT diffraction pattern for thin-Rh on Ag cores.

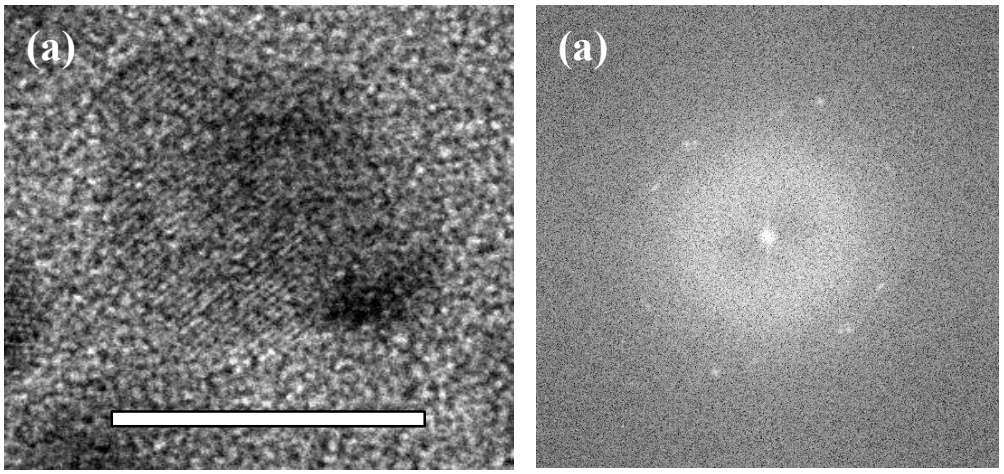

Figure 3.15. (a) HRTEM image (scale bar = 5 nm) and (b) FFT diffraction pattern for thick-Rh on Ag cores.

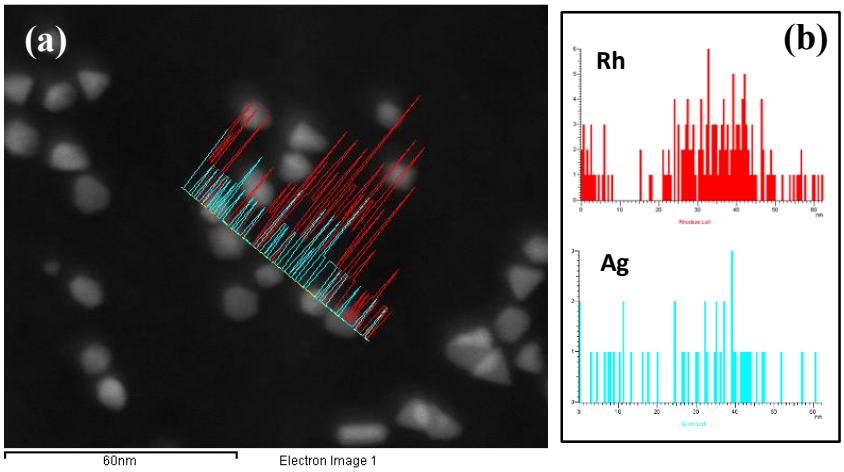

Figure 3.16. (a) TEM image and elemental profile of thin-Rh on Ag seeds and (b) Rh and Ag elemental distribution as determined by EDS analysis.

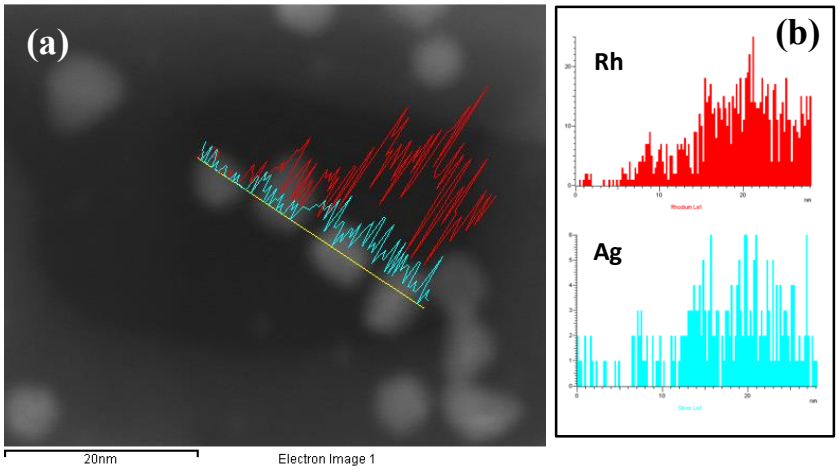

Figure 3.17. (a) TEM image and elemental profile of thick-Rh on Ag cores and (b) Rh and Ag elemental distribution as determined by EDS analysis.

XPS was employed as a *pseudo*-surface technique in order to confirm that only Rh was present on the surface of the Ag-Rh core-shell NPs. Thin-Rh and thick-Rh samples as well as the initial Ag cores were probed using this technique. The silver seeds studied displayed a single peak for Ag(0) (367.8 eV; $3d_{5/2}$), supporting the claim that Ag is very stable towards oxidation (Figure 3.18). As stated previously, pure PVP-capped RhNPs do not display this degree of oxidation stability as they show a peak that can be assigned to Rh(I) (308.5 eV; $3d_{5/2}$) but no signal for metallic Rh could be detected (Figure 3.5). Similarly to the Au-Rh core-shell NPs described earlier, thin-Rh on Ag core-shell NPs displayed a significant decrease in intensity for the peak at 308.5 eV corresponding to Rh(I), while a peak at 307.0 eV emerged indicating the presence of metallic Rh (Rh(0)/Rh(I) = 2.45) (Figure 3.19a). Thus, it seemed that the electronic interaction between the Ag core and the first 2-3 Rh monolayers, decreased the Rh propensity to oxidize. This was further confirmed as the shell thickness increased for thick-Rh. For this sample, the intensity of the Rh(I) (308.6 eV; $3d_{5/2}$) signal increased while the Rh(0)/Rh(I) ratio decreased to 1.76 (Figure 3.20a). Given that the particles had an overlayer of impurities and are stabilized by a bulky polymeric capping agent, it is safe to assume that the escape pathway of the photoelectrons generated during the analysis was severely hindered. Thus, detecting a strong Ag signal, as in the case of 'thin-Rh' NPs (Figure 3.19b), confirmed the presence of a thin Rh shell (Rh/Ag = 29). As expected, the Ag signal became extremely weak as the shell thickness was increased to 4.8 monolayers and the escape pathway of the ejected photoelectrons from the core was further restricted (Figure 3.20b).

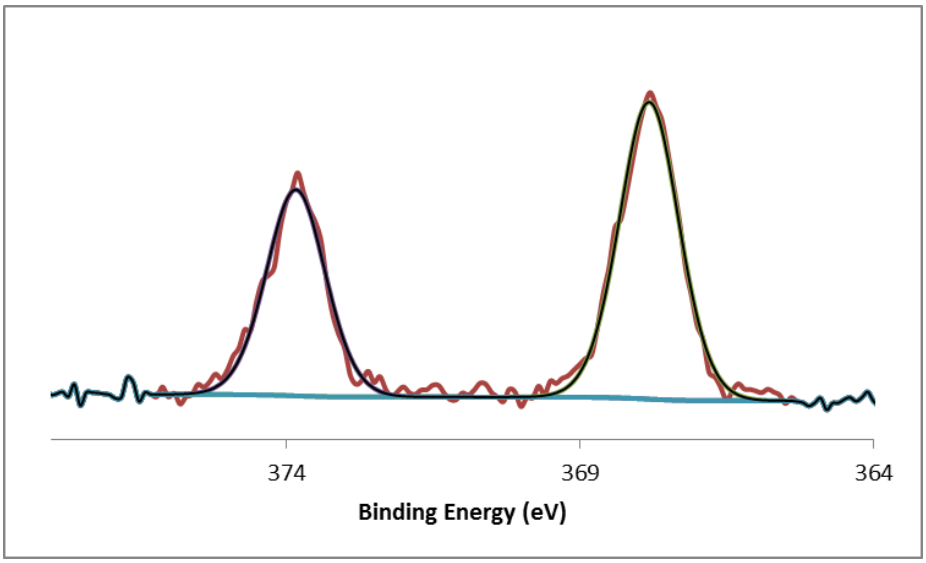

Figure 3.18. Fitted XPS data for PVP-capped microwave-assisted AgNPs (Ag(0): 367.8 eV).

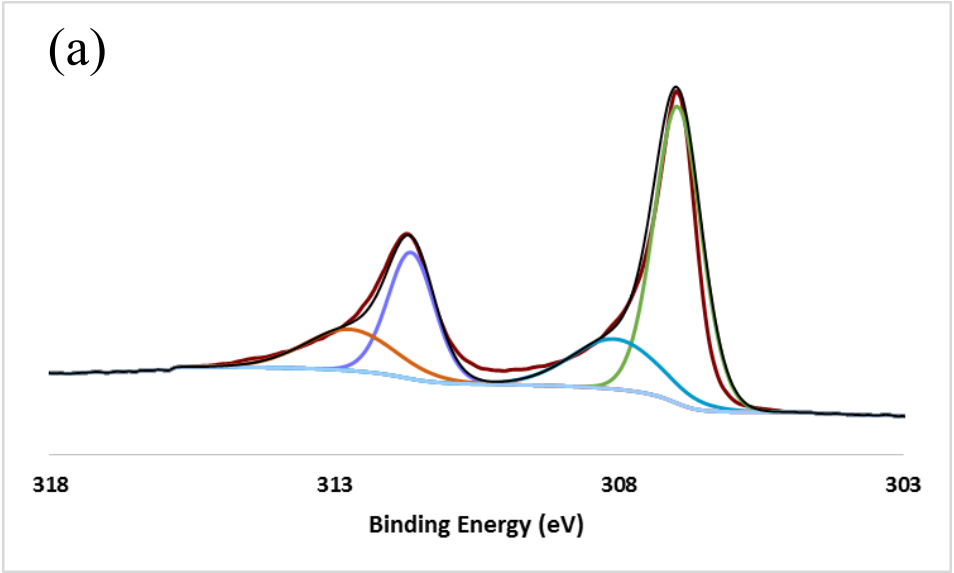

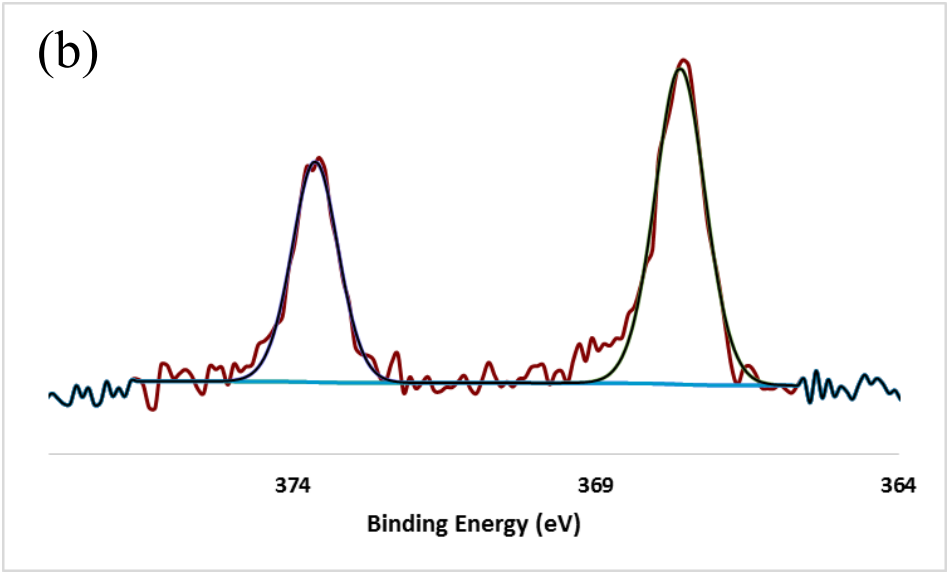

Figure 3.19. Fitted XPS data for Ag-Rh core-shell NPs with a thin Rh layer; (a) Rh 3d signals corresponding to metallic Rh (307.0 eV) and Rh(I) (308.1 eV); (b) Ag 3d signals indicating the presence of metallic Ag (367.6 eV).

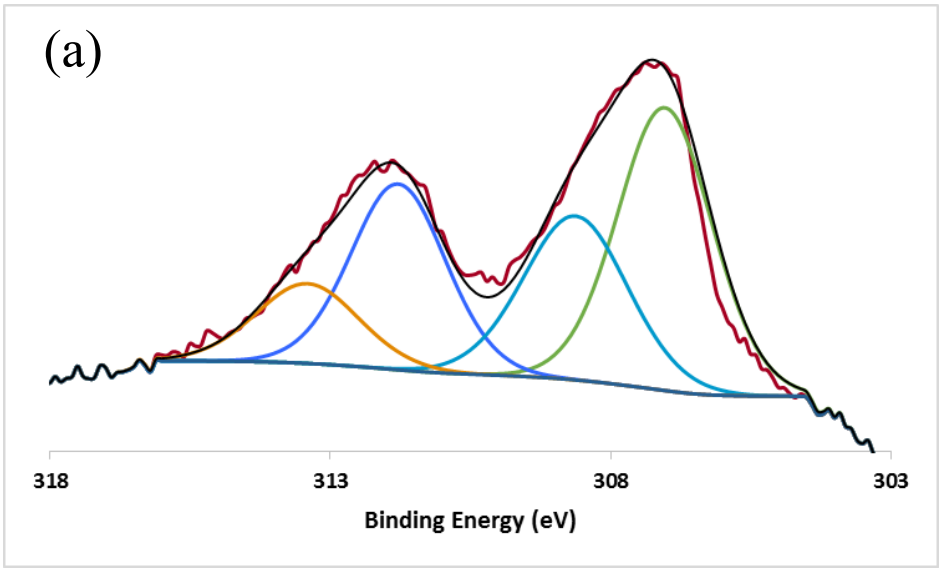

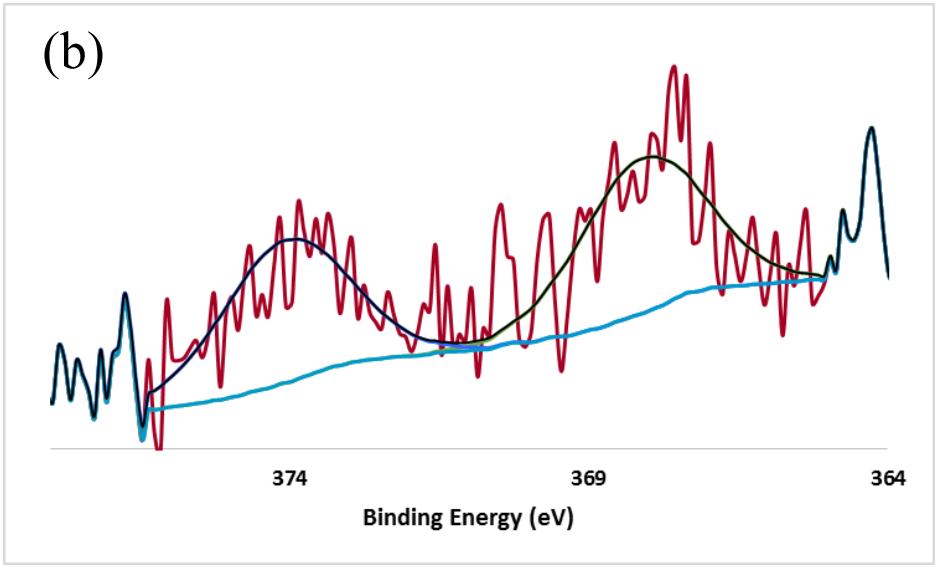

Figure 3.20. Fitted XPS data for Ag-Rh ore-shell NPs with a thick Rh layer; (a) Rh 3d signals assigned to Rh(0) (307.0 eV) and Rh(I) (308.6 eV); (b) Weak Ag signals corresponding to Ag (0) (368.1 eV).

The UV-vis absorption spectra of both thin-Rh and thick-Rh, compared to pure AgNPs also served as proof for the deposition of Rh on Ag seeds (Figure 3.21). The surface plasmon resonance of Ag at 410 nm was completely dampened with the Rh deposition cycles. In the case of thin-Rh on Ag cores, there was a broad plasmon peak at *ca.* 290 nm while thick-Rh NPs displayed a slight feature at *ca.* 250 nm. PXRD provided evidence for the increase in crystallinity for the Ag-Rh core-shell NPs. The initial Ag cores were not crystalline, as observed by their diffraction patterns (Figure 3.22; gray). Nonetheless, as Rh was deposited on the Ag cores and as the shell thickness increased, Rh reflections appeared and intensified in the range of 35 – 90° (Figure 3.22; green and purple). No dramatic increase in definition was observed for the Rh diffraction peaks of thin-Rh and thick-Rh, given that the shell thickness difference between the two samples was not large enough to generate a vast change in the X-ray diffraction pattern.

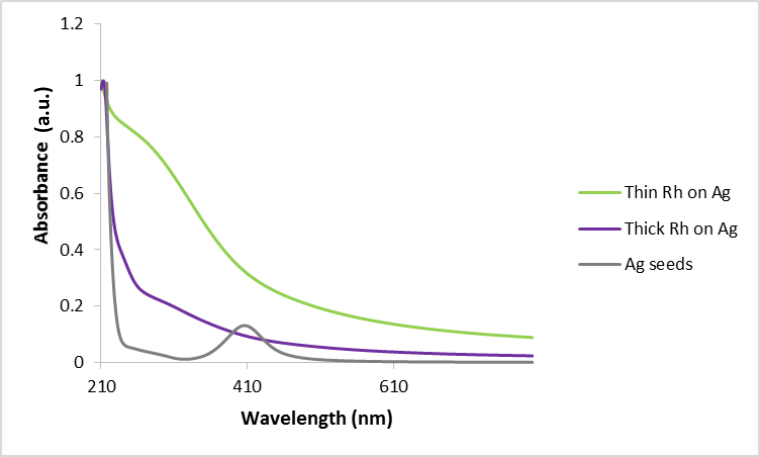

Figure 3.21. Comparative UV-vis spectra for thin-Rh (green), thick-Rh (purple) and Ag cores (gray).

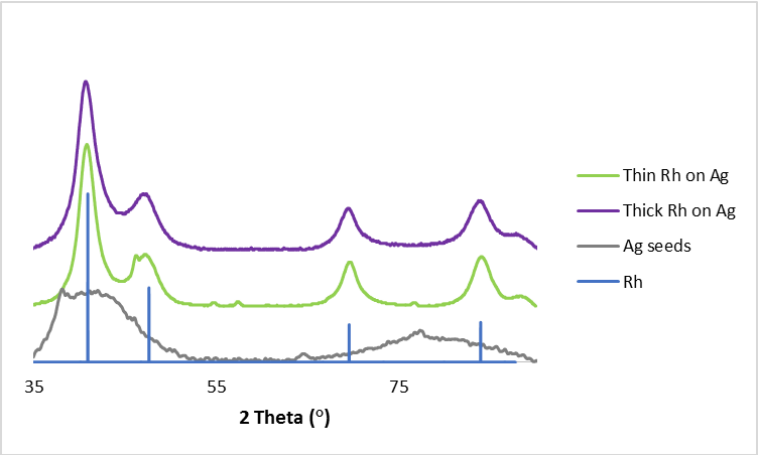

Figure 3.22. Overlayed PXRD spectra for thin-Rh (green), thick-Rh (purple) and Ag seeds (gray) along with reference reflection lines for Rh (blue).

3.4 HYDROGENATION CATALYSIS

3.4.1 Au-Rh core-shell NPs Catalysts

To assess the implications of NP structure upon the resulting surface catalytic properties, vapor-phase cyclohexene hydrogenation was used as a convenient model reaction. First, the Au, Rh and Au-Rh core-shell NPs were each supported on amorphous silica using a method reported previously in Chapter 2 (Figures 3.23 & 3.24). Next, mg quantities of each composite material were studied using single-pass reactor apparatus, in which a low pressure stream of H_2/He and cyclohexene were passed over the catalyst at 30 °C, with automated CG monitoring of the exhaust mixture. It is important to note that the catalysts were studied without any pre-treatment or removal of the capping agent.

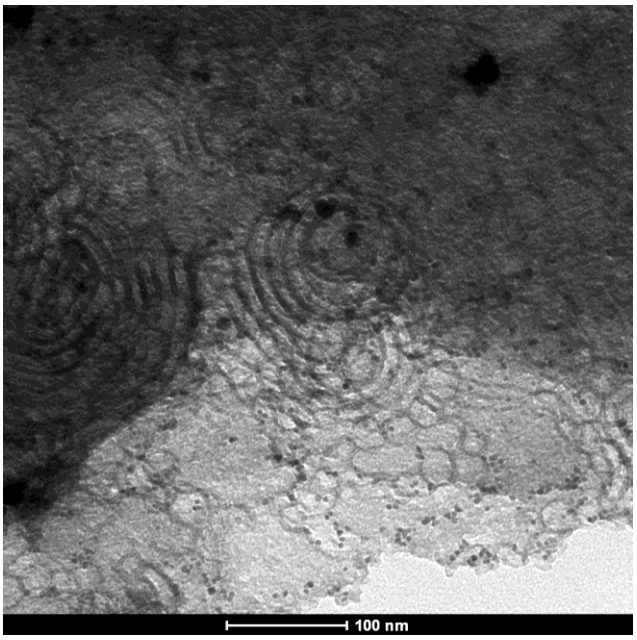

Figure 3.23. TEM image of Au-Rh core-shell NPs with a thin Rh layer supported on amorphous silica.

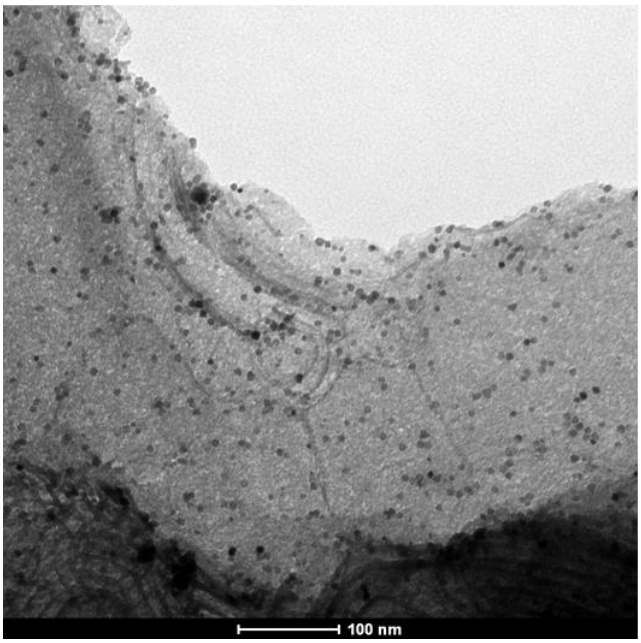

Figure 3.24. TEM image of Au-Rh core-shell NPs with a thick Rh layer supported on amorphous silica.

As expected, no turnover was observed for the AuNP cores alone because molecular hydrogen cannot be dissociatively chemisorbed by Au at elevated temperatures (Figure 3.25, yellow line); meanwhile, the PVP-capped RhNPs showed steady-state activity after a short induction period (~4 min; Figure 3.25, red line). Both the thin-Rh (Figure 3.25, blue line) and thick-Rh (Figure 3.25, green line) catalysts showed high activities for cyclohexene hydrogenation. This was as expected, because the thin-Rh and thick-Rh catalysts contained only 44 and 65 mol% Rh, respectively; TOFs were normalized *per* mol of Rh, assuming uniform cuboctahedra as shown in Scheme 3.1. In contrast to the pure RhNPs, both core-shell catalysts were much slower to reach steady-state activity. The thick-Rh catalyst became stable after *ca*. 1 h on-stream, while the 'thin-Rh' catalyst underwent a continual slow loss of activity up to 2h. We assume that the early catalytic instability observed for the core-shell species was most likely due to adsorbate-induced surface restructuring of some initial higher-energy facets. The steady-state TOF values after 2 h on-stream were almost double that of the pure RhNPs. TEM analysis of the *post*-catalysis revealed that the NPs had retained their bulk morphology and had not become aggregated (Figures 3.23 & 3.24, 3.26 & 3.27). This is not unexpected, since the catalysts were not heated above 30 °C throughout the hydrogenation experiments. Secondly, XPS studies confirmed that the Rh(0)/Rh(I) ratio had increased significantly (thin-Rh = 5.0; thick-Rh = 2.5); meanwhile, there was still no detectable signal for Au, indicating that the core-shell structure was maintained during the catalysis (Figures 3.28 & 3.29 & Table 3.4).

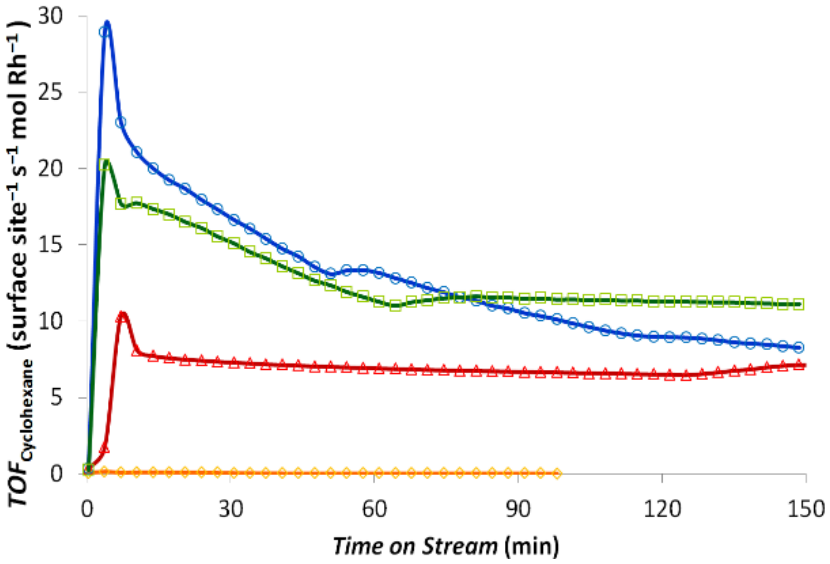

Figure 3.25. Comparative catalysis data for cyclohexene hydrogenation: yellow = 5.1 nm AuNP cores; blue = thin-Rh core-shell NPs; green = thick-Rh core-shell NPs; red = 12.4 ± nm μwH-RhNPs.

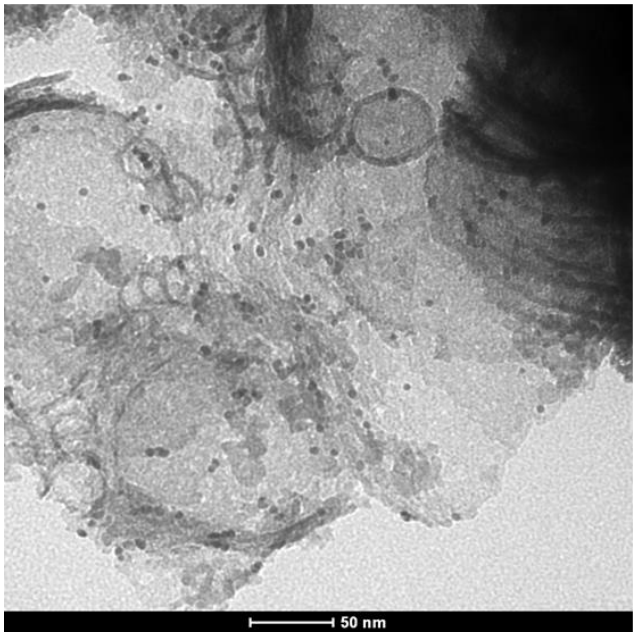

Figure 3.26. TEM image for Rh-Au core-shell NPs with an average of 2.5 Rh monolayers supported on amorphous silica, after catalytic studies were performed.

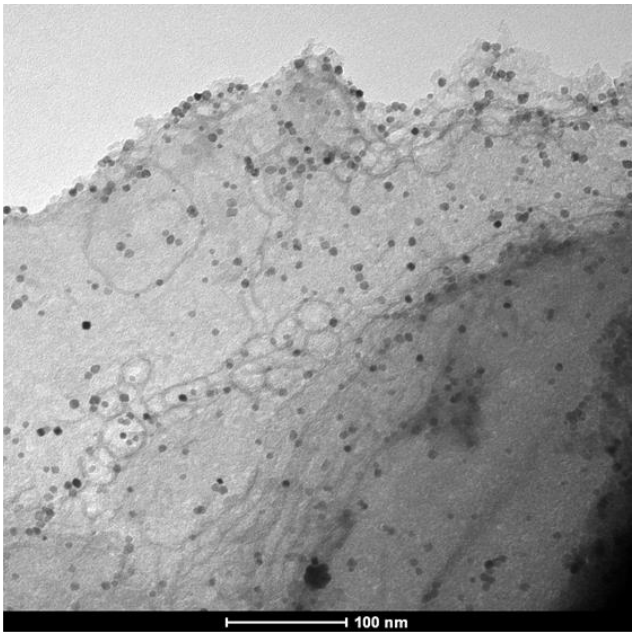

Figure 3.27. TEM image for Au-Rh core-shell catalyst with a thick Rh layer after catalysis was performed.

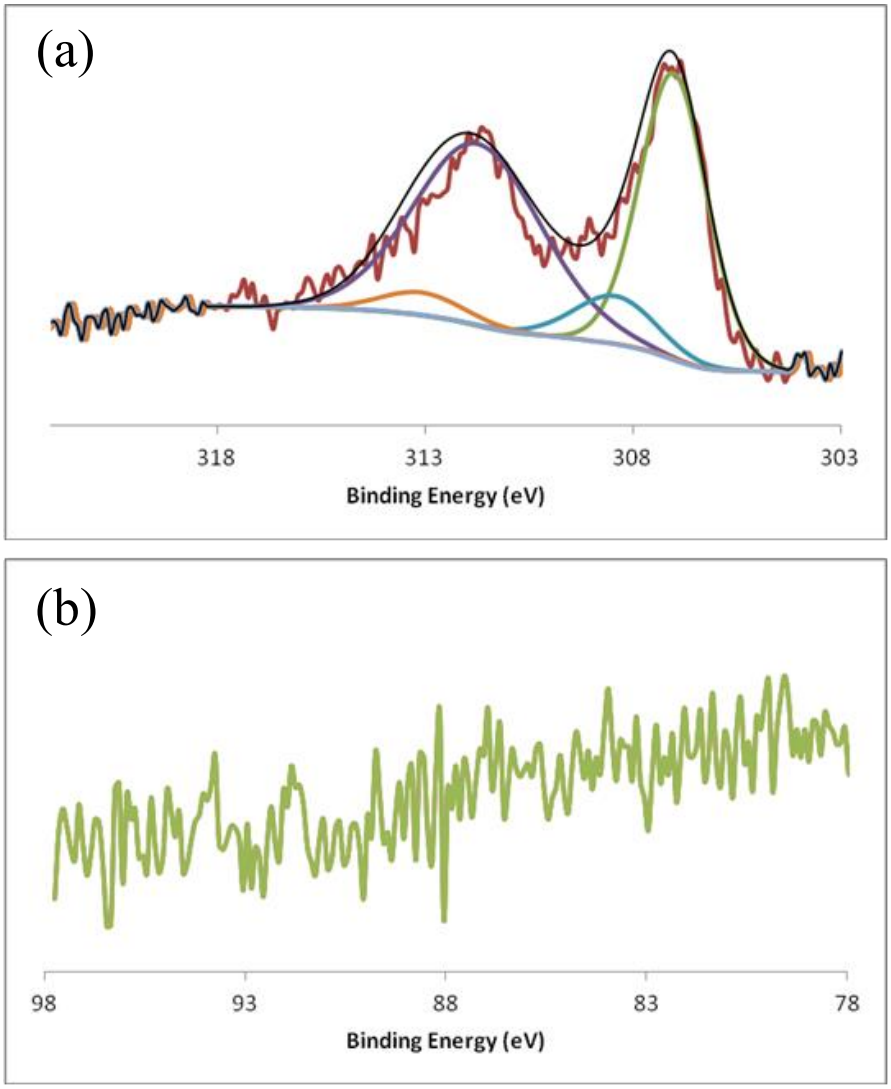

Figure 3.28. Fitted XPS data for Au-Rh core-shell NPs with a thin Rh layer supported on amorphous silica post-catalytic studies; (a) Rh 3d signals assigned to Rh(0) (307.0 eV) and Rh(I) (308.4 eV); (b) Absence of Au 4f signals confirming that no Au is present on the surface.

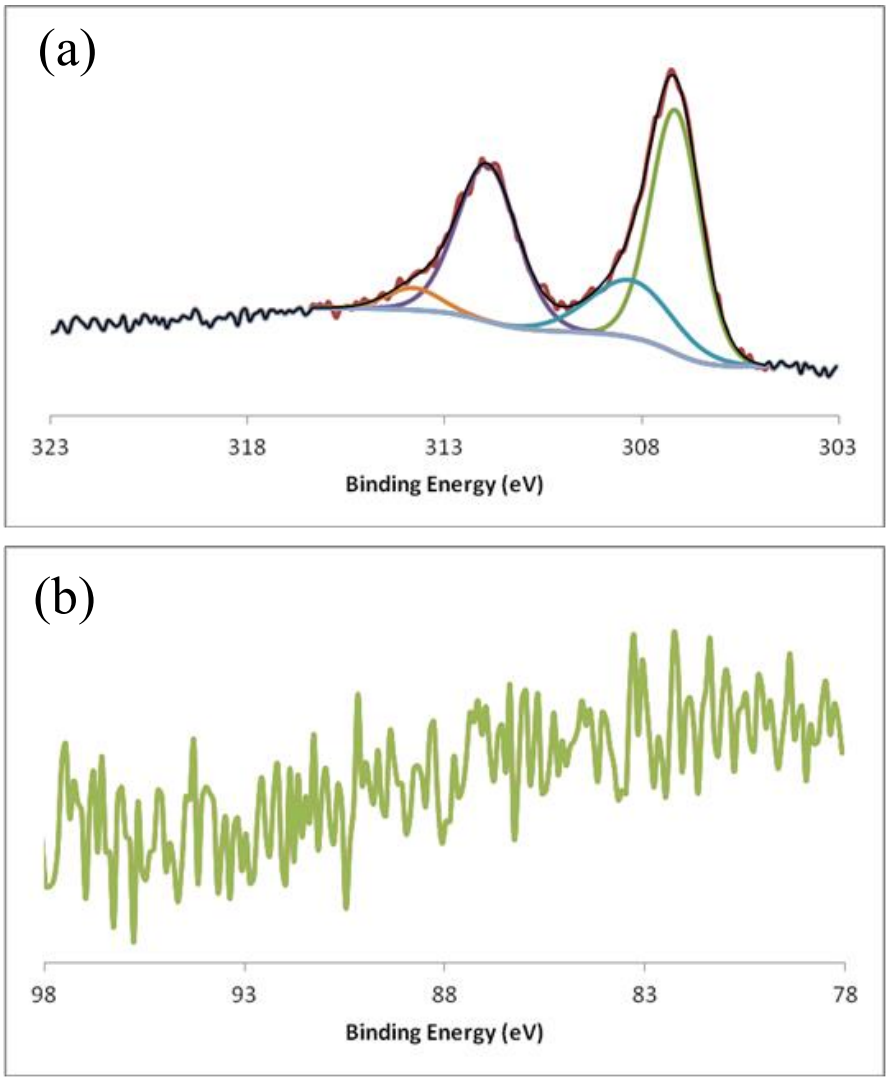

Figure 3.29. Fitted XPS data for Au-Rh core-shell NPs with an average of four Rh monolayers supported on amorphous silica, after catalytic studies were performed; (a) Rh 3d signals corresponding to Rh(0) (307.1 eV) and Rh(I) (308.3 eV); (b) Absence of Au 4f signal.

Table 3.4. Rh(I):Rh(0) and Au(X):Rh(X) ratios, based on XPS values, for thin-Rh and thick-Rh core-shell catalysts after catalytic studies were performed.

	Rh(I) : Rh(0)	**Au : Rh**
Thin-Rh NPs	1 : 5	0 : 1
Thick-Rh NPs	1 : 2.5	0 : 1

3.4.2 Ag-Rh core-shell NPs Catalysts

The catalytic activity of the Ag-Rh core-shell NPs was also tested using the hydrogenation of cyclohexene in the vapor phase as a model reaction. As expected, the Ag cores displayed no activity (Figure 3.30; gray) in this reaction due to the inability of Ag to dissociatively chemisorb H_2 gas. Taking into consideration the amount of Rh in the NPs, Ag-Rh core-shell NPs with a thin Rh shell showed very high activity (*per* mol of Rh) compared to pure RhNPs, given that the bimetallic NPs only contain 63 mol% Rh. Furthermore, the particles are very stable under the catalytic conditions employed as they rapidly achieved steady-state without undergoing any significant loss in activity. When the shell thickness was increased to 4.8 Rh monolayers (81 mol% Rh), the induction period dramatically increased yielding extremely high TOF values (of up to 70) that quickly and steadily declined to reach activity values that resembled those of the thin-Rh NPs after approximately 2.5 h. As described previously, the observed decrease in activity was most likely caused by restructuring of high energy facets after exposure to the mobile phase (H_2 and He) and the organic substrate. However, the catalytic activity never fell below that of pure Rh showing how robust these NPs are even though they only contained a few Rh monolayers. The catalytic behavior of the Ag-Rh core-shell NPs with varying shell thicknesses was very similar to that of the Au-Rh counterparts for the first 2 h of the catalytic run. After this period, the activity of the Au-Rh core-shell NPs with a

thin Rh overlayer quickly decayed while the Ag-Rh core-shell NPs remained highly active and stable (steady-state). The stability of the core-shell NPs can also be observed in the TEM images shown in Figures 3.31 and 3.32. The particles did not undergo any agglomeration or change in morphology or size during the catalytic process, as can be seen by comparing TEM images of the hybrid materials *pre*- and *post*-catalytic experiments.

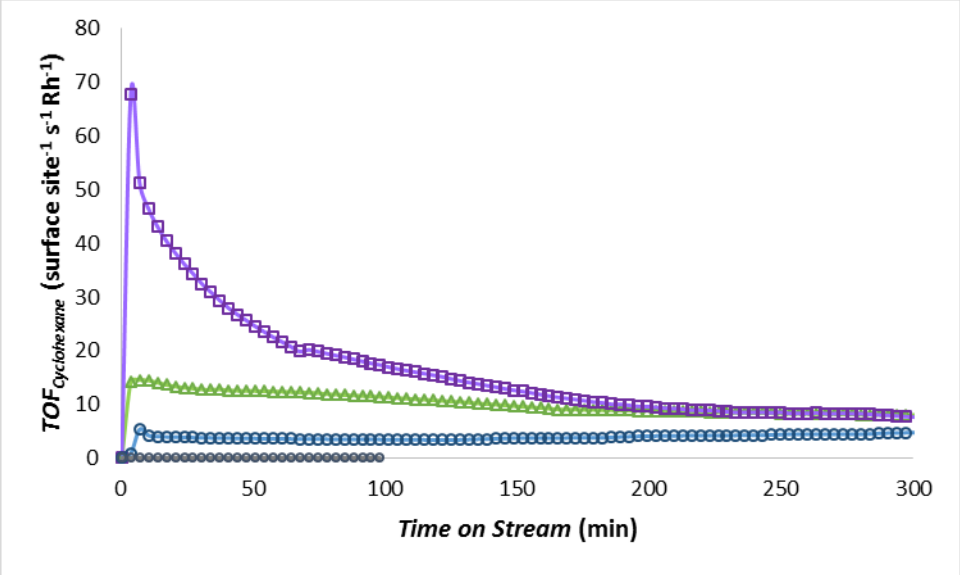

Figure 3.30. Comparative catalysis data for cyclohexene hydrogenation: gray = 4.0 nm AgNP cores; green = thin-Rh core-shell NPs; purple = thick-Rh core-shell NPs; blue = 12.4 nm μwH-RhNPs.

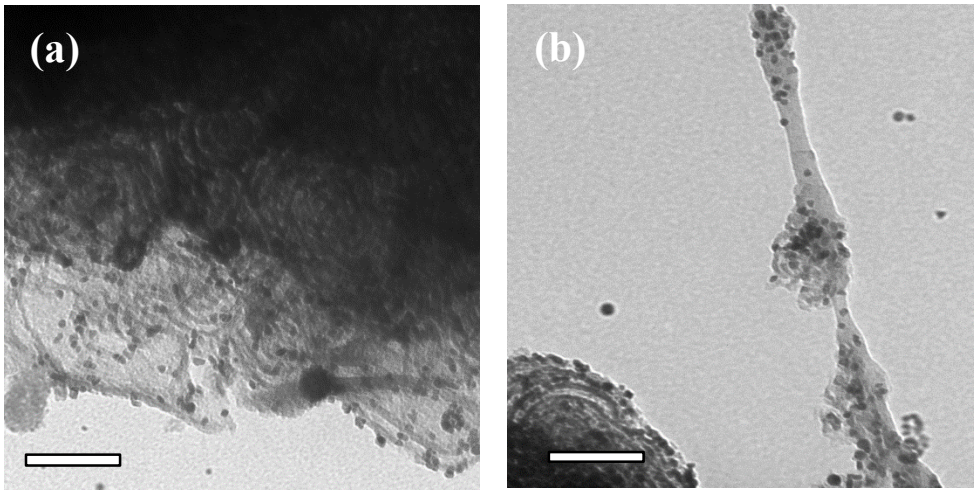

Figure 3.31. TEM images of thin-Rh on Ag NPs supported on amorphous silica; (a) *pre*-catalysis, (b) *post*-catalytic experiments (scale bars = 100 nm).

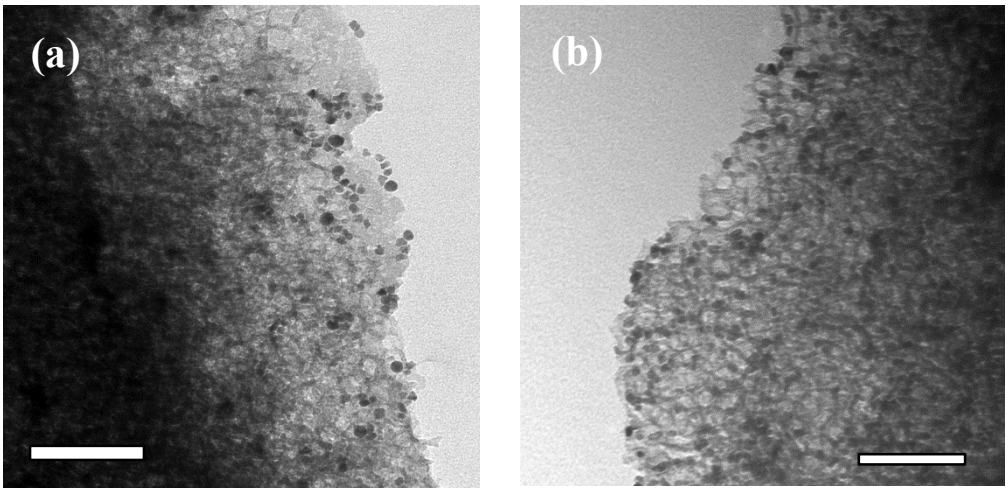

Figure 3.32. TEM images of Ag-Rh core-shell NPs with a thick Rh overlayer supported on amorphous silica; (a) *pre*-catalytic experiments, (b) *post*-catalysis (scale bars = 100 nm).

3.5 CONCLUSION

In summary, μwH has allowed for 'non-equilibrium' core-shell configurations to be achieved on the nanoscale. Furthermore, it has facilitated the convenient and reproducible synthesis of cost-effective nanocatalysts, such as Au-Rh and Ag-Rh core-shell NPs: these serve as examples for the dilution of trace metals (*e.g.* Rh) utilizing sacrificial cores comprised of cheaper and abundant metals (Au and Ag) that are themselves catalytically inactive. It has also been shown that the shell thickness of the synthesized core-shell NPs can be finely tuned using synthetic approaches, which allows for the optimization of catalytic properties. It is possible to take advantage of electronic interactions and/or overlayer strain at the interface by tuning this parameter. The resulting NPs can be employed directly in Rh-catalyzed hydrogenation chemistry, with a significant increase in the relative proportion of catalytically-available surface Rh atoms compared to pure RhNPs.

4. Classically Immiscible RhM (M = Ag or Au) Alloy NPs

4.1 INTRODUCTION

Rapid, efficient and scalable methods for the preparation of noble metal nanoparticle (MNP) catalysts with defined structures and novel compositions are of great interest due to their potential applications in a broad range of industrially-important processes.[21,203–206] Compared to classical colloidal heterogeneous catalysts, NPs provide higher surface area-to-volume ratios, which result in enhanced overall catalytic activities.[10,81,207,208] Fine control over nanoparticle morphology (surface structure) has also been shown to induce superior catalytic reactivity and selectivity.[81,209,210] It is also possible to discover new and potentially useful compositions of matter on the nanoscale, because mixtures of elements that are thermodynamically unstable in the bulk may actually become stable (or metastable) as a result of quantum size-confinement effects.[211–213] Well-defined heterometallic nanostructures are of particular current interest because synergistic effects between metal atoms of different elements can result in enhancement of the catalytic properties by tuning the average binding energy of the NPs surface to specific adsorbates.[214–217] Multimetallic NPs also provide a convenient means to reduce the total amount of the rarest and most expensive metal *via* dilution with readily-available, and potentially catalytically inactive metals. Pertinent examples include

---

The work in this chapter has been previously published as a journal article ("Microwave Synthesis of Clasically Immiscible Rhodium–Silver and Rhodium–Gold Alloy Nanoparticles: Highly Active Hydrogenation Catalysts." Garcia, S.; Zhang, L.; Piburn, G. W.; Henkelman, G.; Humphrey, S. M., *ACS Nano*, **2014**, *8*, 11512.). Humphrey, S. M. conceived the scientific idea; Garcia, S. performed the experiments and data analysis; Zhang, L. and Henkelman, G. carried out the theoretical calculations; Piburn, G. W. aided with data analysis.

core-shell NPs, which consist of thin shells of noble metals supported around cores of inexpensive materials;[113,189,218] the cores may also impart advantageous secondary properties (*e.g.*, ferromagnetic cores to enable NP recovery/separation,[219–221] or strain effects induced at the core-shell interface[99,100]). NPs with ordered intermetallic or randomly alloyed structures that consist of different metallic elements are also highly desirable: *d*-band intermixing between individual atoms allows for broad tuning of the chemical reactivity of the NP surface.[222] In essence, the reactivity of metal 'A' can be enhanced for a specific catalytic purpose by dilution with metal 'B', in the formation of an A_xB_{1-x} alloy.

The chemistry and catalytic behavior of bulk metallic alloys has been extensively studied, and is well understood.[223] Bimetallic alloys are presently utilized in large-scale industrial processes in both bulk and NP forms.[212,224] However, the application of bimetallic alloys in catalysis remains limited to combinations of metals that are miscible.[225] All metals can be mixed at high temperature, but many are deemed to be immiscible; phase segregation occurs upon cooling because alloy phases are unstable with respect to the pure metals. RhAg and RhAu alloys display this behavior. The phase diagrams for these alloys predict no regions of stability below 2177 or 2139 K and 1.0 atm, respectively.[226] For this reason, little or nothing is known about their chemical properties. However, they would be of particular interest in catalysis since Rh is vital in a wide range of catalytic processes, but it is scarce and expensive. Meanwhile, Ag and Au are much more abundant. Ag is also inexpensive, but is not industrially as useful in pure form due to its inherent unreactivity.

This chapter shows that a novel microwave-assisted technique enables the simple, programmable preparation of stable RhAg and RhAu alloy NPs with broadly tunable compositions. Application of the RhM (M=Ag or Au) NPs in model

hydrogenation catalysis studies show that alloys with optimal compositions can be as much as three times more reactive that pure Rh NPs under identical conditions: Rh becomes more reactive when diluted in alloys with Ag or Au, even though the latter are both catalytically inactive for hydrogenation. Theoretical modeling studies that explain the observed increase in reactivity of the RhM alloy NPs are also presented.

4.2 SYNTHESIS AND CHARACTERIZATION

4.2.1 Materials

Rhodium trichloride hydrate ($RhCl_3 \cdot xH_2O$, 98%; Johnson Matthey), hydrogen tetrachloroaurate ($HAuCl_4 \cdot 3H_2O$, 98%; Sigma Aldrich), silver nitrate ($AgNO_3$, 99%; Mallinckrodt Chemicals), sodium borohydride ($NaBH_4$, 98% ; Sigma Aldrich), poly(vinylpyrrolidone) (PVP, $<M_w>$ = 55,000; Sigma Aldrich), ethylene glycol ($\{CH_2OH\}_2$, 99.8%; Fisher Scientific) and 1-cyclohexene (C_6H_{10}, 99%; Alfa Aesar) were used as received. All other reagents and solvents (analytical grade) were employed without further purification unless stated otherwise.

4.2.2 Synthesis Methods

RhAg and RhAu alloy NPs of different compositions were synthesized using the same polyol reduction method. In all instances, *poly*(vinylpyrrolidone) (PVP; M.W. = 58 k, 4.5−9.0 mol monomer *per* mol metal) was dissolved in ethylene glycol (20.0 mL) and the temperature was brought to 150 ^{0}C (± 0.1 ^{0}C) using a MARS microwave reactor (CEM Corp.) operating with fiber-optic temperature feedback control, and magnetic stirring (1,100 rpm) at ambient pressure. Metal precursors dissolved in the same solvent were then concomitantly injected into the reaction mixture at specific rates, controlled

using a programmable dual syringe pump (WPI, Inc.) while the reaction was still exposed to μwH. The reagents were delivered utilizing 1.0 mm PTFE tubing, terminated 0.5 cm above the reaction mixture (See Chapter 2 for a full schematic of the reaction apparatus). Upon completion of a given reaction, the mixture was rapidly cooled by quenching in an ice-water bath. The resulting RhM alloy NPs were purified by initial precipitation with acetone and isolation by ultracentrifugation (5.5 krpm). Two cycles of re-dispersion in ethanol and re-precipitation with hexane followed by centrifugal isolation were then employed to remove excess PVP. The RhM NPs can be stored dry as an amorphous glass, or suspended in ethanol at room temperature.

4.2.3 Characterization Methods

Transmission Electron Microscopy (TEM) images were obtained from a FEI Tecnai microscope operating at 80 kV. The samples were prepared by drop-casting a single aliquot of NPs or composite material dispersed in ethanol onto 200 mesh carbon coated copper formvar grids (Ted Pella Inc.) and allowing for subsequent evaporation in air. Nanoparticle sizes and standard deviations were derived by measuring a minimum of 200 individual particles *per* experiment, and by averaging multiple images from samples obtained from at least two separate syntheses. Individual particles were measured using Image-J (http://rsbweb.nih.gov/ij), which finds the area of each nanoparticle by pixel counting. High-resolution TEM (HRTEM) and energy dispersive X-ray analysis (EDX) were performed using a JEOL 2010F transmission electron microscope. This instrument was operated at 200 keV using a field-emission gun with 0.19 nm point-to-point resolution. Powder X-ray diffraction (PXRD) patterns were recorded with a Bruker AXS D8 diffractometer using a Cu K_α source (1.5418 Å) operated at 40 kV and 40 mA; spectra

were collected using a scan speed of 3° min^{-1} with a step width of 0.020 (2θ). UV-vis data were collected using a Carry 6000i UV-vis NIR spectrometer equipped with a double beam and a wavelength range of 175−3300 nm. X-ray photoelectron spectroscopy (XPS) was performed using a Kratos Axis Ultra Photoelectron Spectrometer. The samples were prepared by drop-casting a single aliquot of NPs or composite material dispersed in ethanol onto glass slides. The XPS spectra were recorded utilizing a monochromated Al-K_α x-ray source ($h\gamma$=1486.5 eV), hybrid optics (employing a magnetic and electrostatic lens simultaneously) and a multi-channel plate coupled to a hemispherical photoelectron kinetic analyzer. All spectra were recorded using four sweeps for signal averaging, a dwell time of 1800 msec, an aperture slot of 300 x 700 μm, a pass energy of 20 eV and 0.1 eV per step. To minimize sample charging and band shape distortion due to charging, the XPS spectra were recorded using the Kratos charge neutralizer (20 eV electrons) while the sample stage was left floating (i.e. not connected to ground (earth)). Casa XPS analysis software was used for peak deconvolution and the stoichiometry of samples was determined from corrected peak areas and employing Kratos sensitivity factors for each element of interest.

4.2.4 Rh_xAg_{100-x} alloys (x = 17–70)

Prior to injection of the metal precursors, HCl (25.0 μM) in ethylene glycol was added to the hot glycol/PVP solution to enhance etching of Ag(0) clusters. Solutions of $AgNO_3$ and $RhCl_3 \cdot xH_2O$ in ethylene glycol (5 mL) were then simultaneously added at a rate of 150 mL hr^{-1}. The relative molar amounts of each precursor were determined by the desired value of x for the Rh_xAg_{100-x} products; in all instances, the total molar amount of added metal was constant (Table 4.1). The mixture was allowed to continue stirring

under μwH at the same temperature for 30 min after completion of precursor addition. Following precipitation treatment, the RhAg NPs were suspended in H_2O and washed with NH_4OH (29.1 % assay, 1.0 mL) to remove any residual AgCl NPs, using the method of Schuette et al.[227]

Table 4.1. Experimental conditions used for the synthesis of RhAg alloyed NPs of different atomic compositions.

	Rh (mmol)	Ag (mmol)	PVP (mmol in terms of repeating unit)
$Rh_{70}Ag_{30}$	0.42	0.15	3.24
$Rh_{60}Ag_{40}$	0.29	0.15	3.24
$Rh_{51}Ag_{49}$	0.14	0.14	3.24
$Rh_{27}Ag_{73}$	0.14	0.29	3.53
$Rh_{17}Ag_{83}$	0.14	0.43	3.98

4.2.5 Rh_xAu_{100-x} (x = 23–70)

RhAu alloy NPs were synthesized using $NaBH_4$ (5 eq. *per* Au(III)) to aid in the reduction of Au(III). A single solution containing both $RhCl_3 \cdot xH_2O$ and $HAuCl_4 \cdot 3H_2O$ dissolved in ethylene glycol (5 mL) was prepared. The relative molar amounts of each precursor were determined by the desired value of x for the desired Rh_xAu_{100-x} products (Table 4.2). 2.5 mL of this solution was added to the hot glycol/PVP/$NaBH_4$ solution at an initial rate of 300 mL hr^{-1} to induce nucleation of RhAu seeds. The mixture was stirred at constant temperature for 30 min, after which time the remaining precursor solution was added at a rate of 20 mL hr^{-1} to promote controlled overgrowth at the

existing seeds. The RuAu NPs were further ripened at 150 °C for 30 min upon completion of the second addition phase.

Table 4.2. Experimental conditions used for the synthesis of RhAu alloyed NPs of different atomic compositions.

	Rh (mmol)	Au (mmol)	$NaBH_4$ (mmol)	PVP (mmol in terms of repeating unit)
$Rh_{70}Au_{30}$	0.30	0.10	0.55	1.79
$Rh_{64}Au_{36}$	0.20	0.10	0.55	1.79
$Rh_{45}Au_{54}$	0.10	0.10	0.56	1.79
$Rh_{23}Au_{77}$	0.10	0.22	0.55	1.79
$Rh_{15}Au_{85}$	0.10	0.29	0.84	1.79

4.3 RESULTS AND DISCUSSION

Microwave heating (μwH) was utilized to prepare defined alloy NPs of composition Rh_xM_{100-x}, where x is broadly tunable in the range 15−70, based on the molar ratios of metal precursors employed. The alloy NPs were synthesized at 150 °C under μwH using a simple polyol method that utilized ethylene glycol as both reducing agent and reaction medium, in addition to secondary reductants and excess PVP as a stabilizing agent. Synthesis of both RhAg and RhAu alloyed NPs was also attempted utilizing the same experimental procedure employing convective heating (oil bath) as the

heat source. In this case, no alloying of the metals was observed in the bulk for the polydisperse samples generated (Figures 4.1 and 4.2).

In a typical synthesis, precursor solutions of $RhCl_3$ and either $HAuCl_4$ or $AgNO_3$ were simultaneously injected into *pre*-heated solvent. The rate of addition was carefully controlled by means of syringe pumps with programmed addition profiles that optimized NP nucleation and growth phases.

The target RhM NPs compositions were 3:1, 2:1, 1:1, 1:2 and 1:3. Actual resulting metal compositions were determined by inductively-coupled plasma mass spectrometry (ICP-MS), which gave good agreement with the target compositions. Representative transmission electron microscopy (TEM) images of Rh_xAg_{100-x} NPs (x = 17−70) and Rh_xAu_{100-x} NPs (x = 15−70) revealed a majority of truncated cubic and cuboctahedral NPs with *pseudo*-Gaussian size distributions (Figures 4.3a and 4.4a). Identical reaction parameters yielded Rh-rich, Ag-rich or Au-rich, and NPs with intermediate compositions with similar average diameters (2−6.8 nm). NP growth control experiments indicated that the metals begin to segregate when the diameter of the particles synthesized using μwH exceed 20 nm (Figure 4.5). UV/vis spectrophotometry of the products suspended in ethanol gave a unique, broad plasmon-enhanced absorption band at *ca*. 250−310 nm that is not observed in either pure Ag, Au or Rh NPs of similar sizes (Figures 4.3b and 4.4b; beige and black dashed lines, respectively). This band was blue-shifted with increasing Rh content, which is indicative of compositionally-dependent *d*-band intermixing at the surfaces of the NPs. The absorption band *ca.* 405 nm that is usually observed for Ag NPs and the plasmon resonance *ca.* 540 nm that is observed for Au NPs were absent in both cases for the alloy NPs. Solid-state PXRD of the bulk RhAg and RhAu NPs showed marked shifting of the lattice parameters due to alloying (Figures 1c and 2c). Rh, Ag and Au all exhibit face-centered cubic (FCC) lattice

structures, but there is an approximate 7% lattice mismatch between them (Rh = 3.80; Ag = 4.08; Au = 4.09 Å). The intense (111) reflection was increasingly shifted to lower angle and became broader as the proportion of Ag or Au was increased. Single NP studied also indicated randomly-alloyed structures. High-resolution TEM imaging of RhAg and RhAu NPs of varying compositions detected a mixture of (111) and (100) lattice planes. Measurement and comparison of the *d*-spacings that correspond to the (111) planes showed a continuous increase of the interatomic separation distance for increasingly Ag-rich and Au rich NPs (Figures 4.3d and 4.4d). Energy-dispersive X-ray analysis (EDX) of the bulk materials gave compositions in good agreement with that observed by ICP-MS (Tables 4.3 and 4.4). EDX line scans of single NPs performed on $Rh_{17}Ag_{83}$, $Rh_{51}Ag_{49}$ and $Rh_{70}Ag_{30}$ samples show comparable compositions to the bulk (Figure 4.6–4.8; Table 4.5). Similar results were observed for single particles of $Rh_{15}Au_{85}$, $Rh_{45}Au_{55}$ and $Rh_{70}Au_{30}$ samples (Figure 4.9–4.11; Table 4.6). XPS is a *pseudo*-surface specific technique because the penetration depth of the photons is only a few monolayers and the RhM NPs are encapsulated in PVP, which further limits the penetration depth into the NPs. Both metals were observed at or near the NP surfaces, with relative intensities that also show good agreement with ICP-MS and EDX values (Figures 4.12–4.21; Tables 4.3 and 4.4).

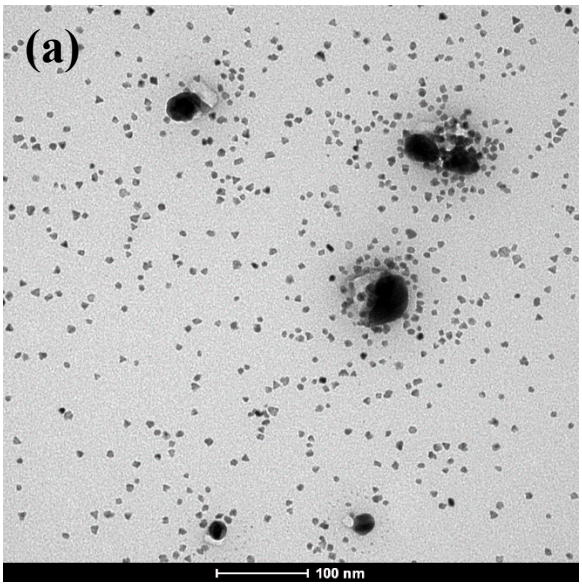

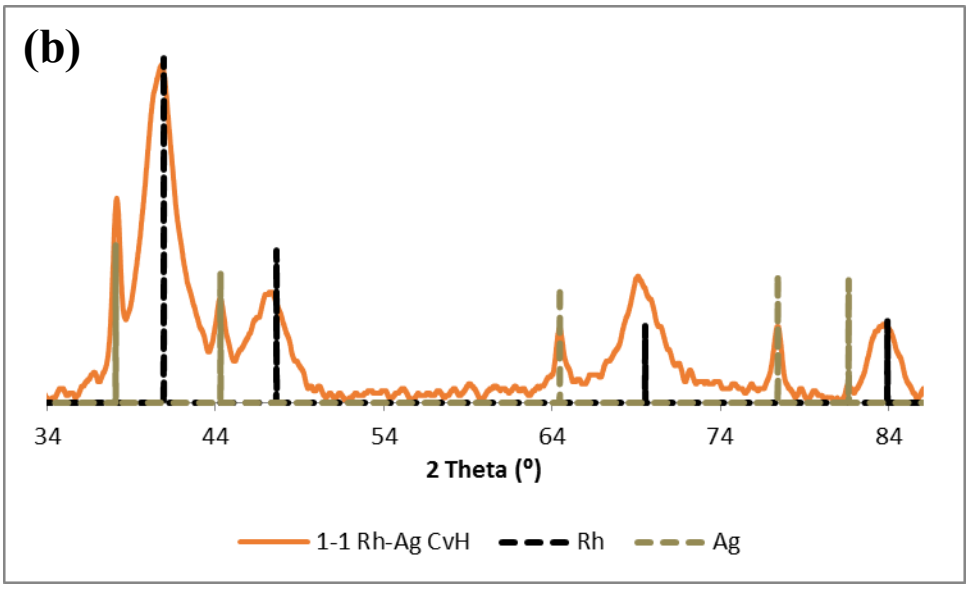

Figure 4.1. (a) TEM image and (b) X-ray diffraction pattern of Rh and Ag NPs synthesized using conventional heating and 1:1 molar ratio of Rh:Ag precursor mixture.

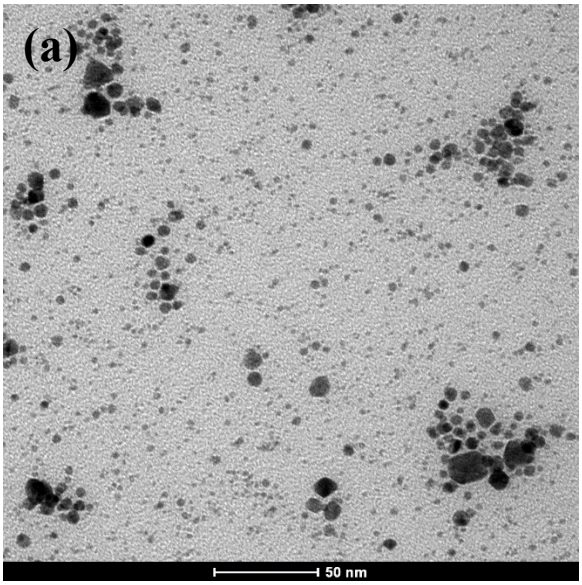

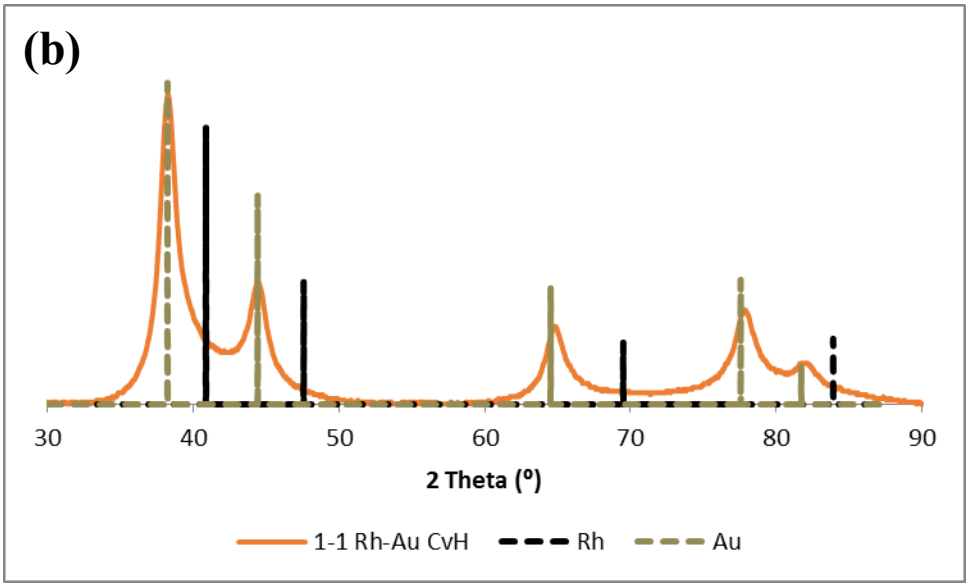

Figure 4.2. (a) TEM image and (b) X-ray diffraction pattern of Rh and Au NPs synthesized using conventional heating and 1:1 molar ratio of Rh:Au precursor mixture.

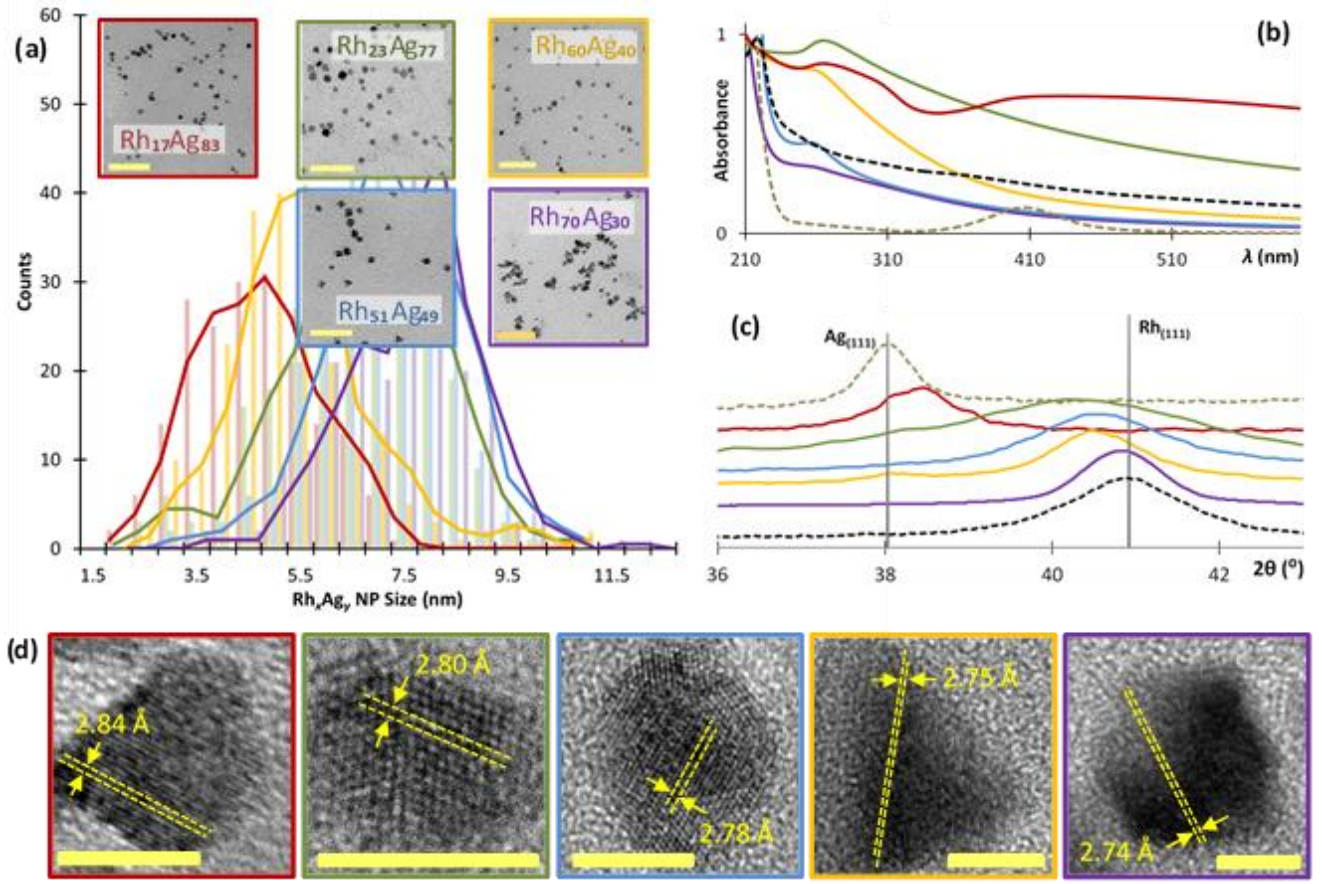

Figure 4.3. Analysis of RhAg NPs. (a) Size histograms and representative low-resolution TEM images (inset; scale bars = 50 nm). (b) UV-vis spectra for the five compositions of RhAg NPs studied along with the spectra for pure 12.1 nm Rh (black dashed line) and 7.8 nm Ag NPs (beige dashed line). (c) Expansion of the (111) region of the PXRD patterns; the standard index positions for the Ag(111) and Rh(111) reflections are shown in grey. (d) HRTEM images for individual NPs and the corresponding measured average lattice spacings (scale bars = 5 nm). Key: red = $Rh_{17}Ag_{83}$; green = $Rh_{23}Ag_{77}$; blue = $Rh_{51}Ag_{49}$; yellow = $Rh_{60}Ag_{40}$; purple = $Rh_{70}Ag_{30}$.

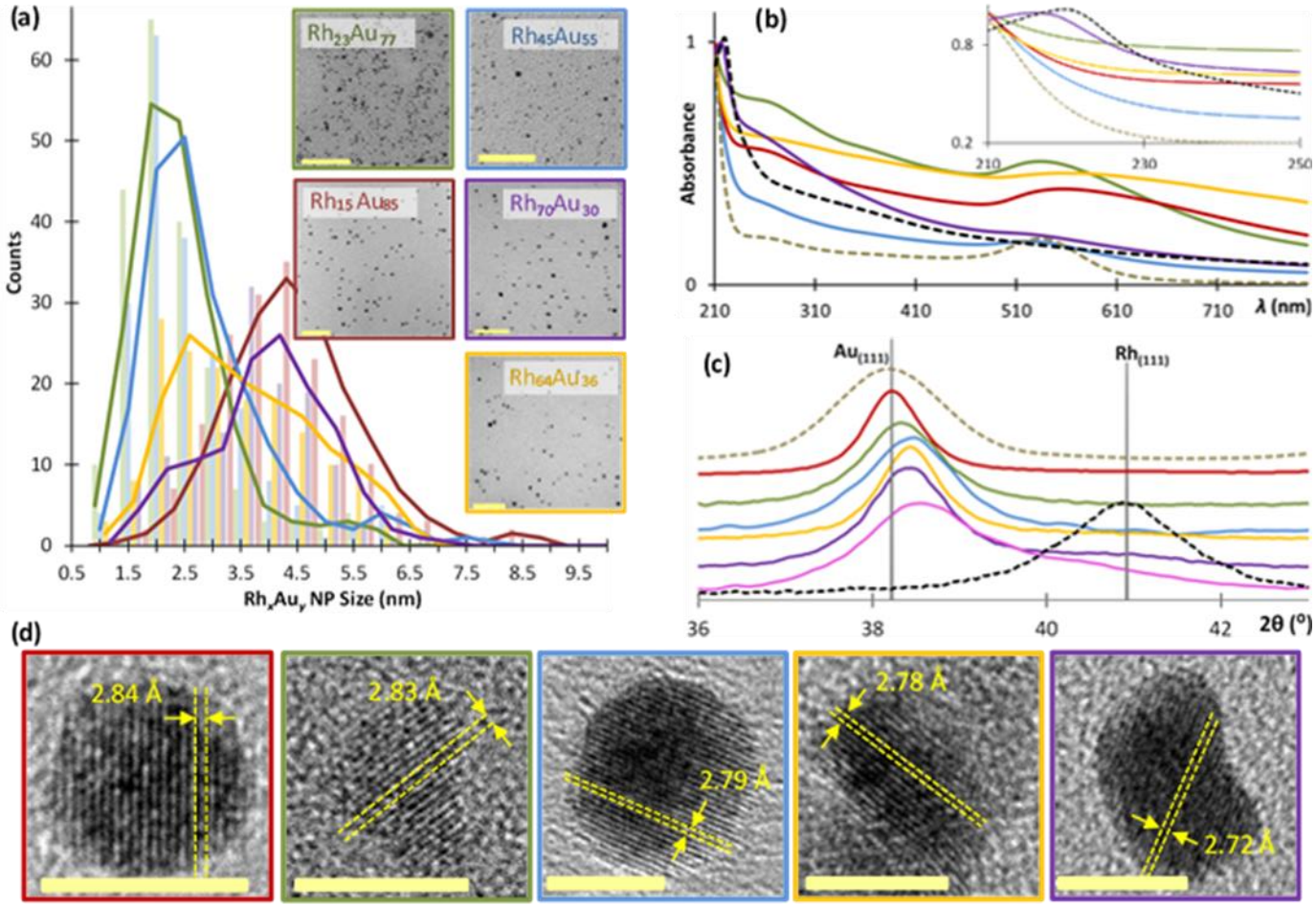

Figure 4.4. Analysis of RhAu NPs. (a) Size histographs and representative low-resolution TEM images (inset; scale bars = 50 nm). (b) UV-vis spectra for the five compositions of RhAu NPs studied along with the spectra for pure 12.1 nm Rh (black dashed line) and 5.6 nm Au NPs (beige dashed line). (c) Expansion of the (111) region of the PXRD patterns; the standard index positions for the Au(111) and Rh(111) reflections are shown in grey. (d) HRTEM images for individual NPs and the corresponding measured average lattice spacings (scale bars = 5 nm). Key: red = $Rh_{15}Au_{85}$; green = $Rh_{23}Au_{77}$; blue = $Rh_{45}Au_{55}$; yellow = $Rh_{64}Au_{36}$; purple = $Rh_{70}Au_{30}$.

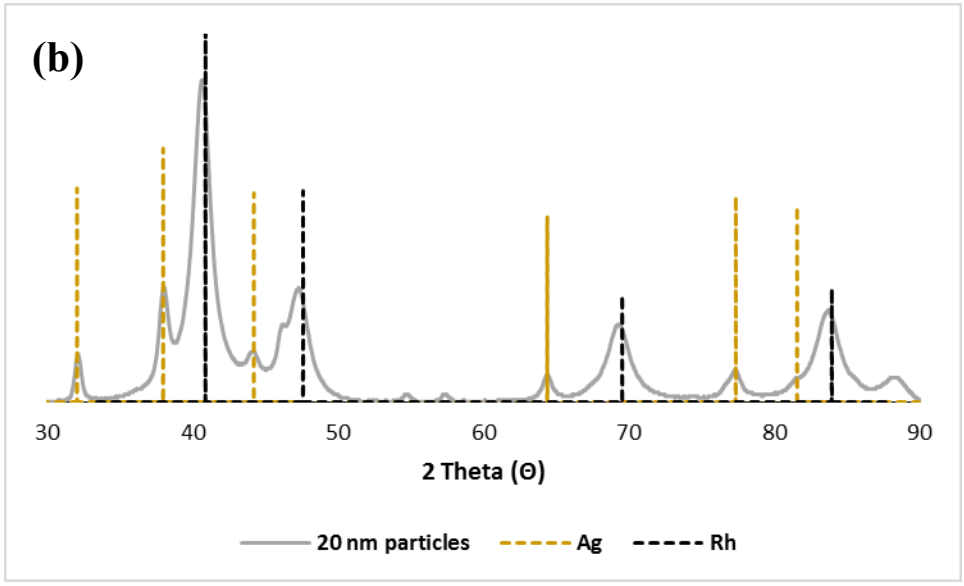

Figure 4.5. (a) Representative TEM image and (b) XRD pattern of NPs generated after four consecutive addition stages (*c.f.* to one in a typical synthesis). Bulk segregation of the metals is clearly displayed.

Table 4.3. Analytical and catalytic parameters for RhAg alloyed NPs.

	Avg. Size (nm)	EDS atomic % (as- synthesized)		XPS atomic % (as- synthesized)		XPS atomic % (post-catalysis)		E_{act} (kJ mol^{-1})
		% Rh	% Ag	% Rh	% Ag	% Rh	% Ag	
Rh	12.1 ± 1.9	100	0	100	0	100	0	57.2
$Rh_{70}Ag_{30}$	6.0 ± 1.2	88	12	88	12	82	18	22.6
$Rh_{60}Ag_{40}$	5.0 ± 1.4	75	25	77	23	75	25	15.4
$Rh_{51}Ag_{49}$	6.8 ± 1.3	53	47	65	35	48	52	28.3
$Rh_{27}Ag_{73}$	6.3 ± 1.5	30	70	33	67	45	55	38.3
$Rh_{17}Ag_{83}$	4.3 ± 1.2	19	81	27	73	37	63	38.1
Ag	7.8 ± 1.5	0	100	0	100	0	100	--

Table 4.4. Analytical and catalytic parameters for RhAu alloyed NPs.

	Avg. Size (nm)	EDS atom % (as- synthesized)		XPS atom % (as- synthesized)		XPS (post-catalysis)		E_{act} (kJ mol^{-1})
		% Rh	% Au	% Rh	% Au	% Rh	% Au	
Rh	12.1 ± 1.9	100	0	100	0	100	0	57.2
$Rh_{70}Au_{30}$	3.3 ± 1.0	88.8	11.2	82.0	18.0	88.1	11.9	38.0
$Rh_{64}Au_{36}$	3.1 ± 1.2	68.1	31.9	71.4	28.6	69.7	30.3	44.5
$Rh_{45}Au_{54}$	2.4 ± 1.1	49.0	51.0	58.3	41.7	52.7	47.3	52.8
$Rh_{23}Au_{77}$	2.0 ± 0.8	32.1	67.8	30.2	69.7	38.3	61.7	45.9
$Rh_{15}Au_{85}$	4.3 ± 1.4	16.0	84.0	17.8	82.2	14.6	85.4	51.9
Au	5.6 ± 1.5	0	100	0	100	0	100	--

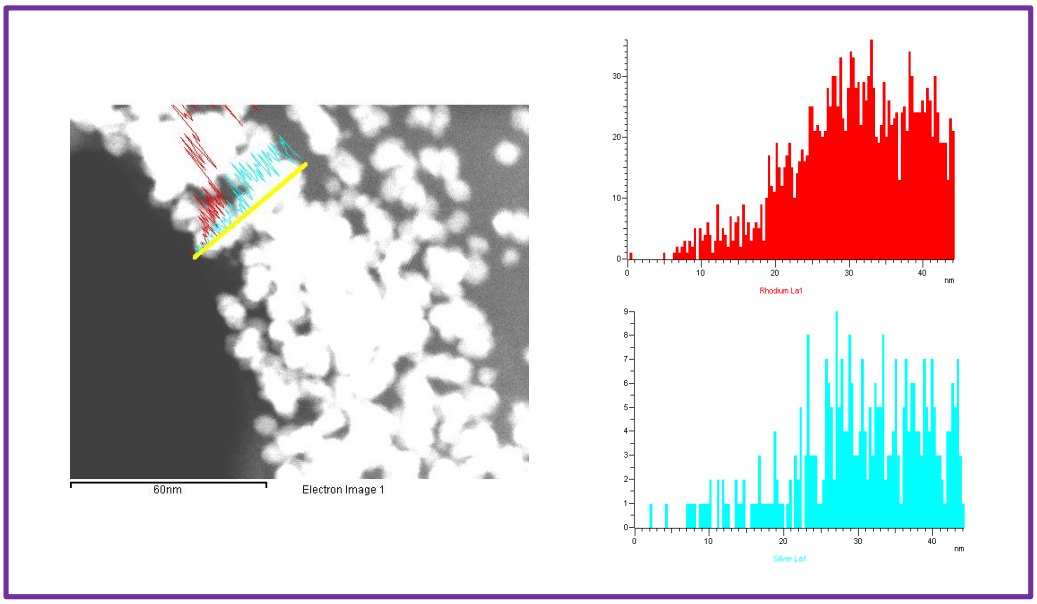

Figure 4.6. EDS line scan for a representative sample of $Rh_{70}Ag_{30}$ NPs.

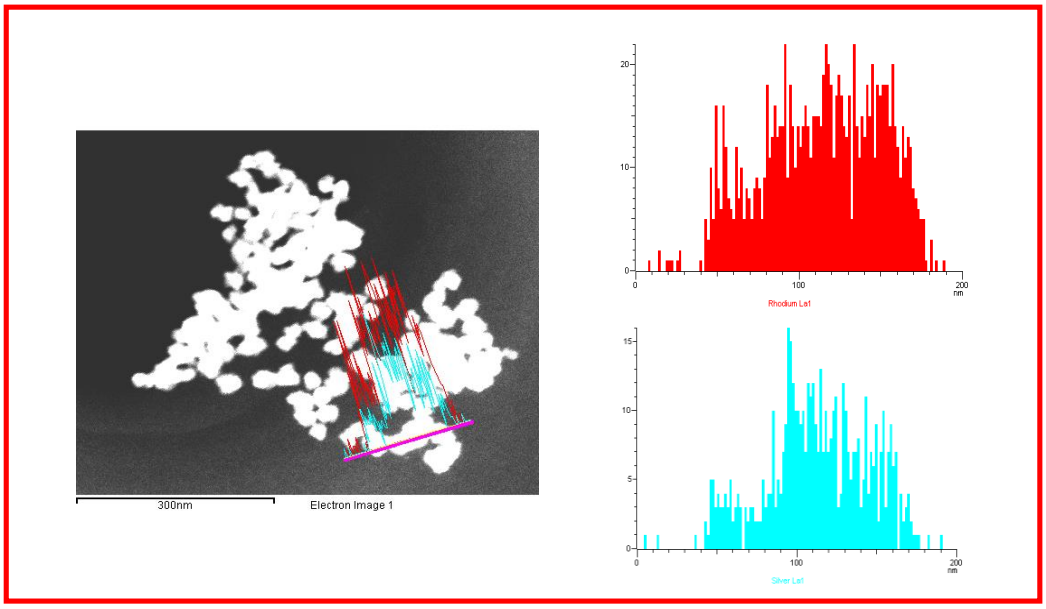

Figure 4.7. EDS line scan of a representative sample of $Rh_{51}Ag_{49}$ NPs.

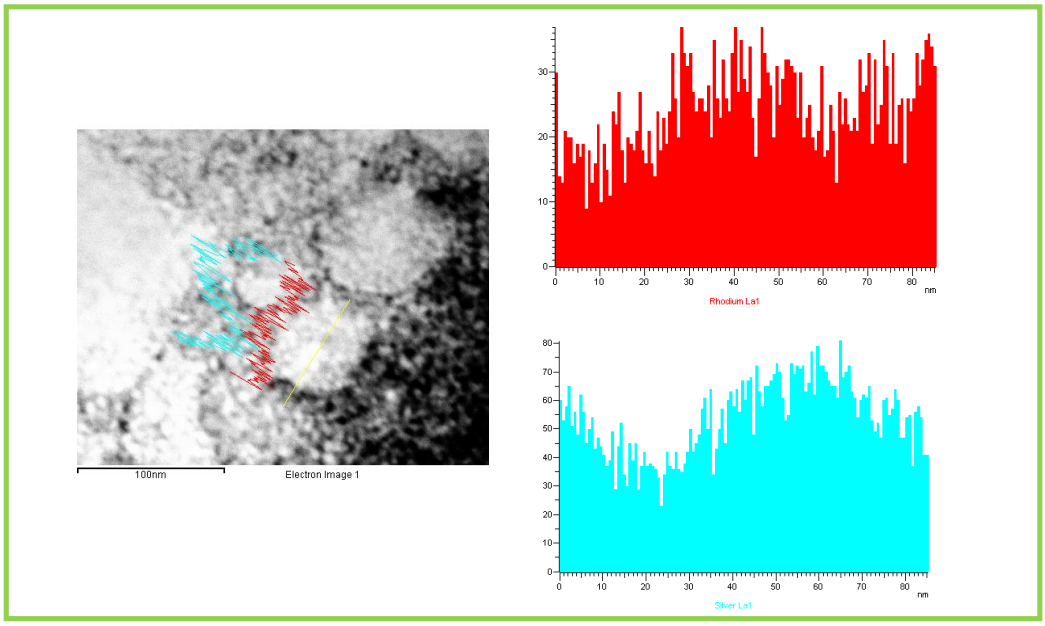

Figure 4.8. EDS line scan of a representative sample of $Rh_{17}Ag_{83}$ NPs.

Table 4.5. EDX data acquired from line scans for $Rh_{70}Ag_{30}$, $Rh_{51}Ag_{49}$ and $Rh_{17}Ag_{83}$.

	% Rh	% Ag
$Rh_{70}Ag_{30}$	79.5	20.5
$Rh_{51}Ag_{49}$	57.9	42.1
$Rh_{17}Ag_{83}$	34.3	65.7

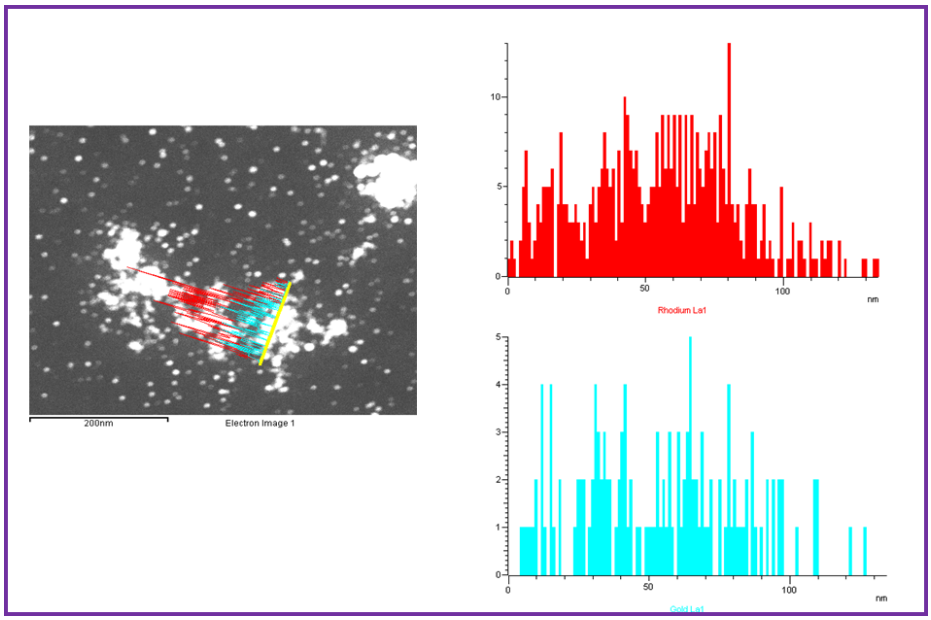

Figure 4.9. EDS line scan for a representative sample of $Rh_{70}Au_{30}$.

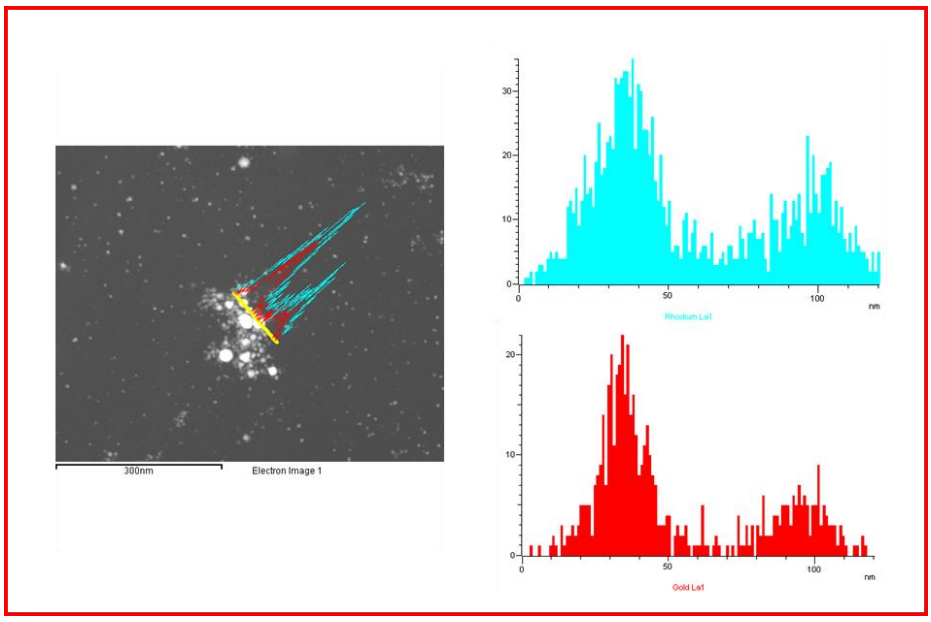

Figure 4.10. EDS line scan for a representative sample of $Rh_{45}Au_{55}$.

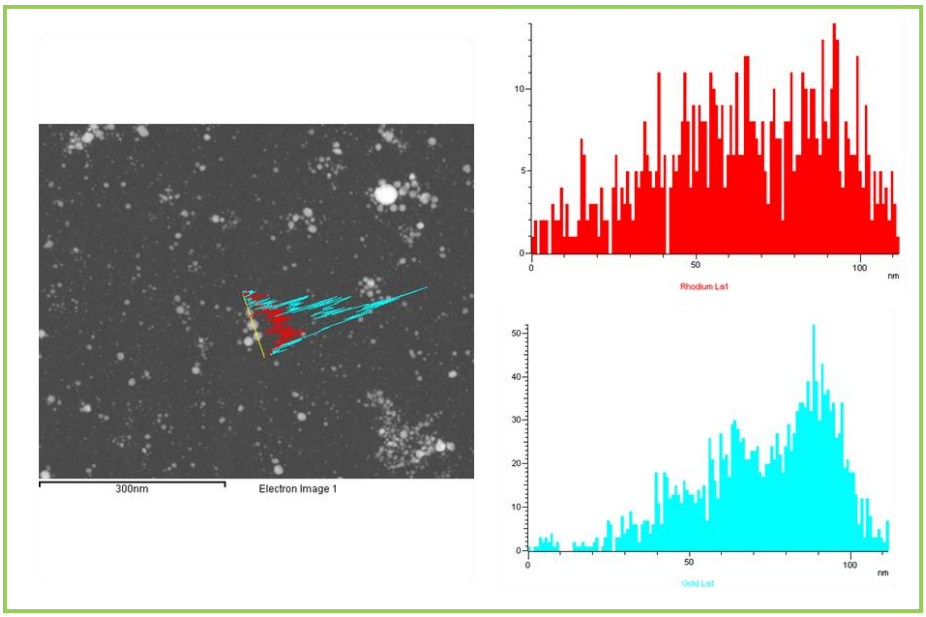

Figure 4.11. EDS line scan for a representative sample of $Rh_{15}Au_{85}$.

Table 4.6. EDX data acquired from line scans for $Rh_{70}Au_{30}$, $Rh_{45}Au_{55}$ and $Rh_{15}Au_{85}$.

	%Rh	%Au
$Rh_{70}Au_{30}$	72.2	27.8
$Rh_{45}Au_{54}$	61.4	38.6
$Rh_{15}Au_{85}$	21.2	78.8

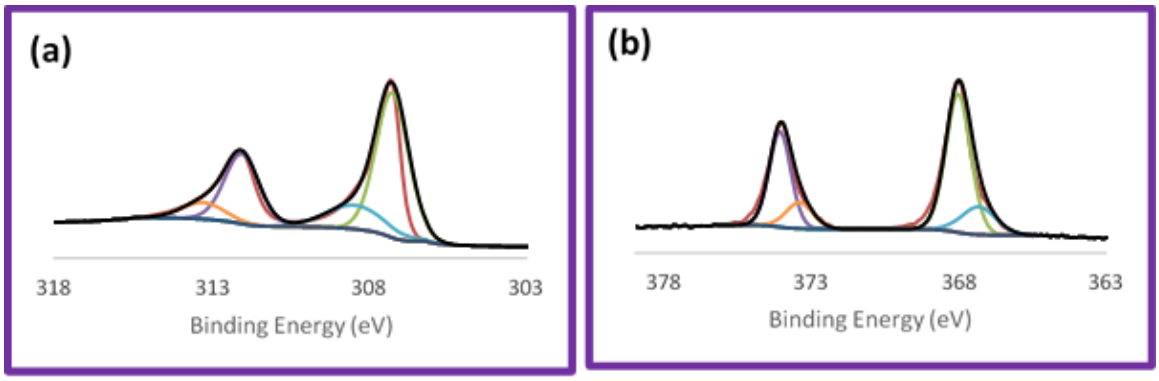

Figure 4.12. (a) Rh 3d and (b) Ag 3d XPS spectra of $Rh_{70}Ag_{30}$ NPs.

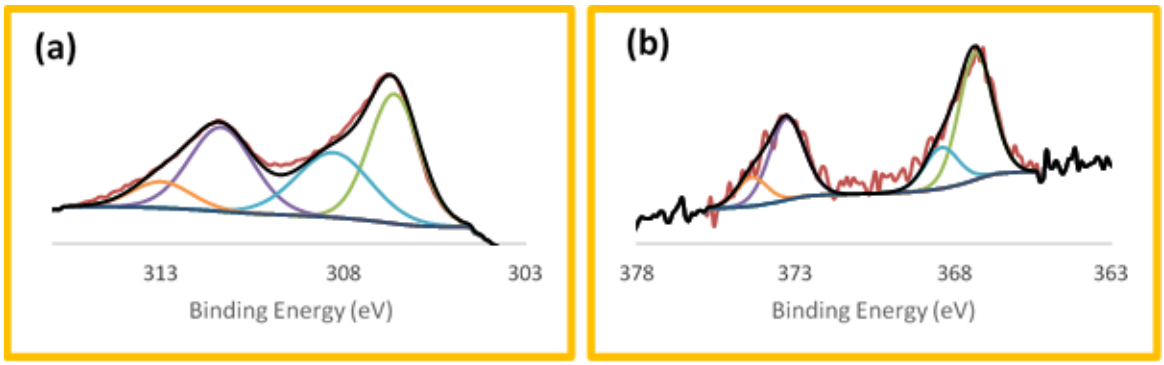

Figure 4.13. (a) Rh 3d and (b) Ag 3d XPS spectra of $Rh_{60}Ag_{40}$ NPs.

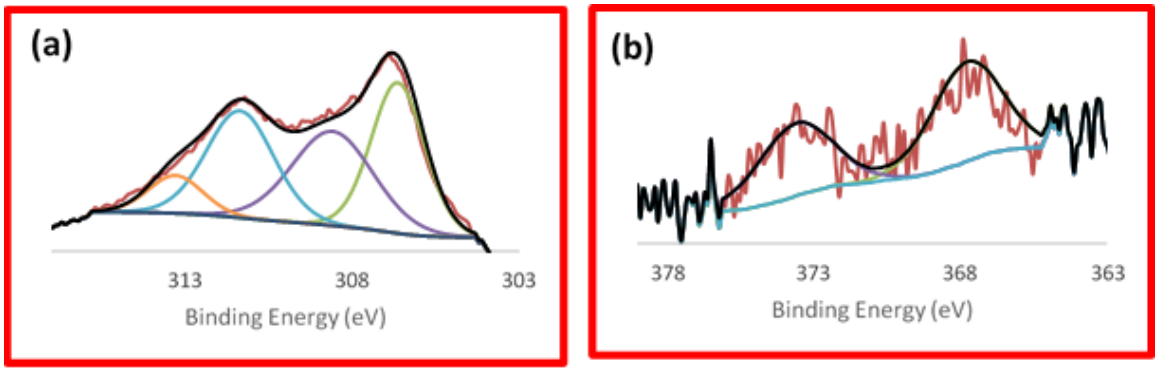

Figure 4.14. (a) Rh 3d and (b) Ag 3d XPS spectra of $Rh_{51}Ag_{49}$ NPs.

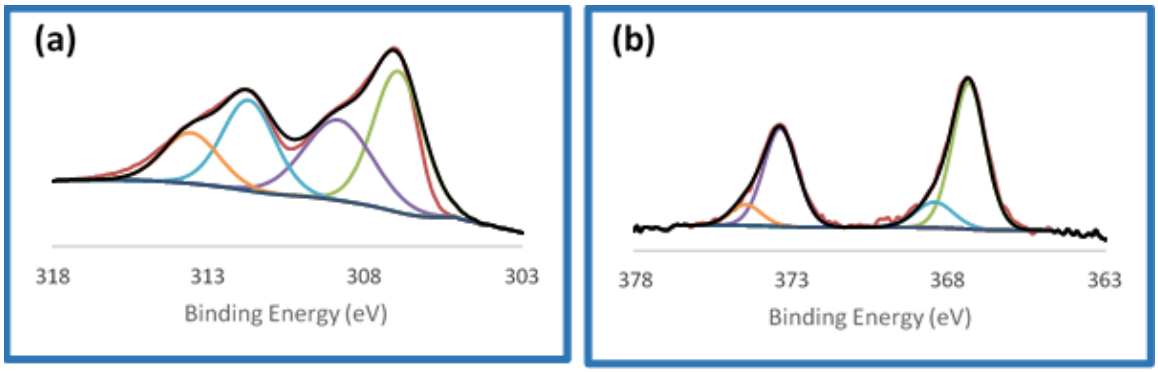

Figure 4.15. (a) Rh 3d and (b) Ag 3d XPS spectra of $Rh_{27}Ag_{73}$ NPs.

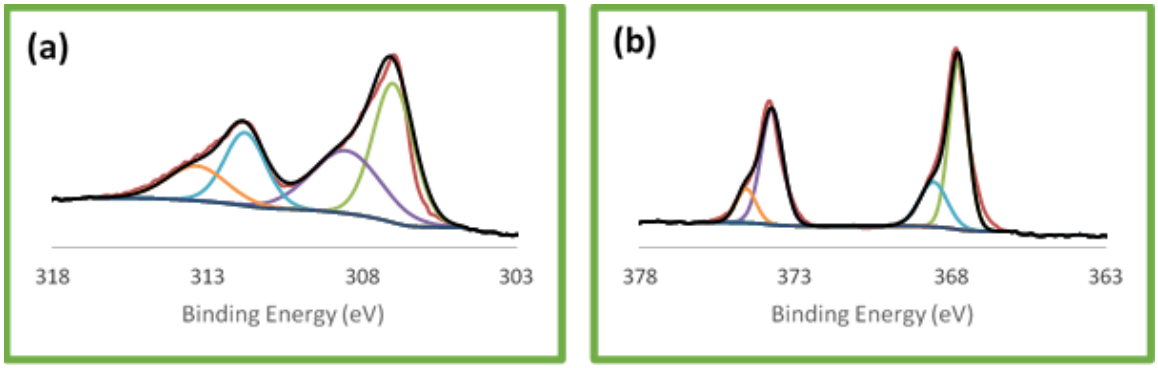

Figure 4.16. (a) Rh 3d and (b) Ag 3d XPS spectra of $Rh_{17}Ag_{83}$ NPs.

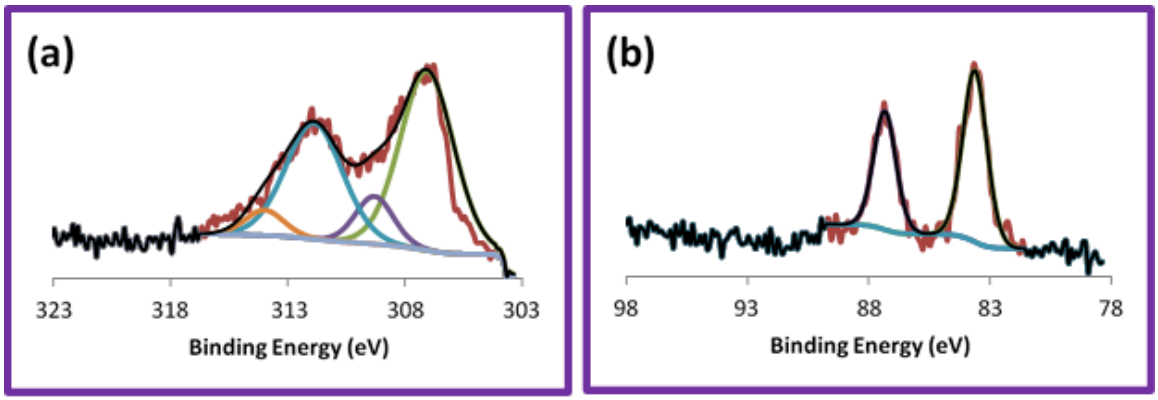

Figure 4.17. (a) Rh 3d and (b) Au 4f XPS spectra $Rh_{70}Au_{30}$ NPs.

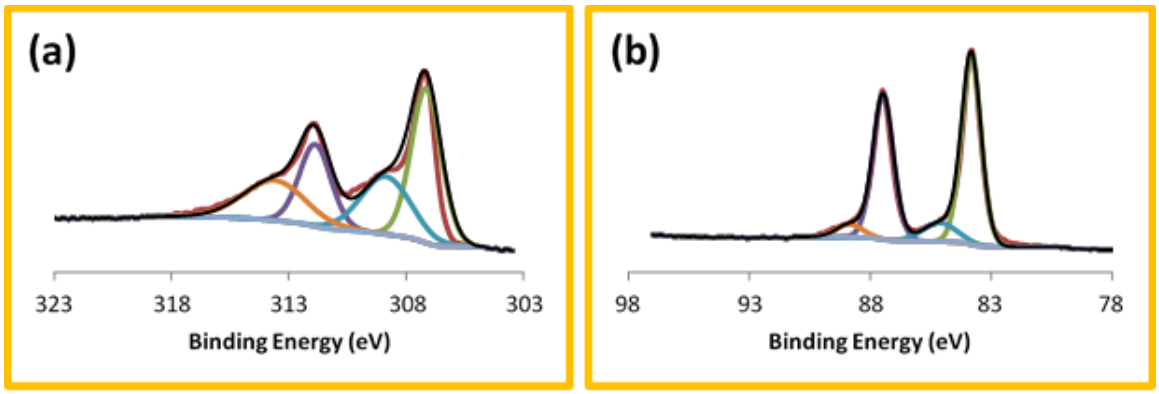

Figure 4.18. (a) Rh 3d and (b) Au 4f XPS spectra $Rh_{64}Au_{36}$ NPs.

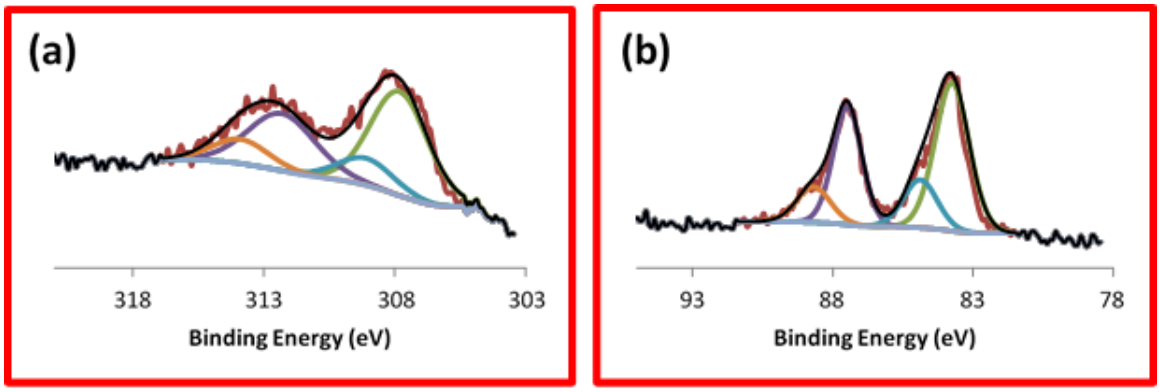

Figure 4.19. (a) Rh 3d and (b) Au 4f XPS spectra $Rh_{45}Au_{55}$ NPs.

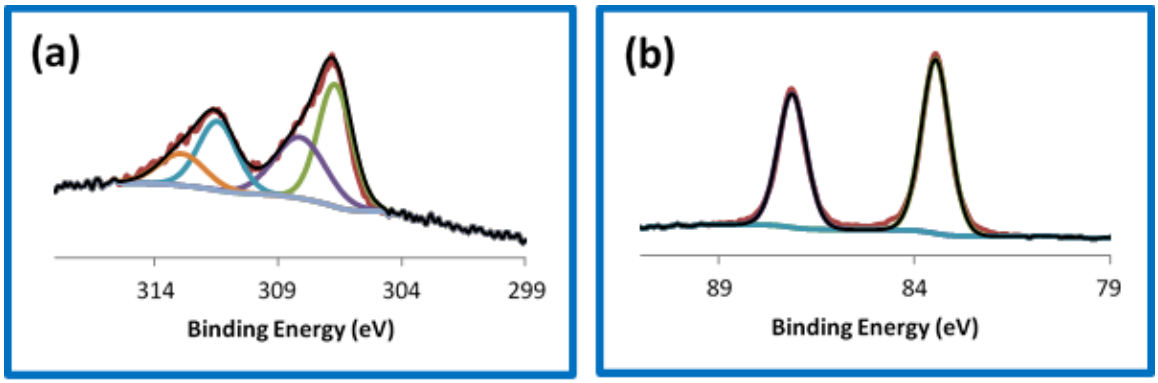

Figure 4.20. (a) Rh 3d and (b) Au 4f XPS spectra $Rh_{23}Au_{77}$ NPs.

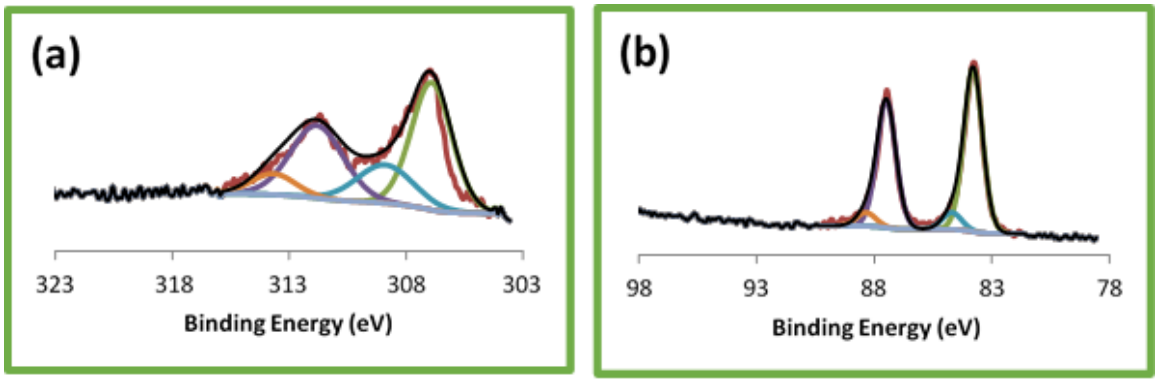

Figure 4.21. (a) Rh 3d and (b) Au 4f XPS spectra $Rh_{15}Au_{85}$ NPs.

4.4 HYDROGENATION CATALYSIS

4.4.1 Catalytic Studies Methods

The catalysts were prepared by addition of pre-calcined SiO_2 (200 mg) to suspensions of 8−12 mg of PVP-capped RhAg and RhAu NPs in ethanol:H_2O (1:1). The slurries were sonicated (20 min), isolated by filtration, washed with ethanol/H_2O and dried at 70 °C. The resulting composites contained between 0.5−3.5 wt% of noble metals as determined by ICP-MS. For each catalytic study, a small amount of catalyst (5–15 mg) was diluted with acid-washed and calcined sand and loaded into a custom made quartz U-tube, suspended above a D3-porosity frit. The sample was held constant at 25 °C using a water bath and circulator, and the entire reactor line (quartz, heated to 90 °C) was purged with the reactant gas mixture (H_2:He 1:1) for 30 min. Catalysis began with the introduction of cyclohexene vapor into the gas stream *via* an in-line saturator fitted with fritted bubbler. The cyclohexene substrate was acquired from Acros Organics (99% pure) and its purity was verified utilizing gas chromatography and ^{1}H and $^{13}C\{^{1}H\}$ NMR spectroscopy. All data was obtained in real-time by automated pneumatically-actuated sampling of the exhaust stream into an HP Agilent 6890 GC fitted with Restex Stabiliwax 15 m column and tandem FID and TCD detectors. Activity and turnover frequency values were obtained based on estimated surface area-to-volume ratios (by TEM). Activation energies were determined by collection of steady-state activity values at five temperatures (in the range 5–30 °C).

4.4.2 Recyclability Studies

After an initial hydrogenation catalysis run, the composites were purged with 1:1 H_2:He mixture at room temperature in the same experimental setup for an average of 1 hr. No further activation or regeneration was required. The supported NPs were then re-exposed to a stream of cyclohexene and hydrogenation catalysis was performed under the exact same experimental conditions stated in the main text.

4.4.3 Catalytic Data Analysis

Activity and turnover frequency values were obtained based on estimated surface area-to-volume ratios calculated using perfect cubeoctahedron dimensions and particle sizes determined by TEM. The activities were calculated by multiplying the products of the rate of injection of the reactant and the normalized area of cyclohexane by the grams of catalyst. The area of the cyclohexane peak (GC data) was normalized by dividing the area count by the molecular weight of the compound (Equation 1). This value was then divided by the sum of the normalized values for both product and reactant (cyclohexane and cyclohexene).

$$\text{g catalyst} \times \left[\frac{\mu\text{mol Cyclohexene}}{\text{min}} \times \frac{\dfrac{\text{Area count}_{\text{Cyclohexane}}}{\text{MW}_{\text{Cyclohexane}}}}{\dfrac{\text{Area count}_{\text{Cyclohexane}}}{\text{MW}_{\text{Cyclohexane}}} + \dfrac{\text{Area count}_{\text{Cyclohexene}}}{\text{MW}_{\text{Cyclohexene}}}} \right] \qquad \text{Eq. 1}$$

The turnover frequency values were calculated by dividing the activity (in mol g^{-1} s^{-1}) by the product of the normalized Rh and M (M = Ag or Au) loading value and the number of bulk atoms to surface atoms ratio (PME value) (Equation 2). To account for the fact that the particles are not entirely composed of Rh atoms, the previous value was multiplied by the inverse of the average % of Rh atoms in each NP (value acquired from ICP-MS analysis). The normalized % Rh loading was acquired by dividing the value for wt% Rh in the catalyst by the atomic weight of Rh. High resolution ICP-MS data was used to determine the total mass %Rh, %Ag and %Au loading.

$$\frac{1}{\text{Avg. \% Rh atoms on NP}} \left[\frac{\text{Activity Cyclohexane (mol } g^{-1} s^{-1})}{\frac{\text{Wt \% (Rh+M) in catalyst}}{\text{Avg. AW}_{Rh/M}} \times \text{PME}} \right] \quad \text{Eq. 2}$$

M = Ag or Au

4.4.4 Hydrogenation Catalysis Results and Discussion

The RhM NPs of varying compositions were dispersed on amorphous silica by direct impregnation from water/ethanol suspensions, followed by drying in air at 70 °C. TEM studies of the composites showed that the NPs were spatially well dispersed and retained their original size and morphology (Figures 4.22 and 4.23). It is noteworthy that the catalysts were highly active as-synthesized and did not require further *pre*-treatment or removal of the capping agent. It has been previously suggested that μwH prepared NPs

are more active than conventionally prepared analogues because less PVP is incorporated possibly due to strong rotational coupling (excitation) of the PVP polymer with the microwaves.[39] Thus, not needing to remove the stabilizing agent was beneficial because potential NP restructuring or sintering prior to catalysis was avoided.

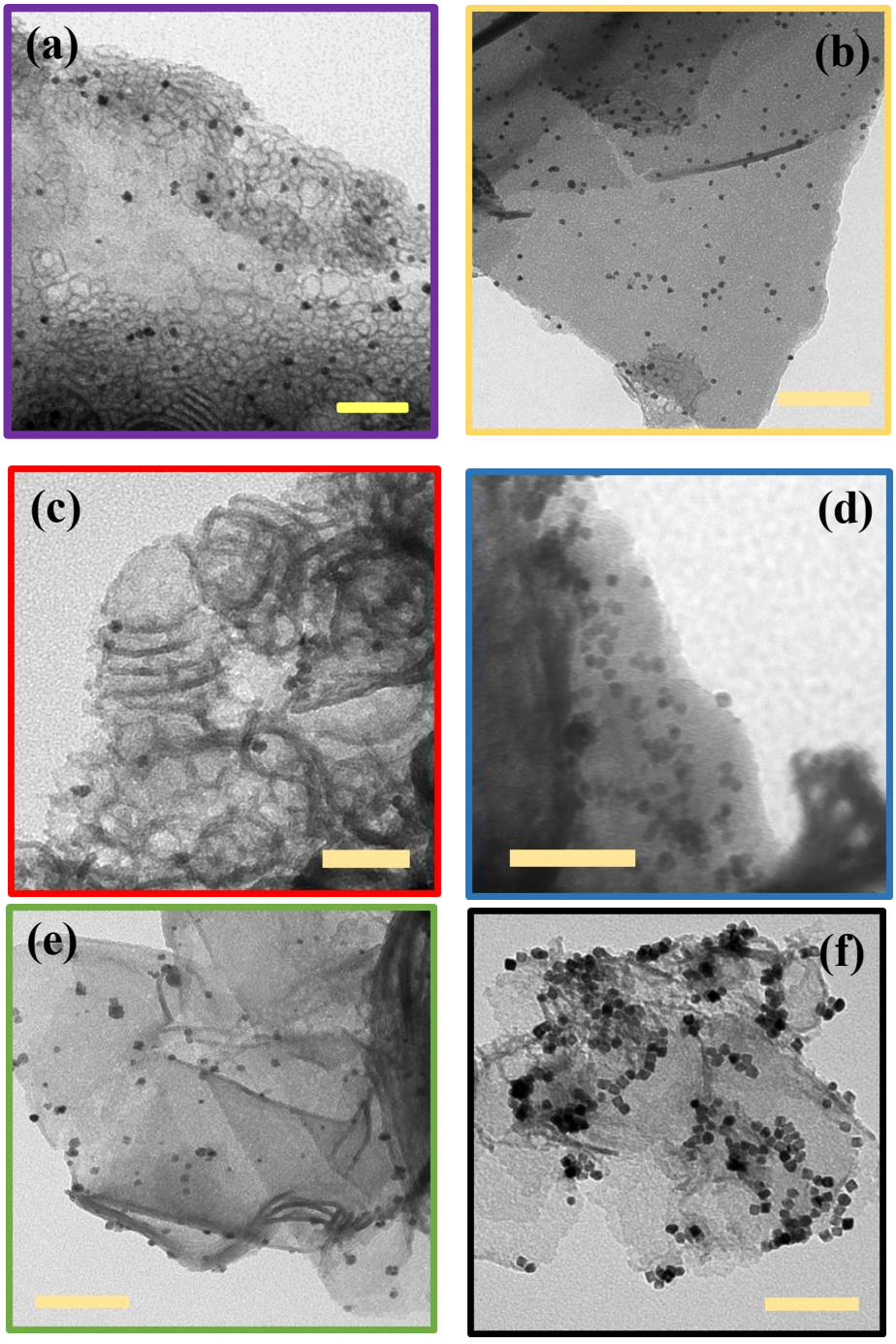

Figure 4.22. TEM images of RhAg NPs supported on amorphous silica *pre*-catalytic studies. (a) $Rh_{70}Ag_{30}$ NPs; (b) $Rh_{60}Ag_{40}$ NPs; (c) $Rh_{51}Ag_{49}$ NPs; (d) $Rh_{27}Ag_{73;}$ (e) $Rh_{17}Ag_{83;}$ (f) microwave-assisted monometallic Rh NPs.

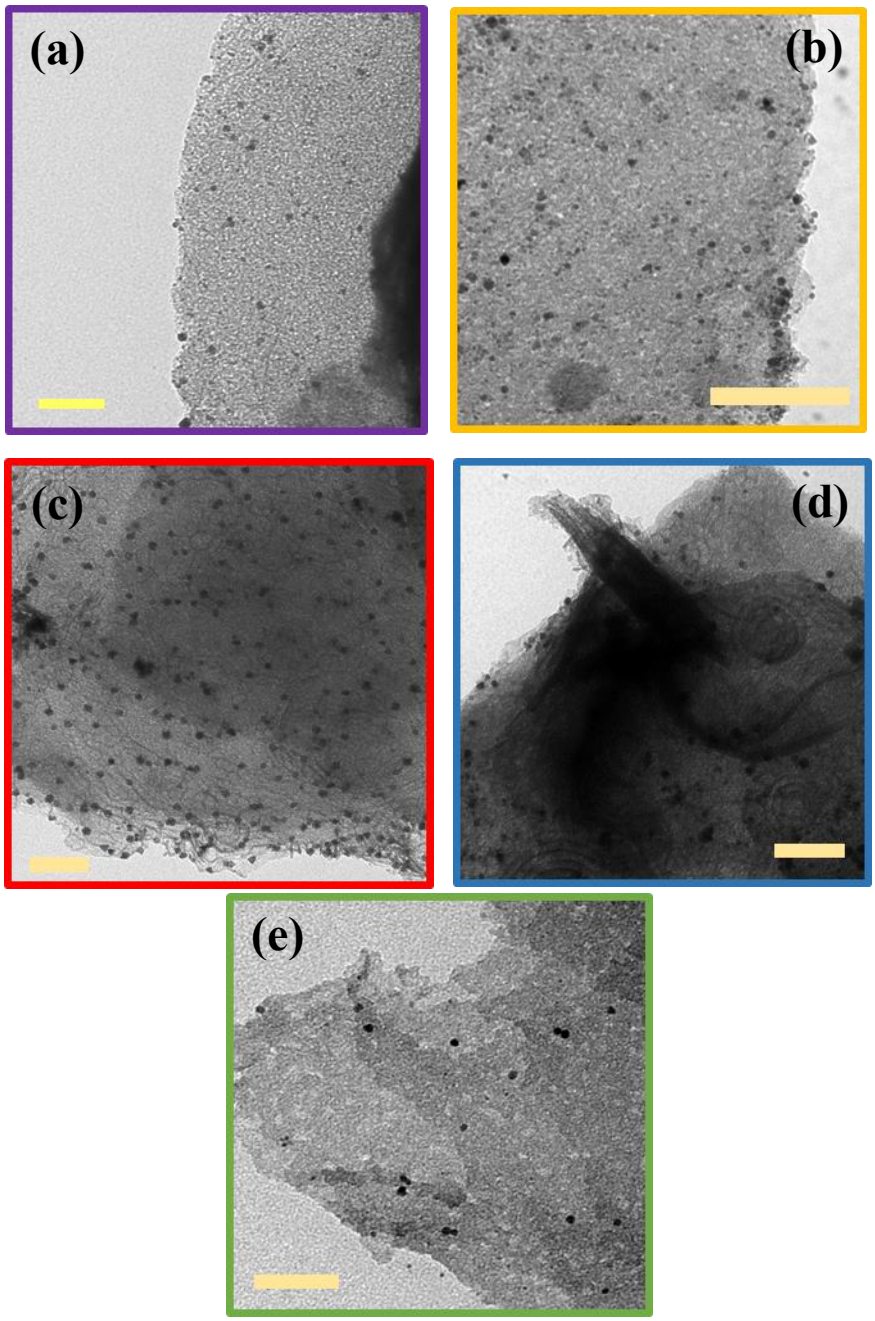

Figure 4.23. TEM images of RhAu NPs supported on amorphous silica *pre*-catalytic studies. (a) $Rh_{70}Ag_{30}$ NPs; (b) $Rh_{64}Ag_{36}$ NPs; (c) $Rh_{45}Ag_{55}$ NPs; (d) $Rh_{23}Ag_{77;}$ (e) $Rh_{15}Ag_{85.}$

The catalytic performances of the RhM NPs of different compositions were assessed using cyclohexene hydrogenation as a model reaction. Catalysis experiments were performed in the vapor phase and a 'single-pass' set-up was used. The catalysis reactor was directly connected to a gas chromatograph which was used to identify the products of the hydrogenation reaction using an FID detector. A minimum of three catalytic experiments were performed under identical conditions utilizing different batches of the same composite material in order to ensure reproducible results. Activity profiles for the as-synthesized catalysts (Figures 4.24 and 4.25) are plotted with turnover frequencies (TOFs) that have been normalized per surface site, by taking into account average NP dimensions. It is apparent from the data that synergistic effects of the alloys induced enhanced turnover frequencies for both alloys since RhM NPs with intermediate or Rh-rich compositions were able to outperform pure Rh NPs. However, it was evident that the activity of the catalysts had a strong dependence on the composition ratios. In the case of RhAg, alloys with 51% or higher Rh content, displayed TOFs up to four times greater than pure Rh NPs as observed in Figure 4.24. Enhanced turnover frequencies for the RhAu system were only observed for $Rh_{70}Au_{30}$ NPs; nonetheless, $Rh_{64}Au_{36}$ NPs displayed comparable catalytic behavior to that of pure Rh (Figure 4.25). From a practical standpoint, this is a stunning result because catalytically inactive Ag or Au can be utilized to dilute Rh and also to increase the apparent hydrogenation activity. In general, the RhM alloy catalysts showed and initial period of increasing activity before steady-state was reached. The catalysts remained stable at steady-state for up to six hours. Activity was also maintained upon recyclability testing, with only modest reduction in steady-state TOFs after the third re-use (Table 4.7 and 4.8). We were also able to measure activation energies for all the catalysts by obtaining steady-state activity data between 5–30 °C (Tables 4.3 and 4.4; Figures 4.26 and 4.27). The measured activation energy for

the most active catalyst ($Rh_{60}Ag_{40}$) was only 15.4 kJ mol^{-1} versus 57.2 kJ mol^{-1} for Rh NPs.

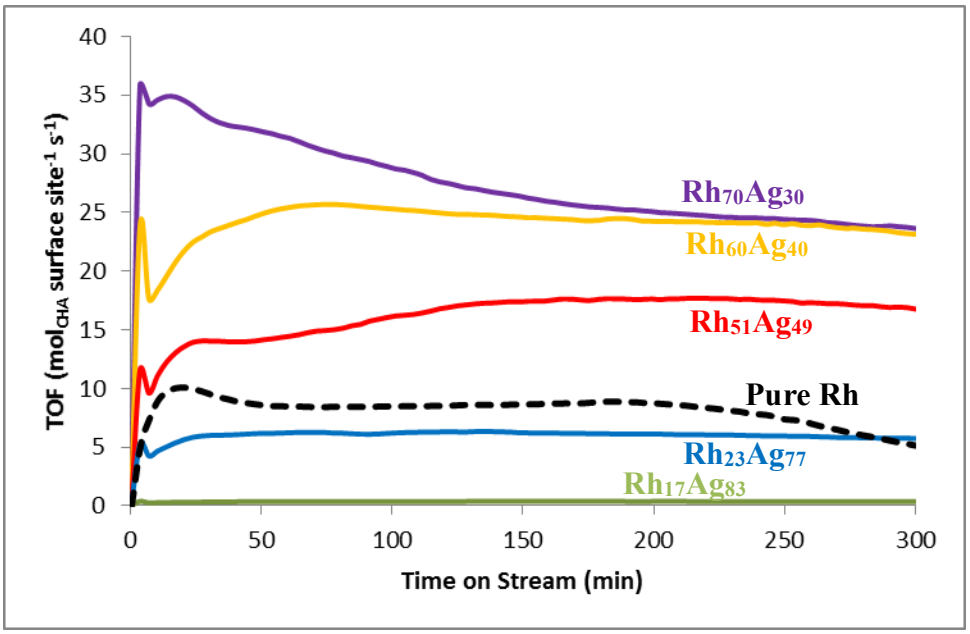

Figure 4.24. Catalytic plots displaying TOF as a function of time, for the hydrogenation of cyclohexene for RhAg alloyed NPs of different compositions.

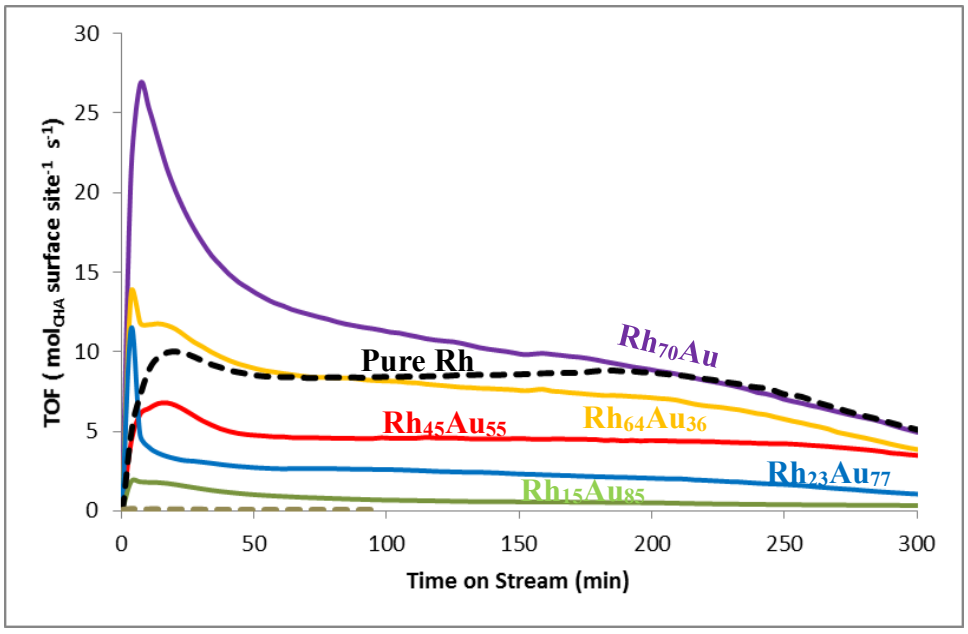

Figure 4.25. Catalytic plots displaying TOF as a function of time, for the hydrogenation of cyclohexene for RhAg alloyed NPs of different compositions.

Table 4.7. Steady-state turnover frequency values and % loss in activity for the hydrogenation of cyclohexene using RhAg alloyed NPs after 3 consecutive runs (recyclability).

	Rh$_{70}$Ag$_{30}$		Rh$_{60}$Ag$_{30}$		Rh$_{51}$Ag$_{49}$		Rh$_{27}$Ag$_{73}$		Rh$_{17}$Ag$_{83}$	
	SS TOF	% Loss	SS TOF	% Loss	SS TOF	% Loss	SS TOF	% Loss	SS TOF	% Loss
Run 1	21.11		25.61		12.06		6.64		0.27	
Run 2	18.58	11.98	25.01	2.34	9.84	18.41	6.84	-2.92	0.3	-10
Run 3	11.43	38.48	23.83	4.72	7.93	19.41	8.24	-16.99	0.39	-23.08

Table 4.8. Steady-state turnover frequency values and % loss in activity for the hydrogenation of cyclohexene using RhAu alloyed NPs after 3 consecutive runs (recyclability).

	$Rh_{70}Au_{30}$		$Rh_{64}Au_{36}$		$Rh_{45}Au_{54}$		$Rh_{23}Au_{77}$		$Rh_{15}Au_{85}$	
	SS TOF	**% Loss**	**SS TOF**	**% Loss**	**SS TOF**	**% Loss**	**SS TOF**	**% Loss**	**SS TOF**	**% Loss**
Run 1	9.85		7.97		4.75		2.8		0.85	
Run 2	4.77	51.57	4.27	46.42	4.39	7.58	1.41	49.64	0.43	49.41
Run 3	0.09	98.11	1.63	61.83	3.74	14.81	0.25	82.27	0.14	67.44

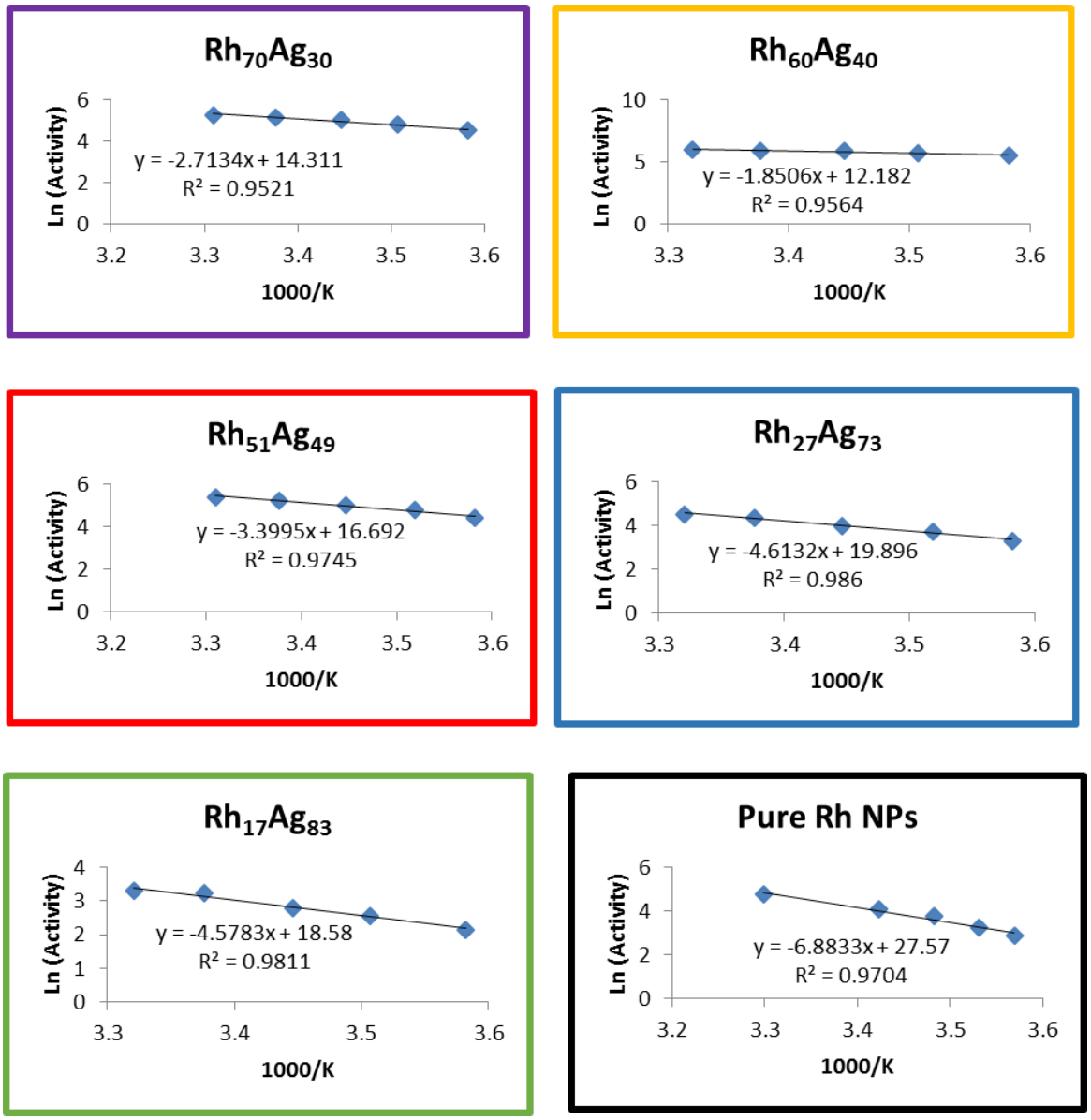

Figure 4.26. Arrhenius plots for the hydrogenation of cyclohexene using RhAg alloy NPs of different compositions and pure Rh NPs.

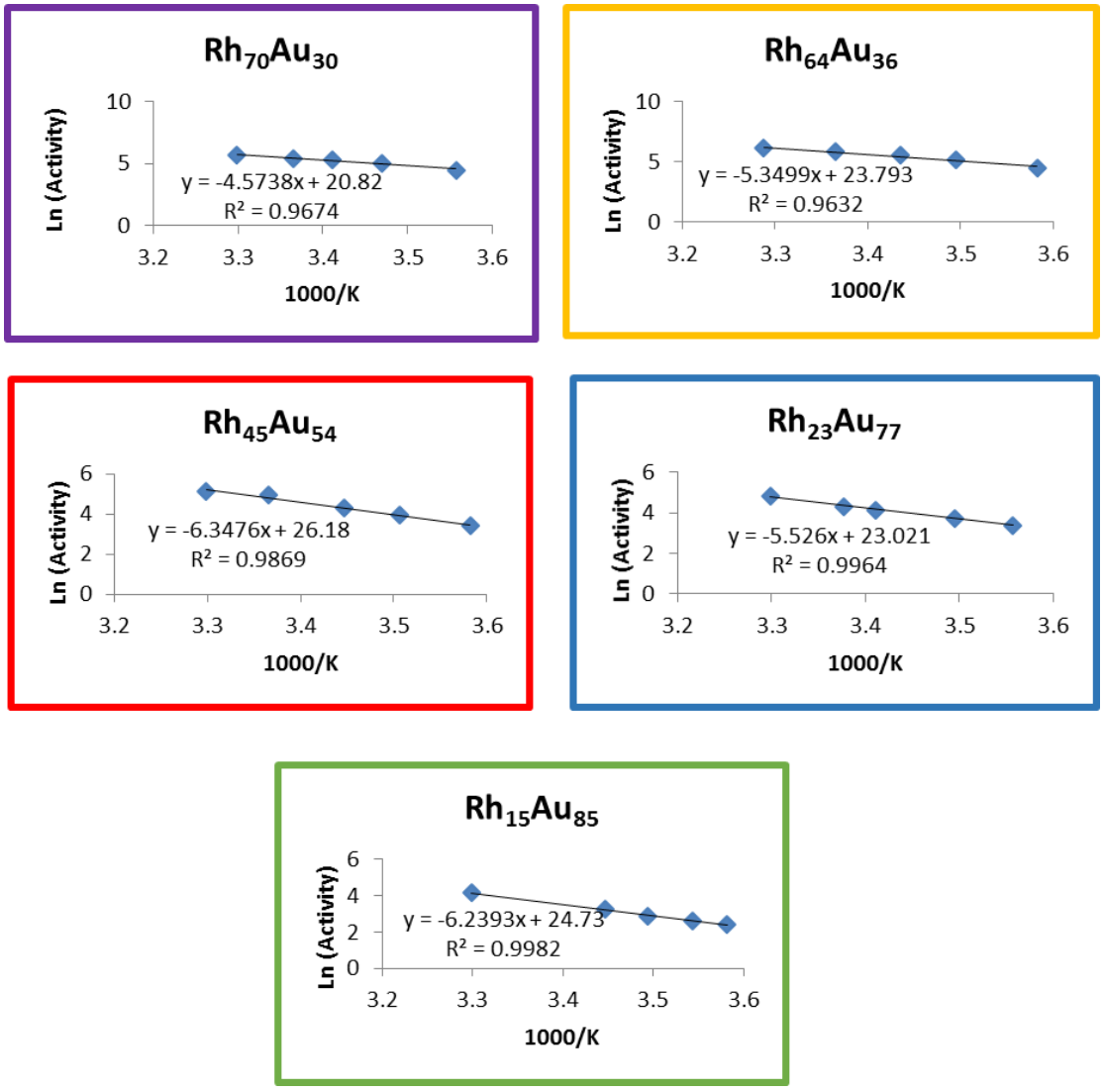

Figure 4.27. Arrhenius plots for the hydrogenation of cyclohexene using RhAu alloy NPs of different compositions.

TEM images of the supported alloy NPs *post*-catalysis confirmed that the particles retained their shape and size during the catalytic process and were not agglomerated (Figures 4.28 and 4.29). Furthermore, XPS and EDX analysis of the used materials indicated that both metals were still present at the NP surface in proportions very similar to those measured in the fresh materials and that the alloyed metals did not undergo segregation during hydrogenation catalysis (Tables 4.3 and 4.4; Figures 4.30 and 4.31). Thus, the decrease in activity of the alloy NPs after the induction period cannot be attributed to phase segregation of the particles to generate other types of assemblies such as core-shell NPs, but rather to surface restructuring due to higher energy facets (edges and corners).

The existence of segregated monometallic NPs and the possibility of these performing the catalysis was also discarded by performing control experiments where 1:1 mixtures of pure Rh and pure M NPs of similar sizes were supported on amorphous silica and used for the same catalytic process under identical experimental conditions. The catalytic behavior observed was comparable to that displayed by pure Rh NPs (Figures 4.32 and 4.33). Since no catalytic enhancement was observed in this case, it is reasonable to assume that the metals have to interact in order for any catalytic improvement to result.

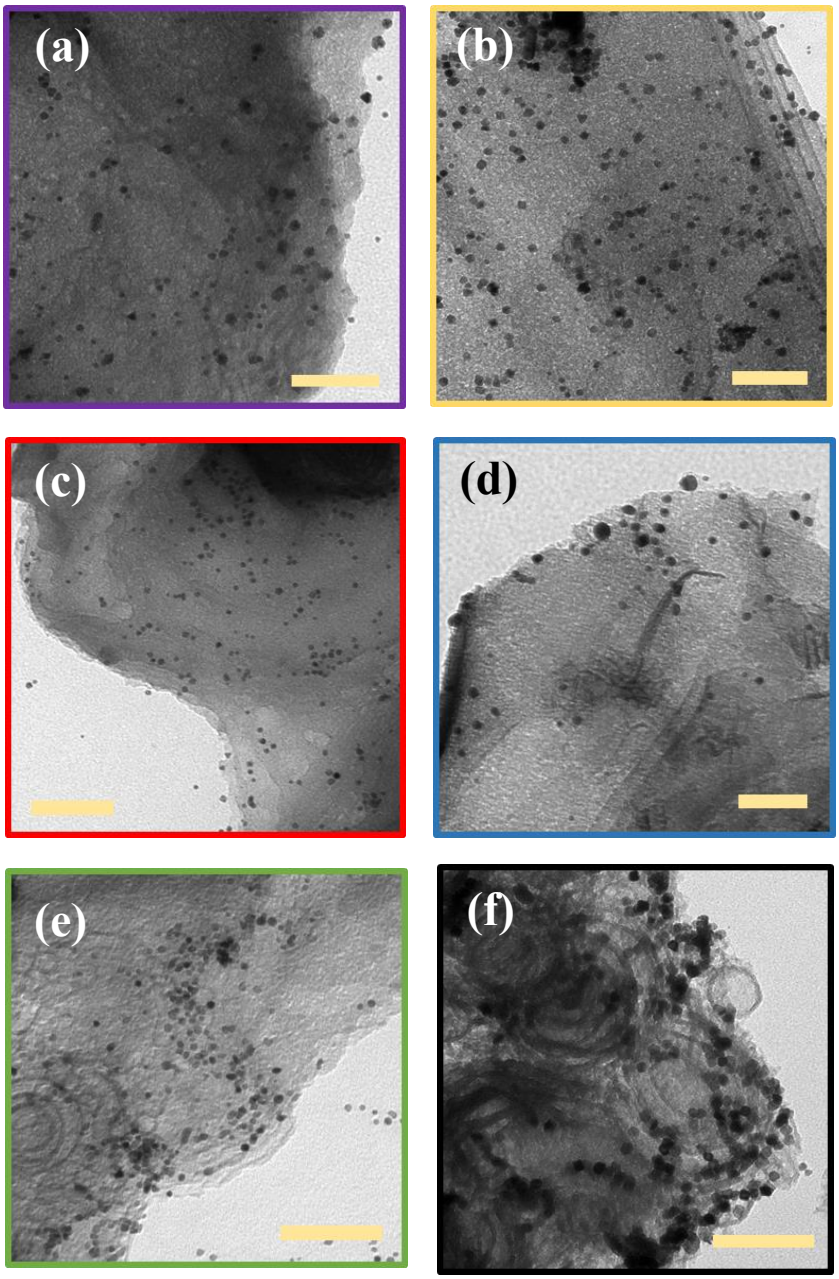

Figure 4.28. TEM images of RhAg NPs supported on amorphous silica *post*-catalytic studies. (a) $Rh_{70}Ag_{30}$ NPs; (b) $Rh_{60}Ag_{40}$ NPs; (c) $Rh_{51}Ag_{49}$ NPs; (d) $Rh_{27}Ag_{73;}$ (e) $Rh_{17}Ag_{83;}$ (f) microwave-assisted monometallic Rh NPs.

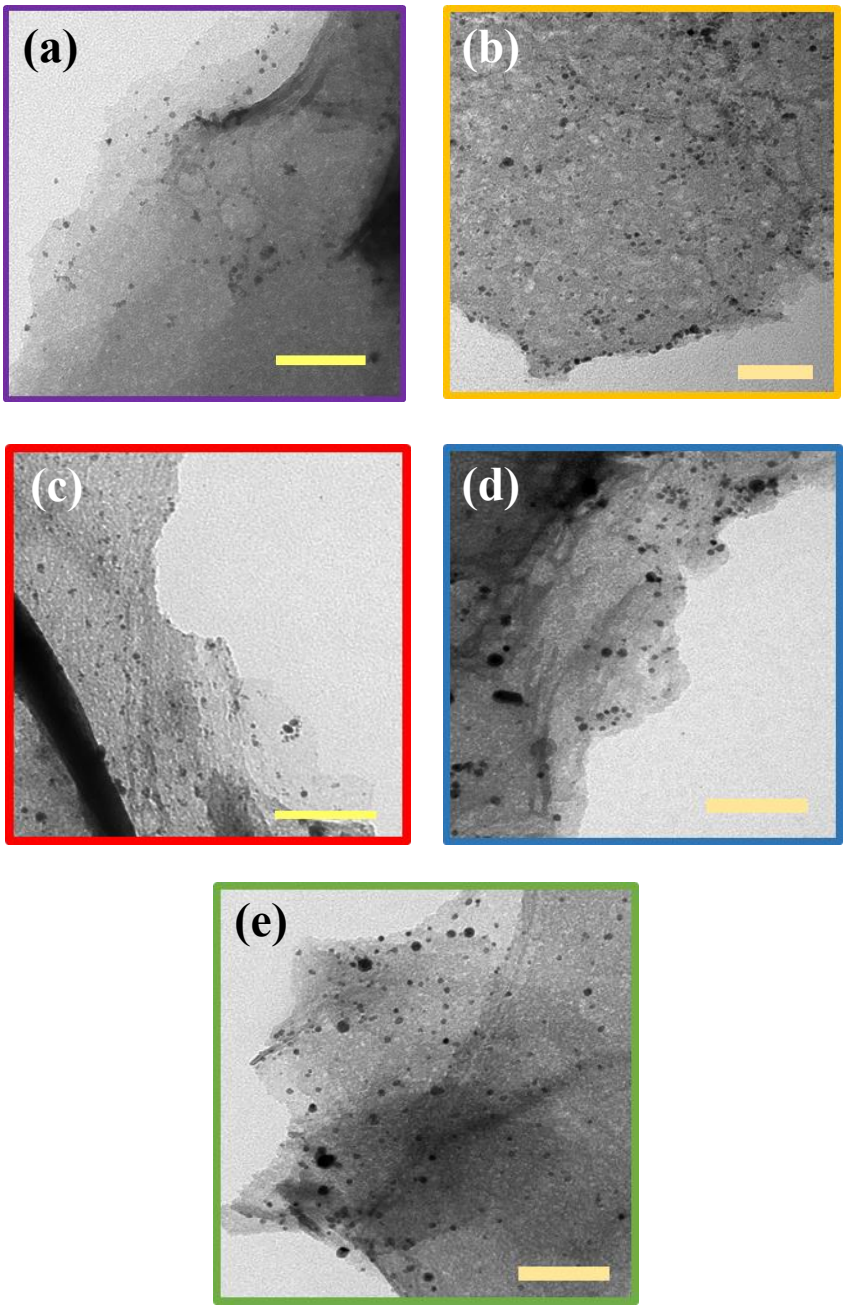

Figure 4.29. TEM images of RhAu NPs supported on amorphous silica *post*-catalytic studies. (a) $Rh_{70}Au_{30}$ NPs; (b) $Rh_{64}Au_{36}$ NPs; (c) $Rh_{45}Au_{55}$ NPs; (d) $Rh_{23}Au_{77;}$ (e) $Rh_{15}Au_{85}$.

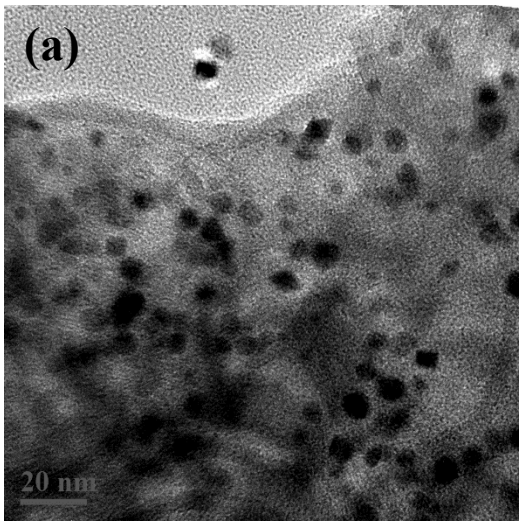

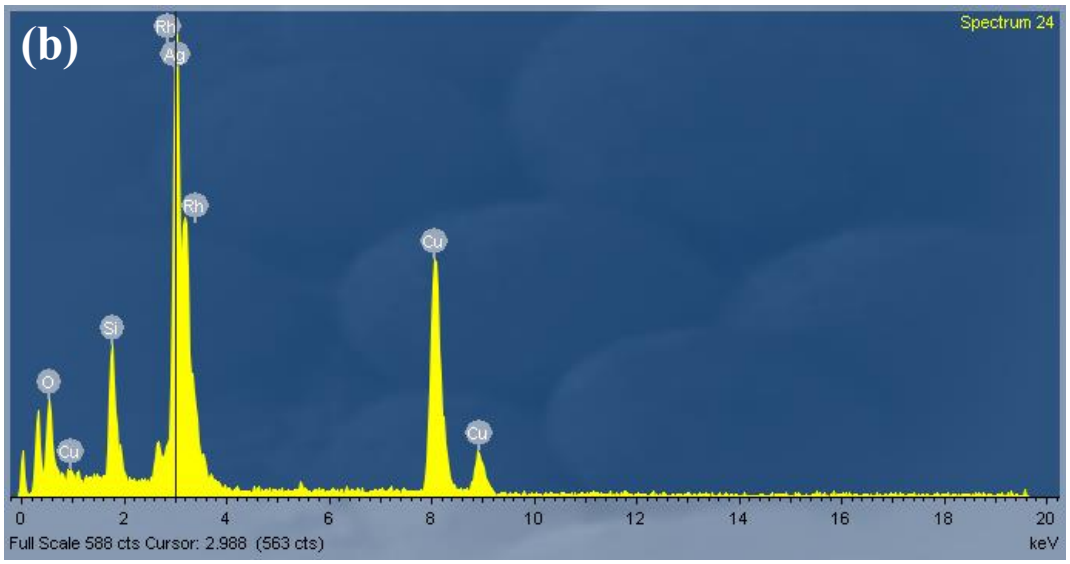

Figure 4.30. (a) Representative HRTEM image and (b) single-particle EDX spectrum of supported $Rh_{51}Ag_{49}$ after hydrogenation catalysis.

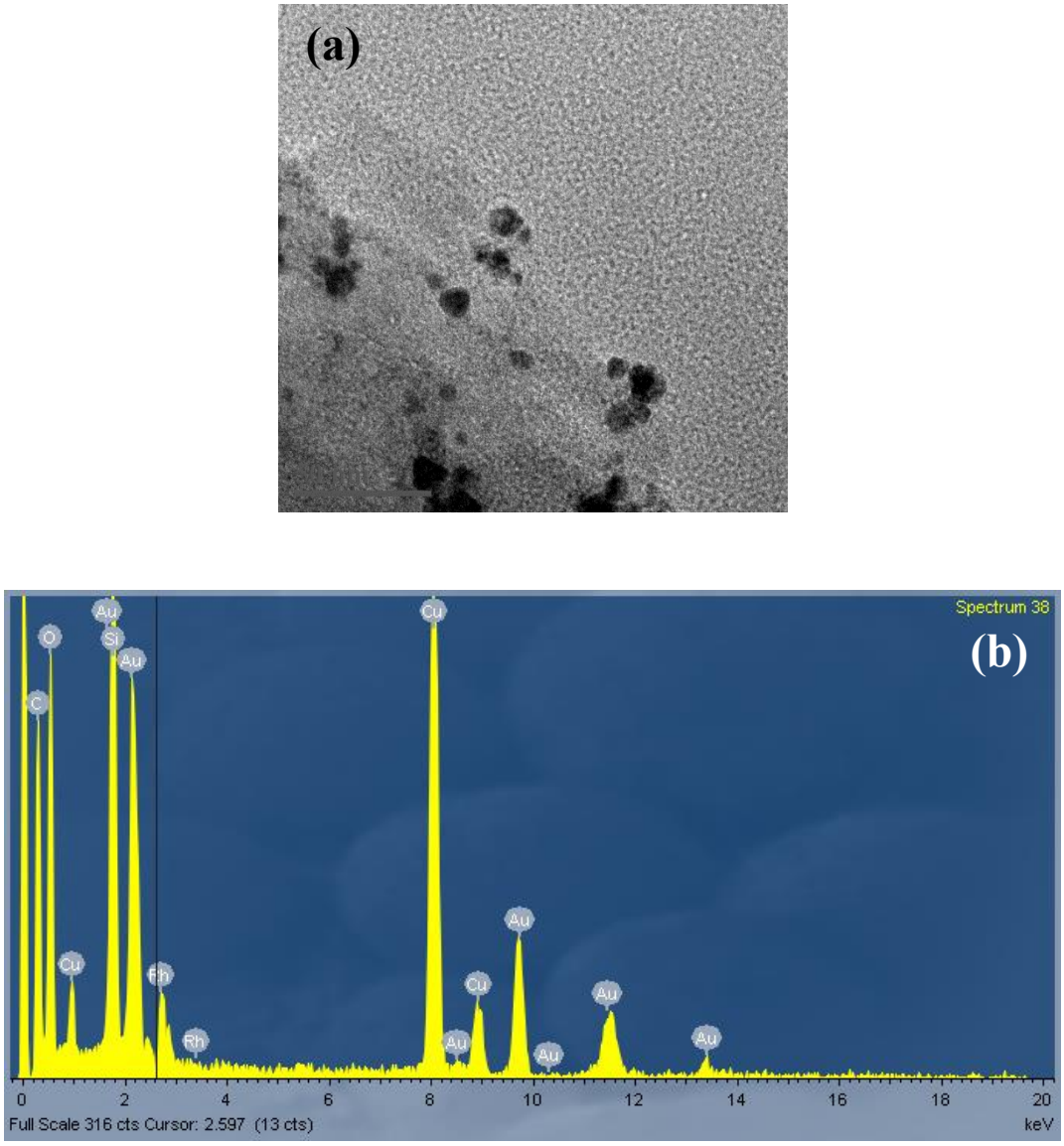

Figure 4.31. (a) Representative HRTEM image and (b) single-particle EDX spectrum of supported $Rh_{45}Au_{55}$ after hydrogenation catalysis.

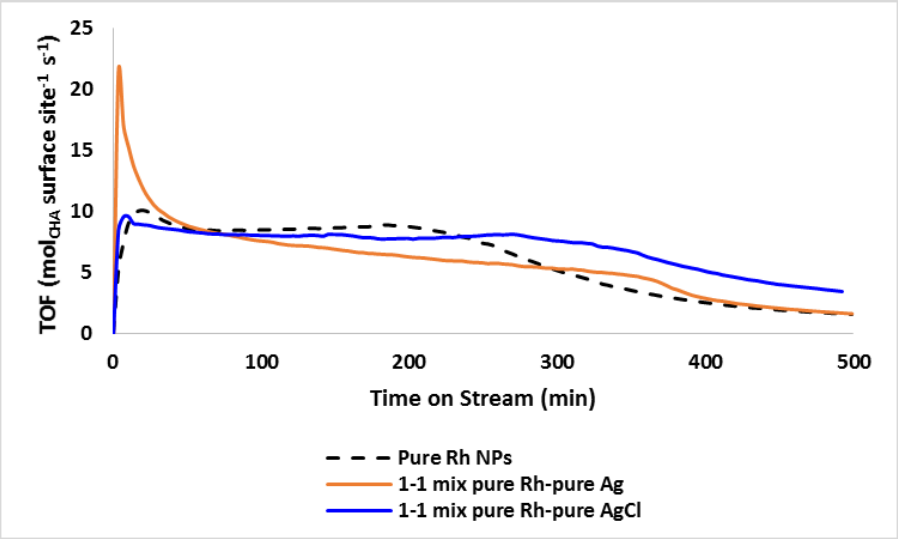

Figure 4.32. Catalytic plots displaying TOF values as a function of time for the hydrogenation of cyclohexene for pure Rh (dashed black line), 1:1 mixture of pure Rh and pure Ag NPs and 1:1 mixture of pure Rh and pure AgCl NPs.

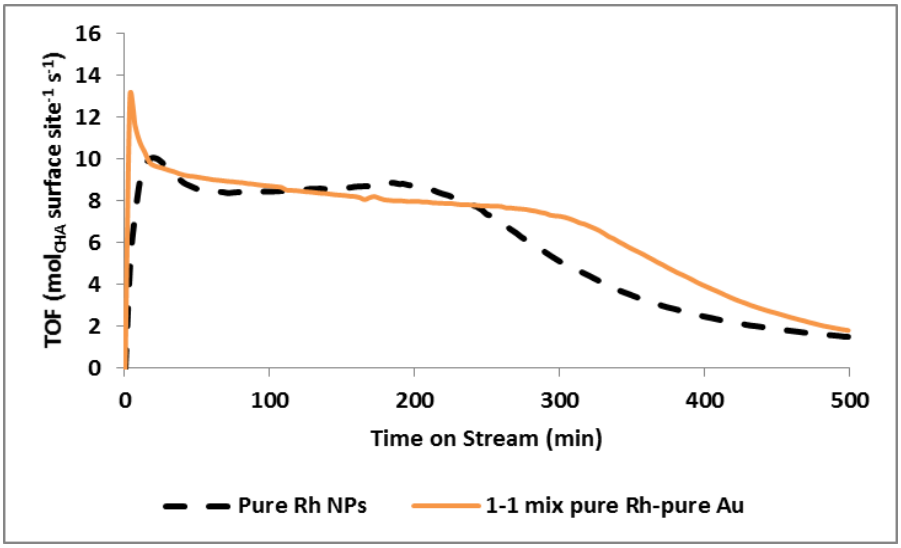

Figure 4.33. Catalytic plots displaying TOF values as a function of time for the hydrogenation of cyclohexene for pure Rh (dashed black line), 1:1 mixture of pure Rh and pure Au NPs.

A direct comparison of the hydrogenation TOFs of supported RhM NPs as a function of composition (Figure 4.34) clearly shows that NPs with optimized compositions out-perform pure Rh NPs. This comparison does not even take into account the fact that Rh is diluted in the alloy NPs. Given that Rh is inherently catalytically active and it is more expensive than both Ag and Au due to its limited availability, from an economic standpoint it is also viable to calculate TOF values based solely on the amount of Rh present in the NPs. Catalytic data analyzed in this way accentuates the enhancement in hydrogenation activity, displaying higher turnover values for all the alloy species in comparison to monometallic Rh particles. An alternative plot that is normalized for Rh surface sites (assuming uniform concentration of Rh throughout the NPs) reveals that RhM NPs of all compositions above 20% Rh are more active than pure Rh NPs (Figures 4.35 – 4.37).

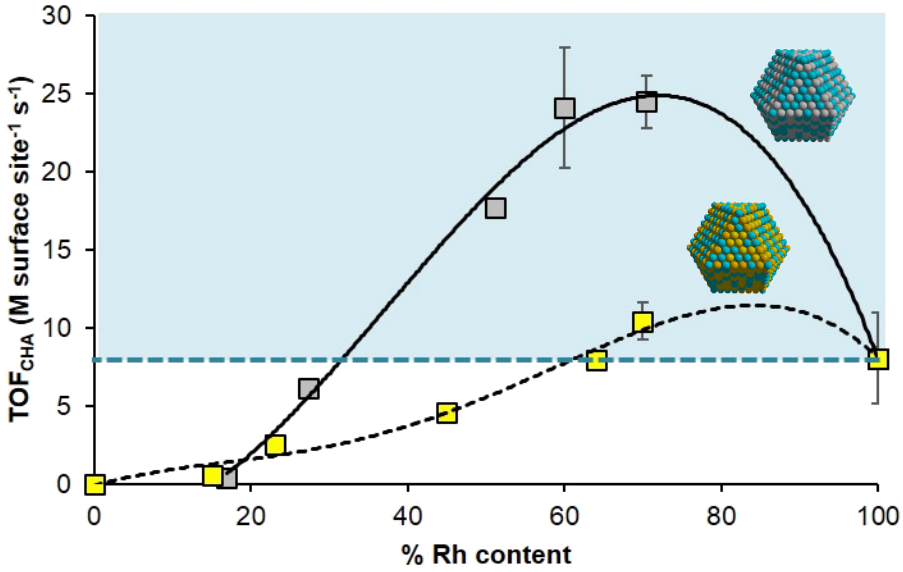

Figure 4.34. A direct comparison of the steady-state rates of cyclohexene hydrogenation at 25.0 °C as a function of %Rh composition for the RhAg (grey) and RhAu (yellow) NPs versus pure Rh NPs (blue dashed line) prepared by μwH.

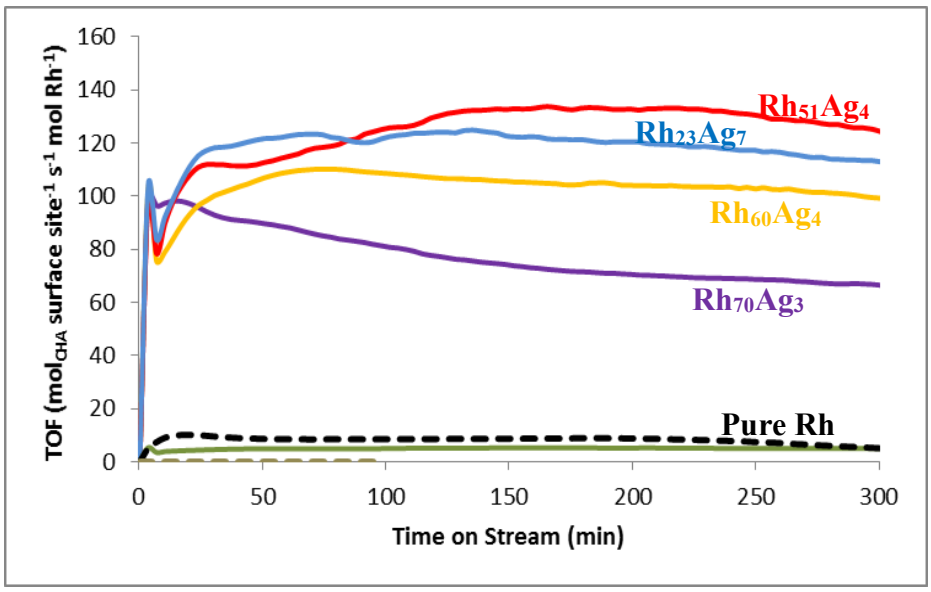

Figure 4.35. Catalytic plots displaying TOFs as a function of time, normalized for percent surface Rh, for the hydrogenation of cyclohexene for RhAg alloyed NPs of varying compositions.

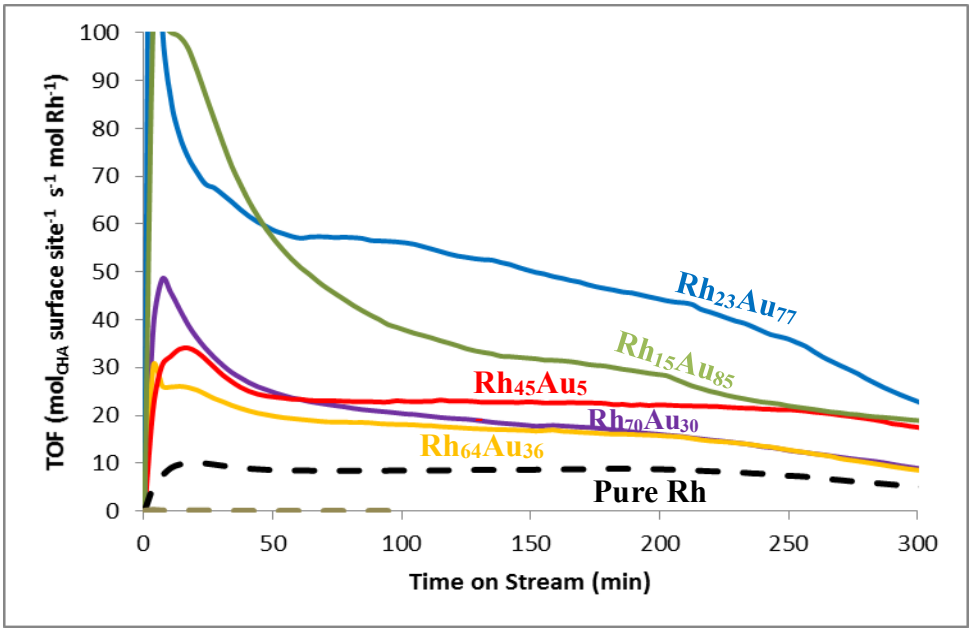

Figure 4.36. Catalytic plots displaying TOFs as a function of time, normalized for percent surface Rh, for the hydrogenation of cyclohexene for RhAu alloyed NPs of different compositions.

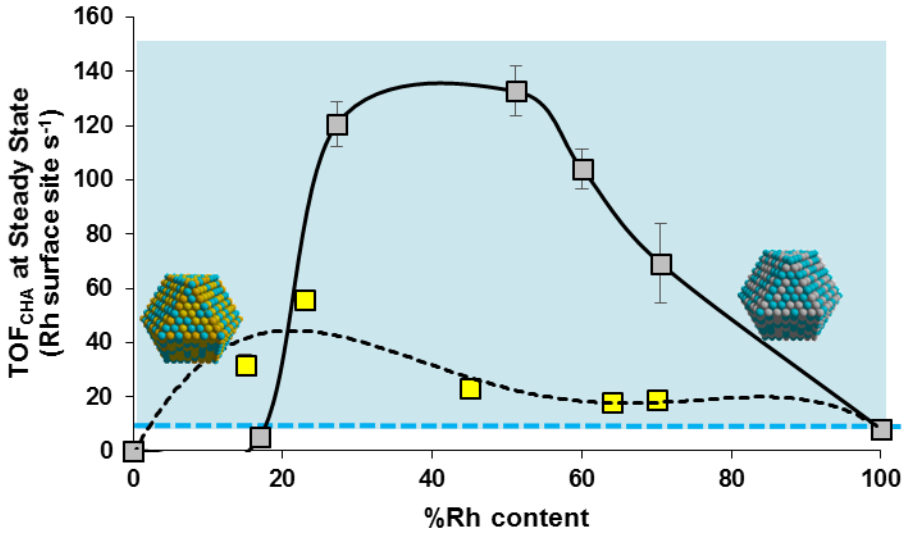

Figure 4.37. A direct comparison of the steady-state rates of cyclohexene hydrogenation at 25.0 °C as a function of %Rh composition for the RhAg (grey) and RhAu (yellow) NPs versus pure Rh NPs (blue dashed line) when plotted using TOFs normalized for percent surface Rh.

4.5 Theoretical Studies and Calculations

4.5.1 Computational Studies Methods

H binding energy calculations were performed with VASP using a 4 layer (3×3) slab model of a (111) facet.[228,229] Core electrons were described using the projector-augmented wave method.[230,231] Exchange-correlation energy was evaluated by generalized gradient approximation (GGA) using the Perdew-Wang 91 functional.[232] The kinetic energy cutoff for the plane-wave basis was set to 280 eV.[233] Convergence of our calculation was tested by increasing the energy cutoff to 400 eV, and H binding energy of

Au(111), Ag(111) and Rh(111) were found to vary by less than 0.01 eV. Spin polarization was tested and used as required.

H binding energies were calculated on the (111) surface of a four-layer, 3×3 unit cell, face centered cubic (FCC) surface. Alloys of RhM (M = Ag, Au) were considered with the following compositions: $X_{0.25}Rh_{0.75}$, $X_{0.5}Rh_{0.5}$, $X_{0.75}Rh_{0.25}$. For each composition, eight random alloy configurations were generated, and for each configuration, the H binding energy on eight FCC hollow sites was calculated to obtain the average H binding energy for each alloy composition (64 total binding sites). The H binding energy was referenced to the H_2 molecule in vacuum. A vacuum of at least 12 Å was used to separate periodic images between slabs. The Brillouin zone was sampled with a 4×4×1 Monkhorst-Pack k-point mesh and integrated using the method of Methfessel and Paxton.[234,235] All atoms in the nanoparticle were allowed to relax; geometries were considered optimized when the force on each atom was <0.005 eV/Å.

4.5.2 Catalytic Data Analysis based on Theoretical Calculations

Determination of the reaction mechanism of cyclohexene (CHE) hydrogenation is key to understanding the volcano-like activity trends seen for the RhAu and RhAg alloys. Thus, we have used density functional theory (DFT) to study the hydrogenation reaction mechanism on a series of close-packed fcc(111) transition metal surfaces. The logic for focusing on the (111) facet is that it has the lowest surface energy for the elements of interest in this study.[236,237] The following elementary steps in the hydrogenation reaction are considered:

$$
\begin{aligned}
&\mathrm{CHE(g)} + * \rightarrow \mathrm{CHE}* && \text{(R1)}\\
&\mathrm{H_2(g)} + 2* \rightarrow 2\mathrm{H}* && \text{(R2)}\\
&\mathrm{H}* + \mathrm{CHE}* \rightarrow \mathrm{HCHE}* + * && \text{(R3)}\\
&\mathrm{H}* + \mathrm{HCHE}* \rightarrow \mathrm{CHA}* + * && \text{(R4)}\\
&\mathrm{CHA}* \rightarrow \mathrm{CHA(g)} + * && \text{(R5)}
\end{aligned}
$$

where CHE, HCHE and CHA represent cyclohexene (C_6H_{10}), singly hydrogenated cyclohexene (C_6H_{11}) and cyclohexane (C_6H_{12}), respectively. The * denotes a binding site on the surface. Figure 4.38a shows the free energy profile of the above reaction on Ag, Au, Cu, Ir, Pd, Pt and Rh under standard conditions (T=298.15K, P=1bar). The barriers of each elementary step are not included, however, this level of thermodynamic analysis has been demonstrated to capture the activity trends in previous studies.[238,239] As shown in Figure 4.38a, noble metals such as Ag and Au bind CHE and hydrogen too weakly so that the adsorption steps are endothermic. Rh on the other hand, binds them too strongly so that the hydrogenation and subsequent release of CHA from the surface are unfavorable.

The catalytic performance is estimated from the free energy that needs to be overcome along the reaction path, ΔG^{up}. Linear correlations between the binding energies of CHE, HCHE, and CHA allow for ΔG^{up} to be expressed simply in terms of the binding energies of H and CHE, as shown in Figure 4.38b. As can also be seen from the free energy diagram in Figure 4.38a, Ag/Au and Rh are located on opposite sides of the ΔG^{up} volcano. This picture validates the observation of enhanced hydrogenation activity for the RhAu and RhAg alloy nanoparticles. As indicated from the white dashed line in Figure 4.38b, alloying Au and Ag to Rh weakens the binding of CHE and H, raising the free energy of S3-5 with respect to S6, and subsequently reducing ΔG^{up}. Another interesting finding from Figure 4.38b is that the binding of CHE and H are also

correlated with each other, for the fcc(111) transition metal surfaces we investigated, which allows us to use the binding energy of hydrogen as a qualitative reactivity descriptor for the hydrogenation reaction in the following discussion.

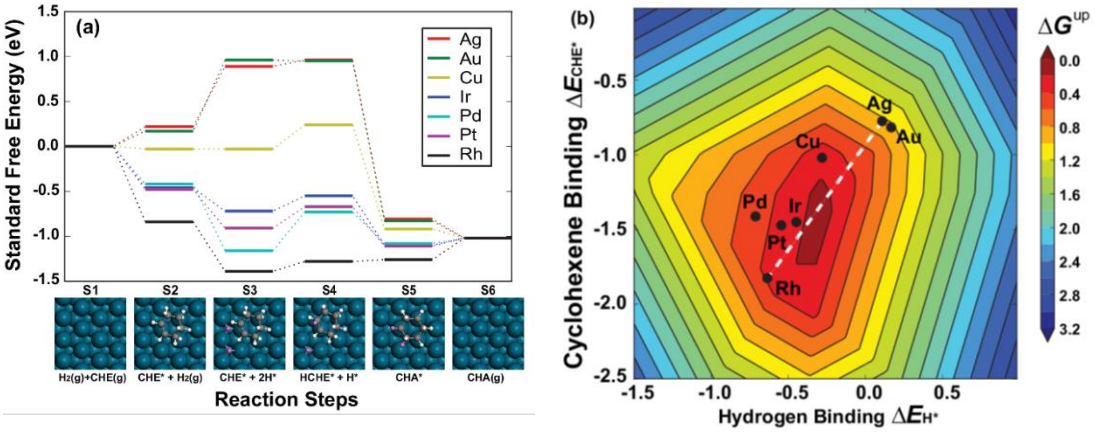

Figure 4.38. (a) Free energy profile for CHE hydrogenation with insets showing the reaction intermediates: blue spheres are metal atoms, grey are C, white are H from CHE, and pink are H from H_2. (b) Contour of ΔG^{up} as a function of the binding energy of CHE and H. A maximum activity can be achieved by alloying metals from different side of the volcano (e.g. white dashed line).

From the above thermodynamic analysis, the peak of volcano is located near ΔE_{H^*}= -0.4 eV. Considering the large difference in reactants affinity between Ag/Au and Rh, it is important to decompose the hydrogen binding at different compositions into ensembles of binding sites.[52,240,241] Figure 4.39 shows that the average binding energy of H increases with Rh composition in both RhAg and RhAu alloys. For each intermediate alloy composition, the average binding energy (Figures 4.40 and 4.41; black lines) is decomposed into individual histograms of binding sites. The target H binding ΔE_{H^*} = -0.4 eV is highlighted by the orange dashed line. Four sites can be distinguished from these data; these correspond to the four possible combinations of Ag or Au, and Rh atoms in each three-fold hollow site, where H atoms can be adsorbed (For instance: Rh_3, Rh_2Ag_1, Rh_1Ag_2, and Ag_3; Figures 4.40 and 4.41, insets). The large disparity in binding energies at these different sites indicates that they should be considered separately, rather than as part of an average. Interestingly, the H binding energy of the Rh_3 and Rh_2Ag_1 sites increases with increasing Ag content, as compared to the pure Rh particle (red and blue dashed line in Figures 4.40 and 4.41, in contrast to the solid black overall trend), indicating that H or CHE will over-bind and saturate these Rh-rich sites. The Ag_3 site binds H too weakly to adsorb reactants. The most active site, that is closest to the peak of the ΔG^{up} volcano, is the Rh_1Ag_2 site. As more Ag is alloyed to Rh, there is a higher ratio of Rh_1Ag_2 sites on the surface, until the surface is dominated by Ag_3 sites. On the other hand, we can also see that a higher Ag ratio increases the H binding of sites containing Rh, away from the target. The trade-off between these two effects results in the volcano-like hydrogenation activity trend of RhAg alloy nanoparticle. The same analysis was performed on RhAu alloys and the same trends were observed (the systems only differ in the quantitative values).

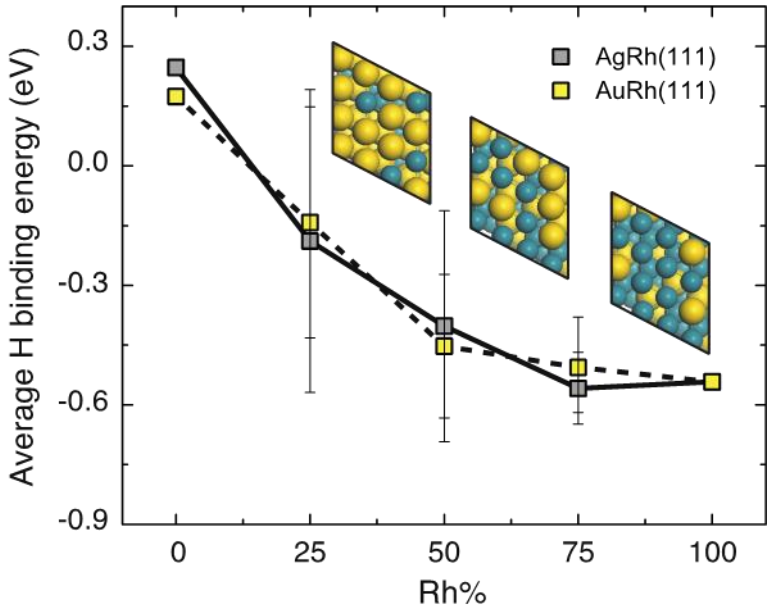

Figure 4.39. Average binding energy of H to RhAg(111) and RhAu(111) random alloy surfaces of varying composition. The overall trend is as expected, with weak binding to the Ag and Au surface and stronger binding with higher Rh content.

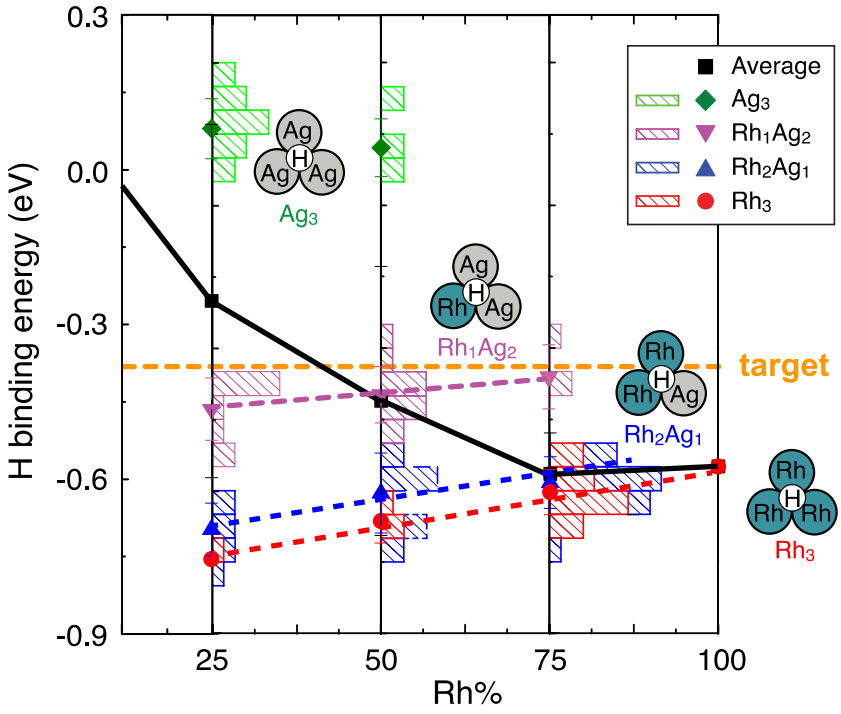

Figure 4.40. Decomposition of the average H binding energy into an ensemble of specific sites determined by the number of Ag vs. Rh atoms at the binding site. The bars indicate the frequency of different binding energies at the three intermediate compositions, and the solid symbols indicate the average binding energy per site. Trends in the activity of the most active Rh-rich sites as a function of composition (red and blue dashed lines) are different from the overall trend (black solid line).

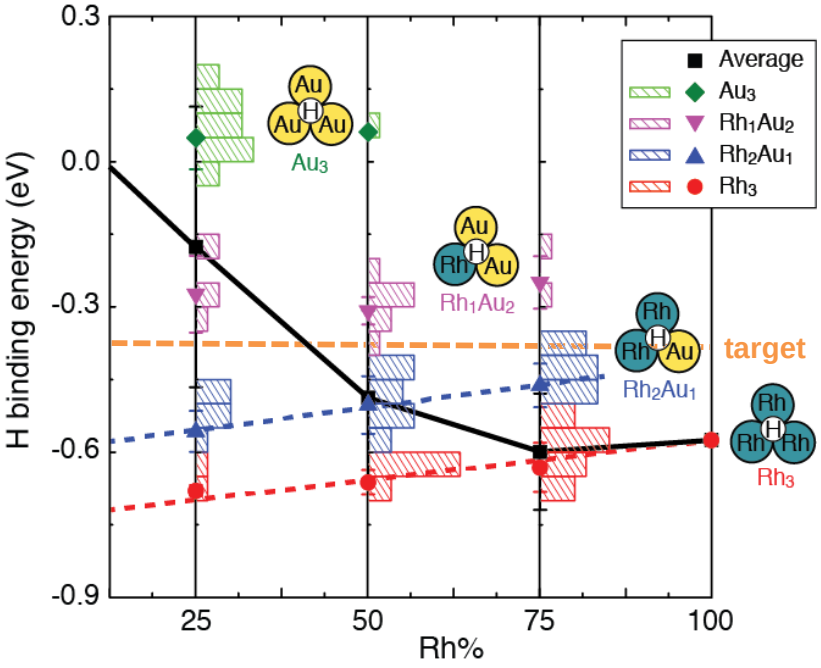

Figure 4.41. Decomposition of the average H binding energy into an ensemble of specific sites determined by the number of Au vs Rh atoms at the binding site. The bars indicate the frequency of different binding energies at the three intermediate compositions, and the solid symbols indicate the average binding energy per site. Trends in the activity of the most active Rh-rich sites as a function of composition (red and blue dashed lines) are different from the overall trend (black solid line).

4.6 CONCLUSION

A novel microwave-assisted solution-phase method allowed for the simple and programmable preparation of unconventional NPs of RhAg and RhAu with randomly – alloyed structures. The composition of the RhM NPs can be systematically varied to optimize their catalytic properties. The combined experimental and theoretical study presented clearly shows that RhAg NPs in particular have great potential in

heterogeneous catalysis. Particular ensembles at the bimetallic NP surfaces result in highly active substrate binding sites, which are generated by dilution of Rh with Ag or Au.

5. Monometallic core – Alloy shell NPs

5.1 INTRODUCTION

Microwave heating (μwH) is able to facilitate synthesis of unconventional RhAg and RhAu nanoparticles (NPs) with randomly alloyed structures, that cannot be otherwise accessed using conventional synthesis methods (as described in Chapter 4). These NPs displayed remarkable enhanced catalytic activities, as compared to pure Rh NPs. Furthermore, the Rh_xM_{100-x} (M = Ag or Au) composition was systematically varied in order to optimize the catalytic properties. Theoretical calculations (DFT) were performed on both RhAg and RhAu systems, using binding affinities for both H and the substrate as reaction descriptors; it was established that the enhancement in hydrogenation catalytic activity observed experimentally was caused by ensemble effects and lattice constant mismatching between the metals involved. Due to the large differences in the Fermi levels of Rh and of Ag or Au, charge transfer occurred (from Rh to M) which ultimately resulted in stronger adsorbate binding to Rh-rich sites on the M rich surfaces. Additionally, the strain caused by the lattice mismatch also increased the adsorbate binding of H to the active Rh-rich sites. Thus, cost-effective and extremely active nanocatalysts were generated by diluting Rh with inexpensive and abundant metals.

Increased attention has been given to the synthesis of multimetallic NPs due to the advantages they provide, such as high selectivity, activity, and chemical/physical stability in comparison to their monometallic components.[248–251] However, the controlled synthesis of NPs consisting of multiple noble metal components (3 or more) has remained relatively unexplored. There has been a few reports on the preparation of trimetallic NPs with well-defined morphologies that include the synthesis of Pd–Au–Ag

nanoboxes from Ag nanocubes by sequential or simultaneous galvanic exchange and Kirkendall growth.[252] Another example is the preparation of spherical Au on Pd on Pt triple-layered core-shell NPs, which displayed higher catalytic activity than bimetallic core-shell NPs.[253,254] Finally, Choi and co-workers reported the production of Pd–Pt–Ag ternary alloy nanotubes.[255]

There has also been several reported examples of noble metal thin shells (1-2 monolayers), such as Pt, being deposited on alloy cores in order to generate stable NPs that show higher catalytic activities even though they have less Pt loading than commercial alternatives.[256–258] Furthermore, it has been observed that alloyed core-monometallic shell NPs combine both the robustness of core-shell assemblies and the tunability of random alloy NPs,[259] since the near-surface alloys can be used to tune the activity of the catalytic surface.[217] The presence of certain metals in the alloyed core can also enhance the stability of the particles under specific catalytic conditions.[260,261]

Given that the enhancement of catalytic activity observed in alloys arises from ensembles at the surface of the NPs, it is only logical to further increase the cost-effectiveness of this type of catalysts by depositing thin shells of the alloys on monometallic cores (reversed architecture from the system described above). The construction of core-shell NPs that display very thin shells (1-4 monolayers) of the most expensive and rarest noble metals supported around cores consisting of less expensive, more abundant elements is emerging as an important synthetic strategy.[195–197] The disparity in lattice constant between the alloy shell and the monometallic core can lead to further strain effects at the interface, which can ultimately make the surface even more reactive. Moreover, the catalytic activity of the alloyed shell can be tuned by varying the composition. The core can also impart some control over the catalytic properties because

it can also affect the binding affinity of the shell for certain adsorbates, depending on the type of metal and morphology, which arises due to charge transfer at the interface.[262]

It is reasonable to suppose that a system comprised of a monometallic core and an alloyed shell could display enhanced chemical stability, tunable and enhanced catalytic activity, and increased cost-effectiveness. Nonetheless, it is extremely difficult to design and synthesize multimetallic NPs with well-defined morphologies due to the challenges in controlling the nucleation and growth kinetics of NPs in the presence of multiple metal precursors with different reduction potentials[262], especially when the metals are immiscible in the bulk. It is also very important to take into account mutual metal interactions and possible complexation of the metal ions with the surfactant(s) and reductant molecules in order to understand the formation mechanism of this type of nanoassemblies.

This chapter reports preliminary results on the synthesis of monometallic core-alloyed shell NPs. Although the metal combinations employed do not display the most cost-effective compositions, they serve as proof of concept that lattice matching is a key factor in the preparation of this type of NPs. Table 5.1 displays the synthetic strategy employed; the metal combinations and the target alloy compositions were paired as a function of lattice matching.

Table 5.1. Metal combinations used for the synthesis of monometallic core-alloy shell NPs, based on lattice parameters.

	Pt	1:1 Rh:Ag	Pd	2:1 Rh:Ag	Ag	1:3 Pd:Au
Lattice Constant (Å)	3.92	3.94	3.89	3.90	4.09	4.03

5.2 SYNTHESIS

5.2.1 Materials

Rhodium trichloride hydrate ($RhCl_3 \cdot xH_2O$, 98%; Johnson Matthey), hydrogen tetrachloroaurate ($HAuCl_4 \cdot 3H_2O$, 98%; Sigma Aldrich), silver nitrate ($AgNO_3$, 99%; Mallinckrodt Chemicals), potassium tetrachloropalladate ($K_2[PdCl_4]$, 99%; Strem Chemicals), potassium tetrachloroplatinate ($K_2[PtCl_4]$, 99.9%, Alfa Aesar), poly(vinylpyrrolidone) (PVP, $<M_w>$ = 55,000; Sigma Aldrich), ethylene glycol ($\{CH_2OH\}_2$, 99.8%; Fisher Scientific), NH_4OH (29.14% assay, Fisher Scientific) were used as received. All other reagents and solvents (analytical grade) were employed without further purification unless stated otherwise.

5.2.2 Synthesis Methods

A MARS 5 (CEM Corp.) microwave system with a maximum power of 1600 W (2.45 GHz) was used to perform all the NP synthesis reactions. The reaction temperature inside the microwave cavity was finely controlled by power modulation *via* a RTP-300+

fiber optic temperature, located in a beaker of solvent identical to that employed in the reaction. *Note: Insertion of the temperature probe directly into the reaction vessel should be avoided; build-up of solid NPs product on the probe sheath during the course of the reaction may lead to sparking and ignition.* A 50 mL round-bottom flask with a fitted water-cooled reflux condenser was placed in the center of the microwave chamber. Both solvent and reactants were magnetically stirred (medium speed setting) and the metal precursors were then added into the solvent using a disposable, fine-bore Teflon tube right above the solution, ensuring that the addition rate was constant. The rate of the precursors addition was controlled using an Aladdin Programmable Syringe Pump (WPI, Inc.) that was directly attached to the Teflon tubing. The reactions were carried-out at ambient pressure in air, with venting at the top of the reflux condenser *via* a three-way stopcock. Prior to each new reaction, glassware was thoroughly cleaned in a two-stage acid-base wash (12.0 M HCl aq., 1−2 d; 5 M NaOH in *i*-PrOH/H2O, 1−2 d), followed by oven drying at 110 °C.

5.2.3 Synthesis of Pt cores

A solution of *poly*(vinylpyrrolidone) (PVP) (422.0 mg, 3.8 mmol) was prepared in ethylene glycol (15.0 mL). This solution was then heated to 150 °C using μwH. A solution of the metal precursor was generated by dissolving $K_2[PtCl_4]$ (78.0 mg, 0.19 mmol) in the same polyol solvent (5.0 mL). After the target temperature was achieved, half of the metal precursor solution was injected into the reaction vessel at 11.40 mmol h^{-1} *via* PTFE tubing, yielding a dark brown solution. Following the metal precursor addition, the reaction underwent a 30 min seed ripening period at the same temperature. After this stage, the remaining Pt^{2+} solution (2.5 mL) was added at 0.76 mmol h^{-1} in

order to promote growth over the existing Pt seeds. After the second addition was completed, the mixture continued stirring at 150 °C for an additional 30 min, followed by immediate quenching in an ice bath. The PtNPs were precipitated with acetone (*ca.* 50.0 mL) followed by isolation using ultracentrifugation (5 krpm, 5 min). The solid NPs then underwent three cycles of redispersion in 10 mL ethanol, precipitation with 70 mL hexanes and isolation by ultracentrifugation, in order to remove any impurities or by-products.

5.2.4 Synthesis of Pt-RhAg core-shell NPs

A suspension of Pt seeds was prepared directly in the reaction vessel by dissolving 5 mg of dried Pt NPs and PVP (240.0 mg, 2.16 mmol) in ethylene glycol (20.0 mL). This mixture was then brought to 120 °C using μwH along with stirring. Two separate solutions of $RhCl_3 \cdot xH_2O$ (4.0 mg, 0.019 mmol) and of $AgNO_3$ (9.0 mg, 0.53 mmol) were each prepared in ethylene glycol (5.0 mL) and loaded to fresh 10.0 mL disposable syringes. After the desired temperature was reached, the Rh and Ag metal precursor solutions were added simultaneously utilizing a dual barrel syringe pump at a rate of 0.019 mmol h^{-1} and 0.53 mmol h^{-1}, respectively, in order to only promote growth on the existing Pt seeds. After the addition period, the reaction continued stirring at 120 °C for an additional 30 min, followed by quenching in an ice bath. The trimetallic particles were precipitated with acetone (240 mL) and isolated by ultracentrifugation (5.5 krpm, 5 min). The solid NPs were then redispersed in 20 mL distilled water and treated with concentrated NH_4OH (0.4 mL) to remove any AgCl that may have formed during the synthetic process. The particles were once again precipitated using acetone (60 mL) and isolated by ultracentrifugation (5.5 krpm, 5 min).

5.2.5 Synthesis of Pd cores

The preparation of Pd seeds followed a similar experimental procedure as the one described in Chapter 2. A solution of PVP (150.0 mg, 1.35 mmol) was prepared in ethylene glycol (20.0 mL) and heated to 150 °C utilizing μwH as the heating source. A separate solution of $K_2[PdCl_4]$ was generated by the dissolution of the aforementioned metal precursor (21.0 mg, 0.064 mmol) in ethylene glycol (5.0 mL). After the PVP solution had reached the desired temperature, half of the Pd^{2+} solution was added at a rate of 3.84 mmol h^{-1} yielding a dark brown mixture. The reaction continued stirring at 150 °C for an additional 30 min. After this period, the remaining metal precursor solution (2.5 mL) was added at 0.256 mmol h^{-1} to solely promote growth on the existing seeds. Once all the Pd^{2+} precursor had been added, a second ripening period of 30 min occurred. The monodisperse PdNPs were precipitated with acetone (65 mL) and ultracentrifugation (5 krpm, 5 min). The particles were further purified by redispersion in ethanol (10 mL) followed by treatment with hexanes (60 mL). The particles were isolated by ultracentrifugation (5 krpm, 5 min).

5.2.6 Attempt of synthesis of Pd-RhAg core-shell NPs

A suspension of Pd seeds was prepared in ethylene glycol (20.0 mL) along with PVP (200.0 mg, 1.8 mmol) and was brought to 150 °C while being exposed to μwH. Two separate Rh^{3+} and Ag^{+} solutions were made in ethylene glycol (5.0 mL) using $RhCl_3 \cdot H_2O$ (5.0 mg, 0.024 mmol) and $AgNO_3$ (5.0 mg, 0.029 mmol) as precursors. These solutions were injected at rates of 0.024 and 0.029 mmol h^{-1}, respectively, to the Pd/PVP mixture in order to avoid any competing Rh or Ag nucleation. After the metal precursors were added, the reaction continued stirring at the same temperature for an additional 30 min,

followed by quenching in an ice bath. The particles were purified as explained earlier for the Pt-RhAg core-shell NPs.

5.2.7 Synthesis of Ag cores

A solution of *poly*(vinylpyrrolidone) (360 mg, 3.24 mmol) in ethylene glycol (20.0 mL) was prepared directly in the reaction vessel and the temperature was increased to 150 °C using μwH along with stirring. After the target temperature was achieved, a dilute HCl solution in ethylene glycol (25.0 μM, 2.25 mL) was quickly added to the hot PVP mixture. A second solution of $AgNO_3$ (45 mg, 0.26 mmol) was prepared in the same solvent (5.0 mL) and loaded into a fresh 10 mL disposable syringe. The precursor solution was injected into the PVP/HCl solution, 5 min after the acid addition, at a rate of 5.2 mmol h^{-1} (100 mL h^{-1}). The colorless solution turned light yellow as the metal precursor was added. The mixture continued stirring at 150 °C for an additional 30 min after the Ag^+ precursor was added. The reaction was then cooled rapidly by transferring the reaction vessel to an ice-water bath. The Ag seeds were precipitated by adding acetone (*ca.* 105 mL) to give a light yellow suspension, which was briefly sonicated (1 min). The precipitate was then isolated by ultracentrifugation (5.5 krpm, 5 min) and the colorless supernatant was decanted away to leave a yellow orange solid. This was further purified to remove excess PVP and ethylene glycol by two cycles of dissolution in ethanol (10 mL) followed by precipitation with hexane (60 mL) and isolation by centrifugation (2.5 krpm, 3 min).

5.2.8 Attempt of synthesis of Ag-PdAu core-shell NPs

A suspension of Ag seeds was prepared by redispersing the particles (see section 5.2.7) and PVP (100.0 mg, 0.9 mmol) in ethylene glycol (20.0 mL) yielding a very pale yellow mixture. The mixture was then heated to 150 °C by exposing the reaction vessel to μwH. In the meantime, two separate Pd^{2+} and Au^{3+} solutions were prepared in the same solvent (5.0 mL each) using $K_2[PdCl_4]$ (4.0 mg, 0.0122 mmol) and $HAuCl_4 \cdot xH_2O$ (11.0 mg, 0.0324 mmol) as precursors. The Pd and Au solutions were then added simultaneously using a dual barrel syringe pump at 0.244 mmol hr^{-1} and 0.648 mmol hr^{-1}, respectively. The pale yellow mixture became dark brown with the metal precursor addition. After this addition period, the reaction continued stirring at the same temperature for an additional 30 min, followed by quenching in an ice bath. The particles were then precipitated using acetone (105 mL) and collected using ultracentrifugation (5 min, 5.5 krpm). This was followed by redispersion in ethanol (10 mL) and treatment with hexanes (60 mL) in order to remove any impurities or unreacted species. The NPs were finally isolated using ultracentrifugation (5 min, 5.5 krpm).

5.3 RESULTS AND DISCUSSION

5.3.1 Characterization Methods

Transmission Electron Microscopy (TEM) images were obtained from a FEI Tecnai microscope operating at 80 kV. The samples were prepared by drop-casting a single aliquot of MNPs dispersed in ethanol onto 200–mesh carbon coated copper formvar grids (Ted Pella Inc.) and allowing for subsequent evaporation in air.

Nanoparticle sizes and standard deviations were derived by measuring a minimum of 200 individual particles per experiment, and by averaging multiple images from samples obtained from at least two separate syntheses. Individual particles were measured using Image-J (http://rsbweb.nih.gov/ij), which finds the area of each nanoparticle by pixel counting. Powder X-ray diffraction (PXRD) patterns were recorded with a Rigaku R-Axis Spider diffractometer with an image plate detector using a graphite monochromator and CuK_α radiation (λ = 1.5418Å) operated at 40 kV and 40 mA; spectra were collected using a scan speed of 3° min^{-1} with a step width of 0.020 (2θ). The instrument was controlled using Rapid/XRD diffractometer control software. The integration of the two dimensional data into a one dimensional pattern was accomplished using 2DP. UV-vis data were collected using a Carry 6000i UV-vis NIR spectrometer equipped with a double beam and a wavelength range of 175−3300 nm. X-ray photoelectron spectroscopy (XPS) was performed using a Kratos Axis Ultra Photoelectron Spectrometer. Samples for XPS analysis were prepared by drop-casting ethanol solutions of the particles on silica wafers allowing evaporation of the solvent in air. The XPS spectra were recorded utilizing a monochromated Al-K_α x-ray source ($h\gamma$=1486.5 eV), hybrid optics (employing a magnetic and electrostatic lens simultaneously) and a multi-channel plate coupled to a hemispherical photoelectron kinetic analyzer. All spectra were recorded using four sweeps for signal averaging, a dwell time of 1800 msec, an aperture slot of 300 x 700 μm, a pass energy of 20 eV and 0.1 eV per step. To minimize sample charging and band shape distortion due to charging, the XPS spectra were recorded using the Kratos charge neutralizer (20 eV electrons) while the sample stage was left floating (*i.e.* not connected to ground (earth)). The effectiveness of the neutralizer under these conditions notably improved the resolution of the spectra for the elements of interest. Casa XPS analysis software was used for peak deconvolution and the stoichiometry of samples was

determined from corrected peak areas and employing Kratos sensitivity factors for each element in question.

5.3.2 Pt-RhAg core-shell NPs

The deposition of RhAg alloyed shells on Pt cores was achieved by the simultaneous addition of Rh^{3+} and Ag^{+} metal precursors to a mixture of Pt seeds and PVP capping agent in ethylene glycol at 150 °C. Pt and a 1:1 Rh:Ag random alloy have very similar lattice constants of 3.92 and 3.94 Å, respectively. For this reason, this trimetallic mixture was chosen in an attempt to demonstrate the importance of lattice matching in the construction of monometallic core-alloyed shell species.

The initial Pt seeds were monodisperse cubeoctahedra displaying an average size of 4.12 ± 0.56 nm (Figure 5.1a). After the RhAg deposition, the NPs enlarged to 5.54 ± 0.91 nm (Figure 5.1b). The 1.42 nm increase in average NP size corresponds to the deposition of 2.5 RhAg monolayers, based on an interatomic distance of 0.279 nm in a 1:1 Rh:Ag random alloyed surface. Due to the formation of AgCl by-product during the synthetic process, the RhAg on Pt particles were treated with concentrated NH_4OH. During this purification scheme, some of the stabilizing polymer was digested, hindering the ability of the NPs to homogeneously disperse. However, the particles remained discrete and no agglomeration occurred, as shown in Figure 5.1b.

As expected, the (111) reflection of these NPs (PXRD; Figure 5.2), appears at 39.7° which corresponds to the reflections for both monometallic Pt and a 1:1 Rh:Ag random alloy. The diffraction peaks observed were broad, so a shift in the diffraction lines caused by the 0.02 Å difference in the lattice constants would not be evident. The broadness of the peaks is also consistent with the formation of small NPs (<10 nm). The

bulk of the material was also probed using UV vis spectroscopy which showed that as RhAg was deposited on the Pt cores, the surface plasmon resonance (SPR) *ca.* 260 nm, which corresponds to Pt, was completely damped (Figure 5.3). Moreover, the absorption spectrum for RhAg on Pt was very similar to that recorded for 1:1 Rh:Ag alloyed NPs (Figure 5.3, dashed black), as reported in Chapter 4.

The surface of these NPs was also studied using XPS as a pseudo-surface technique, given that the particles are stabilized by a thick capping polymer that limits the escape pathway of the photoelectrons generated during the analysis. Signals for all three metals were detected (Figure 5.4), confirming the presence of Rh, Ag and Pt in the system. The signals for Rh 3d indicated the occurrence of both Rh(0) and Rh(I), at 306.7 and 308.1 eV, respectively (Figure 5.4a). Furthermore, Ag signals were detected at 367.3 and 368.3, which can be assigned to Ag(I) and Ag(0) species (Figure 5.4b). Finally, Pt showed signals that correspond to Pt(0) and Pt(II), at 70.6 and 71.5 eV, respectively (Figure 5.4c). The % molar concentrations of the metals was found to be 21:24:55 Rh:Ag:Pt. These values further confirmed that the composition of the alloyed shell was indeed 1:1 (Rh:Ag) and that the alloyed shell deposited on the Pt cores was thin, as determined by the larger amount of Pt detected.

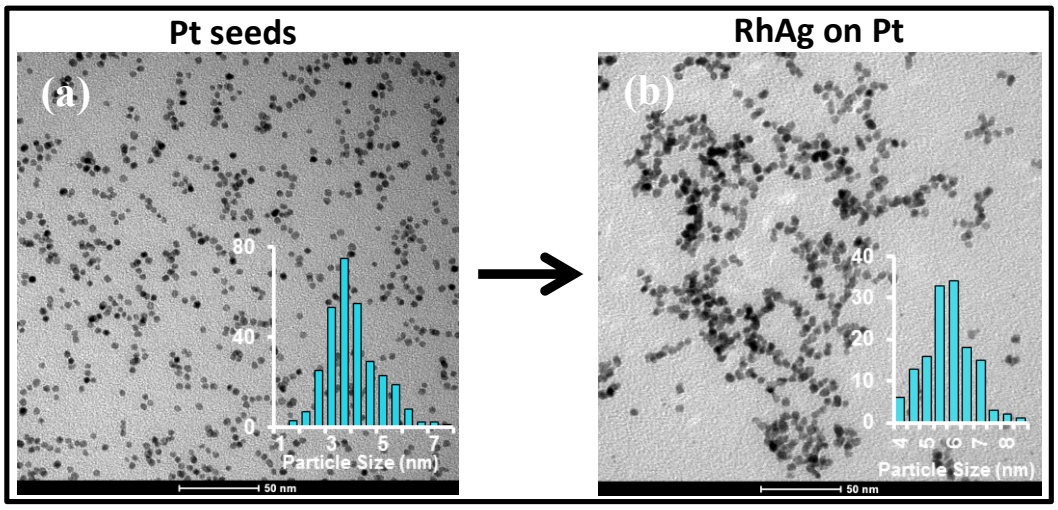

Figure 5.1. TEM images and histograms (insets) of (a) Pt cores with an average size of 4.12 ± 0.56 nm and (b) NPs generated after RhAg deposition on the Pt seeds.

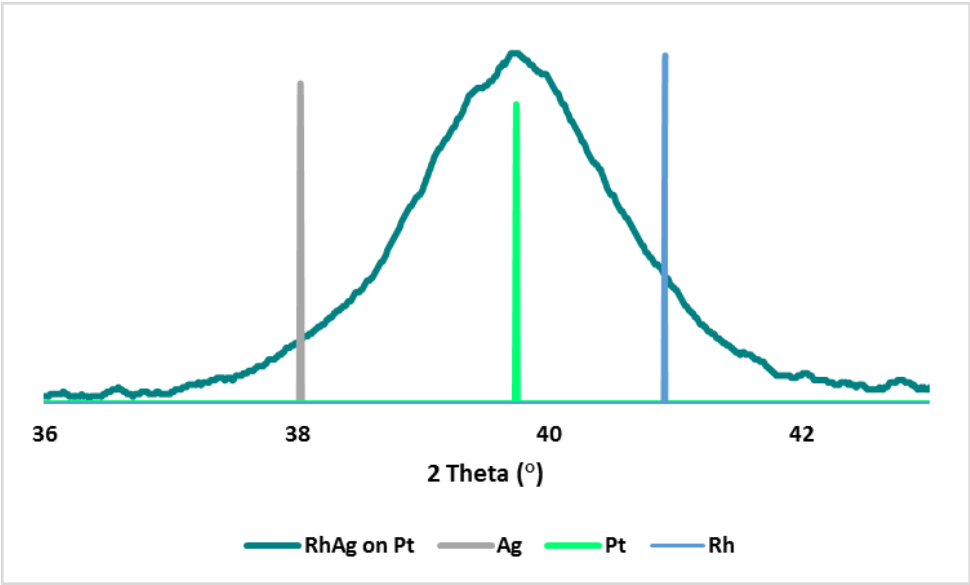

Figure 5.2. PXRD (111) reflection for RhAg on Pt NPs (teal), and reference lines for Ag (gray), Pt (aqua) and Rh (blue).

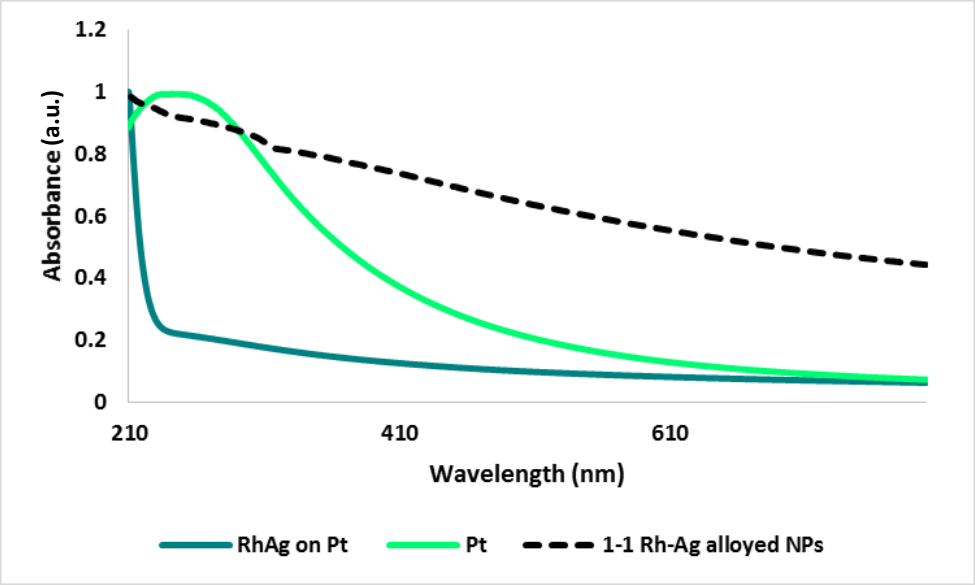

Figure 5.3. Overlayed UV-vis spectra for RhAg on Pt NPs (teal), PVP-capped Pt NPs (aqua) and 1-1 Rh-Ag alloyed NPs (dashed black).

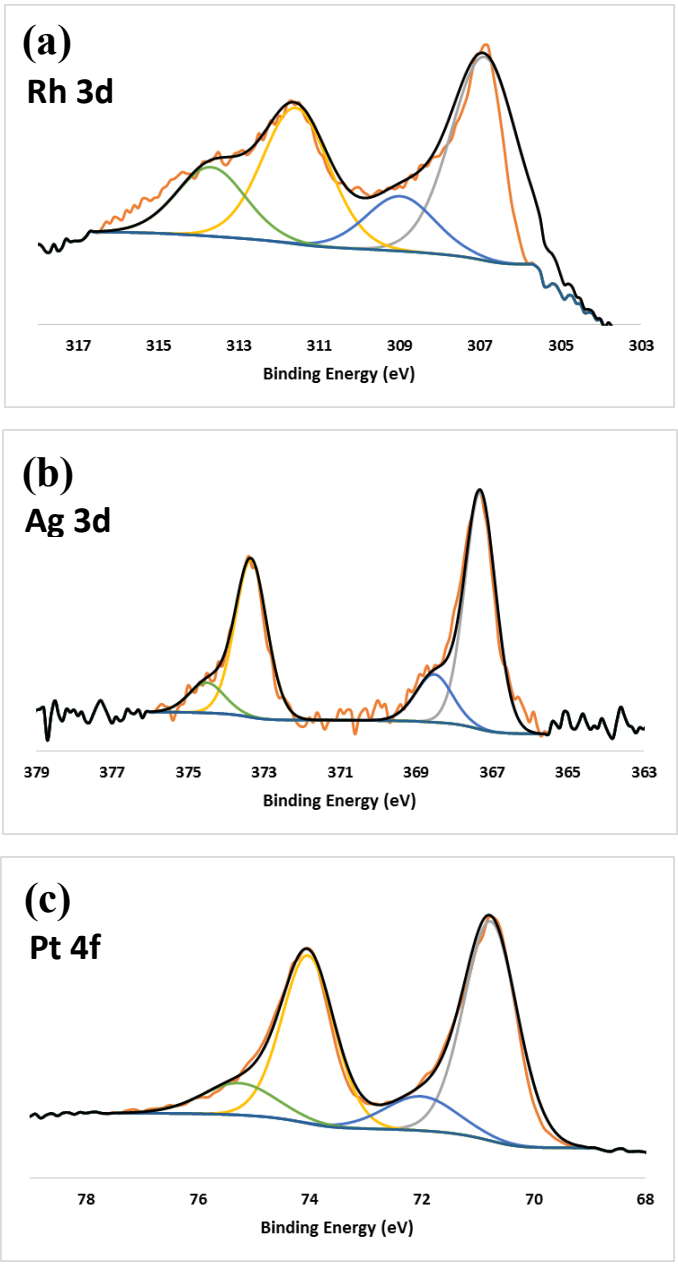

Figure 5.4. Fitted XPS data for RhAg on Pt NPs; (a) Rh 3d signals corresponding to metallic Rh (306.9 eV) and Rh(I) (309.0 eV); (b) Ag 3d signals indicating the presence of Ag(0) (368.5 eV) and Ag(I) (367.3 eV); (c) Pt 4f signals assigned to Pt(0) (70.7 eV) and Pt(II) (72.0 eV).

5.3.3 Rh/Pd/Ag trimetallic NPs

Following a similar experimental procedure to that previously described for the deposition of RhAg on Pt cores, a 2-1 Rh-Ag random alloy was attempted to be overgrown on Pd monodisperse seeds. The initial Pd cores had an average diameter of 4.84 ± 0.96 nm (Figure 5.5a). After the RhAg shell deposition, the particles increased in size to 6.54 ± 1.2 nm (Figure 5.5b) which would correspond to a shell thickness of 3.08 monolayers (based on an average interatomic distance of 0.276 nm in a randomly alloyed 2-1 Rh-Ag surface), assuming that the composition of the alloy deposited was comparable to that of the target ratio. Similar to the RhAg on Pt NPs, some of the capping polymer was digested during the purification treatment with NH_4OH. However, in this case it seemed that particles were not as stable and a higher degree of agglomeration, into nanoflower types, was observed (Figure 5.5b).

The bulk of the material was examined using PXRD. Two sets of (111) reflections were observed (Figure 5.6). The smallest diffraction peak corresponds to monometallic Ag. Nonetheless, the second diffraction peak appears at 39.6° which does not correlate to either monometallic Pd or a random 2-1 Rh-Ag alloy. The (111) reflections for FCC Pd and Rh are observed at 40.2° and 41.1°, respectively. A very weak and broad shoulder was present at the tail end of the dominant (111) diffraction peak, most like due to metallic Rh. Thus, it is suspected that the diffraction pattern may be generated by a NP structure constituted of a PdAg alloyed core with a very thin Rh shell that broadens the features in the PXRD spectrum (the synthetic method must also generate highly crystalline monometallic Ag NPs, given the metallic Ag reflection observed; however, there is no indication that these NPs dominate the system). The absorption spectra of this material (Figure 5.7) shows that the incorporation of Rh and Ag into the Pd NP-containing system, leads to damping of the Pd surface plasmon resonance at 224 nm.

Although the absorption profile of the NPs is very similar to that of the target random alloyed 2:1 Rh:Ag NPs (studied in Chapter 4), the NPs also display a very weak resonance at 260 nm which is best explained by an assembly comprised of a very thin Rh layer on a PdAg alloyed core. The weak Rh absorption band can be attributed to the monometallic shell being very thin; Pd also has a tendency to suppress the surface plasma absorption of other noble metals within the same system.[190,248,263–265] Additionally, despite the PXRD pattern showing reflections for the presence of monometallic Ag, no SPR for Ag(0) was observed in the UV-vis spectrum, most likely due to a very low concentration of this type of NPs.

The surface of the NPs was probed employing XPS and signals for Rh, Ag and Pd were detected in a 61:24:15 molar ratio (Figure 5.8). Rh(0) and Rh(I) peaks appeared in a 1:1.27 ratio at 307.0 and 308.1 eV, respectively (Figure 5.8a). Only metallic signals for Pd and Ag were acquired (Figure 5.8b & 5.8c), which suggest that these metals are mainly located in the core and are then stabilized towards oxidation. These experimental observations and assumptions are consistent with a configuration in which a thin Rh shell was overgrown on a PdAg alloyed core.

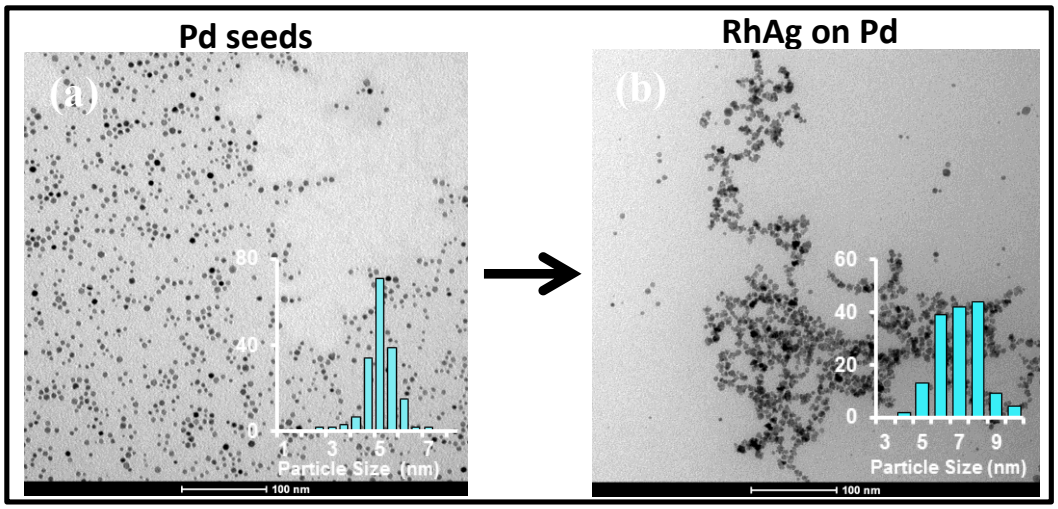

Figure 5.5. TEM images and histograms (insets) of (a) 4.8 nm Pd cores (b) NPs generated after RhAg deposition on the Pd seeds.

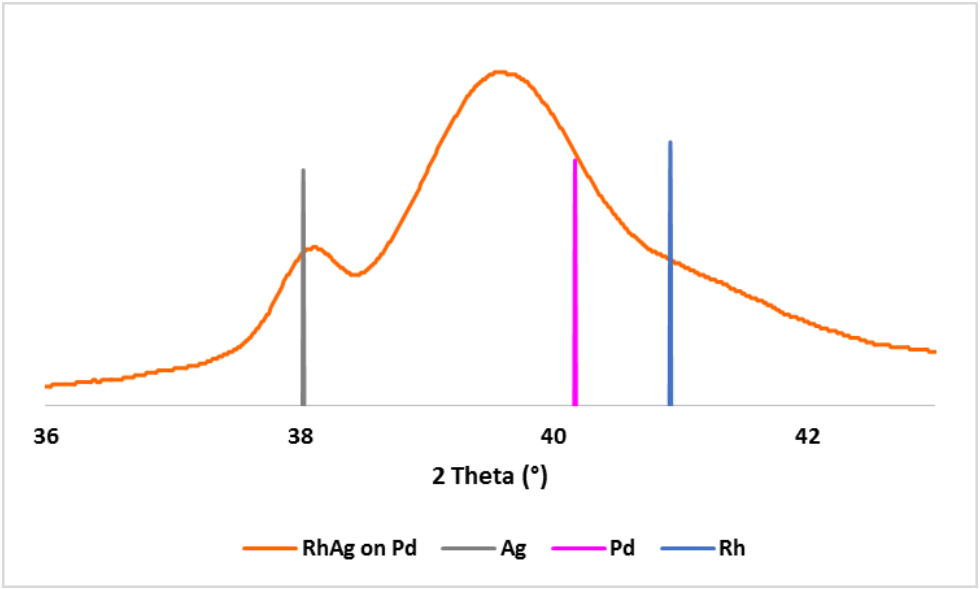

Figure 5.6. PXRD (111) reflection for RhAg on Pd NPs (orange), and reference lines for Ag (gray), Pd (purple) and Rh (blue).

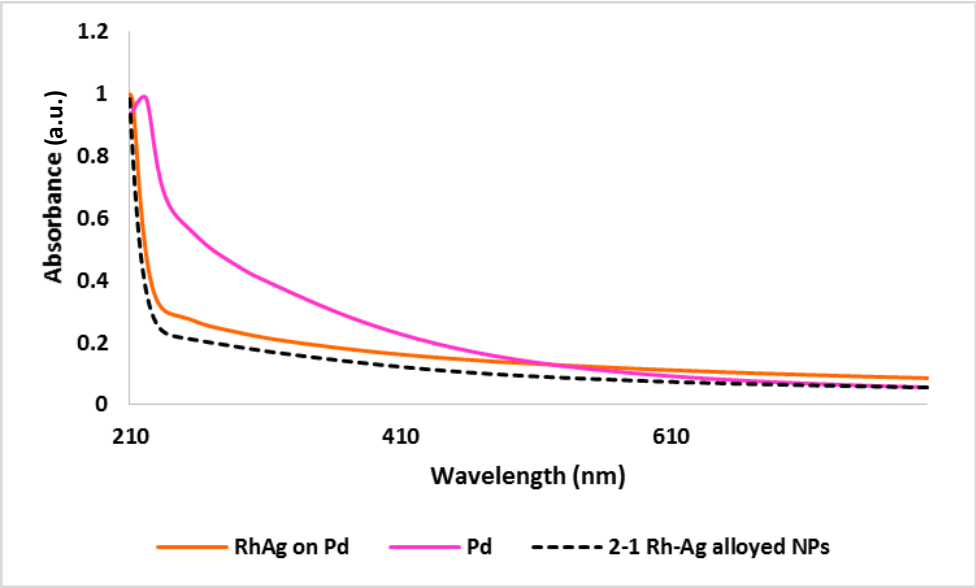

Figure 5.7. Overlayed UV-vis spectra for RhAg on Pd NPs (orange), PVP-capped Pd NPs (purple) and 2-1 Rh-Ag alloyed NPs (dashed black).

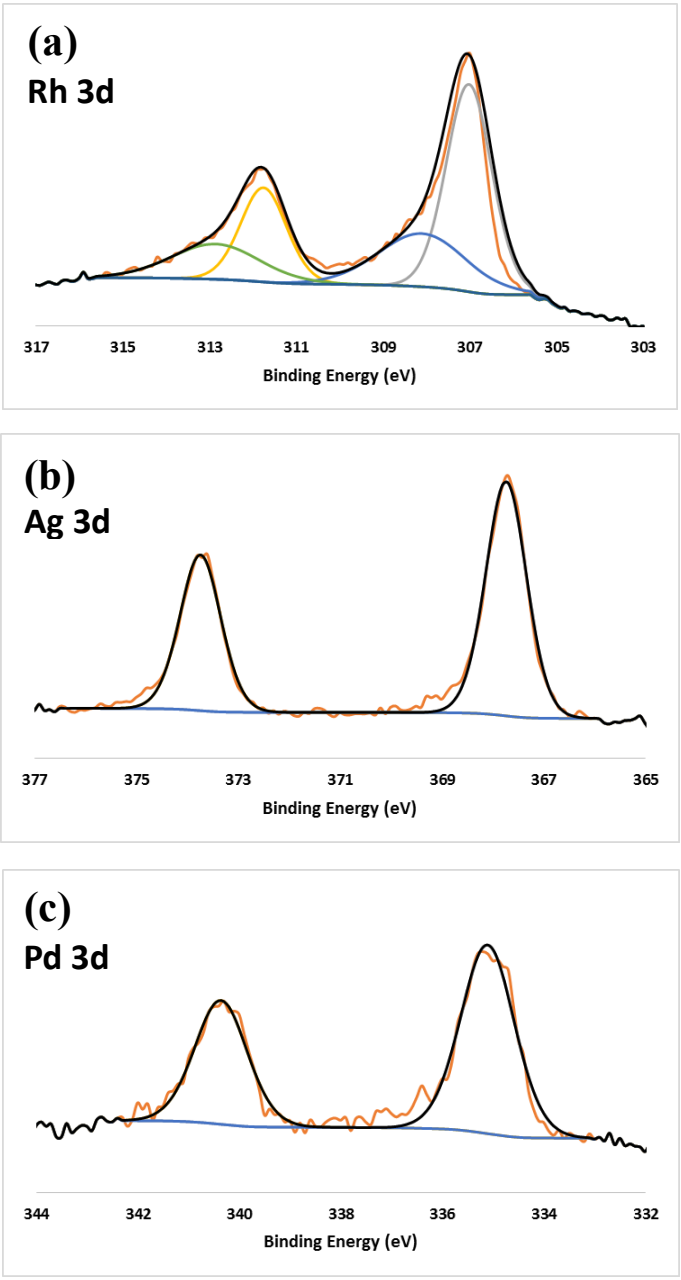

Figure 5.8. Fitted XPS data for RhAg on Pd NPs; (a) Rh 3d signals corresponding to metallic Rh (307.0 eV) and Rh(I) (308.1 eV); (b) Ag 3d signal indicating the presence of Ag(I) (367.7 eV); (c) Pd 3d signals assigned to Pd(0) (335.1 eV).

5.3.4 Pd/Ag/Au trimetallic NPs

Given that Ag has a lattice constant of 4.09 Å, the PdAu alloy that would most closely match this value would have an ideal composition of 25% Pd and 75% Au. The deposition of a PdAu alloyed shell on Ag cores was attempted utilizing Ag seeds that were 6.83 ± 1.71 nm in diameter (Figure 5.9a). The deposition stage was carried out at 150 °C using μwH and $K_2[PdCl_4]$ and $AgNO_3$ as metal precursors in a 1:3 ratio. The NPs generated after this step had enlarged to 10.94 ± 1.86 nm (Figure 5.9b), which would correspond to the overgrowth of a PdAu shell comprised of 7.21 monolayers (based on an interatomic distance of 0.285 nm in a 1:3 Pd:Au randomly alloyed surface) if the specie deposited on the Ag cores was indeed a 1:3 Pd:Au alloy. However, when the bulk of the material was analyzed using XRD, a single set of diffraction bands were observed, with the (111) reflection being the most intense and appearing at 38.8° (Figure 5.10). The position of this peak does not correlate to either metallic Ag, nor to a 1:3 Pd:Au alloy, which indicates that the target assembly was not achieved, but rather a trimetallic random alloy was acquired. This hypothesis was further supported by UV-vis spectroscopy (Figure 5.11). The NPs did not display any significant absorption bands that could be assigned to monometallic species (Ag = 410 nm; Au = 540 nm; Pd: 224 nm). In fact, the absorption spectrum recorded fits the profile of a Pd-rich trimetallic alloy, due to the fact that Pd tends to damp the surface plasmon of other noble metals, when closely interacting with these (see Section 5.3.3).[190,248,263–265]

XPS confirmed that all three metals were incorporated in the system in a 71:13:16 Pd:Au:Ag ratio (Figure 5.12). This observation supports the claim that the species formed was a Pd-rich trimetallic alloy. Signals for both Au(0) and Ag(0) were detected at 83.9 and 367.8 eV, respectively (Figure 5.12a & 5.12b). Au also displayed a weak component at 84.8 eV which corresponds to Au(I) (2:1 Au(0):Au(I)) (Figure 5.12a). Furthermore,

Pd(0) and Pd(II) appeared in a 1:1 ratio at 335.1 and 336.0 eV, respectively (Figure 5.12c). The shift in binding energy values for all three metals (compared to tabulated XPS values; Table 5.2) can be explained by the electronic interactions between the elements involved in the alloy. Since Pd, Ag and Au all have different Fermi levels, charge transfer (*d*-band mixing) occurs in order to maintain a constant Fermi level throughout the alloyed NP, which ultimately shifts the *d*-band center and the binding energies for valence electrons (See Chapter 4).

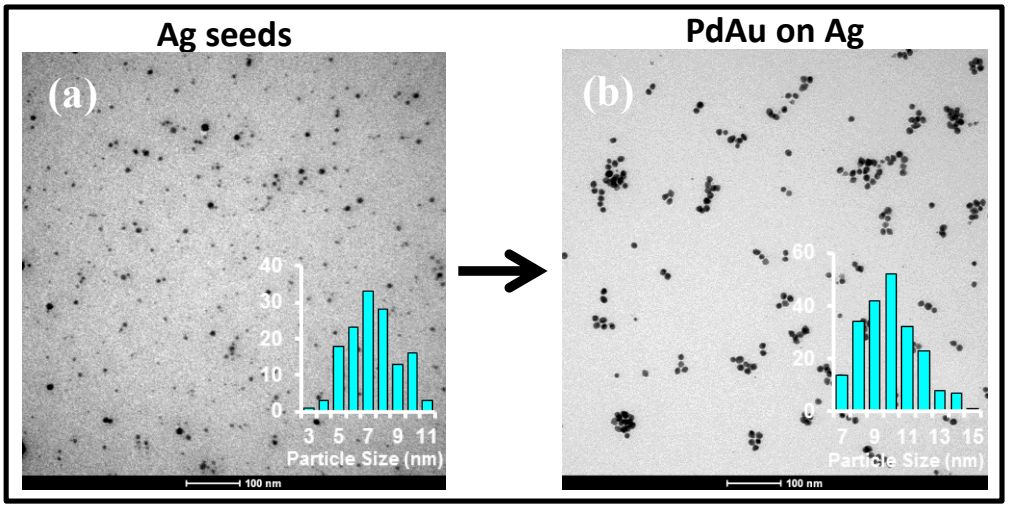

Figure 5.9. TEM images and histograms (insets) of (a) 6.8 nm Ag seeds (b) NPs generated after PdAu deposition on the Ag seeds.

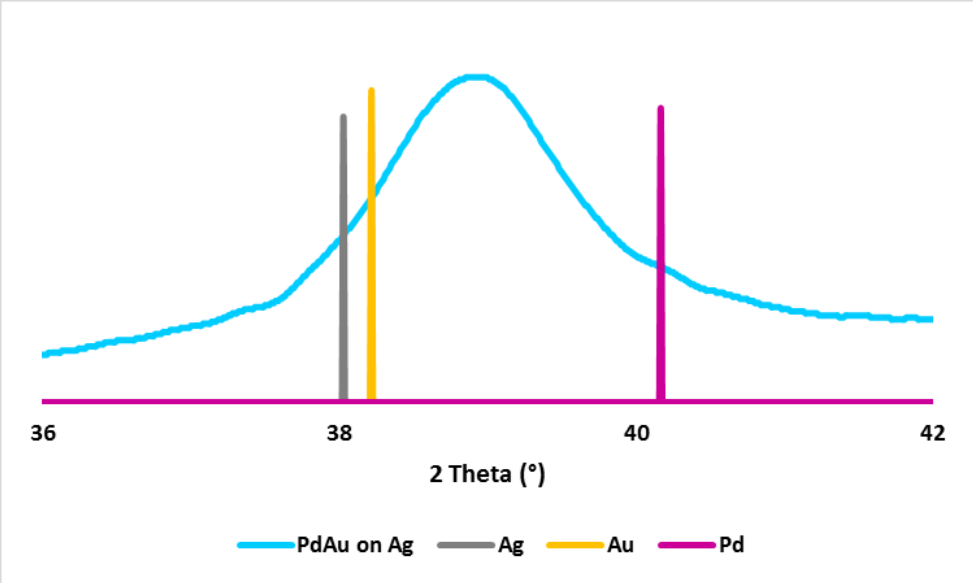

Figure 5.10. PXRD (111) reflection for PdAu on Ag NPs (blue), and reference lines for Ag (gray), Au (yellow) and Pd (purple).

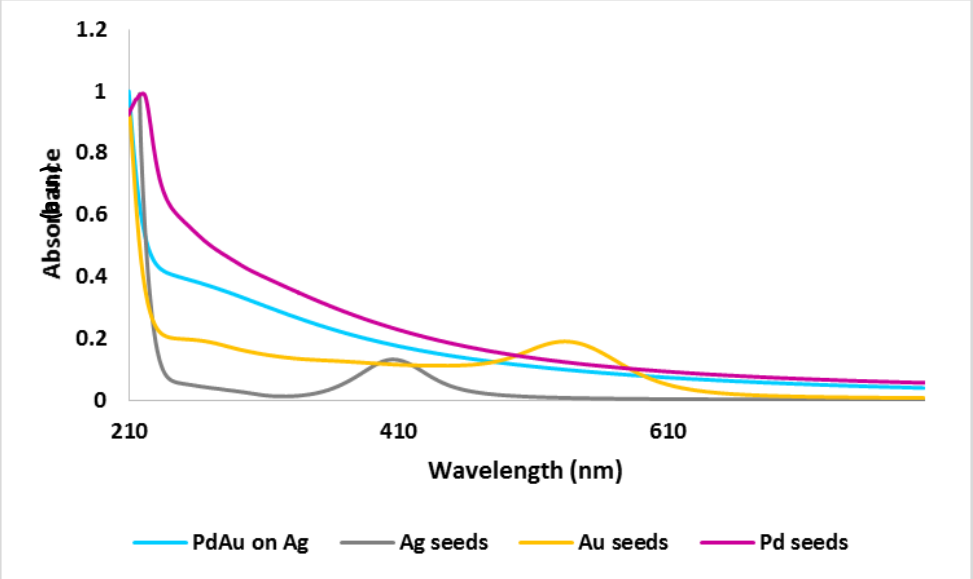

Figure 5.11. Overlayed UV-vis spectra for PdAu on Ag NPs (blue), and PVP-capped Ag seeds (gray), Au NPs (yellow) and Pd NPs (purple).

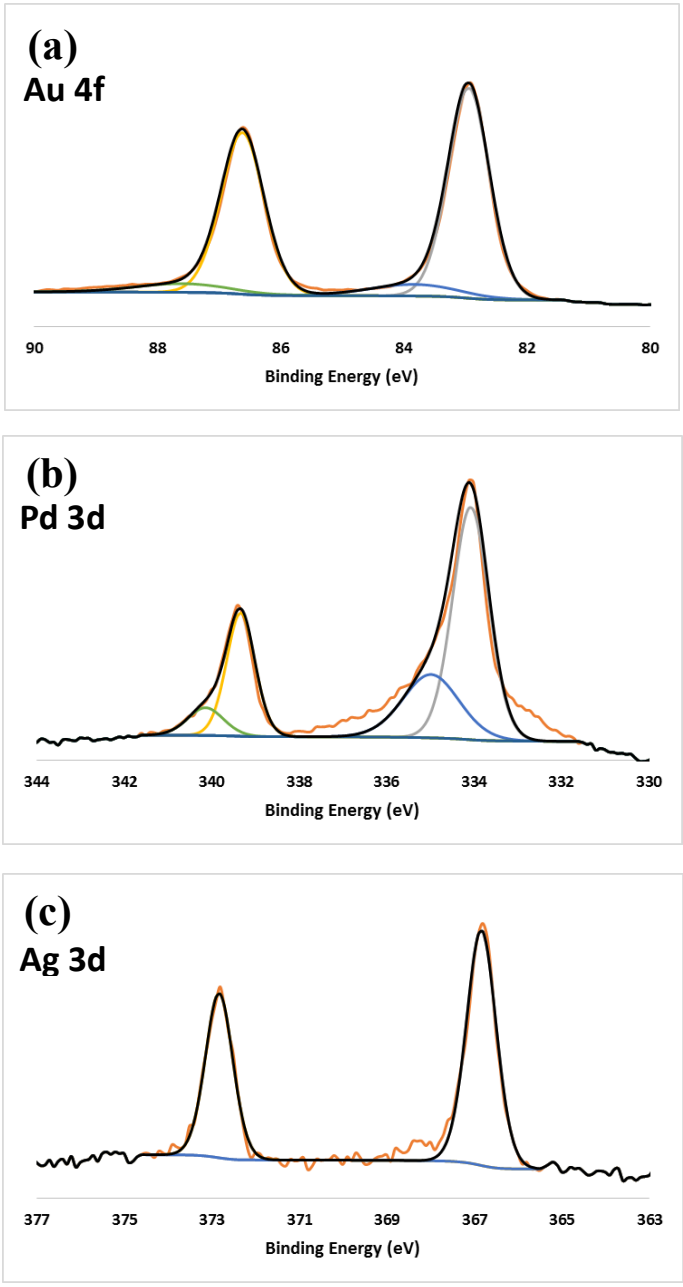

Figure 5.12. Fitted XPS data for PdAu on Ag NPs; (a) Au 4f signals corresponding to metallic Au (83.9 eV) and Au(I) (84.8 eV); (b) Pd 3d signals indicating the presence of Pd(0) (335.1 eV) and Pd(II) (336.0 eV); (c) Ag 3d signal assigned to Ag(0) (367.8 eV).

Table 5.2. Tabulated values for binding energies (acquired using XPS) for Au 4f, Pd 3d and Ag 3d in various oxidation states.

	Au(0)	Au(I)	Pd(0)	Pd(II)	Ag(0)
Binding Energy (eV)	84.0	85.5	335.1	338.2	368.3

5.4 CONCLUSION

This chapter reports the synthetic methods and characterization for trimetallic NPs. Based on the metal combinations used, the initial target assembly was meant to be comprised of a monometallic core enveloped by a thin alloyed shell of catalytic active species such as RhAg and PdAu. These types of nanostructures have proven to have many advantages over their monometallic counterparts including enhanced chemical stability, tunable and enhanced catalytic activity, and increased cost-effectiveness. Due to the complexity of the nucleation and growth kinetics of multimetallic particles that arise from the disparity in reduction potential of the metal precursors and the wide range of possible interactions between the metals, reducing agents and surface stabilizers, this chapter serves as proof of concept that lattice matching (one of the many important synthetic parameters) is a key factor in the preparation of this type of heterostructures.

NPs with a thin RhAg layer on Pt seeds were successfully achieved using μwH. Nonetheless, the same experimental conditions did not yield comparable results for the desired RhAg on Pd, and PdAu on Ag particles. In an attempt to prepare RhAg on Pd NPs, it is believed that a very thin Rh layer was deposited instead on a PdAg alloyed core. On the other hand, the attempted experiment for the overgrowth of a PdAu alloyed shell on Ag seeds yielded trimetallic randomly alloyed NPs. It is evident then, from the preliminary results here presented, that although lattice matching provides some control

over the kinetics of formation of alloyed shell-monometallic core NPs, it is not the driving force in the synthesis of this type of NPs. Thus, it is necessary to consider other thermodynamic and kinetic parameters in the future in order to develop a successful approach to the preparation of trimetallic NPs comprised of a monometallic core and an alloyed shell.

6. Novel Monomeric Organic Capping Agents

6.1 INTRODUCTION

Noble metallic nanoparticles (MNPs) are desired materials due to their tunable magnetic,[3,4,266] optical,[7,267,268] and catalytic[8,10,269] properties. Fine kinetic control of the size and shape of the particles is of vital importance because the aforementioned properties are dependent on the size and shape of the NPs.[12] Nanomaterials have previously been generated by physical methods such as laser ablation and evaporation. However, chemical methods have been proven to be more effective, for they offer better size and morphology control, and also allow for multiple functionalization techniques to be employed.[1] These methods rely on kinetic control over growth mechanisms. Organic capping agents such as surfactants and polymers that stabilize particular faces of growing MNPs can contribute to the control of size and shape of resulting products.[12] *Poly*(vinylpyrrolidone) (PVP) has been extensively used as a stabilizing agent for metallic nanocrystals with different shapes and as a flexible membrane for metallic colloids because it affords some degree of control of the structural parameters mentioned above based on differing binding strengths to different crystallographic faces of cuboctahedral MNPs of FCC metals.[15,33] However, it has also been reported that certain surfactants like PVP can diminish the catalytic activity of the nanoclusters produced,[34–36] since they can interact so strongly with the catalytic metal surfaces that reagents cannot reach the surfaces.[33,37] Manipulation of the interaction between the stabilizer and the nanoparticle surface can lead to the design of more efficient stabilizing ligands that can help to provide a balance between catalytic activity *vs.* stability.[38] Thus, it is also

imperative to control the properties of the capping agents used for stabilization, in order to maximize the catalytic potential of the NPs.

Due to the importance of particle monodispersity for application purposes, an attractive synthetic route for the generation of MNPs is based on the formation of well-defined seeds, followed by control growth procedures. The ideal seeds for MNP growth are uniform in size and also near-monodisperse. Schmid and co-workers have reported a series of clusters that are said to be two-shell cuboctahedrons containing 55 metal atoms (Rh, Au, Pd and Pt)[16] and are stabilized by chloride and phosphine ligands.[22] It has been previously reported that geometries that arise from 'magic number' clusters and their crystal packing, are not observable or non-existent[22] because polytetrahedral structures are more stable.[270,271] However, it is believed that 55 atom cubectahedrons are the exception because they have a greater bond energy than any other known polytetrahedral structure.[22] The formation of this type of particles in solution heavily relies on the nature and concentration of the stabilizing ligands. The shielding effect that the ligand has on the particle, by creating a plane of coverage over the surface of the metal cluster,[22] is of vital importance. Thus, phosphines with bulky aryl and alkyl groups (such as phenyl rings and *t*-butyl groups) have proven to be very effective stabilizers for M_{55} cuboctahedral particles.[22] It is believed that the phosphines bind to the corner atoms while the chloride ligands occupy the interstices, binding to the central atom of the six square faces in the cuboctahedron.[16,22]

Despite the controversy about magic numbers and the actual chemical formula of the compound reported by Schmid and co-workers,[16,272–275] the narrow size distribution and dispersity of the as synthesized material is remarkable. Phosphine-stabilized NPs are intriguing precursors to other functionalized NPs building blocks as they possess well-defined metallic cores[272–275] and the phosphine ligands are very labile.[276,277]

There have been several examples of phosphine ligand stabilized NPs whose core size can be tuned from 1.4 to 10 nm by introducing different functional groups into the ligand shell *via* ligand exchange reactions.[277–279] The lability of the phosphine ligand is not only important for size tunability, but it also allows for the incorporation of different capping agents that may improve the catalytic performance of the nanoclusters. Ligands with long aliphatic tails can stabilize the particles in aliphatic apolar solvents and promote their incorporation into support species, by avoiding agglomeration during catalytic processes. In addition, the presence of two or more functional head groups ensures that the ligand will preserve the active and selective surface geometry of the MNPs. Presumably, these head groups can also undergo chemical changes under facile conditions in a catalytic environment, leading to self-activation and removal from the MNP surface. This can potentially completely remove any capping agent surface blocking effects, unlike what is often observed for PVP. Hence, extremely active, yet selective, naked NPs can be generated *in situ*.

This chapter reports the reactions of novel capping agents derived from 12-C chain containing-glycinates with PPh_3-capped Rh NPs in order to determine the stability of these nanomaterials. These novel stabilizing ligands have promising features that can enhance the activity and selectivity capabilities of the NPs during catalytic processes.

6.2 SYNTHESIS AND CHARACTERIZATION

6.2.1 Synthesis and Characterization Methods

All molecular complexes synthesized were characterized by ^{1}H and $^{13}C\{^{1}H\}$ NMR, and FT-IR spectroscopy. NMR spectra were recorded in a Varian 300 MHz spectrometer in varying deuterated solvents at room temperature, referenced to TMS. FT-IR spectra were collected utilizing a Thermo Nicolet iS50 spectrometer with attenuated total reflection (ATR).

Microwave syntheses were carried out in a CEM MARS synthesis microwave and all the Transmission Electron Microscopy (TEM) images were acquired in an FEI Tecnai Spirit BioTwin operating at 80 kV. High-resolution TEM (HRTEM) and energy dispersive X-ray analysis (EDX) were performed using a JEOL 2010F transmission electron microscope. This instrument was operated at 200 keV using a field-emission gun with 0.19 nm point-to-point resolution.

6.2.2 Synthesis of $Rh_{55}(PPh_3)_{12}Cl_6$ seeds

Rh seeds stabilized by triphenyl phosphines were prepared as reported by Schmid and Huster.[22] In summary, freshly synthesized $RhCl(PPh_3)_3$ in benzene was reduced under a stream of B_2H_6 generated *in situ* for approximately 40 min at 60 °C. The B_2H_6 gas was synthesized by the addition of BF_3-etherate to a mixture of $NaBH_4$ in dry dimethoxyethane. Dry petroleum ether was added very slowly to the mixture generated after the reduction period and the dark brown precipitate was isolated under N_2 and then washed with dry benzene and dry petroleum ether. $^{31}P\{^{1}H\}$ (C_5D_5N, 300 MHz) δ: 26.717 ppm.

6.2.3 Synthesis of Novel Organic Capping Agents

6.2.3.1 Dodecyl Iminoglycinate

A mixture of dodecylamine (44.79 g, 0.24 mol) and potassium carbonate (32.24 g, 0.23 mol) was heated to 50 °C. Ethyl bromoacetate (80.03 g, 0.48 mol) was added dropwise, and deionized water was then added to the reactants to decrease the viscosity of the solution. The reaction ran under these conditions for 1 hour. The reaction was then stirred at 95 °C for 20 hours. After the mixture was cooled to room temperature, the product was extracted using diethyl ether. The product was further purified by distillation, providing the target compound (55.69 g, 65%) as a yellow oil. B.P. 212 °C/0.1 mmHg. Figure 6.1: ^{1}H NMR ($CDCl_3$, 300 MHz) δ: 4.166 ppm (q, *J*= 7.20 Hz, 4H), 3.539 ppm (s, 4H), 2.578 ppm (t, *J*= 6.90 Hz, 2H), 1.477 ppm (quintet, *J*= 7.20 Hz, 2H), 1.183 - 1.130 ppm (m, 24H), 0.879 ppm (t, *J*= 7.20, 3H).

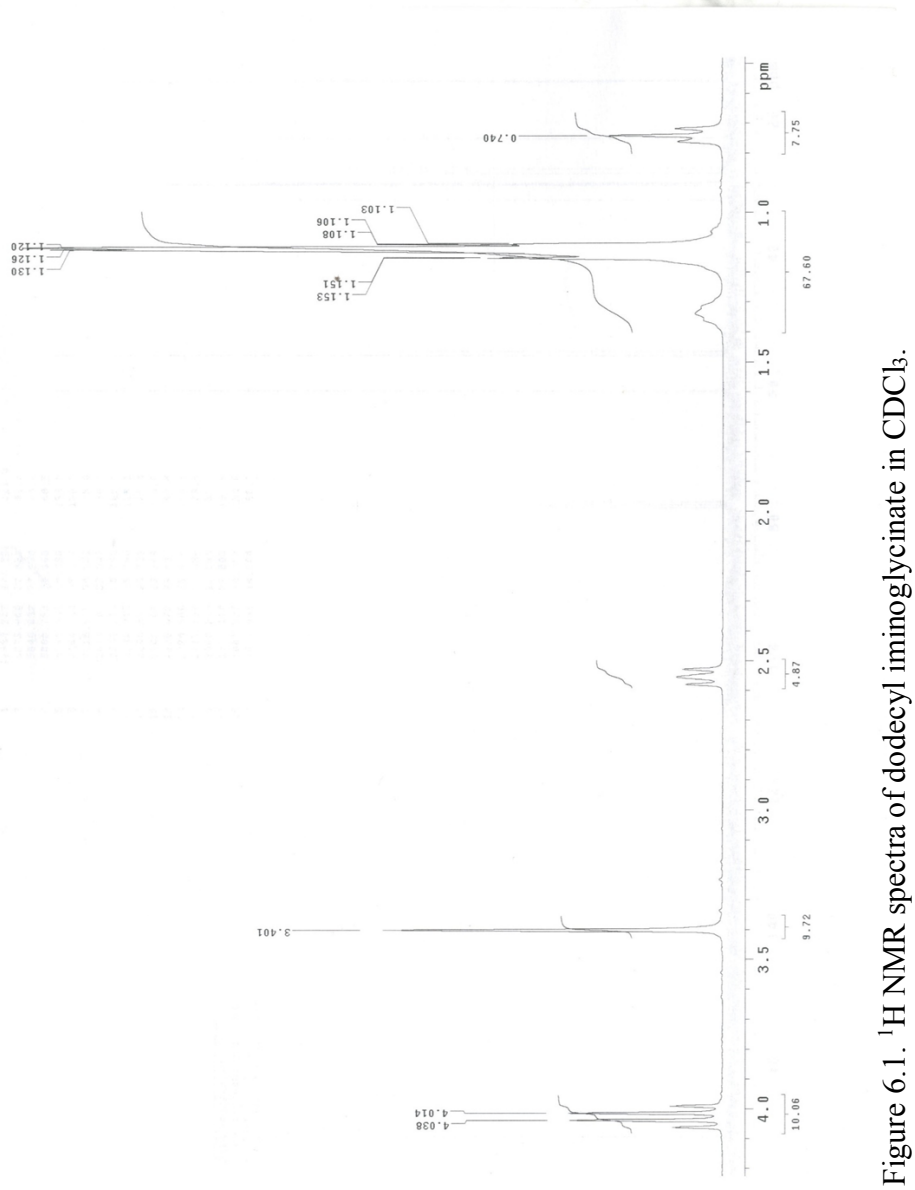

Figure 6.1. ^{1}H NMR spectra of dodecyl iminoglycinate in $CDCl_3$.

6.2.3.2 Dodecyl Iminodicarboxylate (DAc)

Dodecyl iminoglycinate (12.14 g, 0.34 mol) was refluxed with sodium hydroxide aqueous solution (2 M) to yield the desired compound as a white solid (5.65 g, 55%). The sodium salt of this organic compound can be recrystallized from hot methanol. It can be seen in the crystal structure (Figure 6.4) that despite the long aliphatic tail, the compound packs neatly in the solid state facilitated by the Na^+ counterions that bridge between adjacent carboxylate functional groups. The bulkiness of the head groups and the network of molecules they form have caused the angle between the pendant N-groups to be slightly distorted compared to an expected tetrahedral geometry (112.95°) around the central N atom. Furthermore, the Na^+ ion are further stabilized by a methoxy ligand coming from the recrystallizing solvent. This generates a large and very organized network of molecules with optimal distances between the functional head groups for the desired capability of surface stabilization.

Figure 6.2: ^{1}H NMR (D_2O, 300 MHz) δ: 3.463 ppm (s, 4H), 2.897 ppm (t, *J*= 8.70 Hz, 2H), 1.538 ppm (m, 2H), 1.162 (m, 20H), 0.753 ppm (t, *J*= 6.30 Hz, 3H). m/z = 301.33. Figure 6.3: $\gamma_{C=O}$ = 1632 cm^{-1}, γ_{C-O} = 1385 cm^{-1}. Elemental Analysis (%) for $C_{16}H_{31}NO_4$ calcd: C, 63.79, H, 10.30, N, 4.65; found: C, 47.28, H, 8.80, N, 3.44.

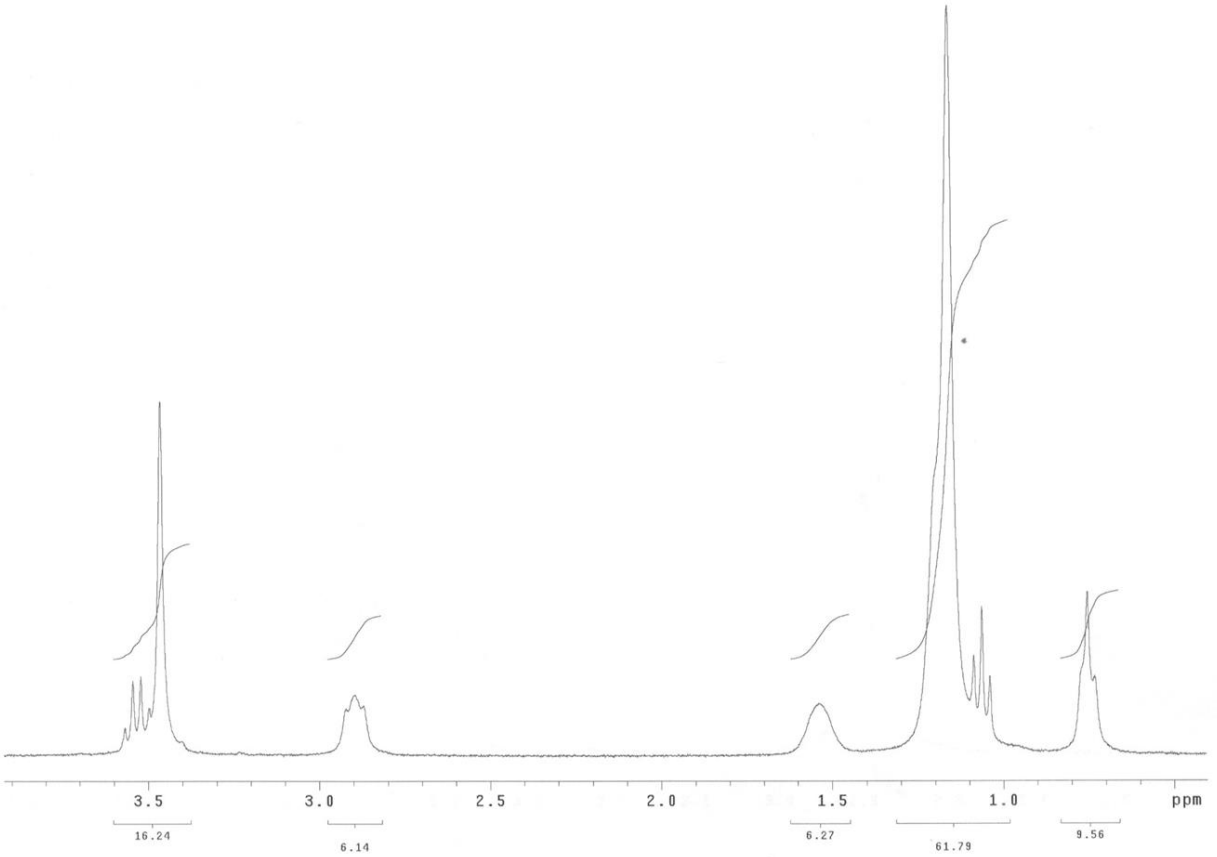

Figure 6.2. ^{1}H NMR spectra of dodecyl iminodiacetate in D_2O.

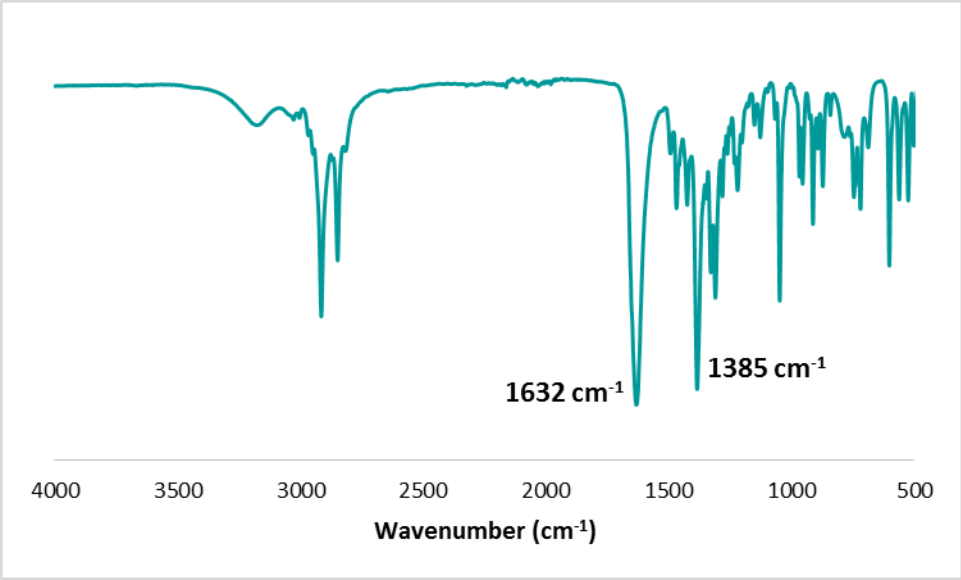

Figure 6.3. FT-IR spectrum for dodecyl iminodiacetate (DAc).

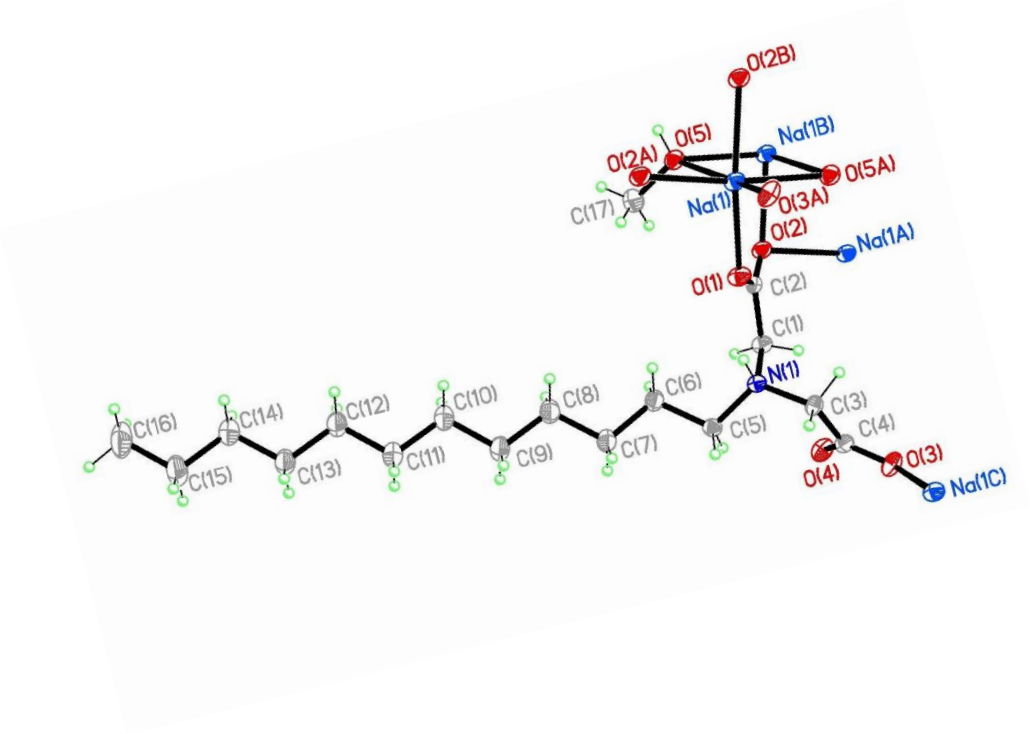

Figure 6.4. Crystal structure for dodecyl iminodiacetate (DAc).

6.2.3.3 Dodecyl Iminodiacetamide Synthesis (DAm)

Dodecylamine (50.379 g, 0.27 mol) and sodium carbonate (28.260 g, 0.27 mol) were stirred in 60 mL ethanol. Chloroacetamide (50.122 g, 0.54 mol) was dissolved in 110 mL ethanol in a separate reaction vessel, and this solution was then added to the dodecylamine slush. The mixture was refluxed at 88°C for 20 hours. The resulting solid was collected using vacuum filtration and was washed with water and ethanol. It was finally recrystallized from $CHCl_3$ yielding a white fluffy solid (58% yield). The crystal structure (Figure 6.7) revealed that the angle of separation between the N-substituents is 109.64°, which is large enough for all three N atoms (two from the amide functional groups and one from the central N atom) to be able to interact simultaneously with a MNP surface, as is desired for capping purposes. Unlike dodecyl iminodiacetate, this ligand does not contain ionic species that can bridge several molecules together. Thus, the molecules pack solely based on dispersion forces between the long aliphatic tails.

Figure 6.5: ^{1}H NMR (DMSO, 300 MHz) δ: 7.564 ppm (s, 2H), 7.103 ppm (s, 2H), 2.953 ppm (s, 4H), 2.383 ppm (t, *J*= 7.35 Hz, 2H), 1.379 ppm (m, 2H), 1.224 (m, 18H), 0.841 ppm (t, *J*= 6.45 Hz, 3H). m/z = 299.2. Figure 6.6: γ_{CO} = 1681 cm^{-1}, γ_{NH} = 3241 cm^{-1}. Elemental Analysis (%) for $C_{16}H_{33}N_3O_2$ calcd: C, 64.2, H, 11.0, N, 14.0; found: C, 64.8, H, 11.7, N, 13.4.

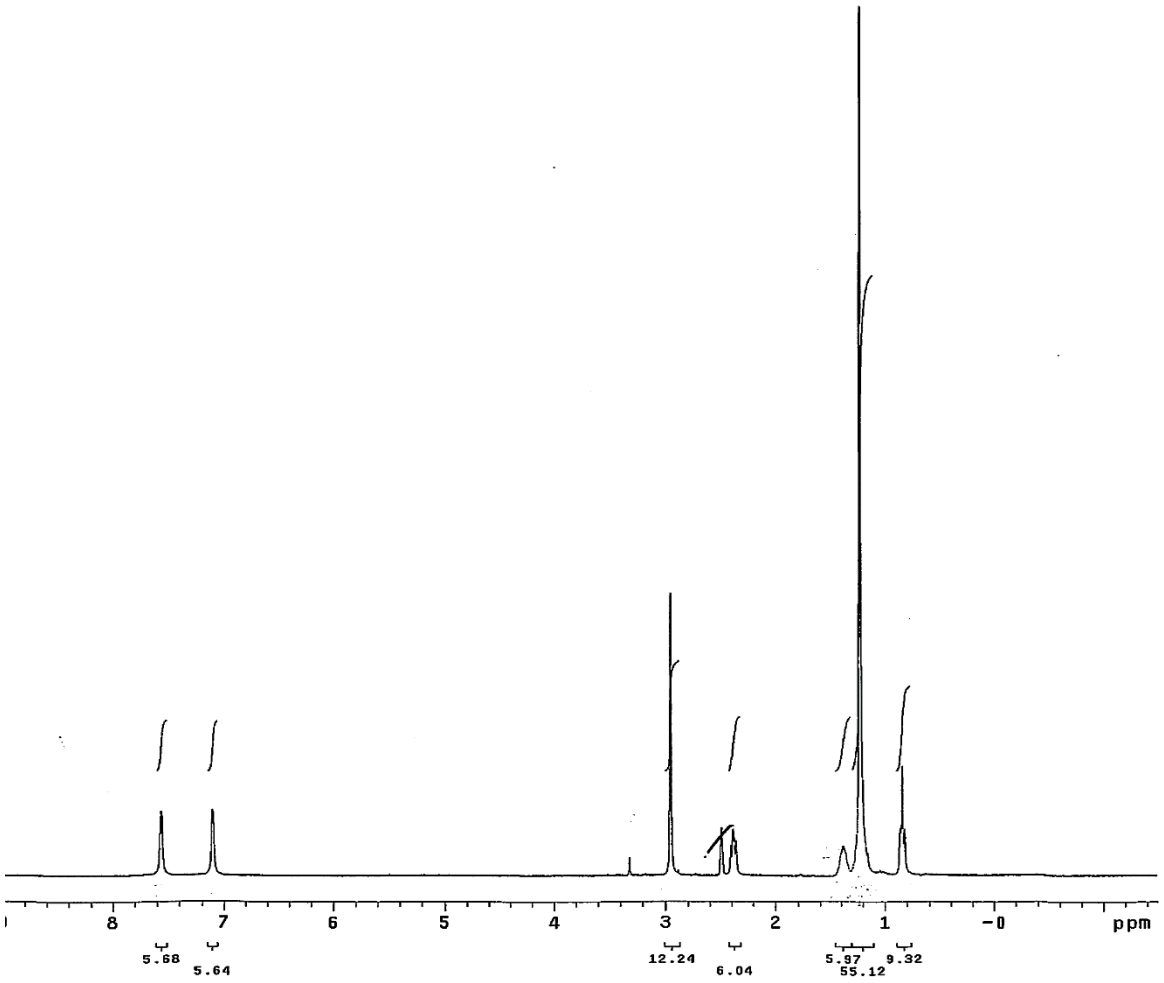

Figure 6.5. ^{1}H NMR spectrum (in DMSO) of dodecyl iminoacetamide.

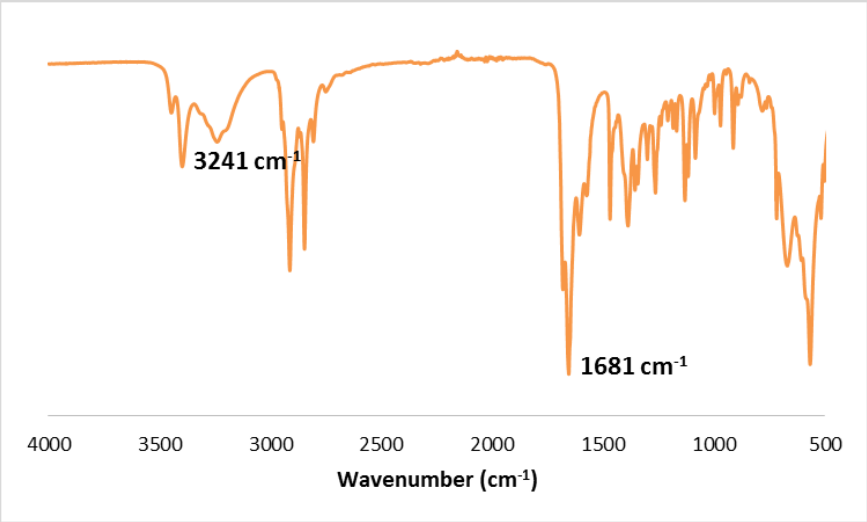

Figure 6.6. FT-IR spectrum for dodecyl iminodiacetamide (DAm).

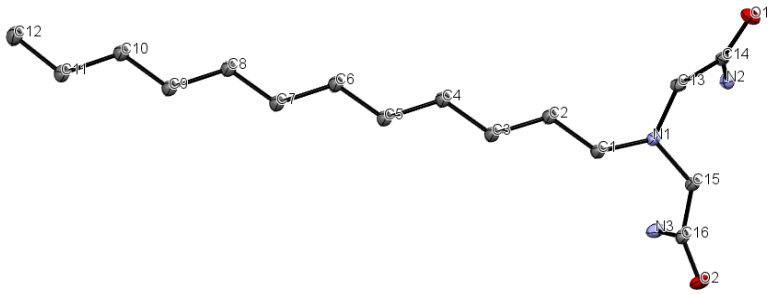

Figure 6.7. Crystal structure for dodecyl iminodiacetamide.

6.2.4 Ligand Exchange Reactions

A solution of THF:DCM (1:1, 20.0 mL) was used to disperse 13 mg batches of $Rh_{55}(PPh_3)_{12}Cl_6$ under N_2. The capping agents (DAc, DAm and PVP which was used as a control) were then dissolved in 10–20 mL methanol and this solution was added to the NP mixture under inert conditions. After 17 hours stirring at room temperature, all the solvents were removed under reduced pressure. The solid collected was first washed with hexanes and collected using ultracentrifugation (5 min, 5.5 krpm). The product was finally washed with acetone and isolated utilizing ultracentrifugation (5 min, 5.5 rpm). The last step was repeated three times in order to remove any residual PPh_3 or solvents.

6.2.4.1 $Rh_{55}(PPh_3)_{12}Cl_6$

The reduction of $Rh(PPh_3)_3Cl$ with B_2H_6 generated *in situ* produced monodisperse RhNPs with well-defined cubeoctahedral morphology. The particles are initially pyrophoric in air, presumably due to presence of an abundance of high energy facets on the NPs, inherent to the small size (large surface area to volume ratio), and to the high surface energy of metallic Rh (2.8 J/m^2).[280] However, TEM images (Figure 6.8) show that once the particles are anchored on a support (*e.g.*, a holey carbon TEM grid) they are stable in ambient conditions. The particles have an average size of 1.75 ± 0.26 nm and it is evident that PPh_3 ligands effectively passivate the NP surface as no agglomeration is observed.

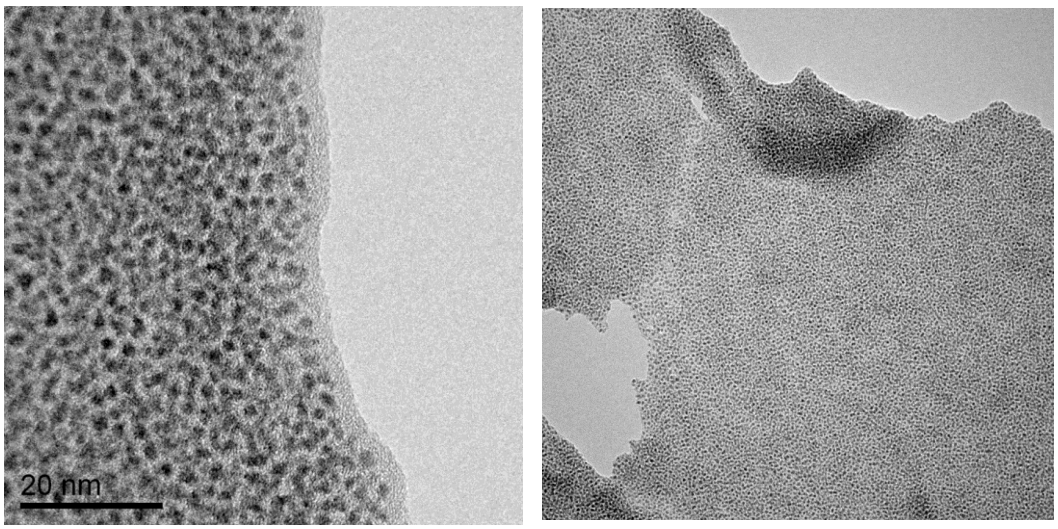

Figure 6.8. TEM images for as-synthesized $Rh_{55}(PPh_3)_{12}Cl_6$ NP seeds.

EDX and elemental microanalysis studies yielded results that support the formation of cubeoctahedral nanoseeds comprised of 55 Rh atoms (Figure 6.9, Table 6.11). In EDX spectroscopy, only the values for P and Rh where monitored, given that all the other elements present in the stabilizing ligands are also present on the TEM grid (Figure 6.9). In the case of elemental analyses, weight % values for P, C, and H were examined. All the experimental values correlate to the calculated values for NP clusters that are constituted of 55 Rh atoms, $Rh_{55}(PPh_3)_{12}Cl_6$ (Table 6.1). Since the ultimate purpose was to displace the PPh_3 ligands with other novel monomeric capping agents that contain N, this element was also monitored in elemental analysis in order to ensure that any N that was detected after ligand exchange reactions was indeed coming from the new passivating agents.

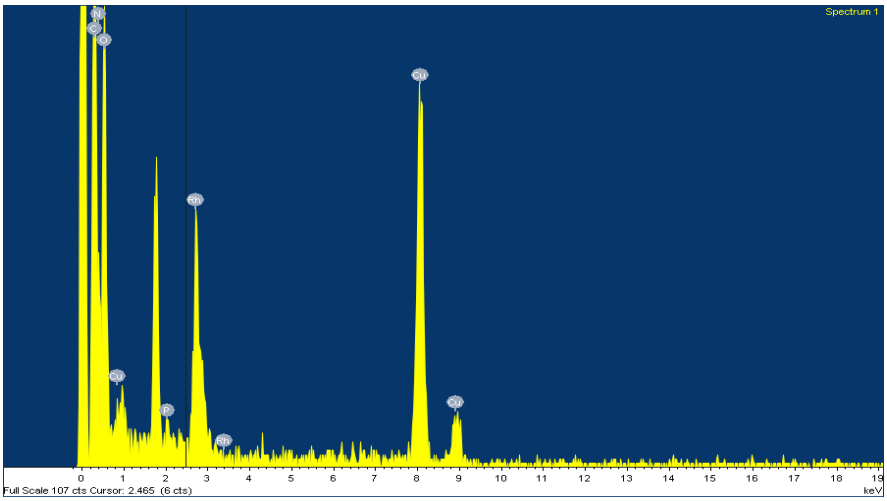

Figure 6.9. EDX spectrum for $Rh_{55}(PPh_3)_{12}Cl_6$ clusters.

Table 6.1. Tabulated wt% values acquired from elemental analysis for P, C, H and N in $Rh_{55}(PPh_3)Cl_6$ NPs.

Elemental Analysis (wt%)	**P**	**C**	**H**	**N**
Calculated	4.1%	28.7%	2.0%	0.00%
Experimental	3.7%	23.4%	2.8%	0.00%

The Rh_{55} NPs were also analyzed using FT-IR and $^{31}P\{^1H\}$ NMR spectroscopy. FT-IR studies showed stretching frequencies above 3000 cm^{-1}, indicative of unsaturated organic species such as phenyl rings (Figure 6.10). Furthermore, there are no peaks were observed in the carbonyl region which facilitated the analysis of the RhNPs after ligand exchange reactions (all the capping agents utilized for ligand exchange contain C=O

moieties). The $^{31}P\{^{1}H\}$ NMR spectrum of $Rh_{55}(PPh_3)_{12}Cl_6$ showed a single peak at 26.7 ppm which is consistent with the presence of PPh_3 (Figure 6.11).

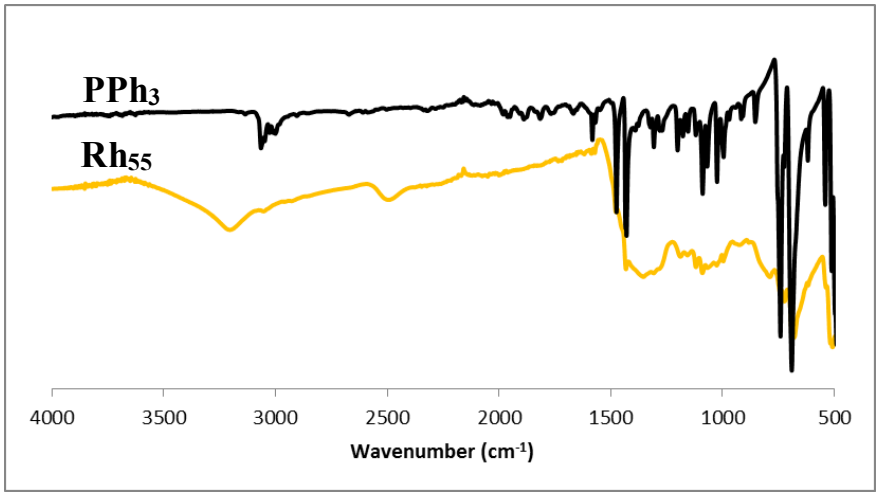

Figure 6.10. Overlayed FT-IR spectra of free PPh_3 and $Rh_{55}(PPh_3)_{12}Cl_6$ clusters.

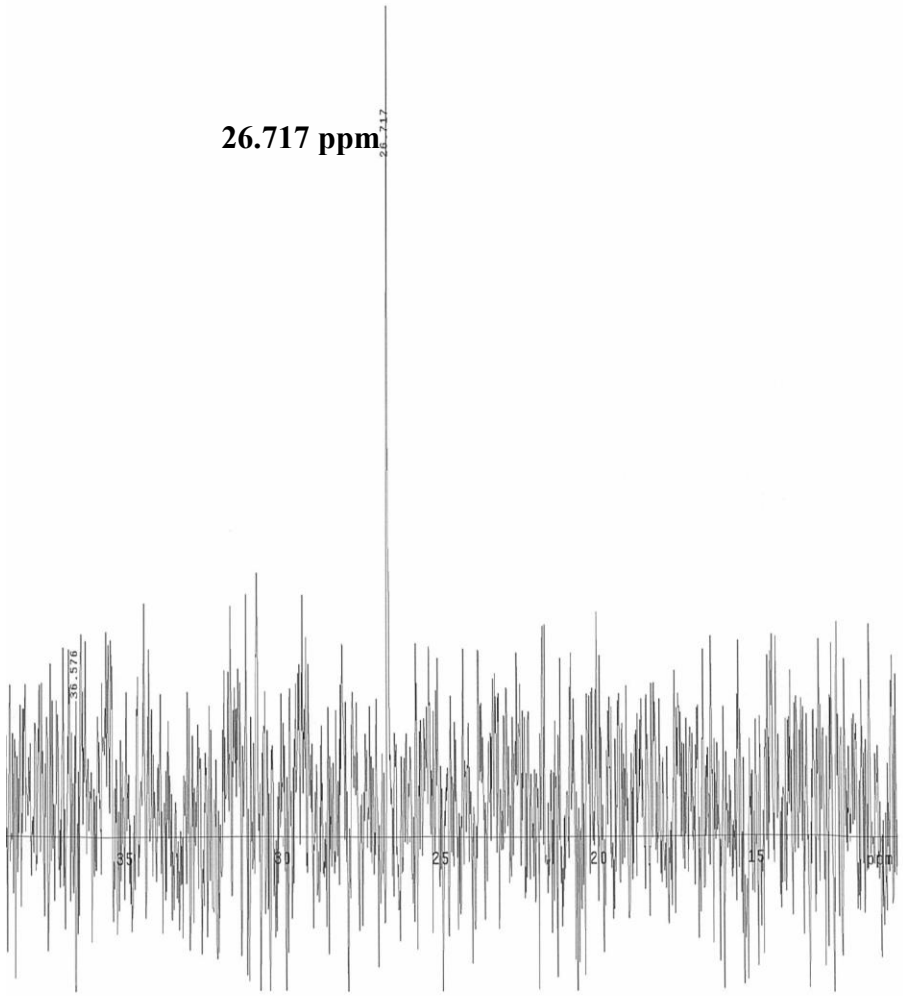

Figure 6.11. $^{31}P\{^{1}H\}$ NMR spectrum of $Rh_{55}(PPh_3)_{12}Cl_6$ clusters.

6.2.4.2 Rh_{55}–dodecyl iminodiacetate (Rh_{55}-DAc)

TEM images of the Rh seeds after replacement of the PPh_3 with dodecyl iminodiacetate as the monomeric capping agent showed that the particles retained their well-defined morphology, retained monodispersity and were still nicely dispersed (Figure 6.12). The particles were also probed using EDX spectroscopy, which revealed elemental

signals for Rh, Na and C while an insignificant amount of P was detected, as expected (Figure 6.13, Table 6.2). The previous observation was complemented by elemental analysis studies (Table 6.3) which showed a drastic decrease in the weight % value of P (3.73% to 0.62%) and confirmed the removal of PPh_3 ligands from the NP surfaces. Furthermore, all the wt% experimental values acquired for C, H and N correlated to the theoretical values calculated based on the amount of DAc stabilizing agent used in the ligand exchange reaction; thus, the exchange reaction was very effective. FT-IR analysis showed a marked shift in the C=O stretching frequency of the DAc ligand, from 1632 to 1616 cm^{-1} (Figure 6.14), due to the interaction of this moiety with the surface of the NP surface. As the C=O stretch weakened, the C–O stretching frequency of the acetate group became stronger, shifting from 1385 to 1398 cm^{-1} (Figure 6.14).

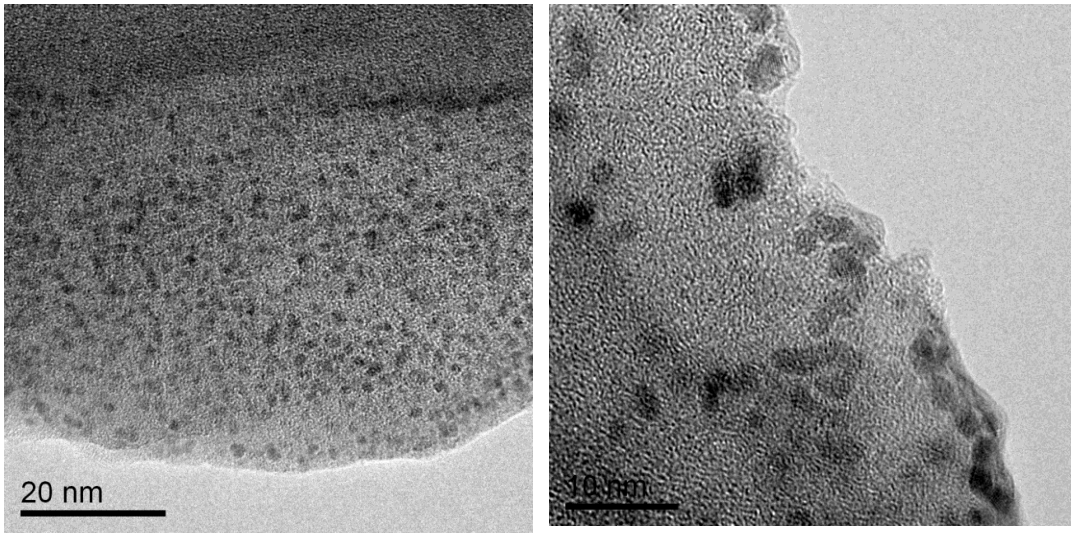

Figure 6.12. TEM images of Rh_{55} seeds after ligand exchange reactions with dodecyl iminodiacetate (DAc).

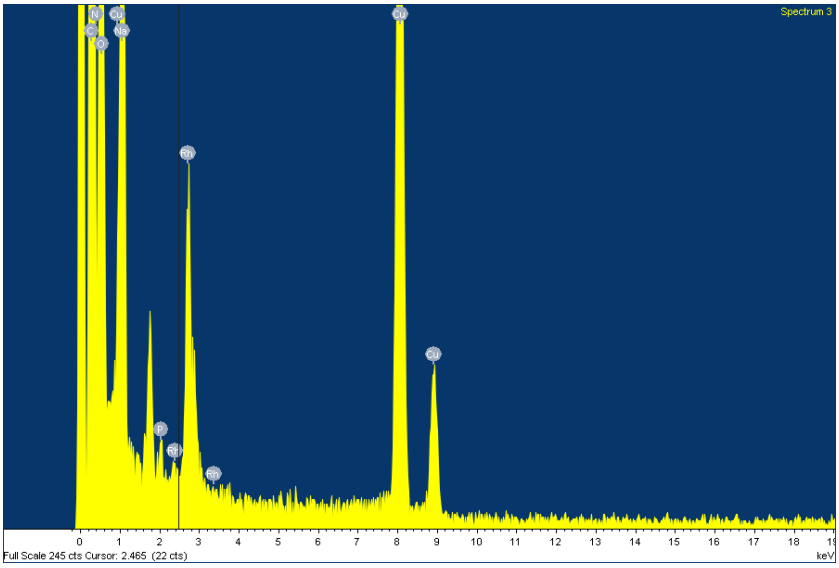

Figure 6.13. EDX spectrum of Rh_{55} seeds after ligand exchange reactions with dodecyl iminodiacetate (DAc).

Table 6.2. Tabulated EDX results for Rh55 seeds after ligand exchange reactions with DAc.

EDX (atomic %)	P	C	Na	Rh
Rh_{55}-DAc	0.15%	75.86%	4.75%	0.88%

Table 6.3. Tabulated wt% values acquired from elemental analysis for P, C, H and N in Rh_{55} seeds after ligand exchange reactions with DAc.

Elemental Analysis (wt%)	P	C	H	N
Calculated	0.00%	59.22%	9.57%	4.32%
Experimental	0.62%	53.96%	8.53%	4.07%

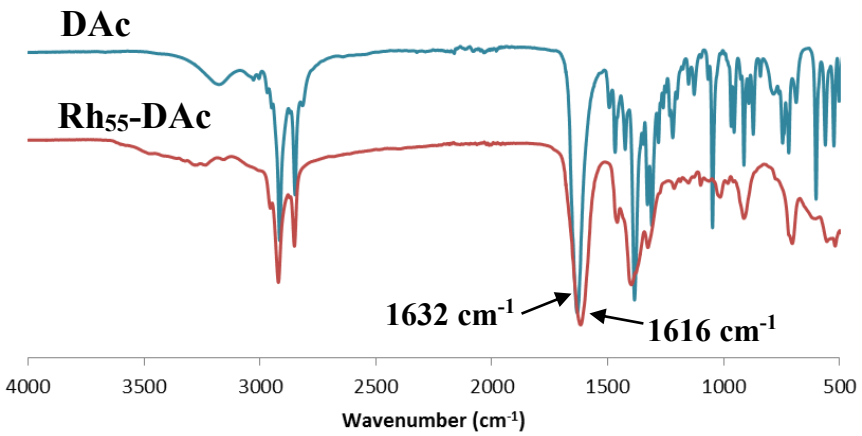

Figure 6.14. Overlayed IR spectra of DAc and Rh_{55} seeds after ligand exchange reaction with DAc displaying a shift in the carbonyl stretch region.

6.2.4.3 Rh_{55}–dodecyl iminodiacetamide (Rh_{55}-DAm)

When the PPh_3 passivating agents in $Rh_{55}(PPh_3)_{12}Cl_6$ are exchanged for dodecyl iminodiacetamide, the particles remain well-defined as is observed in the TEM images in Figure 6.15. Furthermore, it is evident that the monodispersity of the particles is not compromised after the exchange reaction, given that the particles have an average diameter of 1.53 ± 0.21 nm, which is very similar to the size of the initial Rh_{55} seeds. The Rh_{55}-DAm NPs were also analyzed using EDX spectroscopy. The EDX spectrum shown in Figure 6.16 displays peaks that correspond to Rh, C, O and N as expected for Rh_{55} clusters stabilized with dodecyl iminodiacetamide (the Cu signal detected comes from the TEM grid). EDX area scans also confirmed that the detected signal for P significantly decreased compared to the PPh_3 capped–Rh_{55} clusters (Table 6.4), indicating the effective replacement of PPh_3 with DAm ligands. Elemental analysis studies were unable to detect the presence of any P in the nanomaterial, as seen in Table 6.15 (the lower resolution

limit for the elemental analysis instrument is 0.25%). Moreover, the acquired weight % values for C, H and N in the Rh_{55}-DAm NPs were comparable to those achieved using yield calculations (Table 6.5), which further proves that the ligand exchange is effective and proceeds in a clean fashion. Finally, FT-IR analysis (Figure 6.17) revealed that the C=O stretch shifts by 10 cm^{-1} (1681 to 1671 cm^{-1}) when the organic ligand is involved in the passivation of the metallic surface. The N–H stretch absorption also decreased in strength, shifting from 3241 to 3189 cm^{-1} as the N in the amide interacts with the NP surface.

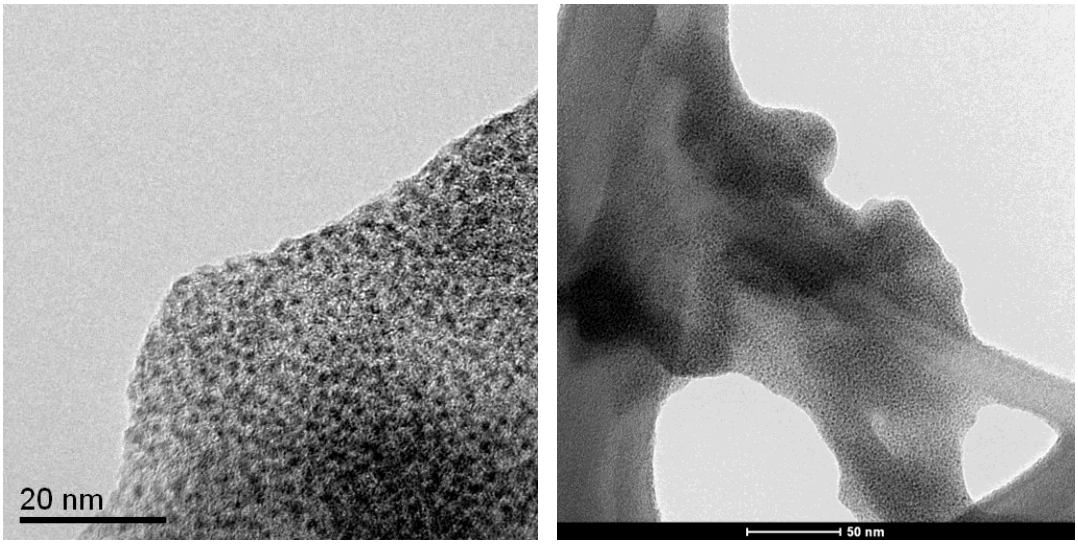

Figure 6.15. TEM images of Rh_{55} seeds after ligand exchange reactions with dodecyl iminodiacetamide (DAm).

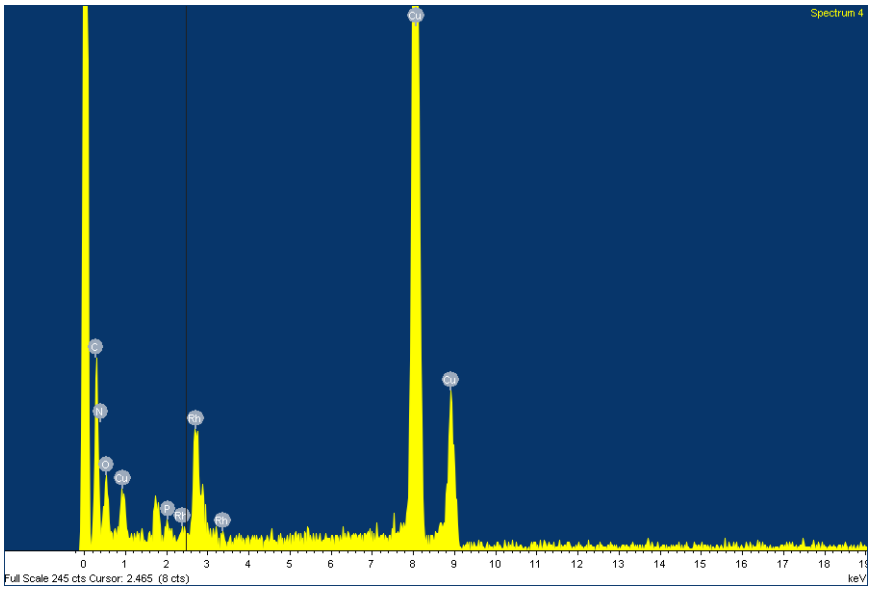

Figure 6.16. TEM images of Rh_{55} seeds after ligand exchange reactions with dodecyl iminodiacetamide (DAm).

Table 6.4. Tabulated EDX results for Rh_{55} seeds after ligand exchange reactions with DAm.

EDX (atomic %)	P	C	O	Rh
Rh_{55}-DAm	0.55%	33.48%	3.04%	3.13%

Table 6.5. Tabulated wt% values acquired from elemental analysis for P, C, H and N in Rh_{55} seeds after ligand exchange reactions with DAm.

Elemental Analysis (wt%)	P	C	H	N
Calculated	0.0%	57.6%	9.9%	12.6%
Experimental	Undet.	58.55%	9.88%	12.59%

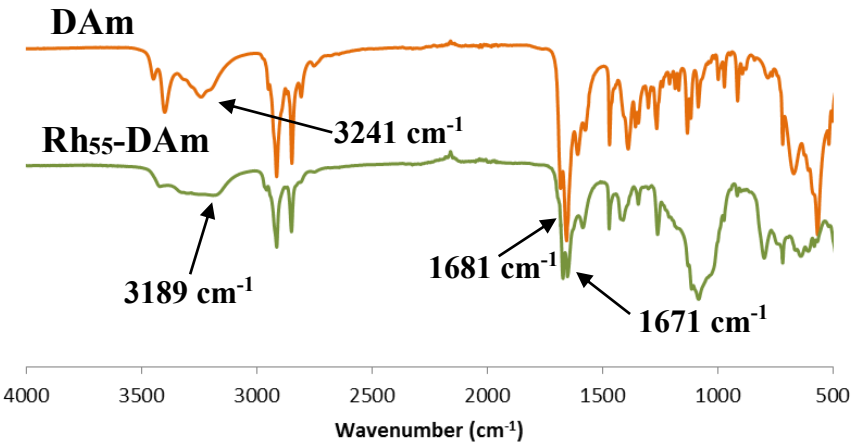

Figure 6.17. Overlayed IR spectra of DAm and Rh_{55} seeds after ligand exchange reaction with DAm displaying a shift in the carbonyl stretch region.

6.2.4.4 Rh_{55}-PVP

PVP was used as a control as it is a widely used polymer for the successful stabilization of NPs but that also contains similar functional groups as those in the novel monomeric capping agents discussed above. TEM images in Figure 6.18 confirm that the particles are still monodisperse and stable after the replacement of PPh_3 ligands with PVP, which is expected, as the polymer can create many contact points with the RhNP surface. Furthermore, it is also evident that the particle size does not dramatically change from the original Rh_{55} seeds (1.93 ± 0.19 nm). The PVP stabilized Rh_{55} clusters were also probed utilizing EDX spectroscopy, which displayed distinct signals for Rh, C and N (Figure 6.19 and Table 6.16) indicating the incorporation of PVP as a passivating agent for the Rh seeds. It was noted that the atomic % of P detected in area scans decreased to less than 1% (Table 6.6), further confirming the removal of the PPh_3 ligands. The results discussed above were supported by elemental analysis studies (Table 6.7) which showed the unequivocal presence of N coming from the polymeric stabilizing agent, and the drastic decrease in detectable P signal.

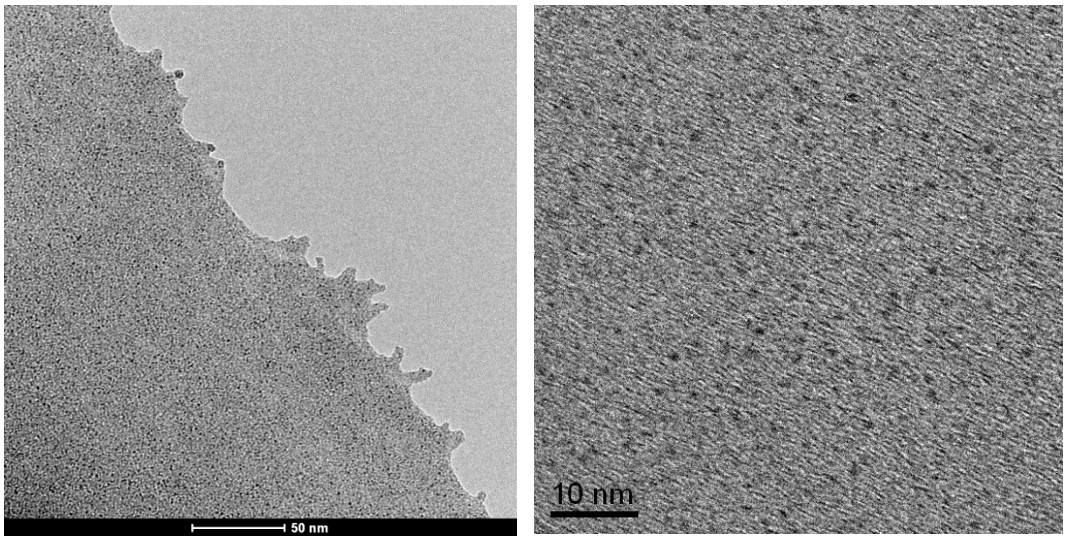

Figure 6.18. TEM images of Rh_{55} seeds after ligand exchange reactions with PVP (polymeric capping agent).

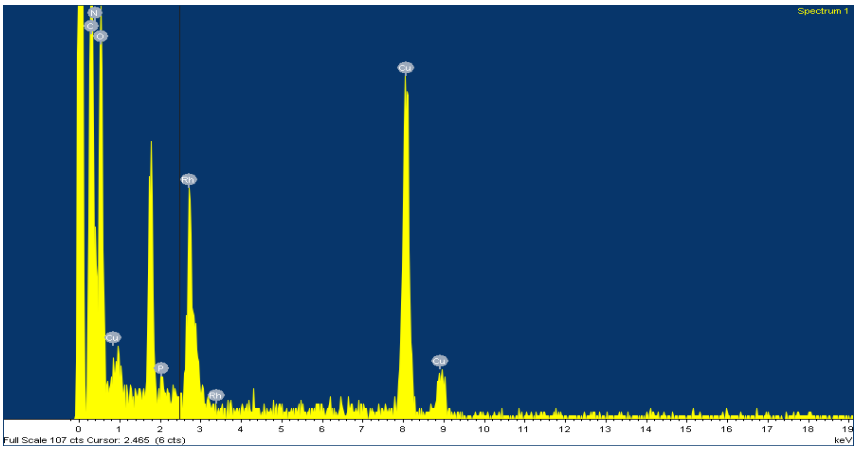

Figure 6.19. EDX spectra of Rh_{55} seeds after ligand exchange reactions with PVP.

Table 6.6. Tabulated EDX results for Rh_{55} seeds after ligand exchange reactions with PVP.

EDX (atomic %)	P	C	N	Rh
Rh_{55}-PVP	0.97%	53.99%	10.65%	3.17%

Table 6.7. Tabulated wt% values acquired from elemental analysis for P, C, H and N in Rh_{55} seeds after ligand exchange reactions with PVP.

Elemental Analysis (wt%)	P	C	H	N
Rh_{55}-PVP	Undet.	56.17%	8.96%	7.54%

6.3 Self-Activation Experiments

6.3.1 Experimental

6.3.1.1 Solution Phase Hydrogenation Attempt (MeOH, Room Temperature)

Pre-catalysts were formed by the addition of pre-calcined amorphous SiO_2 (100 mg) to a suspension of 30-50 mg of Rh_{55}-CA (CA = DAc, DAm or PVP) NPs in 1:1 MeOH:H_2O. The slurries were sonicated for 20 min, isolated by vacuum filtration, followed by washing with MeOH and drying in air at 50 °C for 14 hours. The Rh_{55} seeds

were placed on a support to prevent any agglomeration of the NPs after removal of the stabilizing agents.

The pre-catalysts (20.0 mg) were then individually placed in 20 mL MeOH and these slurries were purged with H_2 for 2.5 h. After this process was completed, the supported Rh_{55}-CA particles were isolated *via* ultracentrifugation (10 min, 5.5 krpm), washed with MeOH and dried under reduced pressure. The supernatant left behind was then pumped to dryness under vacuum and analyzed using mass spectrometry (MS) and ^{1}H NMR.

6.3.1.2 Solution Phase Hydrogenation Attempt (High Boiling Point Solvents)

The pre-catalysts were prepared as stated in the previous section. In the case of Rh_{55}-DAc pre-catalyst, the hybrid material (20.0 mg) was mixed in 1-butanol in a 25 mL Schlenk tube. The reaction vessel was then heated to 118 °C using an oil bath. Once the target temperature was reached in the reaction mixture, H_2 was bubbled through the suspension for approximately 21 h. After the slurry cooled down to room temperature, it was transferred to a centrifuge tube and the solid was isolated using ultracentrifugation (10 min, 8.5 krpm), yielding a colorless supernatant. The supernatant solvent was completely removed under reduced pressure and it was then analyzed using ^{1}H NMR (DMSO or MeOD), FT-IR and MS.

The Rh_{55}-DAm and Rh_{55}-PVP pre-catalysts were treated in DMF at 160 °C. All other experimental conditions remained as stated above.

6.3.1.3 Vapor Phase Self-activation and Hydrogenation Catalysis Attempt

Vapor phase self-activation of the stabilizing ligands was also attempted. Scheme 6.1 clearly portrays the experimental setup utilized for this set of experiments. The composite materials were loaded into a custom made quartz U-tube, suspended above a D3-porosity frit. The organic reactant (which is contained in an in-line saturator held at 0 °C and fitted with a fritted bubbler) and carrier gases traveled through a quartz reactor line that was heated to 90 °C. Conversion data was obtained in real-time by automated pneumatically-gated sampling of the exhaust stream, which was vented directly into an HP Agilent 6890 gas chromatograph fitted with Restex Stabiliwax 15 m column and tandem FID and TCD detectors. Peak areas were integrated and correction factors obtained from control studies were applied to obtain raw conversion values. Normalized turnover frequency (TOF) values were obtained based on estimation of the number of Rh surface sites (by measuring average supported particle sizes from TEM images) and from ICP-MS data for % Rh loading on the SiO_2 supports.

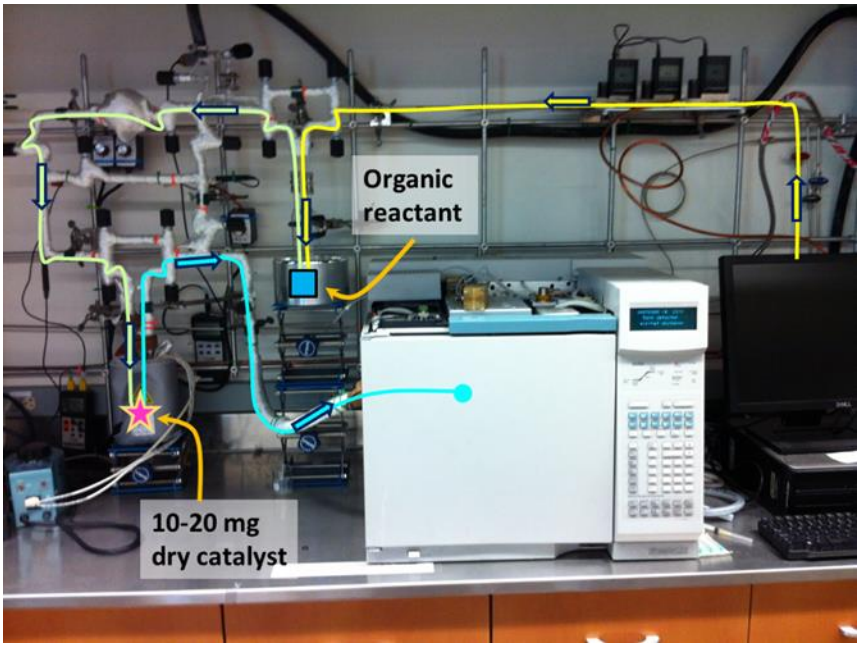

Scheme 6.1. Diagram of the experimental set-up for the vapor-phase self-activation of novel monomeric capping agents and for the hydrogenation of cyclohexene.

The pre-catalysts (8.0 – 9.0 mg) were mixed in with acid washed/calcined sand and were exposed to a stream of H_2/He at room temperature for 1 h. After this period, cyclohexene vapor was introduced to the gas stream and the catalytic conversion of cyclohexene to cyclohexane was monitored using gas chromatography for a period of 2.5 h. The cyclohexene flow was then terminated and the catalysts were purged just with H_2/He at 40 °C (heating tape was coiled around the quartz U-tube where the catalysts were loaded in order to achieve the desired activation temperature) for 3 h. After the composite materials cooled down to room temperature, cyclohexene hydrogenation was performed again at 25 °C for 2 h. The catalysts were then heated to 60–70 °C for 3 h, while still being exposed to the H_2/He stream. Cyclohexene hydrogenation catalysis was

then performed at room temperature once again. This was followed by two more cycles of activation (120 °C and 140–150 °C) and hydrogenation catalysis, as explained above.

6.3.2 Characterization and Analysis

6.3.2.1 Solution Phase Hydrogenation (MeOH, Room Temperature)

The mass spectrometry spectrum (Figure 6.20) acquired of the supernatant generated after purging the slurry of silica supported Rh_{55}-DAc in MeOH with H_2 shows the detection of a compound with an average molecular weight of 273.2 g mol^{-1}. This molecular weight is compatible with the hydrogenation of the DAc ligand, generating a diol and carbon monoxide as a by-product (Scheme 6.2). However, ^1H NMR results indicated that the reaction does not proceed in a clean fashion. No protons were observed downfield, corresponding to the proposed alcohol species. Furthermore, the integration and chemical shifts of the peaks observed were not consistent with either the original capping agent or the proposed structure (Figure 6.21). Thus, this experiment was inconclusive even though there was evidence of chemical changes occurring in the system.

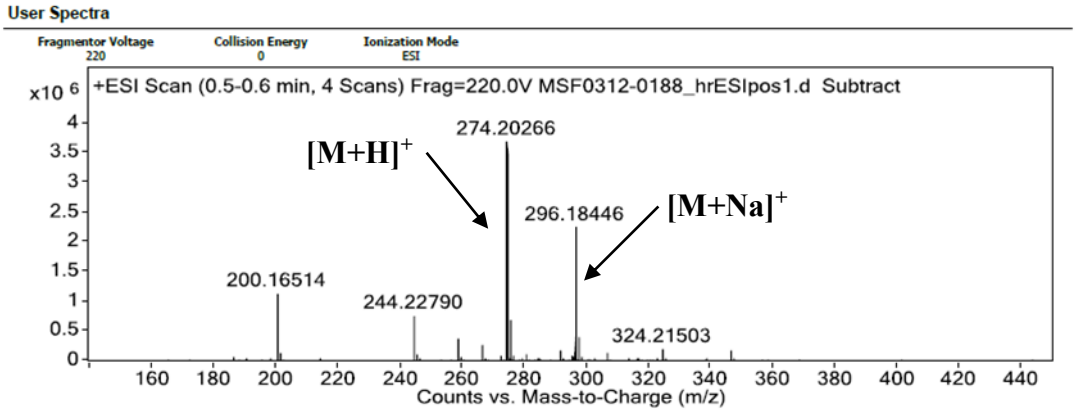

Figure 6.20. Spectrum acquired using mass spectrometry after H_2 purging silica supported Rh_{55}-DAc seeds in MeOH at room temperature.

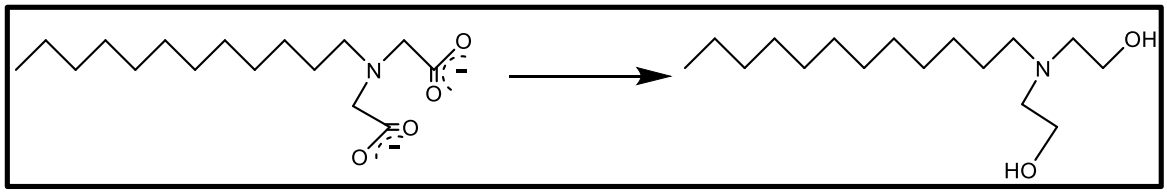

Scheme 6.2. Proposed reaction scheme for the self-activation of DAc after silica supported Rh_{55}-DAc clusters were purged with H_2 in MeOH.

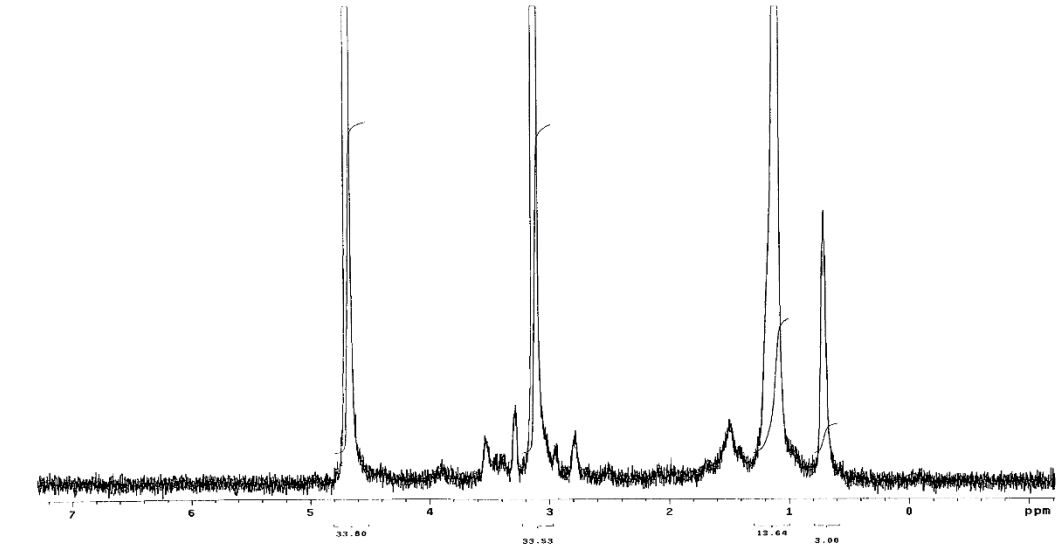

Figure 6.21. ^{1}H NMR spectrum acquired after H_2 purge of silica supported Rh_{55}-DAc seeds in MeOH at room temperature.

The supernatant that was isolated after the supported Rh_{55}-DAm clusters was also analyzed using MS and ^{1}H NMR spectroscopy. Mass spectrometry only detected dodecyl iminodiacetamide (neat ligand) as can be observed in Figure 6.22; no other products were identified. Similarly to what was observed for Rh_{55}-DAc NPs under the same experimental conditions, the ^{1}H NMR spectrum (Figure 6.23) displayed a mixture of peaks that were not consistent with the sole presence of pure ligand. Moreover, there were no peaks downfield where the protons of the NH_2 in the amide functional group of DAm appear. Thus, this experiment also yielded inconclusive results.

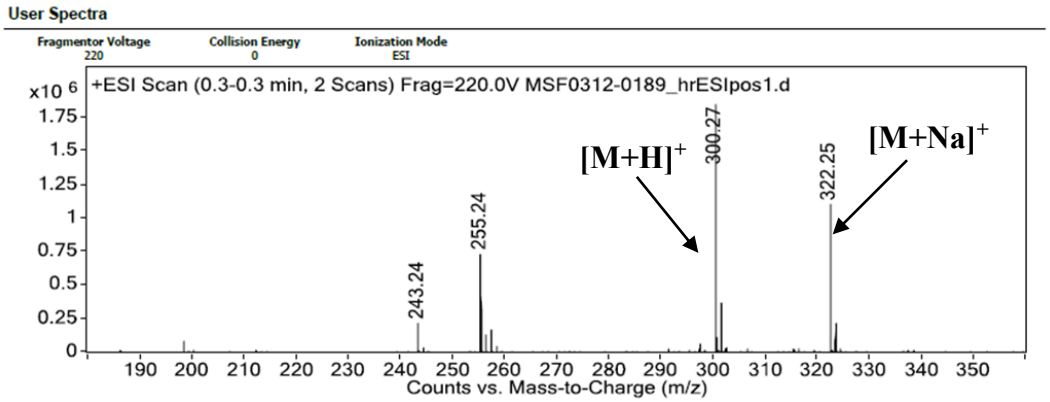

Figure 6.22. Spectrum acquired using mass spectrometry after silica supported Rh_{55}-DAm seeds were purged with H_2 in MeOH at room temperature.

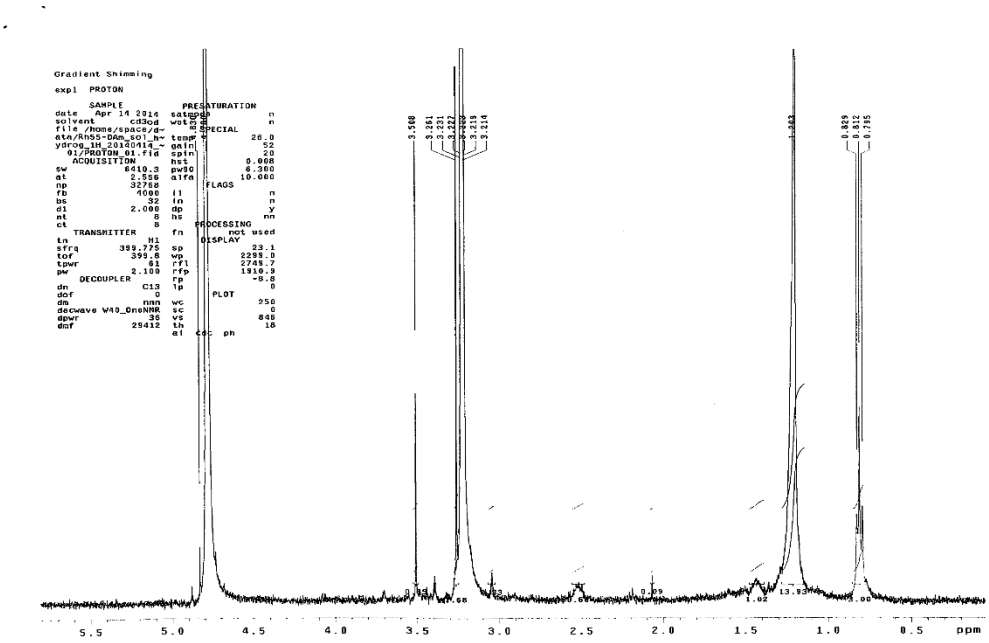

Figure 6.23. ^1H NMR spectrum acquired after H_2 purge of silica supported Rh_{55}-DAm seeds in MeOH at room temperature.

6.3.2.2 Solution Phase Hydrogenation (High Boiling Point Solvents)

Given that the experiments conducted at room temperature were not successful, the same set of reactions were carried out at higher temperatures (118 °C for Rh_{55}-DAc NPs, and 160 °C for Rh_{55}-DAm and Rh_{55}-PVP clusters). The products of the catalytic reactions were characterized as described in the previous section.

Mass spectrometry analysis of the reaction products after the silica supported Rh_{55}-DAc seeds were placed in ^{n}BuOH and purged with H_2 for approximately 21 h revealed the potential existence of a compound with molecular weight of 390.3 g mol^{-1} along with unaltered free DAc ligand (Figure 6.24).

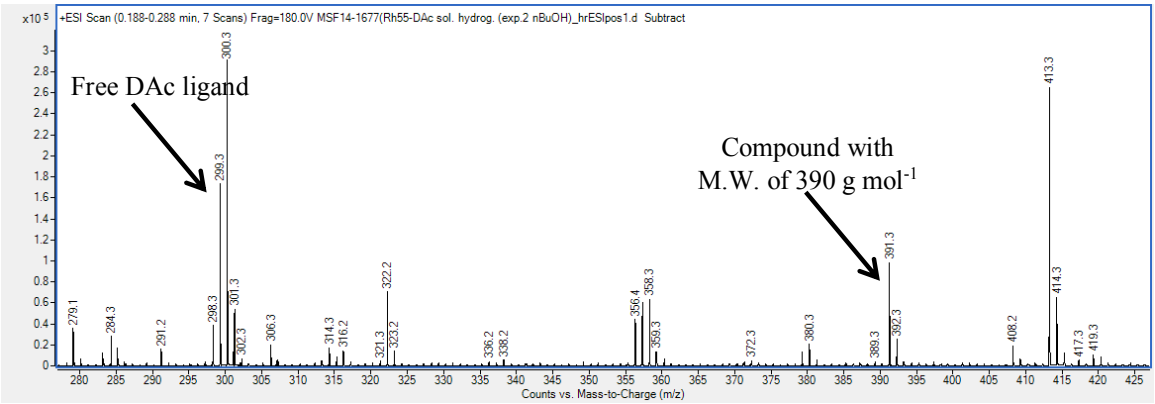

Figure 6.24. Spectrum acquired using mass spectrometry after H_2 purging silica supported Rh_{55}-DAc seeds in ^{n}BuOH at 118 °C for 21 h.

FT-IR experiments showed that the carbonyl band, that originally appeared at 1616 cm^{-1} for Rh_{55}-DAc clusters, had completely vanished after the H_2 purge at elevated temperatures (Figure 6.25). Unfortunately, no O–H stretches were observed; the presence of this type of bands would be indicative of the hydrogenation of the carbonyl groups and

conversion of the ligand to a diol. New stretching frequencies at 1082 and 1012 cm^{-1} also appear after the reaction, which are consistent with C–O stretches of an ester functional group. These bands only appear after the prolonged H_2 purge at raised temperatures and cannot be assigned to amorphous silica or the reaction solvent. It is reasonable to believe then that these stretching frequencies emerge from a mixture of products and impurities. This hypothesis is supported by ^1H NMR analysis (Figure 6.26). The integrations observed can only be rationalized if there is a mixture of products in the sample being analyzed.

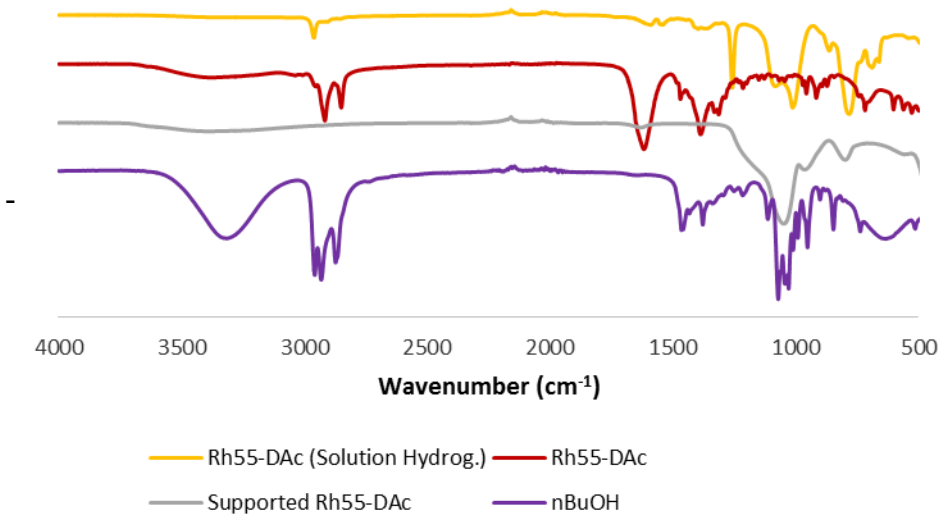

Figure 6.25. Overlayed FT-IR spectra of the solution hydrogenation attempt of DAc stabilized-Rh_{55} NPs at 118 °C in ^{n}BuOH (gold yellow), the neat Rh_{55}-DAc particles (red), the silica supported Rh_{55}-DAc NPs (gray) and the ^{n}BuOH solvent (purple).

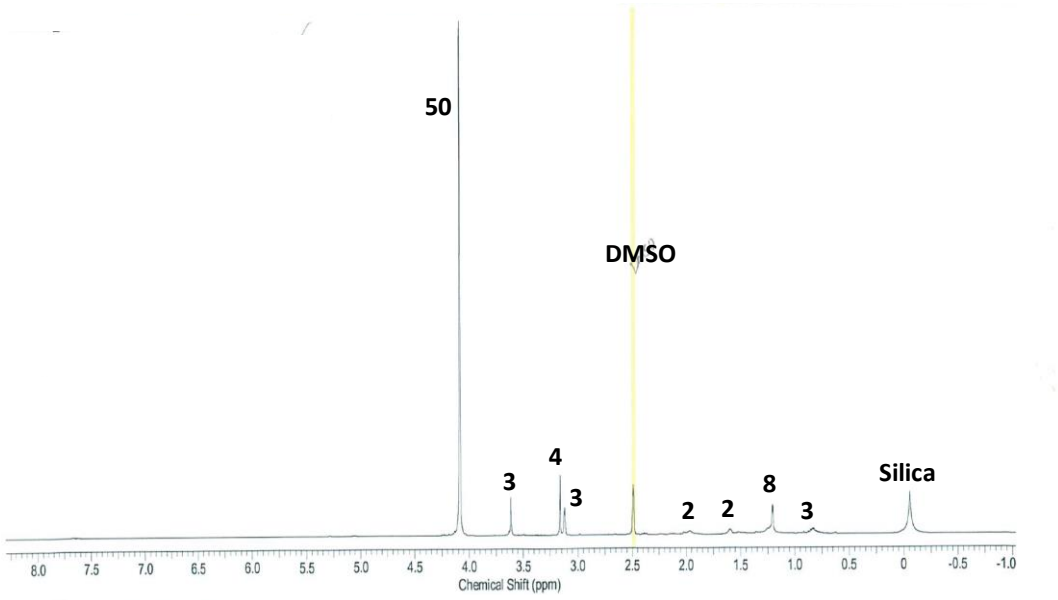

Figure 6.26. ^{1}H NMR spectrum acquired purging silica supported Rh_{55}-DAc seeds with H_2 in ^{n}BuOH at 118 °C for 21 h.

Analysis of the products generated after Rh_{55}-DAm NPs were purged with molecular hydrogen at 160 °C, also showed the generation of a mixture of species. Mass spectrometry results were not consistent or reproducible, as different trials of the same experiment yielded different masses. Unlike the hydrogenation attempts performed using Rh_{55}-DAc seeds, FT-IR of the hydrogenation attempts carried out utilizing Rh_{55}-DAm clusters displayed a marked shift (and broadening) of the carbonyl band from 1671 cm^{-1} to 1628 cm^{-1} (Figure 6.27) and not a disappearance of the carbonyl band. However, the same stretching frequencies at 1085 and 1011 cm^{-1} emerged, as observed above with Rh_{55}-DAc NPs, along with an additional frequency at 1259 cm^{-1}. The ^{1}H NMR spectrum

also displayed a mixture of products (Figure 6.28), confirming that the experimental conditions do not allow the desired chemical reaction to proceed in a clean and effective manner.

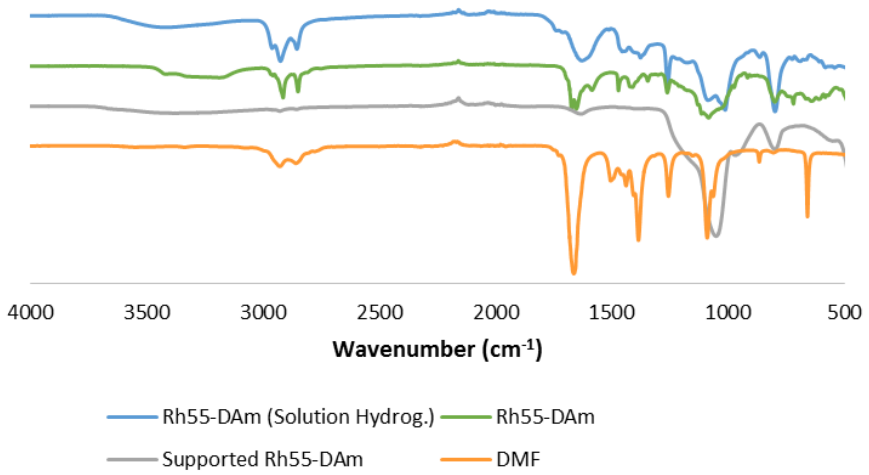

Figure 6.27. Overlayed FT-IR spectra of the solution hydrogenation attempt of DAm stabilized-Rh_{55} NPs at 160 °C in DMF (blue), the neat Rh_{55}-DAm particles (green), the silica supported Rh_{55}-DAc NPs (gray) and the DMF solvent (orange).

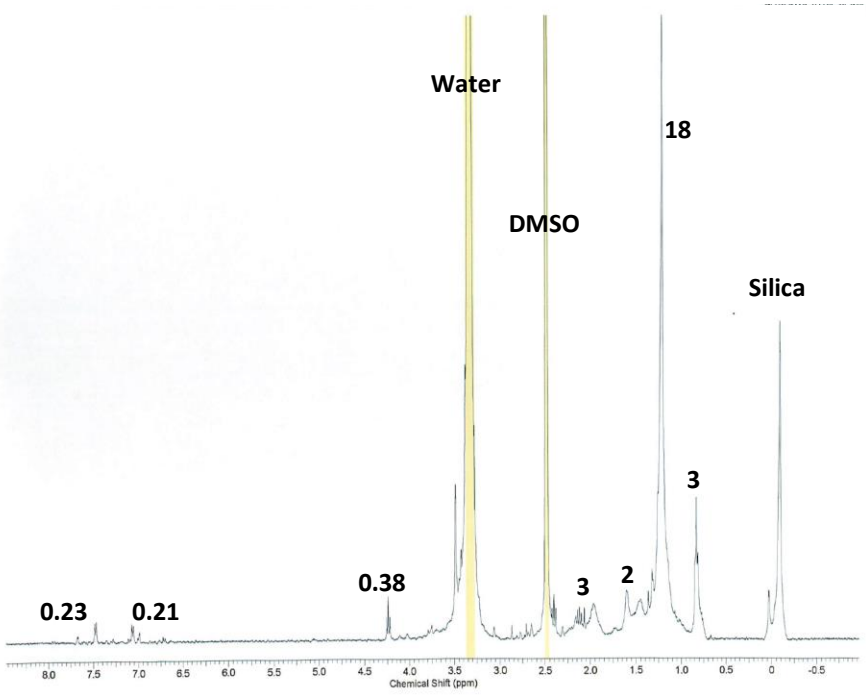

Figure 6.28. ^{1}H NMR spectrum acquired purging silica supported Rh_{55}-DAm seeds with H_2 in DMF at 160 °C for 21 h.

6.3.2.3 Vapor Phase Hydrogenation

The pre-catalysts were heated to a wide range of temperatures (40–150 °C) under a hydrogenation catalysis environment in an attempt to trigger the catalytic hydrogenation of the head groups in the novel monomeric capping agents. The hydrogenation of these functional groups will inhibit the interaction between the ligand and the NP surface, ultimately leading to higher catalytic activities caused by a greater amount of the surface being exposed. In order to gauge the degree of self-activation of

the Rh_{55} derivatives, if any, cyclohexene hydrogenation catalysis was performed after every activation period.

In the case of DAc stabilized-Rh_{55} NPs, a systematic increase in TOF and decrease in induction period length was observed for activation temperatures up to 100 °C (Figure 6.29). When the catalysts were activated at 120 °C, the activity during the induction period was greater than that observed for any of the other activation temperatures. Nonetheless, the particles reached steady state at approximately 2.5, which is comparable to the turnover frequency observed when the particles were activated at 60–70 °C. Activation at even higher temperatures led to significant loss in activity as shown by the orange line in Figure 6.29.

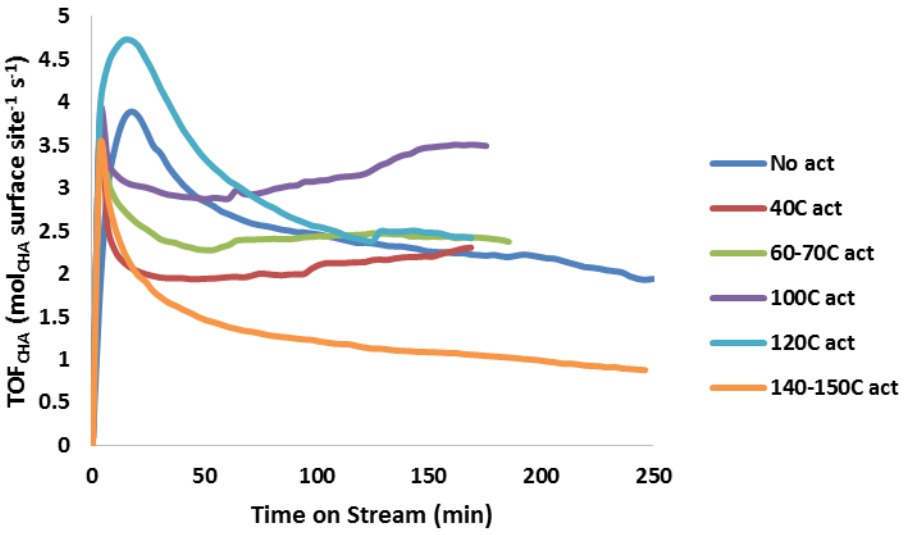

Figure 6.29. Turnover frequency values for the vapor-phase catalytic hydrogenation of cyclohexene using Rh_{55}-DAc seeds after being activated at a variety of temperatures.

Rh_{55}-DAm NPs proved to be approximately four times more active, and more stable than the Rh_{55}-DAc seeds. It is worth noting that the NPs reached steady state in the first 5 min of the catalysis runs and there was no activity loss throughout time for any given run. The DAm capped-Rh NPs displayed TOF values of 10 (compared to 2.5 for Rh_{55}-DAc seeds) without activation at elevated temperatures (Figure 6.30). As the temperature was increased in every activation period, a slight increase in activity was observed until the temperature reached 100 °C. After this point, a 20 °C increase generated no enhancement of the catalytic activity. However, when the particles were activated at 140–150 °C, the activity displayed by the particles was comparable to that of the same material when no activation had been performed.

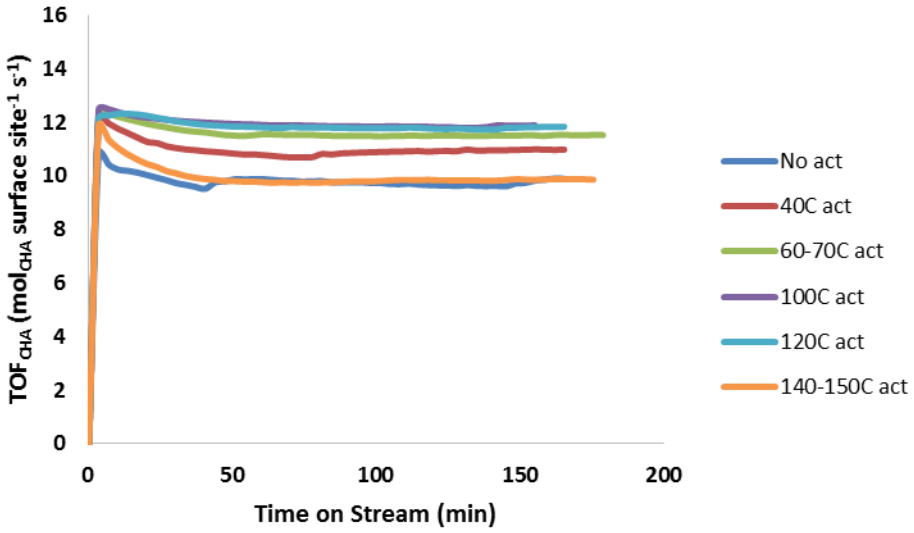

Figure 6.30. Turnover frequency values for the vapor-phase catalytic hydrogenation of cyclohexene using Rh_{55}-DAm clusters after being activated at a wide range of temperatures.

To our surprise, Rh_{55}-PVP seeds displayed the highest activity of all of the NPs stabilized by the different capping agents studied. After a distinct induction period, the catalytic activity of the PVP capped-Rh NPs that had not been activated, reached steady state at TOFs of approximately 10 (Figure 6.31), similar to what was observed for the Rh_{55}-DAm clusters. When the particles were activated at 40 °C, the hydrogenation catalysis experienced *ca.* a two-fold increase in activity. Activation at 60–70 °C, also led to catalytic enhancement. When the activation temperature surpassed 100 °C, a decrease in activity was observed as seen in Figure 6.31 (purple line = 100 °C activation, teal line = 120 °C activation, orange line = 140–150 °C). Despite the loss in activity, the catalytic performance of the PVP capped NPs at higher temperatures was still higher than that of

the Rh_{55}-PVP NPs that had not undergone any activation, and than both Rh_{55}-DAc and Rh_{55}-DAm seeds.

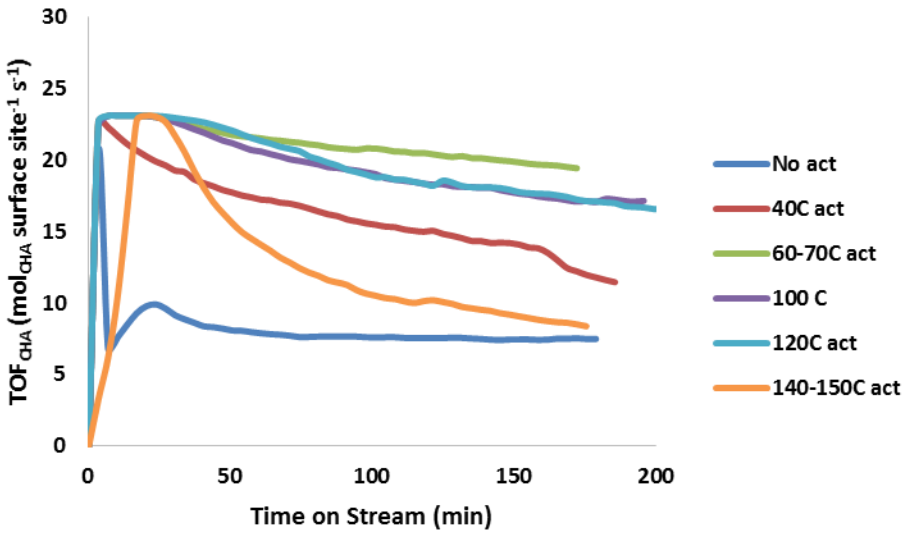

Figure 6.31. Turnover frequency values for the vapor-phase catalytic hydrogenation of cyclohexene using Rh_{55}-PVP NPs after being activated at a variety of temperatures.

6.4 CONCLUSION

In summary, very effective novel monomeric capping agents have been synthesized and successful ligand exchange reactions have been carried out using Rh_{55} seeds. Nonetheless, self-activation experiments of these capping agents utilizing the well-defined metallic seeds as triggers (hydrogenation catalysts), have yielded no conclusive results. Different sets of experimental conditions (and even different trials of the same set of conditions) displayed too much variability. Thus, it is still necessary to determine the

precise experimental conditions that will drive the target reaction forward, in a clean and controlled fashion. This way, extremely active catalysts can be generated under very mild and environmentally-friendly conditions.

7. Significant Results and Future Directions

7.1 KEY RESULTS

- Microwave heating (μwH) provided fine control over the kinetic parameters of formation for Rh, Pd and Pt monometallic nanoparticles (NPs).
- With the aid of μwH, the facile and effective replacement of polymeric capping agents (such as PVP) with monomeric ligands (such as oleic acid and oleylamine) was achieved even though this represent a thermodynamically challenging process.
- μwH allowed for the accessibility of 'non-equilibrium' configurations in the case of Au-Rh and Ag-Rh core-shell NPs, due to the fact that both Au and Ag have lower surface energies than Rh. Furthermore, it was possible to tune the shell thickness in order to tailor the NPs for specific applications.
- Significant catalytic enhancement, *per* mole of Rh used, was observed when the most expensive and rare metal in core-shell structures was diluted by using a sacrificial monometallic core.
- Immiscible metals were made miscible in the nanoscale, by employing μwH, and it was also possible to tune the composition of these alloys over a wide range.
- Dramatic enhancements in activity (for hydrogenation catalysis) were observed not only due to dilution factors (*per* mole of Rh employed), but also due *d*-band mixing effects that ultimately shift the Fermi level

throughout the alloy and generate specific tree-fold surface sites with strong H adsorption (H binding is used as a reaction descriptor for H_2 activation, which is considered to be the rate-limiting step). Theoretical calculations support this claim.

- Novel monomeric capping agents were successfully synthesized. These stabilizing agents can easily displace other monomeric ligands such as PPh_3 for the effective surface passivation of small metallic clusters such as Rh_{55} seeds.

7.2 FUTURE DIRECTIONS

- Develop a successful synthetic method for the preparation of monometallic core-alloyed shell nanostructures. It is relevant to study the kinetics of formations of these NPs such as reduction potentials, metal-metal interactions and possible complexation of the metal ions to reductants and surface passivating agents.
- Perform hydrogenation catalysis utilizing monometallic core-alloyed shell NPs.
- Study the oxidation catalytic capabilities of RhAg and RhAu alloyed NPs. Due to the particular mixture of metals in these alloys, this type of NPs can potentially be used in dual catalytic systems such as automotive catalytic converters (simultaneously perform hydrogenation and oxidation catalysis).
- Optimize the experimental conditions for the solution-phase self-activation of novel capping ligands. The ultimate goal is to generate

particles that when placed in a hydrogenation catalysis environment (reducing conditions), these will chemically rid themselves of the stabilizing agents in a clean and controlled fashion under mild conditions.

- Perform catalytic selectivity studies on all the systems developed (core-shell assemblies, alloyed structures and monometallic core-alloy shell architectures), particularly for hydrogenation catalysis.

8. Appendix: Crystallographic Data

Table 8.1. Crystal data and structure refinement for dodecyl iminodiacetate.

Identification code	**shelx**	
Empirical formula	C17 H34 N Na O5	
Formula weight	355.44	
Temperature	153(2) K	
Wavelength	0.71075 Å	
Crystal system	Triclinic	
Space group	P -1	
Unite cell dimensions	a = 5.280 (2) Å	α= 92.565(6)°
	b = 9.448(3) Å	β= 91.231(6)°
	c = 20.087 Å	γ= 97.010(6)°
Volume	993.2(6) $Å^3$	
Z	2	
Density (calculated)	1.189 Mg/m^3	
Absorption coefficient	0.104 mm-1	
F(000)	388	
Crystal size	0.660 x 0.100 x 0.050 mm^3	
Theta range for data collection	3.659 to 27.481°	
Index ranges	-6<=h<=6, -12<=h<=12, -26<=l<=26	
Reflections collected	10097	
Independent reflections	4497 [R(int) = 0.0414]	
Completeness to theta = 25.242°	99.6%	

Table 8.1 Continued

Refinement method	Full-matrix least squares on F^2
Data / restraints / parameters	4497 / 0 / 261
Goodness-of-fit on F^2	1.013
Final R indices [I>2sigma(I)]	R1 = 0.0450, wR2 = 0.1040
R indices (all data)	R1 = 0.0674, wR2 = 0.1154
Extinction coefficient	n/a
Largest diff. peak and hole	0.267 and -0.214 e. $Å^{-3}$

Table 8.2. Atomic coordinates (x 10^4) and equivalent isotropic displacement parameters ($Å^2$x 10^3) for dodecyl iminodiacetate. U(eq) is defined as one third of the trace of the orthogonalized U^{ij} tensor.

	x	y	z	U(eq)
C(1)	-3783(3)	2969(2)	8832(1)	20(1)
C(2)	-2313(3)	1933(2)	9202(1)	19(1)
C(3)	-2539(3)	5519(2)	9207(1)	20(1)
C(4)	-5111(3)	6082(2)	9104(1)	20(1)
C(5)	-1772(3)	4717(2)	8025(1)	20(1)
C(6)	-462(3)	3611(2)	7633(1)	25(1)
C(7)	837(3)	4190(2)	7015(1)	27(1)
C(8)	2287(3)	3089(2)	6661(1)	30(1)
C(9)	3750(3)	3628(2)	6061(1)	31(1)
C(10)	5241(3)	2521(2)	5728(1)	32(1)
C(11)	6735(3)	3055(2)	5131(1)	32(1)
C(12)	8216(3)	1950(2)	4793(1)	32(1)

Table 8.2 Continued

C(13)	9680(3)	2491(2)	4193(1)	33(1)
C(14)	11157(4)	1399(2)	3846(1)	34(1)
C(15)	12554(4)	1940(2)	3238(1)	44(1)
C(16)	14029(5)	833(3)	2897(1)	58(1)
C(17)	871(4)	-941(2)	8580(1)	35(1)
N(1)	-2045(2)	4320(1)	8736(1)	17(1)
O(1)	36(2)	2309(1)	9303(1)	24(1)
O(2)	-3616(2)	810(1)	9358(1)	22(1)
O(3)	-5385(2)	7135(1)	9490(1)	26(1)
O(4)	-6668(2)	5480(1)	8676(1)	27(1)
O(5)	910(2)	-1159(1)	9273(1)	23(1)
Na(1)	2564(1)	1016(1)	9976(1)	20(1)

Table 8.3. Bond lengths [Å] and angles [°] for dodecyl iminodiacetate.

C(1)-N(1)	1.5009(19)	C(5)-H(5B)	0.954(17)
C(1)-C(2)	1.528(2)	C(5)-H(5A)	0.991(17)
C(1)-H(1B)	0.944(17)	C(6)-C(7)	1.521(2)
C(1)-H(1A)	0.978(17)	C(6)-H(6A)	0.9900
C(2)-O(2)	1.2493(18)	C(6)-H(6B)	0.9900
C(2)-O(1)	1.2574(19)	C(7)-C(8)	1.525(2)
C(3)-N(1)	1.494(2)	C(7)-H(7A)	0.9900
C(3)-C(4)	1.531(2)	C(7)-H(7B)	0.9900
C(3)-H(3B)	0.973(19)	C(8)-C(9)	1.519(2)
C(3)-H(3A)	0.974(17)	C(8)-H(8A)	0.9900
C(4)-O(4)	1.2437(19)	C(8)-H(8B)	0.9900
C(4)-O(3)	1.2582(18)	C(9)-C(10)	1.524(2)
C(5)-N(1)	1.4997(19)	C(9)-H(9A)	0.9900
C(5)-C(6)	1.522(2)	C(9)-H(9B)	0.9900

Table 8.3 Continued

C(10)-C(11)	1.521(2)	O(5)-Na(1)	2.4950(14)
C(10)-H(10A)	0.9900	O(5)-H(5M)	0.85(2)
C(10)-H(10B)	0.9900	Na(1)-O(2)#1	2.3419(13)
C(11)-C(12)	1.524(2)	Na(1)-O(3)#3	2.3562(14)
C(11)-H(11A)	0.9900	Na(1)-O(5)#1	2.4128(14)
C(11)-H(11B)	0.9900	Na(1)-O(2)#4	2.4140(14)
C(12)-C(13)	1.520(2)	Na(1)-Na(1)#1	3.1284(14)
C(12)-H(12A)	0.9900	Na(1)-Na(1)#5	3.3954(15)
C(12)-H(12B)	0.9900	N(1)-C(1)-C(2)	109.18(12)
C(13)-C(14)	1.521(2)	N(1)-C(1)-H(1B)	107.8(10)
C(13)-H(13A)	0.9900	C(2)-C(1)-H(1B)	109.8(10)
C(13)-H(13B)	0.9900	N(1)-C(1)-H(1A)	108.4(10)
C(14)-C(15)	1.516(3)	C(2)-C(1)-H(1A)	112.7(10)
C(14)-H(14A)	0.9900	H(1B)-C(1)-H(1A)	108.9(14)
C(14)-H(14B)	0.9900	O(2)-C(2)-O(1)	128.43(14)
C(15)-C(16)	1.527(3)	O(2)-C(2)-C(1)	115.14(13)
C(15)-H(15A)	0.9900	O(1)-C(2)-C(1)	116.42(13)
C(15)-H(15B)	0.9900	N(1)-C(3)-C(4)	115.33(13)
C(16)-H(16A)	0.9800	N(1)-C(3)-H(3B)	108.5(11)
C(16)-H(16B)	0.9800	C(4)-C(3)-H(3B)	110.8(11)
C(16)-H(16C)	0.9800	N(1)-C(3)-H(3A)	107.3(10)
C(17)-O(5)	1.418(2)	C(4)-C(3)-H(3A)	107.7(10)
C(17)-H(17B)	0.95(3)	H(3B)-C(3)-H(3A)	106.9(15)
C(17)-H(17A)	0.99(3)	O(4)-C(4)-O(3)	127.55(14)
C(17)-H(17C)	0.97(3)	O(4)-C(4)-C(3)	119.51(13)
N(1)-H(1N)	0.915(19)	O(3)-C(4)-C(3)	112.94(13)
O(1)-Na(1)	2.3591(13)	N(1)-C(5)-C(6)	110.28(12)
O(2)-Na(1)#1	2.3419(13)	N(1)-C(5)-H(5B)	107.0(10)
O(2)-Na(1)#2	2.4140(14)	C(6)-C(5)-H(5B)	115.0(10)
O(3)-Na(1)#3	2.3561(13)	N(1)-C(5)-H(5A)	106.2(9)
O(5)-Na(1)#1	2.4127(14)	C(6)-C(5)-H(5A)	111.1(9)

Table 8.3 Continued

H(5B)-C(5)-H(5A)	106.8(13)	C(10)-C(11)-C(12)	114.14(15)
C(7)-C(6)-C(5)	113.20(13)	C(10)-C(11)-H(11A)	108.7
C(7)-C(6)-H(6A)	108.9	C(12)-C(11)-H(11A)	108.7
C(5)-C(6)-H(6A)	108.9	C(10)-C(11)-H(11B)	108.7
C(7)-C(6)-H(6B)	108.9	C(12)-C(11)-H(11B)	108.7
C(5)-C(6)-H(6B)	108.9	H(11A)-C(11)-H(11B)	107.6
H(6A)-C(6)-H(6B)	107.8	C(13)-C(12)-C(11)	113.69(15)
C(6)-C(7)-C(8)	111.91(14)	C(13)-C(12)-H(12A)	108.8
C(6)-C(7)-H(7A)	109.2	C(11)-C(12)-H(12A)	108.8
C(8)-C(7)-H(7A)	109.2	C(13)-C(12)-H(12B)	108.8
C(6)-C(7)-H(7B)	109.2	C(11)-C(12)-H(12B)	108.8
C(8)-C(7)-H(7B)	109.2	H(12A)-C(12)-H(12B)	107.7
H(7A)-C(7)-H(7B)	107.9	C(12)-C(13)-C(14)	114.43(15)
C(9)-C(8)-C(7)	114.55(15)	C(12)-C(13)-H(13A)	108.7
C(9)-C(8)-H(8A)	108.6	C(14)-C(13)-H(13A)	108.7
C(7)-C(8)-H(8A)	108.6	C(12)-C(13)-H(13B)	108.7
C(9)-C(8)-H(8B)	108.6	C(14)-C(13)-H(13B)	108.7
C(7)-C(8)-H(8B)	108.6	H(13A)-C(13)-H(13B)	107.6
H(8A)-C(8)-H(8B)	107.6	C(15)-C(14)-C(13)	113.88(16)
C(8)-C(9)-C(10)	113.48(15)	C(15)-C(14)-H(14A)	108.8
C(8)-C(9)-H(9A)	108.9	C(13)-C(14)-H(14A)	108.8
C(10)-C(9)-H(9A)	108.9	C(15)-C(14)-H(14B)	108.8
C(8)-C(9)-H(9B)	108.9	C(13)-C(14)-H(14B)	108.8
C(10)-C(9)-H(9B)	108.9	H(14A)-C(14)-H(14B)	107.7
H(9A)-C(9)-H(9B)	107.7	C(14)-C(15)-C(16)	113.24(18)
C(11)-C(10)-C(9)	113.88(15)	C(14)-C(15)-H(15A)	108.9
C(11)-C(10)-H(10A)	108.8	C(16)-C(15)-H(15A)	108.9
C(9)-C(10)-H(10A)	108.8	C(14)-C(15)-H(15B)	108.9
C(11)-C(10)-H(10B)	108.8	C(16)-C(15)-H(15B)	108.9
C(9)-C(10)-H(10B)	108.8	H(15A)-C(15)-H(15B)	107.7
H(10A)-C(10)-H(10B)	107.7	C(15)-C(16)-H(16A)	109.5

Table 8.3 Continued

C(15)-C(16)-H(16B)	109.5	O(2)#1-Na(1)-O(5)#1	84.75(5)
H(16A)-C(16)-H(16B)	109.5	O(3)#3-Na(1)-O(5)#1	96.46(5)
C(15)-C(16)-H(16C)	109.5	O(1)-Na(1)-O(5)#1	82.07(5)
H(16A)-C(16)-H(16C)	109.5	O(2)#1-Na(1)-O(2)#4	88.90(4)
H(16B)-C(16)-H(16C)	109.5	O(3)#3-Na(1)-O(2)#4	79.51(5)
O(5)-C(17)-H(17B)	114.9(16)	O(1)-Na(1)-O(2)#4	105.37(5)
O(5)-C(17)-H(17A)	108.3(17)	O(5)#1-Na(1)-O(2)#4	172.07(5)
H(17B)-C(17)-H(17A)	105(2)	O(2)#1-Na(1)-O(5)	78.32(5)
O(5)-C(17)-H(17C)	112.9(18)	O(3)#3-Na(1)-O(5)	161.38(5)
H(17B)-C(17)-H(17C)	106(2)	O(1)-Na(1)-O(5)	87.64(5)
H(17A)-C(17)-H(17C)	109(2)	O(5)#1-Na(1)-O(5)	100.82(4)
C(3)-N(1)-C(5)	114.46(12)	O(2)#4-Na(1)-O(5)	82.49(4)
C(3)-N(1)-C(1)	112.95(12)	O(2)#1-Na(1)-Na(1)#1	76.58(4)
C(5)-N(1)-C(1)	114.56(12)	O(3)#3-Na(1)-Na(1)#1	147.42(5)
C(3)-N(1)-H(1N)	105.8(11)	O(1)-Na(1)-Na(1)#1	81.99(4)
C(5)-N(1)-H(1N)	105.4(12)	O(5)#1-Na(1)-Na(1)#1	51.57(4)
C(1)-N(1)-H(1N)	102.1(12)	O(2)#4-Na(1)-Na(1)#1	131.27(4)
C(2)-O(1)-Na(1)	122.00(10)	O(5)-Na(1)-Na(1)#1	49.25(3)
C(2)-O(2)-Na(1)#1	130.54(10)	O(2)#1-Na(1)-Na(1)#5	45.30(3)
C(2)-O(2)-Na(1)#2	117.96(9)	O(3)#3-Na(1)-Na(1)#5	87.09(4)
Na(1)#1-O(2)-Na(1)#2	91.10(4)	O(1)-Na(1)-Na(1)#5	146.15(4)
C(4)-O(3)-Na(1)#3	134.45(10)	O(5)#1-Na(1)-Na(1)#5	129.87(4)
C(17)-O(5)-Na(1)#1	126.83(12)	O(2)#4-Na(1)-Na(1)#5	43.60(3)
C(17)-O(5)-Na(1)	113.94(11)	O(5)-Na(1)-Na(1)#5	76.55(4)
Na(1)#1-O(5)-Na(1)	79.18(4)	Na(1)#1-Na(1)-Na(1)#5	107.99(4)
C(17)-O(5)-H(5M)	108.3(13)		
Na(1)#1-O(5)-H(5M)	120.4(13)		
Na(1)-O(5)-H(5M)	99.7(13)		
O(2)#1-Na(1)-O(3)#3	96.56(5)		
O(2)#1-Na(1)-O(1)	158.57(5)		
O(3)#3-Na(1)-O(1)	101.64(5)		

Symmetry transformations used to generate equivalent atoms:

#1 -x,-y,-z+2 #2 x-1,y,z #3 -x,-y+1,-z+2 #4 x+1,y,z #5 -x+1,-y,-z+2

Table 8.4. Anisotropic displacement parameters ($Å^2 x\ 10^3$) for dodecyl iminodiacetate. The anisotropic displacement factor exponent takes the form: $-2\pi^2[h^2 a^{*2} U^{11} + \ldots + 2\ h\ k\ a^*\ b^*\ U^{12}]$

	U^{11}	U^{22}	U^{33}	U^{23}	U^{13}	U^{12}
C(1)	16(1)	17(1)	28(1)	4(1)	1(1)	0(1)
C(2)	18(1)	20(1)	18(1)	1(1)	4(1)	5(1)
C(3)	17(1)	20(1)	22(1)	-2(1)	1(1)	2(1)
C(4)	17(1)	17(1)	27(1)	3(1)	4(1)	2(1)
C(5)	18(1)	20(1)	21(1)	4(1)	1(1)	2(1)
C(6)	24(1)	24(1)	26(1)	-1(1)	4(1)	4(1)
C(7)	26(1)	31(1)	25(1)	0(1)	4(1)	5(1)
C(8)	30(1)	34(1)	28(1)	-1(1)	5(1)	7(1)
C(9)	31(1)	33(1)	30(1)	-2(1)	7(1)	6(1)
C(10)	32(1)	36(1)	28(1)	-2(1)	6(1)	7(1)
C(11)	31(1)	36(1)	30(1)	-1(1)	6(1)	7(1)
C(12)	33(1)	37(1)	28(1)	0(1)	7(1)	7(1)
C(13)	33(1)	35(1)	30(1)	-1(1)	7(1)	6(1)
C(14)	33(1)	38(1)	31(1)	-3(1)	6(1)	7(1)
C(15)	44(1)	51(1)	36(1)	-2(1)	14(1)	6(1)
C(16)	55(2)	75(2)	47(1)	-7(1)	21(1)	19(1)
C(17)	47(1)	36(1)	25(1)	-1(1)	3(1)	10(1)
N(1)	12(1)	17(1)	22(1)	2(1)	0(1)	1(1)
O(1)	15(1)	24(1)	34(1)	8(1)	1(1)	4(1)
O(2)	21(1)	17(1)	29(1)	5(1)	5(1)	3(1)
O(3)	20(1)	25(1)	34(1)	-6(1)	1(1)	7(1)
O(4)	18(1)	27(1)	35(1)	-5(1)	-4(1)	5(1)
O(5)	20(1)	24(1)	26(1)	2(1)	2(1)	6(1)
Na(1)	16(1)	18(1)	27(1)	3(1)	2(1)	3(1)

Table 8.5. Torsion angles [°] for dodecyl iminodiacetate.

N(1)-C(1)-C(2)-O(2)	174.55(13)
N(1)-C(1)-C(2)-O(1)	-6.06(19)
N(1)-C(3)-C(4)-O(4)	4.2(2)
N(1)-C(3)-C(4)-O(3)	-176.69(13)
N(1)-C(5)-C(6)-C(7)	-156.63(13)
C(5)-C(6)-C(7)-C(8)	176.00(14)
C(6)-C(7)-C(8)-C(9)	-176.77(15)
C(7)-C(8)-C(9)-C(10)	178.38(15)
C(8)-C(9)-C(10)-C(11)	-179.42(15)
C(9)-C(10)-C(11)-C(12)	-179.63(15)
C(10)-C(11)-C(12)-C(13)	179.43(16)
C(11)-C(12)-C(13)-C(14)	-179.61(15)
C(12)-C(13)-C(14)-C(15)	178.54(16)
C(13)-C(14)-C(15)-C(16)	179.93(18)
C(4)-C(3)-N(1)-C(5)	66.38(17)
C(4)-C(3)-N(1)-C(1)	-67.14(17)
C(6)-C(5)-N(1)-C(3)	161.90(13)
C(6)-C(5)-N(1)-C(1)	-65.34(17)
C(2)-C(1)-N(1)-C(3)	-103.48(15)
C(2)-C(1)-N(1)-C(5)	123.05(14)
O(2)-C(2)-O(1)-Na(1)	-8.4(2)
C(1)-C(2)-O(1)-Na(1)	172.34(10)
O(1)-C(2)-O(2)-Na(1)#1	8.8(2)
C(1)-C(2)-O(2)-Na(1)#1	-171.92(10)
O(1)-C(2)-O(2)-Na(1)#2	127.63(15)
C(1)-C(2)-O(2)-Na(1)#2	-53.07(16)
O(4)-C(4)-O(3)-Na(1)#3	-152.30(13)
C(3)-C(4)-O(3)-Na(1)#3	28.7(2)

Symmetry transformations used to generate equivalent atoms:

#1 -x,-y,-z+2 #2 x-1,y,z #3 -x,-y+1,-z+2 #4 x+1,y,z #5 -x+1,-y,-z+2

Table 8.6. Crystallographic data and structure refinement for dodecyl iminodiacetamide.

Identification code	**shelx**	
Empirical formula	C16 H33 N3 O2	
Formula weight	299.45	
Temperature	293(2) K	
Wavelength	0.71073 Å	
Crystal system	Triclinic	
Space group	P -1	
Unite cell dimensions	a = 5.319 Å	α= 79.71°
	b = 8.094 Å	β= 89.62°
	c = 20.987 Å	γ= 82.32°
Volume	880.9 $Å^3$	
Z	2	
Density (calculated)	1.129 Mg/m^3	
Absorption coefficient	0.075 mm-1	
F(000)	332	
Crystal size	0.100 x 0.100 x 0.100 mm^3	
Theta range for data collection	3.520 to 28.000°	
Index ranges	-6<=h<=6, -10<=h<=10, -26<=l<=27	
Reflections collected	9846	
Independent reflections	3959 [R(int) = 0.0328]	
Completeness to theta = 25.242°	99.6%	
Refinement method	Full-matrix least squares on F^2	
Data / restraints / parameters	3959 / 0 / 207	

Table 8.6 Continued

Goodness-of-fit on F^2	0.799
Final R indices [I>2sigma(I)]	R1 = 0.0469, wR2 = 0.1272
R indices (all data)	R1 = 0.0606, wR2 = 0.1416
Extinction coefficient	n/a
Largest diff. peak and hole	0.354 and -0.332 e. $Å^{-3}$

Table 8.7. Atomic coordinates (x 10^4) and equivalent isotropic displacement parameters ($Å^2$x 10^3) for dodecyl iminodiacetamide. U(eq) is defined as one third of the trace of the orthogonalized U^{ij} tensor.

	x	y	z	U(eq)
C(1)	4635(2)	4151(2)	2927(1)	21(1)
C(2)	2145(2)	4456(2)	2565(1)	25(1)
C(3)	2459(3)	5336(2)	1855(1)	25(1)
C(4)	-1(3)	5633(2)	1477(1)	26(1)
C(5)	244(3)	6588(2)	777(1)	25(1)
C(6)	-2246(3)	6911(2)	411(1)	27(1)
C(7)	-2045(3)	7899(2)	-286(1)	26(1)
C(8)	-4554(3)	8222(2)	-645(1)	27(1)
C(9)	-4391(3)	9237(2)	-1338(1)	26(1)
C(10)	-6895(3)	9540(2)	-1698(1)	27(1)
C(11)	-6770(3)	10605(2)	-2383(1)	27(1)
C(12)	-9222(3)	10794(2)	-2753(1)	36(1)
C(13)	3989(2)	1637(2)	3744(1)	21(1)
C(14)	2748(2)	979(2)	4395(1)	20(1)
C(15)	6666(2)	3616(2)	3959(1)	20(1)
C(16)	6747(2)	5400(2)	4082(1)	21(1)
N(1)	4388(2)	3430(1)	3625(1)	19(1)
N(2)	1787(2)	2108(2)	4743(1)	22(1)
N(3)	4520(2)	6363(2)	4099(1)	26(1)
O(1)	2655(2)	-571(1)	4561(1)	29(1)
O(2)	8818(2)	5849(1)	4175(1)	29(1)

Table 8.8. Bond lengths [Å] and angles [°] for dodecyl iminodiacetamide.

C(1)-N(1)	1.4890(15)	C(11)-H(11A)	0.9700
C(1)-C(2)	1.5001(17)	C(11)-H(11B)	0.9700
C(1)-H(1A)	0.9700	C(12)-H(12A)	0.9600
C(1)-H(1B)	0.9700	C(12)-H(12B)	0.9600
C(2)-C(3)	1.5502(18)	C(12)-H(12C)	0.9600
C(2)-H(2A)	0.9700	C(13)-N(1)	1.4710(16)
C(2)-H(2B)	0.9700	C(13)-C(14)	1.5520(18)
C(3)-C(4)	1.5038(17)	C(13)-H(13A)	0.9700
C(3)-H(3A)	0.9700	C(13)-H(13B)	0.9700
C(3)-H(3B)	0.9700	C(14)-O(1)	1.2488(15)
C(4)-C(5)	1.5472(18)	C(14)-N(2)	1.3184(17)
C(4)-H(4A)	0.9700	C(15)-N(1)	1.4426(15)
C(4)-H(4B)	0.9700	C(15)-C(16)	1.5177(17)
C(5)-C(6)	1.5037(18)	C(15)-H(15A)	0.9700
C(5)-H(5A)	0.9700	C(15)-H(15B)	0.9700
C(5)-H(5B)	0.9700	C(16)-O(2)	1.2321(15)
C(6)-C(7)	1.5467(18)	C(16)-N(3)	1.3324(17)
C(6)-H(6A)	0.9700	N(2)-H(2)	0.887(18)
C(6)-H(6B)	0.9700	N(2)-H(1)	0.884(19)
C(7)-C(8)	1.5062(18)	N(3)-H(3)	0.835(19)
C(7)-H(7A)	0.9700	N(3)-H(4)	0.87(2)
C(7)-H(7B)	0.9700	N(1)-C(1)-C(2)	112.42(10)
C(8)-C(9)	1.5458(19)	N(1)-C(1)-H(1A)	109.1
C(8)-H(8A)	0.9700	C(2)-C(1)-H(1A)	109.1
C(8)-H(8B)	0.9700	N(1)-C(1)-H(1B)	109.1
C(9)-C(10)	1.5043(18)	C(2)-C(1)-H(1B)	109.1
C(9)-H(9A)	0.9700	H(1A)-C(1)-H(1B)	107.9
C(9)-H(9B)	0.9700	C(1)-C(2)-C(3)	110.50(11)
C(10)-C(11)	1.5445(19)	C(1)-C(2)-H(2A)	109.6
C(10)-H(10A)	0.9700	C(3)-C(2)-H(2A)	109.6
C(10)-H(10B)	0.9700	C(1)-C(2)-H(2B)	109.6
C(11)-C(12)	1.4991(19)	C(3)-C(2)-H(2B)	109.6

Table 8.8 Continued

H(2A)-C(2)-H(2B)	108.1	C(7)-C(8)-C(9)	112.39(11)
C(4)-C(3)-C(2)	111.69(11)	C(7)-C(8)-H(8A)	109.1
C(4)-C(3)-H(3A)	109.3	C(9)-C(8)-H(8A)	109.1
C(2)-C(3)-H(3A)	109.3	C(7)-C(8)-H(8B)	109.1
C(4)-C(3)-H(3B)	109.3	C(9)-C(8)-H(8B)	109.1
C(2)-C(3)-H(3B)	109.3	H(8A)-C(8)-H(8B)	107.9
H(3A)-C(3)-H(3B)	107.9	C(10)-C(9)-C(8)	112.18(11)
C(3)-C(4)-C(5)	112.48(11)	C(10)-C(9)-H(9A)	109.2
C(3)-C(4)-H(4A)	109.1	C(8)-C(9)-H(9A)	109.2
C(5)-C(4)-H(4A)	109.1	C(10)-C(9)-H(9B)	109.2
C(3)-C(4)-H(4B)	109.1	C(8)-C(9)-H(9B)	109.2
C(5)-C(4)-H(4B)	109.1	H(9A)-C(9)-H(9B)	107.9
H(4A)-C(4)-H(4B)	107.8	C(9)-C(10)-C(11)	112.49(11)
C(6)-C(5)-C(4)	111.77(11)	C(9)-C(10)-H(10A)	109.1
C(6)-C(5)-H(5A)	109.3	C(11)-C(10)-H(10A)	109.1
C(4)-C(5)-H(5A)	109.3	C(9)-C(10)-H(10B)	109.1
C(6)-C(5)-H(5B)	109.3	C(11)-C(10)-H(10B)	109.1
C(4)-C(5)-H(5B)	109.3	H(10A)-C(10)-H(10B)	107.8
H(5A)-C(5)-H(5B)	107.9	C(12)-C(11)-C(10)	112.01(12)
C(5)-C(6)-C(7)	112.39(11)	C(12)-C(11)-H(11A)	109.2
C(5)-C(6)-H(6A)	109.1	C(10)-C(11)-H(11A)	109.2
C(7)-C(6)-H(6A)	109.1	C(12)-C(11)-H(11B)	109.2
C(5)-C(6)-H(6B)	109.1	C(10)-C(11)-H(11B)	109.2
C(7)-C(6)-H(6B)	109.1	H(11A)-C(11)-H(11B)	107.9
H(6A)-C(6)-H(6B)	107.9	C(11)-C(12)-H(12A)	109.5
C(8)-C(7)-C(6)	111.84(11)	C(11)-C(12)-H(12B)	109.5
C(8)-C(7)-H(7A)	109.2	H(12A)-C(12)-H(12B)	109.5
C(6)-C(7)-H(7A)	109.2	C(11)-C(12)-H(12C)	109.5
C(8)-C(7)-H(7B)	109.2	H(12A)-C(12)-H(12C)	109.5
C(6)-C(7)-H(7B)	109.2	H(12B)-C(12)-H(12C)	109.5
H(7A)-C(7)-H(7B)	107.9	N(1)-C(13)-C(14)	116.42(10)

Table 8.8 Continued

N(1)-C(13)-H(13A)	108.2
C(14)-C(13)-H(13A)	108.2
N(1)-C(13)-H(13B)	108.2
C(14)-C(13)-H(13B)	108.2
H(13A)-C(13)-H(13B)	107.3
O(1)-C(14)-N(2)	122.94(12)
O(1)-C(14)-C(13)	119.38(11)
N(2)-C(14)-C(13)	117.67(11)
N(1)-C(15)-C(16)	113.59(10)
N(1)-C(15)-H(15A)	108.8
C(16)-C(15)-H(15A)	108.8
N(1)-C(15)-H(15B)	108.8
C(16)-C(15)-H(15B)	108.8
H(15A)-C(15)-H(15B)	107.7
O(2)-C(16)-N(3)	124.48(12)
O(2)-C(16)-C(15)	119.00(11)
N(3)-C(16)-C(15)	116.50(11)
C(15)-N(1)-C(13)	109.64(10)
C(15)-N(1)-C(1)	107.92(9)
C(13)-N(1)-C(1)	113.53(9)
C(14)-N(2)-H(2)	118.8(11)
C(14)-N(2)-H(1)	118.4(12)
H(2)-N(2)-H(1)	121.3(16)
C(16)-N(3)-H(3)	119.6(12)
C(16)-N(3)-H(4)	123.5(12)
H(3)-N(3)-H(4)	116.0(17)

Table 8.9. Anisotropic displacement parameters ($Å^2 x\ 10^3$) for dodecyl iminodiacetamide. The anisotropic displacement factor exponent takes the form: $-2\pi^2[h^2 a^{*2} U^{11} + \ldots + 2\ h\ k\ a^*\ b^*\ U^{12}]$

	U^{11}	U^{22}	U^{33}	U^{23}	U^{13}	U^{12}
C(1)	21(1)	25(1)	18(1)	-2(1)	0(1)	-7(1)
C(2)	23(1)	30(1)	21(1)	-2(1)	-2(1)	-7(1)
C(3)	25(1)	30(1)	20(1)	-2(1)	-2(1)	-7(1)
C(4)	26(1)	31(1)	21(1)	-2(1)	-2(1)	-6(1)
C(5)	25(1)	30(1)	21(1)	-3(1)	-3(1)	-6(1)
C(6)	26(1)	32(1)	22(1)	-2(1)	-3(1)	-5(1)
C(7)	26(1)	30(1)	21(1)	-2(1)	-3(1)	-6(1)
C(8)	26(1)	31(1)	24(1)	-2(1)	-4(1)	-6(1)
C(9)	26(1)	31(1)	22(1)	-3(1)	-2(1)	-6(1)
C(10)	26(1)	31(1)	24(1)	-3(1)	-2(1)	-6(1)
C(11)	30(1)	30(1)	22(1)	-4(1)	-2(1)	-5(1)
C(12)	34(1)	43(1)	30(1)	1(1)	-8(1)	-4(1)
C(13)	24(1)	20(1)	21(1)	-7(1)	1(1)	-4(1)
C(14)	15(1)	21(1)	22(1)	-3(1)	-2(1)	-2(1)
C(15)	18(1)	22(1)	20(1)	-4(1)	-2(1)	-3(1)
C(16)	22(1)	23(1)	17(1)	-4(1)	-1(1)	-5(1)
N(1)	20(1)	20(1)	17(1)	-3(1)	-2(1)	-5(1)
N(2)	22(1)	23(1)	21(1)	-3(1)	2(1)	-2(1)
N(3)	22(1)	23(1)	37(1)	-11(1)	-2(1)	-4(1)
O(1)	29(1)	20(1)	36(1)	-2(1)	7(1)	-3(1)
O(2)	21(1)	33(1)	36(1)	-13(1)	-2(1)	-8(1)

Table 8.10. Torsion angles [°] for dodecyl iminodiacetamide.

N(1)-C(1)-C(2)-C(3)	175.53(10)
C(1)-C(2)-C(3)-C(4)	179.09(11)
C(2)-C(3)-C(4)-C(5)	177.24(11)
C(3)-C(4)-C(5)-C(6)	-178.60(11)
C(4)-C(5)-C(6)-C(7)	178.78(11)
C(5)-C(6)-C(7)-C(8)	-179.74(11)
C(6)-C(7)-C(8)-C(9)	178.98(11)
C(7)-C(8)-C(9)-C(10)	179.42(12)
C(8)-C(9)-C(10)-C(11)	178.06(11)
C(9)-C(10)-C(11)-C(12)	175.92(12)
N(1)-C(13)-C(14)-O(1)	-170.93(11)
N(1)-C(13)-C(14)-N(2)	10.39(16)
N(1)-C(15)-C(16)-O(2)	-157.85(11)
N(1)-C(15)-C(16)-N(3)	23.91(16)
C(16)-C(15)-N(1)-C(13)	-158.37(10)
C(16)-C(15)-N(1)-C(1)	77.51(12)
C(14)-C(13)-N(1)-C(15)	81.12(13)
C(14)-C(13)-N(1)-C(1)	-158.10(10)
C(2)-C(1)-N(1)-C(15)	-164.57(11)
C(2)-C(1)-N(1)-C(13)	73.69(13)

9. References

(1) Rao, C. N. R.; Vivekchand, S. R. C.; Biswas, K.; Govindaraj, A. *Dalton Trans.* **2007**, 3728–3749.
(2) Magnani, M.; Galluzzi, L.; Bruce, I. J. *J. Nanosci. Nanotechnol.* **2006**, *6*, 2302–2311.
(3) Mornet, S.; Vasseur, S.; Grasset, F.; Veverka, P.; Goglio, G.; Demourgues, A.; Portier, J.; Pollert, E.; Duguet, E. *Prog. Solid State Chem.* **2006**, *34*, 237–247.
(4) Hochbaum, A. I.; Yang, P. *Chem. Rev.* **2010**, *110*, 527–546.
(5) Kim, T.; Kim, D.-S.; Lee, B. Y.; Kim, Z. H.; Hong, S. *Adv. Mater.* **2009**, *21*, 1238–1242.
(6) Zhang, L. Z.; Tang, G.-Q. *Opt. Mater.* **2004**, *27*, 217–220.
(7) Sun, Y.; Wiederrecht, G. P. *Small* **2007**, *3*, 1964–1975.
(8) Pohl, M.; Lyon, D. K.; Mizuno, N.; Nomiya, K.; Finke, R. G. *Inorg. Chem.* **1995**, *34*, 1413–1429.
(9) Daniel, M.-C.; Astruc, D. *Chem. Rev.* **2004**, *104*, 293–346.
(10) Roucoux, A.; Schulz, J.; Patin, H. *Chem. Rev.* **2002**, *102*, 3757–3778.
(11) Grzelczak, M.; Pérez-Juste, J.; Mulvaney, P.; Liz-Marzán, L. M. *Chem. Soc. Rev.* **2008**, *37*, 1783–1791.
(12) Hamaguchi, K.; Kawasaki, H.; Arakawa, R. *Colloids Surf. Physicochem. Eng. Asp.* **2010**, *367*, 167–173.
(13) Jiang, H.-L.; Xu, Q. *J. Mater. Chem.* **2011**, *21*, 13705–13725.
(14) Van Hardeveld, R.; Hartog, F. *Surf. Sci.* **1969**, *15*, 189–230.
(15) Pan, H.-B.; Wai, C. M. *J. Phys. Chem. C* **2010**, *114*, 11364–11369.
(16) Rapoport, D. H.; Vogel, W.; Cölfen, H.; Schlögl, R. *J. Phys. Chem. B* **1997**, *101*, 4175–4183.
(17) Shen, L.; Bao, N.; Yanagisawa, K.; Domen, K.; Gupta, A.; Grimes, C. A. *Nanotechnology* **2006**, *17*, 5117.
(18) Wang, J.; Yin, S.; Komatsu, M.; Zhang, Q.; Saito, F.; Sato, T. *Appl. Catal. B Environ.* **2004**, *52*, 11–21.
(19) Eustis, S.; El-Sayed, M. A. *Chem. Soc. Rev.* **2006**, *35*, 209.
(20) Murray, C. B.; Norris, D. J.; Bawendi, M. G. *J. Am. Chem. Soc.* **1993**, *115*, 8706–8715.
(21) Burda, C.; Chen, X.; Narayanan, R.; El-Sayed, M. A. *Chem. Rev.* **2005**, *105*, 1025–1102.
(22) Schmid, G.; Giebel, U.; Huster, W.; Schwenk, A. *Inorganica Chim. Acta* **1984**, *85*, 97–102.
(23) Templeton, A. C.; Wuelfing, W. P.; Murray, R. W. *Acc. Chem. Res.* **2000**, *33*, 27–36.
(24) Kim, Y.-G.; Oh, S.-K.; Crooks, R. M. *Chem. Mater.* **2004**, *16*, 167–172.

(25) Kawazoe, Y.; Kondow, T.; Ohno, K. *Clusters and nanomaterials: Theory and experiment*; Springer: Berlin, 2002.
(26) Fievet, F.; Lagier, J. P.; Blin, B.; Beaudoin, B.; Figlarz, M. *Solid State Ion.* **1989**, *32–33, Part 1*, 198–205.
(27) Fievet, F.; Lagier, J. p.; Figlarz, M. *MRS Bull.* **1989**, *14*, 29–34.
(28) Ahmadi, T. S.; Wang, Z. L.; Green, T. C.; Henglein, A.; El-Sayed, M. A. *Science* **1996**, *272*, 1924–1925.
(29) Li, M.; Schnablegger, H.; Mann, S. *Nature* **1999**, *402*, 393–395.
(30) Sau, T. K.; Murphy, C. J. *J. Am. Chem. Soc.* **2004**, *126*, 8648–8649.
(31) Bakshi, M. S.; Thakur, P.; Sachar, S.; Kaur, G.; Banipal, T. S.; Possmayer, F.; Petersen, N. O. *J. Phys. Chem. C* **2007**, *111*, 18087–18098.
(32) Kuhn, J. N.; Tsung, C.-K.; Huang, W.; Somorjai, G. A. *J. Catal.* **2009**, *265*, 209–215.
(33) Borodko, Y.; Humphrey, S. M.; Tilley, T. D.; Frei, H.; Somorjai, G. A. *J. Phys. Chem. C* **2007**, *111*, 6288–6295.
(34) Yu, H.; Gibbons, P. C.; Kelton, K. F.; Buhro, W. E. *J. Am. Chem. Soc.* **2001**, *123*, 9198–9199.
(35) Stowell, C. A.; Korgel, B. A. *Nano Lett.* **2005**, *5*, 1203–1207.
(36) Li, Y.; El-Sayed, M. A. *J. Phys. Chem. B* **2001**, *105*, 8938–8943.
(37) Grass, M. E.; Joo, S. H.; Zhang, Y.; Somorjai, G. A. *J. Phys. Chem. C* **2009**, *113*, 8616–8623.
(38) Yan, N.; Yuan, Y.; Dyson, P. J. *Chem. Commun.* **2011**, *47*, 2529–2531.
(39) Dahal, N.; García, S.; Zhou, J.; Humphrey, S. M. *ACS Nano* **2012**, *6*, 9433–9446.
(40) Oliveira, M. M.; Ugarte, D.; Zanchet, D.; Zarbin, A. J. G. *J. Colloid Interface Sci.* **2005**, *292*, 429–435.
(41) Pamplin, B. R. *Crystal Growth*; Pergamon Press: New York, 1975.
(42) Humphrey, S. M.; Grass, M. E.; Habas, S. E.; Niesz, K.; Somorjai, G. A.; Tilley, T. D. *Nano Lett.* **2007**, *7*, 785–790.
(43) Volokitin, Y.; Sinzig, J.; de Jongh, L. J.; Schmid, G.; Vargaftik, M. N.; Moiseevi, I. I. *Nature* **1996**, *384*, 621–623.
(44) Gilbert, B.; Huang, F.; Zhang, H.; Waychunas, G. A.; Banfield, J. F. *Science* **2004**, *305*, 651–654.
(45) Tsuji, M.; Hashimoto, M.; Nishizawa, Y.; Kubokawa, M.; Tsuji, T. *Chem. - Eur. J.* **2005**, *11*, 440–452.
(46) Bilecka, I.; Niederberger, M. *Nanoscale* **2010**, *2*, 1358.
(47) LaMer, V. K.; Dinegar, R. H. *J. Am. Chem. Soc.* **1950**, *72*, 4847–4854.
(48) Park, J.; Joo, J.; Kwon, S. G.; Jang, Y.; Hyeon, T. *Angew. Chem. Int. Ed.* **2007**, *46*, 4630–4660.
(49) Tompsett, G. A.; Conner, W. C.; Yngvesson, K. S. *ChemPhysChem* **2006**, *7*, 296–319.
(50) Gerbec, J. A.; Magana, D.; Washington, A.; Strouse, G. F. *J. Am. Chem. Soc.* **2005**, *127*, 15791–15800.

(51) Mingos, D. M. P.; Baghurst, D. R. *Microwave-Enhanced Chemistry: Fundamentals, Sample Preparation and Applications*; American Chemical Society: Washington D.C., 1997.
(52) Galema, S. A. *Chem. Soc. Rev.* **1997**, *26*, 233–238.
(53) Kappe, C. O.; Dallinger, D.; Murphree, S. S. *Practical Microwave Synthesis for Organic Chemists*; Wiley-VCH: Weinheim, 2009.
(54) Leadbeater, N. E. *Microwave Heating as a Tool for Sustainable Chemistry*; CRC Press: Boca Raton, 2011.
(55) Nüchter, M.; Ondruschka, B.; Bonrath, W.; Gum, A. *Green Chem.* **2004**, *6*, 128–141.
(56) Hollas, J. M. *Modern Spectroscopy*; Wiley: Chichester, 2004.
(57) Gabriel, C.; Gabriel, S.; Grant, E. H.; Grant, E. H.; Halstead, B. S. J.; Mingos, D. M. P. *Chem. Soc. Rev.* **1998**, *27*, 213–224.
(58) Kappe, C. O. *Angew. Chem. Int. Ed.* **2004**, *43*, 6250–6284.
(59) Kappe, C. O. *Acc. Chem. Res.* **2013**, *46*, 1579–1587.
(60) Nadagouda, M. N.; Speth, T. F.; Varma, R. S. *Acc. Chem. Res.* **2011**, *44*, 469–478.
(61) Mingos, D. M. P.; Baghurst, D. R. *Chem. Soc. Rev.* **1991**, *20*, 1–47.
(62) Abdelsayed, V.; Aljarash, A.; El-Shall, M. S.; Al Othman, Z. A.; Alghamdi, A. H. *Chem. Mater.* **2009**, *21*, 2825–2834.
(63) Panda, A. B.; Glaspell, G.; El-Shall, M. S. *J. Am. Chem. Soc.* **2006**, *128*, 2790–2791.
(64) Hayes, B. L. *Microwave Synthesis: Chemistry at the Speed of Light*; CEM publishing: Matthews, 2002.
(65) Schanche, J.-S. *Mol. Divers.* **2003**, *7*, 291–298.
(66) Herring, N. P.; AbouZeid, K.; Mohamed, M. B.; Pinsk, J.; El-Shall, M. S. *Langmuir* **2011**, *27*, 15146–15154.
(67) Abdelsayed, V.; Panda, A. B.; Glaspell, G. P.; El-Shall, M. S. *Nanoparticles: Synthesis, Stabilization, Passivation and Functionalization*; American Chemical Society: Washington D.C., 2008.
(68) Mohamed, M. B.; AbouZeid, K. M.; Abdelsayed, V.; Aljarash, A. A.; El-Shall, M. S. *ACS Nano* **2010**, *4*, 2766–2772.
(69) Jézéquel, D.; Guenot, J.; Jouini, N.; Fiévet, F. *J. Mater. Res.* **1995**, *10*, 77–83.
(70) Feldmann, C.; Jungk, H.-O. *Angew. Chem. Int. Ed.* **2001**, *40*, 359–362.
(71) Feldmann, C. *Adv. Funct. Mater.* **2003**, *13*, 101–107.
(72) Bonet, F.; Delmas, V.; Grugeon, S.; Herrera Urbina, R.; Silvert, P.-Y.; Tekaia-Elhsissen, K. *Nanostructured Mater.* **1999**, *11*, 1277–1284.
(73) Hoz, A. de la; Díaz-Ortiz, Á.; Moreno, A. *Chem. Soc. Rev.* **2005**, *34*, 164–178.
(74) Berlan, J. *Radiat. Phys. Chem.* **1995**, *45*, 581–589.
(75) Santos, T.; Valente, M. A.; Monteiro, J.; Sousa, J.; Costa, L. C. *Appl. Therm. Eng.* **2011**, *31*, 3255–3261.
(76) Veerakumar, P.; Velayudham, M.; Lu, K.-L.; Rajagopal, S. *Appl. Catal. Gen.* **2013**, *455*, 247–260.

(77) Blavo, S. O.; Qayyum, E.; Baldyga, L. M.; Castillo, V. A.; Sanchez, M. D.; Warrington, K.; Barakat, M. A.; Kuhn, J. N. *Top. Catal.* **2013**, *56*, 1835–1842.
(78) Zhu, Z.; Gao, F.; Lei, J.; Dong, H.; Ju, H. *Chem. – Eur. J.* **2012**, *18*, 13871–13876.
(79) Lin, L.; Weng, S.; Zhao, C.; Liu, Q.; liu, A.; Lin, X. *Electrochimica Acta* **2013**, *108*, 808–813.
(80) Adeyemi, O. S.; Whiteley, C. G. *Int. J. Biol. Macromol.* **2013**, *62*, 450–456.
(81) Cuenya, B. R. *Thin Solid Films* **2010**, *518*, 3127–3150.
(82) Kundu, S.; Peng, L.; Liang, H. *Inorg. Chem.* **2008**, *47*, 6344–6352.
(83) Liu, F.-K.; Ker, C.-J.; Chang, Y.-C.; Ko, F.-H.; Chu, T.-C.; Dai, B.-T. *Jpn. J. Appl. Phys.* **2003**, *42*, 4152.
(84) Hu, B.; Wang, S.-B.; Wang, K.; Zhang, M.; Yu, S.-H. *J. Phys. Chem. C* **2008**, *112*, 11169–11174.
(85) Chen, J.; Wang, J.; Zhang, X.; Jin, Y. *Mater. Chem. Phys.* **2008**, *108*, 421–424.
(86) Sharma, V. K.; Yngard, R. A.; Lin, Y. *Adv. Colloid Interface Sci.* **2009**, *145*, 83–96.
(87) Pastoriza-Santos, I.; Liz-Marzán, L. M. *Langmuir* **2002**, *18*, 2888–2894.
(88) Yu, W.; Tu, W.; Liu, H. *Langmuir* **1999**, *15*, 6–9.
(89) Tu, W.; Liu, H. *J. Mater. Chem.* **2000**, *10*, 2207–2211.
(90) Luo, Y. *Mater. Lett.* **2007**, *61*, 1873–1875.
(91) Ren, L.; Meng, L.; Lu, Q.; Fei, Z.; Dyson, P. J. *J. Colloid Interface Sci.* **2008**, *323*, 260–266.
(92) Soares, P. I. P.; Alves, A. M. R.; Pereira, L. C. J.; Coutinho, J. T.; Ferreira, I. M. M.; Novo, C. M. M.; Borges, J. P. M. R. *J. Colloid Interface Sci.* **2014**, *419*, 46–51.
(93) Komarneni, S.; Pidugu, R.; Li, Q. H.; Roy, R. *J. Mater. Res.* **1995**, *10*, 1687–1692.
(94) Suryawanshi, Y. R.; Chakraborty, M.; Jauhari, S.; Mukhopadhyay, S.; Shenoy, K. T.; Shridharkrishna, R. *Cryst. Res. Technol.* **2013**, *48*, 69–74.
(95) Li, D.; Komarneni, S. *J. Am. Ceram. Soc.* **2006**, *89*, 1510–1517.
(96) Barret, C. S. *Structure of Metals: Crystallographic Methods, Principles and Data*; McGraw-Hill Book Co.: New York, 1943.
(97) Kobayashi, H.; Morita, H.; Yamauchi, M.; Ikeda, R.; Kitagawa, H.; Kubota, Y.; Kato, K.; Takata, M.; Toh, S.; Matsumura, S. *J. Am. Chem. Soc.* **2012**, *134*, 12390–12393.
(98) Pearson, W. B. *The Crystal Chemistry and Physics of Metals and Alloys*; John Wiley & Sons, Inc.: New York, 1972.
(99) Mavrikakis, M.; Hammer, B.; Nørskov, J. K. *Phys. Rev. Lett.* **1998**, *81*, 2819–2822.
(100) Strasser, P.; Koh, S.; Anniyev, T.; Greeley, J.; More, K.; Yu, C.; Liu, Z.; Kaya, S.; Nordlund, D.; Ogasawara, H.; Toney, M. F.; Nilsson, A. *Nat. Chem.* **2010**, *2*, 454–460.

(101) Chen, Z.; Mochizuki, D.; Maitani, M. M.; Wada, Y. *Nanotechnology* **2013**, *24*, 265602.
(102) Patel, K.; Kapoor, S.; Dave, D. P.; Mukherjee, T. *Res. Chem. Intermed.* **2006**, *32*, 103–113.
(103) Harpeness, R.; Gedanken, A. *Langmuir* **2004**, *20*, 3431–3434.
(104) Patel, K.; Kapoor, S.; Dave, D. P.; Mukherjee, T. *J. Chem. Sci.* **2005**, *117*, 311–316.
(105) Tang, W.; Henkelman, G. *J. Chem. Phys.* **2009**, *130*, 194504.
(106) Bensebaa, F.; Patrito, N.; Page, Y. L.; L'Ecuyer, P.; Wang, D. *J. Mater. Chem.* **2004**, *14*, 3378–3384.
(107) Taufany, F.; Pan, C.-J.; Lai, F.-J.; Chou, H.-L.; Sarma, L. S.; Rick, J.; Lin, J.-M.; Lee, J.-F.; Tang, M.-T.; Hwang, B.-J. *Chem. – Eur. J.* **2013**, *19*, 905–915.
(108) Mehta, S. K.; Gupta, S. *Sci. Adv. Mater.* **2013**, *5*, 1377–1383.
(109) Du, J.-Q.; Zhang, Y.; Tian, T.; Yan, S.-C.; Wang, H.-T. *Mater. Res. Bull.* **2009**, *44*, 1347–1351.
(110) Ugalde, M.; Chavira, E.; Ochoa-Lara, M. T.; Figueroa, I. A.; Quintanar, C.; Tejeda, A. *J. Nanotechnol.* **2013**, *2013*, e578684.
(111) Pal, A.; Shah, S.; Devi, S. *Colloids Surf. Physicochem. Eng. Asp.* **2007**, *302*, 51–57.
(112) Shafii, S. *J. Chem. Eng. Process Technol.* **2012**, *03*.
(113) García, S.; Anderson, R. M.; Celio, H.; Dahal, N.; Dolocan, A.; Zhou, J.; Humphrey, S. M. *Chem. Commun.* **2013**, *49*, 4241–4243.
(114) Gu, G.; Xu, J.; Wu, Y.; Chen, M.; Wu, L. *J. Colloid Interface Sci.* **2011**, *359*, 327–333.
(115) Quang, D. V.; Sarawade, P. B.; Hilonga, A.; Kim, J.-K.; Shim, Y. H.; Shao, G. N.; Kim, H. T. *Mater. Lett.* **2012**, *68*, 350–353.
(116) Ortiz-Ibarra, H.; Casillas, N.; Soto, V.; Barcena-Soto, M.; Torres-Vitela, R.; de la Cruz, W.; Gómez-Salazar, S. *J. Colloid Interface Sci.* **2007**, *314*, 562–571.
(117) Pasini, T.; Piccinini, M.; Blosi, M.; Bonelli, R.; Albonetti, S.; Dimitratos, N.; Lopez-Sanchez, J. A.; Sankar, M.; He, Q.; Kiely, C. J.; Hutchings, G. J.; Cavani, F. *Green Chem.* **2011**, *13*, 2091–2099.
(118) Kakade, B. A.; Sahoo, S.; Halligudi, S. B.; Pillai, V. K. *J. Phys. Chem. C* **2008**, *112*, 13317–13319.
(119) Bhattacharyya, S.; Gedanken, A. *J. Phys. Chem. C* **2008**, *112*, 659–665.
(120) Rogemond, E.; Essayem, N.; Frety, R.; Perrichon, V.; Primet, M.; Mathis, F. *J. Catal.* **1997**, *166*, 229–235.
(121) Sugiura, Y.; Mukai, D.; Murai, Y.; Tochiya, S.; Sekine, Y. *Int. J. Hydrog. Energy* **2013**, *38*, 7822–7829.
(122) Zhang, P.; Huang, S.-Y.; Popov, B. N. *J. Electrochem. Soc.* **2010**, *157*, B1163–B1172.
(123) Campelo, J. M.; Luna, D.; Luque, R.; Marinas, J. M.; Romero, A. A. *ChemSusChem* **2009**, *2*, 18–45.

(124) Khanal, S.; Bhattarai, N.; Velázquez-Salazar, J. J.; Bahena, D.; Soldano, G.; Ponce, A.; Mariscal, M. M.; Mejía-Rosales, S.; José-Yacamán, M. *Nanoscale* **2013**, *5*, 12456–12463.
(125) Zhao, J.; Wang, P.; Chen, W.; Liu, R.; Li, X.; Nie, Q. *J. Power Sources* **2006**, *160*, 563–569.
(126) Li, X.; Chen, W.-X.; Zhao, J.; Xing, W.; Xu, Z.-D. *Carbon* **2005**, *43*, 2168–2174.
(127) Li, W.; Liang, C.; Qiu, J.; Zhou, W.; Han, H.; Wei, Z.; Sun, G.; Xin, Q. *Carbon* **2002**, *40*, 791–794.
(128) Campelo, J. M.; Conesa, T. D.; Gracia, M. J.; Jurado, M. J.; Luque, R.; Marinas, J. M.; Romero, A. A. *Green Chem.* **2008**, *10*, 853–858.
(129) González-Arellano, C.; Campelo, J. M.; Macquarrie, D. J.; Marinas, J. M.; Romero, A. A.; Luque, R. *ChemSusChem* **2008**, *1*, 746–750.
(130) Glaspell, G.; Hassan, H. M. A.; Elzatahry, A.; Abdalsayed, V.; El-Shall, M. S. *Top. Catal.* **2008**, *47*, 22–31.
(131) Glaspell, G.; Fuoco, L.; El-Shall, M. S. *J. Phys. Chem. B* **2005**, *109*, 17350–17355.
(132) Liang, Y.; Zhang, H.; Zhong, H.; Zhu, X.; Tian, Z.; Xu, D.; Yi, B. *J. Catal.* **2006**, *238*, 468–476.
(133) Boxall, D. L.; Deluga, G. A.; Kenik, E. A.; King, W. D.; Lukehart, C. M. *Chem. Mater.* **2001**, *13*, 891–900.
(134) Siamaki, A. R.; Khder, A. E. R. S.; Abdelsayed, V.; El-Shall, M. S.; Gupton, B. F. *J. Catal.* **2011**, *279*, 1–11.
(135) Zhu, J.-F.; Zhu, Y.-J. *J. Phys. Chem. B* **2006**, *110*, 8593–8597.
(136) Wada, Y.; Kobayashi, T.; Yamasaki, H.; Sakata, T.; Hasegawa, N.; Mori, H.; Tsukahara, Y. *Polymer* **2007**, *48*, 1441–1444.
(137) Mukherjee, P.; Patra, C. R.; Ghosh, A.; Kumar, R.; Sastry, M. *Chem. Mater.* **2002**, *14*, 1678–1684.
(138) Chen, W.; Zhao, J.; Lee, J. Y.; Liu, Z. *Mater. Chem. Phys.* **2005**, *91*, 124–129.
(139) Tuval, T.; Gedanken, A. *Nanotechnology* **2007**, *18*, 255601.
(140) Harpeness, R.; Peng, Z.; Liu, X.; Pol, V. G.; Koltypin, Y.; Gedanken, A. *J. Colloid Interface Sci.* **2005**, *287*, 678–684.
(141) Chaloner, P. A.; Esteruelas, M. A.; Joo, F.; Oro, L. A. *Homogeneous Hydrogenation*; Kluwer Academic Publishers: Dordrecht, 1994; Vol. 15.
(142) James, B. R. *Homogeneous Hydrogenation*; John Wiley & Sons, Inc.: New York, 1973.
(143) James, B. R. In *Advances in Organometallic Chemistry*; F.G.A. Stone and Robert West, Ed.; Catalysis and Organic Syntheses; Academic Press, 1979; Vol. Volume 17, pp. 319–405.
(144) Hommeltoft, S. I.; Berry, D. H.; Eisenberg, R. *J. Am. Chem. Soc.* **1986**, *108*, 5345–5347.
(145) Debus, H. *Justus Liebigs Ann. Chem.* **1863**, *128*, 200–215.
(146) Nishimura, S. *Handbook of Heterogeneous Catalytic Hydrogenation for Organic Synthesis*; John Wiley & Sons, Inc.: New York, 2001.

(147) Beeck, O. *Discuss. Faraday Soc.* **1950**, *8*, 118–128.
(148) Gilman, G.; Cohn, G. In *Advances in Catalysis*; Adalbert Farkas, Ed.; Proceedings of the International Congress on Catalysis; Academic Press, 1957; Vol. Volume 9, pp. 733–742.
(149) Nishimura, S. *Bull. Chem. Soc. Jpn.* **1960**, *33*, 566–567.
(150) Dyson, P. J. *Dalton Trans.* **2003**, 2964–2974.
(151) Widegren, J. A.; Finke, R. G. *J. Mol. Catal. Chem.* **2003**, *198*, 317–341.
(152) Hagen, C. M.; Vieille-Petit, L.; Laurenczy, G.; Süss-Fink, G.; Finke, R. G. *Organometallics* **2005**, *24*, 1819–1831.
(153) deVries, J. G.; Elsevier, C. J. *Handbook of Homogeneous Hydrogenation*; Wiley-VCH Verlag GmbH: Weinheim, Germany, 2007; Vol. 1.
(154) Ashida, T.; Miura, K.; Nomoto, T.; Yagi, S.; Sumida, H.; Kutluk, G.; Soda, K.; Namatame, H.; Taniguchi, M. *Surf. Sci.* **2007**, *601*, 3898–3901.
(155) Biacchi, A. J.; Schaak, R. E. *ACS Nano* **2011**, *5*, 8089–8099.
(156) Durap, F.; Zahmakıran, M.; Özkar, S. *Appl. Catal. Gen.* **2009**, *369*, 53–59.
(157) Ewers, T. D.; Sra, A. K.; Norris, B. C.; Cable, R. E.; Cheng, C.-H.; Shantz, D. F.; Schaak, R. E. *Chem. Mater.* **2005**, *17*, 514–520.
(158) Harada, M.; Abe, D.; Kimura, Y. *J. Colloid Interface Sci.* **2005**, *292*, 113–121.
(159) Hoefelmeyer, J. D.; Liu, H.; Somorjai, G. A.; Tilley, T. D. *J. Colloid Interface Sci.* **2007**, *309*, 86–93.
(160) Hoefelmeyer, J. D.; Niesz, K.; Somorjai, G. A.; Tilley, T. D. *Nano Lett.* **2005**, *5*, 435–438.
(161) Jang, K.; Kim, H. J.; Son, S. U. *Chem. Mater.* **2010**, *22*, 1273–1275.
(162) Léger, B.; Denicourt-Nowicki, A.; Olivier-Bourbigou, H.; Roucoux, A. *Inorg. Chem.* **2008**, *47*, 9090–9096.
(163) Mittendorfer, F.; Seriani, N.; Dubay, O.; Kresse, G. *Phys. Rev. B* **2007**, *76*, 233413.
(164) Mu, X.; Meng, J.; Li, Z.-C.; Kou, Y. *J. Am. Chem. Soc.* **2005**, *127*, 9694–9695.
(165) Ojeda, M.; Rojas, S.; Boutonnet, M.; Pérez-Alonso, F. J.; Javier García-García, F.; Fierro, J. L. G. *Appl. Catal. Gen.* **2004**, *274*, 33–41.
(166) Pradhan, M.; Sarkar, S.; Sinha, A. K.; Basu, M.; Pal, T. *J. Phys. Chem. C* **2010**, *114*, 16129–16142.
(167) Quek, X.-Y.; Guan, Y.; van Santen, R. A.; Hensen, E. J. M. *ChemSusChem* **2010**, *3*, 1264–1267.
(168) Redel, E.; Krämer, J.; Thomann, R.; Janiak, C. *J. Organomet. Chem.* **2009**, *694*, 1069–1075.
(169) Zhang, H.; Li, W.; Jin, M.; Zeng, J.; Yu, T.; Yang, D.; Xia, Y. *Nano Lett.* **2011**, *11*, 898–903.
(170) Zhang, Y.; Grass, M. E.; Kuhn, J. N.; Tao, F.; Habas, S. E.; Huang, W.; Yang, P.; Somorjai, G. A. *J. Am. Chem. Soc.* **2008**, *130*, 5868–5869.
(171) Mayer, A. B. R.; Mark, J. E. *Polym. Bull.* **1996**, *37*, 683–690.
(172) Mayer, A. B. R.; Mark, J. E. *J. Macromol. Sci. Part A* **1996**, *33*, 451–459.
(173) Hirai, H. *J. Macromol. Sci. Part - Chem.* **1979**, *13*, 633–649.

(174) Shiraishi, Y.; Nakayama, M.; Takagi, E.; Tominaga, T.; Toshima, N. *Inorganica Chim. Acta* **2000**, *300–302*, 964–969.
(175) Pillai, U. R.; Sahle-Demessie, E. *J. Mol. Catal. Chem.* **2004**, *222*, 153–158.
(176) Zhang, Y.; Grass, M. E.; Huang, W.; Somorjai, G. A. *Langmuir* **2010**, *26*, 16463–16468.
(177) Mayer, A. B. R.; Mark, J. E.; Morris, R. E. *Polym. J.* **1998**, *30*, 197–205.
(178) Seregina, M. V.; Bronstein, L. M.; Platonova, O. A.; Chernyshov, D. M.; Valetsky, P. M.; Hartmann, J.; Wenz, E.; Antonietti, M. *Chem. Mater.* **1997**, *9*, 923–931.
(179) Lidström, P.; Tierney, J.; Wathey, B.; Westman, J. *Tetrahedron* **2001**, *57*, 9225–9283.
(180) Bagaria, H. G.; Ada, E. T.; Shamsuzzoha, M.; Nikles, D. E.; Johnson, D. T. *Langmuir* **2006**, *22*, 7732–7737.
(181) Haruta, M. *Gold Bull.* **2004**, *37*, 27–36.
(182) Hutchings, G. J. *Chem. Commun.* **2008**, 1148–1164.
(183) Lewis, L. N. *Chem. Rev.* **1993**, *93*, 2693–2730.
(184) Narayanan, R.; El-Sayed, M. A. *J. Phys. Chem. B* **2005**, *109*, 12663–12676.
(185) Semagina, N.; Kiwi-Minsker, L. *Catal. Rev.* **2009**, *51*, 147–217.
(186) Kortan, A. R.; Hull, R.; Opila, R. L.; Bawendi, M. G.; Steigerwald, M. L.; Carroll, P. J.; Brus, L. E. *J. Am. Chem. Soc.* **1990**, *112*, 1327–1332.
(187) Lee, H.; Habas, S. E.; Kweskin, S.; Butcher, D.; Somorjai, G. A.; Yang, P. *Angew. Chem. Int. Ed.* **2006**, *45*, 7824–7828.
(188) Dodd, A. C. *Powder Technol.* **2009**, *196*, 30–35.
(189) Ghosh Chaudhuri, R.; Paria, S. *Chem. Rev.* **2012**, *112*, 2373–2433.
(190) Kobayashi, H.; Yamauchi, M.; Ikeda, R.; Kitagawa, H. *Chem. Commun.* **2009**, 4806–4808.
(191) Poulston, S.; Tikhov, M.; Lambert, R. M. *Catal. Lett.* **1996**, *42*, 167–172.
(192) Storm, J.; Lambert, R. M.; Memmel, N.; Onsgaard, J.; Taglauer, E. *Surf. Sci.* **1999**, *436*, 259–268.
(193) Beaumont, S. K.; Kyriakou, G.; Lambert, R. M. *J. Am. Chem. Soc.* **2010**, *132*, 12246–12248.
(194) Slanac, D. A.; Hardin, W. G.; Johnston, K. P.; Stevenson, K. J. *J. Am. Chem. Soc.* **2012**, *134*, 9812–9819.
(195) Wang, J. X.; Inada, H.; Wu, L.; Zhu, Y.; Choi, Y.; Liu, P.; Zhou, W.-P.; Adzic, R. R. *J. Am. Chem. Soc.* **2009**, *131*, 17298–17302.
(196) Alayoglu, S.; Eichhorn, B. *J. Am. Chem. Soc.* **2008**, *130*, 17479–17486.
(197) Sun, Y.; Gates, B.; Mayers, B.; Xia, Y. *Nano Lett.* **2002**, *2*, 165–168.
(198) DeSantis, C. J.; Sue, A. C.; Bower, M. M.; Skrabalak, S. E. *ACS Nano* **2012**, *6*, 2617–2628.
(199) Newville, M. *J. Synchrotron Radiat.* **2001**, *8*, 322–324.
(200) Loferski, P. *2010 Minerals Yearbook: Platinum-group metals*; U.S. Geological Survey, 2010.

(201) Essinger-Hileman, E. R.; DeCicco, D.; Bondi, J. F.; Schaak, R. E. *J. Mater. Chem.* **2011**, *21*, 11599–11604.
(202) Altman, E. I.; Colton, R. J. *Surf. Sci.* **1994**, *304*, L400–L406.
(203) Stratakis, M.; Garcia, H. *Chem. Rev.* **2012**, *112*, 4469–4506.
(204) Gross, E.; Liu, J. H.-C.; Toste, F. D.; Somorjai, G. A. *Nat. Chem.* **2012**, *4*, 947–952.
(205) Bell, A. T. *Science* **2003**, *299*, 1688–1691.
(206) Heveling, J. *J. Chem. Educ.* **2012**, *89*, 1530–1536.
(207) He, J.; Ichinose, I.; Kunitake, T.; Nakao, A.; Shiraishi, Y.; Toshima, N. *J. Am. Chem. Soc.* **2003**, *125*, 11034–11040.
(208) Wang, C.; Daimon, H.; Lee, Y.; Kim, J.; Sun, S. *J. Am. Chem. Soc.* **2007**, *129*, 6974–6975.
(209) Bratlie, K. M.; Lee, H.; Komvopoulos, K.; Yang, P.; Somorjai, G. A. *Nano Lett.* **2007**, *7*, 3097–3101.
(210) Narayanan, R.; El-Sayed, M. A. *Nano Lett.* **2004**, *4*, 1343–1348.
(211) Hills, C. W.; Mack, N. H.; Nuzzo, R. G. *J. Phys. Chem. B* **2003**, *107*, 2626–2636.
(212) Ferrando, R.; Jellinek, J.; Johnston, R. L. *Chem. Rev.* **2008**, *108*, 845–910.
(213) Buhro, W. E.; Colvin, V. L. *Nat. Mater.* **2003**, *2*, 138–139.
(214) Liu, J.-H.; Wang, A.-Q.; Chi, Y.-S.; Lin, H.-P.; Mou, C.-Y. *J. Phys. Chem. B* **2005**, *109*, 40–43.
(215) Wang, D.; Villa, A.; Porta, F.; Prati, L.; Su, D. *J. Phys. Chem. C* **2008**, *112*, 8617–8622.
(216) Mott, D.; Luo, J.; Njoki, P. N.; Lin, Y.; Wang, L.; Zhong, C.-J. *Catal. Today* **2007**, *122*, 378–385.
(217) Zhang, L.; Iyyamperumal, R.; Yancey, D. F.; Crooks, R. M.; Henkelman, G. *ACS Nano* **2013**, *7*, 9168–9172.
(218) Zhang, J.; Lima, F. H. B.; Shao, M. H.; Sasaki, K.; Wang, J. X.; Hanson, J.; Adzic, R. R. *J. Phys. Chem. B* **2005**, *109*, 22701–22704.
(219) Yan, J.-M.; Zhang, X.-B.; Akita, T.; Haruta, M.; Xu, Q. *J. Am. Chem. Soc.* **2010**, *132*, 5326–5327.
(220) Zeng, H.; Li, J.; Wang, Z. L.; Liu, J. P.; Sun, S. *Nano Lett.* **2004**, *4*, 187–190.
(221) Zeng, H.; Sun, S.; Li, J.; Wang, Z. L.; Liu, J. P. *Appl. Phys. Lett.* **2004**, *85*, 792–794.
(222) Yi, C.-W.; Luo, K.; Wei, T.; Goodman, D. W. *J. Phys. Chem. B* **2005**, *109*, 18535–18540.
(223) Wang, W. H.; Dong, C.; Shek, C. H. *Mater. Sci. Eng. R Rep.* **2004**, *44*, 45–89.
(224) Thomas, J. M.; Johnson, B. F. G.; Raja, R.; Sankar, G.; Midgley, P. A. *Acc. Chem. Res.* **2003**, *36*, 20–30.
(225) Wang, F. E. *Bonding Theory for Metals and Alloys*; 1st ed.; Elsevier B. V., 2005.
(226) Davies, R.; Dinsdale, A.; Gisby, J.; Robinson, J.; Martin, S. *Calphad* **2002**, *26*, 229–271.
(227) Schuette, W. M.; Buhro, W. E. *ACS Nano* **2013**, *7*, 3844–3853.
(228) Kresse, G. *Phys. Rev. B* **2000**, *62*, 8295–8305.

(229) Kresse, G.; Hafner, J. *Surf. Sci.* **2000**, *459*, 287–302.
(230) Blöchl, P. E. *Phys. Rev. B* **1994**, *50*, 17953–17979.
(231) Kresse, G.; Joubert, D. *Phys. Rev. B* **1999**, *59*, 1758–1775.
(232) Perdew, J. P.; Wang, Y. *Phys. Rev. B* **1992**, *45*, 13244–13249.
(233) Hohenberg, P.; Kohn, W. *Phys. Rev.* **1964**, *136*, B864–B871.
(234) Monkhorst, H. J.; Pack, J. D. *Phys. Rev. B* **1976**, *13*, 5188–5192.
(235) Methfessel, M.; Paxton, A. T. *Phys. Rev. B* **1989**, *40*, 3616–3621.
(236) Vitos, L.; Ruban, A. V.; Skriver, H. L.; Kollár, J. *Surf. Sci.* **1998**, *411*, 186–202.
(237) Tkatchenko, A.; Scheffler, M. *Phys. Rev. Lett.* **2009**, *102*, 073005.
(238) Rossmeisl, J.; Qu, Z.-W.; Zhu, H.; Kroes, G.-J.; Nørskov, J. K. *J. Electroanal. Chem.* **2007**, *607*, 83–89.
(239) Nørskov, J. K.; Rossmeisl, J.; Logadottir, A.; Lindqvist, L.; Kitchin, J. R.; Bligaard, T.; Jónsson, H. *J. Phys. Chem. B* **2004**, *108*, 17886–17892.
(240) Maroun, F.; Ozanam, F.; Magnussen, O. M.; Behm, R. J. *Science* **2001**, *293*, 1811–1814.
(241) Liu, P.; Nørskov, J. K. *Phys. Chem. Chem. Phys.* **2001**, *3*, 3814–3818.
(242) Hammer, B.; Nørskov, J. K. In *Advances in Catalysis*; Bruce C. Gates, H. K., Ed.; Impact of Surface Science on Catalysis; Academic Press, 2000; Vol. Volume 45, pp. 71–129.
(243) Ruban, A.; Hammer, B.; Stoltze, P.; Skriver, H. L.; Nørskov, J. K. *J. Mol. Catal. Chem.* **1997**, *115*, 421–429.
(244) Sigalas, M.; Papaconstantopoulos, D. A.; Bacalis, N. C. *Phys. Rev. B* **1992**, *45*, 5777–5783.
(245) Tang, W.; Henkelman, G. *J. Chem. Phys.* **2009**, *130*, 194504.
(246) Kitchin, J. R.; Nørskov, J. K.; Barteau, M. A.; Chen, J. G. *Phys. Rev. Lett.* **2004**, *93*, 156801.
(247) Kitchin, J. R.; Nørskov, J. K.; Barteau, M. A.; Chen, J. G. *J. Chem. Phys.* **2004**, *120*, 10240–10246.
(248) Toshima, N.; Yonezawa, T. *New J. Chem.* **1998**, *22*, 1179–1201.
(249) Kang, S. W.; Lee, Y. W.; Kim, M.; Hong, J. W.; Han, S. W. *Chem. – Asian J.* **2011**, *6*, 909–913.
(250) Wang, L.; Nemoto, Y.; Yamauchi, Y. *J. Am. Chem. Soc.* **2011**, *133*, 9674–9677.
(251) Xia, Y.; Xiong, Y.; Lim, B.; Skrabalak, S. E. *Angew. Chem. Int. Ed.* **2009**, *48*, 60–103.
(252) Gonzalez, E.; Arbiol, J.; Puntes, V. F. *Science* **2011**, *334*, 1377–1380.
(253) Wang, L.; Yamauchi, Y. *J. Am. Chem. Soc.* **2010**, *132*, 13636–13638.
(254) Wang, L.; Yamauchi, Y. *Chem. Mater.* **2011**, *23*, 2457–2465.
(255) Choi, B.-S.; Lee, Y. W.; Kang, S. W.; Hong, J. W.; Kim, J.; Park, I.; Han, S. W. *ACS Nano* **2012**, *6*, 5659–5667.
(256) Adzic, R. R.; Zhang, J.; Sasaki, K.; Vukmirovic, M. B.; Shao, M.; Wang, J. X.; Nilekar, A. U.; Mavrikakis, M.; Valerio, J. A.; Uribe, F. *Top. Catal.* **2007**, *46*, 249–262.
(257) Adzic, R. R. *Electrocatalysis* **2012**, *3*, 163–169.

(258) Wang, C.; Chi, M.; Li, D.; Strmcnik, D.; van der Vliet, D.; Wang, G.; Komanicky, V.; Chang, K.-C.; Paulikas, A. P.; Tripkovic, D.; Pearson, J.; More, K. L.; Markovic, N. M.; Stamenkovic, V. R. *J. Am. Chem. Soc.* **2011**, *133*, 14396–14403.
(259) Zhang, L.; Henkelman, G. *J. Phys. Chem. C* **2012**, *116*, 20860–20865.
(260) Sasaki, K.; Naohara, H.; Choi, Y.; Cai, Y.; Chen, W.-F.; Liu, P.; Adzic, R. R. *Nat. Commun.* **2012**, *3*, 1115.
(261) Koenigsmann, C.; Sutter, E.; Adzic, R. R.; Wong, S. S. *J. Phys. Chem. C* **2012**, *116*, 15297–15306.
(262) Kang, S. W.; Lee, Y. W.; Park, Y.; Choi, B.-S.; Hong, J. W.; Park, K.-H.; Han, S. W. *ACS Nano* **2013**, *7*, 7945–7955.
(263) Harada, M.; Asakura, K.; Toshima, N. *J. Phys. Chem.* **1993**, *97*, 5103–5114.
(264) Liu, H.; Mao, G.; Meng, S. *J. Mol. Catal.* **1992**, *74*, 275–284.
(265) Wu, M.-L.; Chen, D.-H.; Huang, T.-C. *Langmuir* **2001**, *17*, 3877–3883.
(266) Magnani, M.; Galluzzi, L.; Bruce, I. J. *J. Nanosci. Nanotechnol.* **2006**, *6*, 2302–2311.
(267) Kim, T.; Kim, D.-S.; Lee, B. Y.; Kim, Z. H.; Hong, S. *Adv. Mater.* **2009**, *21*, 1238–1242.
(268) Zhang, L. Z.; Tang, G.-Q. *Opt. Mater.* **2004**, *27*, 217–220.
(269) Daniel, M.-C.; Astruc, D. *Chem. Rev.* **2004**, *104*, 293–346.
(270) Hoare, M. R.; Pal, P. *Adv. Phys.* **1975**, *24*, 645–678.
(271) Hoare, M. R.; Pal, P. *Nature* **1971**, *230*, 5–8.
(272) Gutierrez, E.; Powell, R. D.; Furuya, F. R.; Hainfeld, J. F.; Schaaff, T. G.; Shafigullin, M. N.; Stephens, P. W.; Whetten, R. L. *The European Physical Journal D* **1999**, *9*, 647–651.
(273) McNeal, C. J.; Hughes, J. M.; Pignolet, L. H.; Nelson, L. T. J.; Gardner, T. G.; Fackler, J. P.; Winpenny, R. E. P.; Irgens, L. H.; Vigh, G.; Macfarlane, R. D. *Inorg. Chem.* **1993**, *32*, 5582–5590.
(274) Fackler, J. P.; McNeal, C. J.; Pignolet, L. H.; Winpenny, R. E. P. *J. Am. Chem. Soc.* **1989**, *111*, 6434–6435.
(275) Vogel, W.; Rosner, B.; Tesche, B. *J. Phys. Chem.* **1993**, *97*, 11611–11616.
(276) Schmid, G. In *Clusters*; Structure and Bonding; Springer Berlin Heidelberg, 1985; pp. 51–85.
(277) Petroski, J.; Chou, M. H.; Creutz, C. *Inorg. Chem.* **2004**, *43*, 1597–1599.
(278) Brown, L. O.; Hutchison, J. E. *J. Am. Chem. Soc.* **1997**, *119*, 12384–12385.
(279) Brown, L. O.; Hutchison, J. E. *J. Am. Chem. Soc.* **1999**, *121*, 882–883.
(280) Mehl, M. J.; Papaconstantopoulos, D. A. *Phys. Rev. B* **1996**, *54*, 4519–4530.